RL932

A COHERENT POLARIMETRIC MICROWAVE SCATTERING MODEL FOR GRASSLAND STRUCTURES AND CANOPIES

James Stiles

1996

A COHERENT, POLARIMETRIC MICROWAVE SCATTERING MODEL FOR GRASSLAND STRUCTURES AND CANOPIES

by

James Marion Stiles

A dissertation submitted in partial fulfillment
of the requirements for the degree of
Doctor of Philosophy
(Electrical Engineering)
in The University of Michigan
1996

Doctoral Committee:
Assistant Professor Kamal Sarabandi, Co-Chair
Professor Fawwaz T. Ulaby, Co-Chair
Professor Anthony W. England
Professor Linda Katehi
Professor Sushil Atreya

To my parents, William and Laveta Stiles, for their support and encouragement,

and in loving memory of my grandparents,

Thomas and Eula Lowry, and William and Marie Stiles.

ACKNOWLEDGEMENTS

I must first gratefully acknowledge and thank my dissertation committee for their help and support. My gratitude, however, is especially focused on my two advisors, Dr. Kamal Sarabandi and Dr. Fawwaz Ulaby, who have steadfastly supported me over the past five years in both financial and academic terms. With particular gratitude I thank Dr. Sarabandi for the tremendous amount of time he spent with me, at first patiently dealing with my extreme ignorance, and then in recent years just as patiently dealing with my long-winded orations. I hope by passing your knowledge onto my future students, I can repay you for this gift.

I wish also to express my sincere gratitude and affection to my fellow graduate students in the Radiation Laboratory. I have shared with you grueling work days, enlightening discussions, gratifying experiments, and most importantly, much hearty laughter. There are literally too many of you to mention, but I must specifically recognize my long-time office mates with whom I spent the large majority of the past five years. To Dr. John Galantowitz, Dr. John Kendra, Mr. Ed Kim, and Dr. Adib Nashashibi, I thank you for providing friendship and support - as well as for enduring my endless series of "fascinating" anecdotes. I also must express my gratitude to Dr. Leland Pierce, whose incredible knowledge of all things digital was an invaluable

contribution to my graduate school success.

I thank my friends and colleagues at Texas Instruments, who kept me on LOA status despite my many years in Michigan. A special thanks, however, must be given to my former boss, Mr. Dwayne Olson. Without your selfless help, and the skills I learned from you while at TI, I would have surely failed in this academic endeavor. I do not expect to ever again work with a finer man.

I struggle to adequately thank my family. Your support, love, and faith alone kept me going in the worst times. I include in this group my great friend, Mr. Phil Walker, who provided many memorable weekend diversions in the past years. Finally, especially, my parents; a portion of this degree should be conferred on you. I can never adequately express my love and gratitude for all you have done for me. This work is both mine and yours, it is ours together.

TABLE OF CONTENTS

LIST OF TABLES

LIST OF FIGURES

CHAPTER I

INTRODUCTION

Because of their fundamental importance to earth climate dynamics and the atmosphere's carbon cycle, forest vegetation has in recent years justifiably attracted the majority of interest in the field of microwave remote sensing of vegetation targets [14, 15, 8]. However, another vegetation class which must not be overlooked is the category of grassland vegetation, both natural and cultural. At approximately 30 million square kilometers, this vegetation type covers 20 percent of the earth's dry surface, accounting for more than 30 billion metric tons of total biomass. These facts alone attest to the importance of grassland targets to the overall understanding of earth's climatic, hydrologic, and atmospheric dynamics. An understanding on a global scale of the biophysical parameters which describe this vegetation is thus highly desirable, parameters which include soil moisture, biomass, and leaf area.

Additionally, a significant amount of the cultivated land on the earth's surface is occupied by members of the grass family. The most important of these crops are rice and wheat, however many other plants such as barely and oats are included in this category. Add to this the pastureland used to graze cattle and other domesticated animals, and it is readily apparent that a vast amount of the world's food supply is dependent, either directly or indirectly, on grassland vegetation. This fact leads to another motivation for determining on a global scale accurate and timely descriptions

of the earth's cultural grasslands; the detection of drought and desertification, and the prediction of crop yields to detect famine potential or to stabilize agricultural markets.

To obtain this global understanding, electromagnetic sensors can be placed on spaceborne platforms such as satellites. Sensors of this type include hardware operating in the optical, infrared, and millimeter wave spectral regions. However, the scope of this study is limited to microwave sensors only. It has been demonstrated that the backscattered energy from a microwave radar is sensitive not only to the biophysical parameters of vegetation, but to the parameters of the underlying soil surface as well. This sensitivity is a function of radar parameters such as frequency, incidence angle and polarization, and therefore multi-frequency polarimetric radars are desirable to obtain the maximum information about an illuminated vegetation target.

However, the difficulty arises when interpreting this backscattered data; mapping the scattering data correctly into a vegetation parameter space which includes the desired biophysical parameters. Adding to this problem is the fact that the backscattered energy is sensitive to *multiple* vegetation parameters, parameters which may be of little interests to the interpreter. Among these parameters are those associated with plant structure, an entire class of descriptors which can significantly if not dramatically effect the scattered energy. To accomplish this mapping, a necessary (although far from sufficient) step is to determine the relationship between *all* the biophysical parameters of a vegetation canopy to the observed backscattered data.

This relationship can be achieved by two means. The first is by observation; collecting scattering data over a sufficient collection of known targets to accurately define the relationship between scattering and target class. For simple targets with a small number of significant parameters, this method is possible and perhaps even

desirable. However, as the target class becomes more and more complex, this method becomes impractical, as no reasonably sized collection of observations can contain the information required to define the relationship between scattering and a complex target. In this case, deterministic scattering models must be implemented, scattering models which computationally evaluate the electromagnetic interaction with a physical analog of the vegetation structure. It is the goal of this study to produce such a model for grassland vegetation, to validate its performance, and to implement it to study the microwave backscattering from grass canopies.

1.1 Grassland Botany

Although grasses would seem to be the simplest of plant structures, the general plant family consists of thousands of species, exhibiting multiple sizes, shapes, and structures of varying complexity. It would be impossible to construct a model to accurately comprehend them all, so this study is limited to structures which can be described as a set or subset of the elements shown in Figure 1.1. This figure exhibits three elements; a stem or stalk element which protrudes from the ground, leaf elements which grow out from along the axis of the stem, and the caryopsis or grain which extends from the apex of the stalk. The grain is considered to be approximately cylindrical, whereas the leaf is assumed to be "blade" shaped. The stalk element can either be modeled as a circular cylinder or as a structure with a grass blade cross-section. These elements can be combined in various ways to model a variety of grassland canopies, as shown in Figure 1.2. The top illustration (a) shows a structure which is an accurate representation of such grass species as wheat, barley, oats, and fescue. The middle illustration (b) shows a structure suitable for modeling

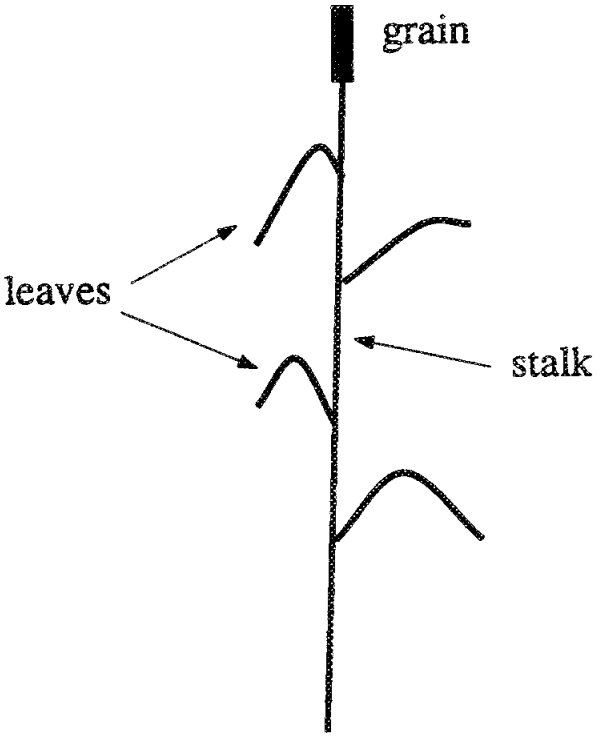

Figure 1.1: Illustration showing the basic structure of the grass model, including the stalk, grain, and leaf elements.

the previously mentioned grasses in their immature stages, before the grain element emerges from the plant. The final illustration (c) represents the simple grass blade structures which often make up the vegetation of prairies and savannahs.

1.2 Scattering Solutions

As vegetation is a random medium, that is a medium which can be described only in a statistical sense, the various techniques for determining the scattering from random media must be employed. Basically, these techniques can be divided into three categories, analytical wave theory, radiative transfer, and discrete scattering

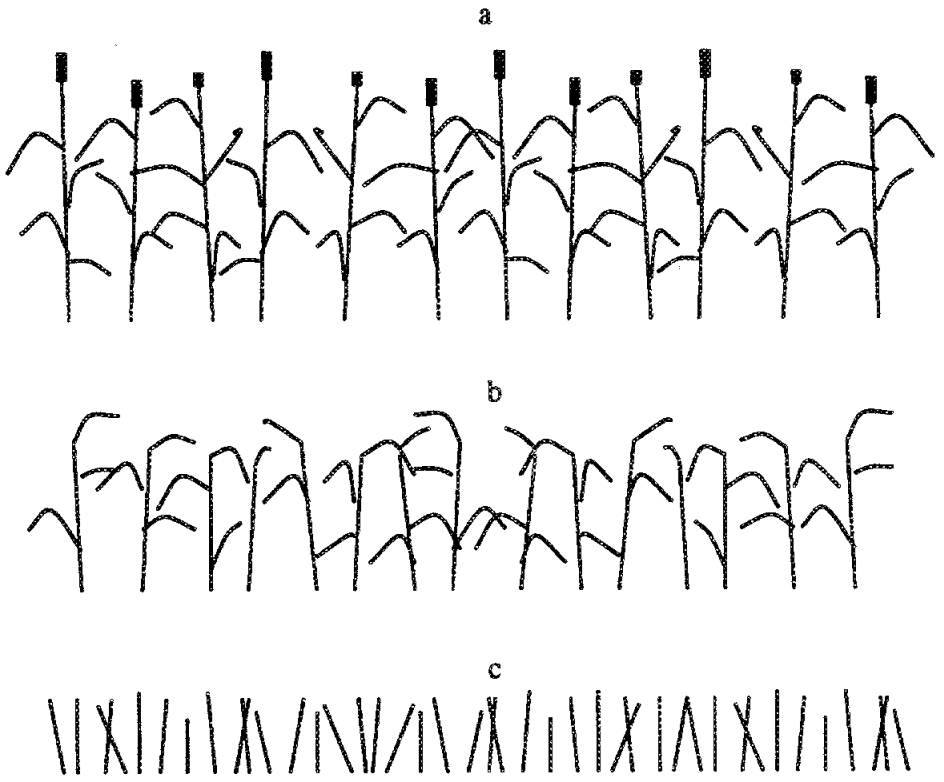

Figure 1.2: Illustration showing the various types of vegetation which can be modeled using (a) all three elements, (b) stalk and leaf elements, and (c) stalk (blade) elements only.

theory [30]. Analytical wave theory involves representing the scattering layer as an inhomogeneous dielectric. The value of the dielectric within the layer is modeled as a stochastic process of position variable $\bar{r}$, and thus defined in terms of its statistical moment as a function of position. The scattering solution is thus iteratively solved using successively higher statistical moments. This method is relevant to media such as sand and dry snow, where the dielectric at each point is on the order of mean and the correlation statistics can be accurately determined. However for vegetation, plant structure leads to complex correlation relations, and the dielectric contrast is large. As a result, multiple iterations would be required to provide an accurate solution, and therefore this technique is rarely applied to vegetation.

A technique which has been widely and successfully used for modeling vegetation is radiative transfer [3]. Radiative transfer is a heuristic solution which accounts for the power lost (from ohmic loss and scattering) and gained (from bistatic scattering) over an incremental propagation path ds through a random collection of scattering particles. In its scaler form, radiative transfer is defined by the following differential equation.

$$\frac{dI(\bar{r},\hat{s})}{ds} = -\kappa_e I(\bar{r},\hat{s}) + \int_{4pi} P(\hat{s},\hat{s}')I(\bar{r},\hat{s}')d\Omega' \tag{1.1}$$

The value κ_e is the extinction coefficient accounting for the loss, and $P(\hat{s},\hat{s})$ is the phase function describing the coupling of intensity $I(\bar{r},\hat{s})$ from direction $\hat{s}'$ into $\hat{s}'$. The phase function is determined from the averaged bistatic scattering coefficients of the particles which make up the layer, and the extinction coefficient is likewise dependent on the scattering of the individual particles. As this is an incoherent scattering solution (power, not fields are considered), the scattered fields from the

particles must be uncorrelated. Since the bistatic scattering coefficients of the individual elements in the collection is implemented in the solution, the effect of shape, structure and orientation of the particles is accounted for. For example, a radiative transfer solution for forest vegetation may model a tree as a collection of cylinders and disks of random sizes, shapes and orientations, representing branches, needles and leaves. In this way, the scattering layer is treated as a collection of individual (and uncorrelated) scatterers, and the radiative transfer solution seeks to describe their interaction with each other and the incident electromagnetic energy. As with analytic wave theory, equation(1.1) can be solved in an iterative manner, with the first iteration corresponding to the first-order, or single scattering terms. This first-order radiative transfer solution has been utilized in the majority of cases to model the microwave scattering from grasslands[34, 29, 1, 31].

The third method which will be considered is discrete scattering theory[30, chp6]. This method is similar to radiative transfer in that the scattering layer is considered to be a collection of particles of random shapes, sizes, and orientations, each described by a bistatic scattering coefficient. However, in this case the scattered *fields* are considered, and the total scattered field from the scattering layer is the *coherent* summation of the scattered fields from each element. Thus, instead of determining the extinction coefficient for the layer, an effective propagation constant, describing the mean or coherent wave in the layer must be determined. One advantage of this approach is that the scattered fields from dissimilar elements no longer must be uncorrelated. For example, Yueh et al.[37] demonstrated a coherent scattering model for soybeans where the correlation between the constituents of a single plant was considered. For grass scattering, this method has also been used to determine the incoherent, first-order scattering power, a solution which mathematically is identical

to first-order radiative transfer[25].

1.3 Applications to Grassland Scattering

When applying any of these scattering techniques to grassland canopies, several unique problems arise which must be overcome. The first is the structure of the plant constituents. When modeling the scattering from forests, trees are often modeled as a random collection of circular cylinders. This is of course a good analog to the actual structure of a tree, the branch being roughly circular and straight before subdividing into smaller branches, each in turn oriented in a new and random direction. This model has the added benefit in that the bistatic scattering from a circular dielectric cylinder is well known.

Determining an equivalent structural analog for grass canopies, however, is problematic. The elements of a grass canopy (with the exception of the grain) can be considered as long, thin dielectric elements. However, unlike tree branches, these elements are often neither straight, nor circular in cross-section. For example, the leaf and stalk elements are often have the "v" shaped cross-section of a grass-blade, and the leaves almost always display significant axial curvature, resulting often in a complex curve of the type displayed in Figure 1.1. Additionally, the width of leaf elements often taper at the end of the structures, coming to a point at the end, in a shape similar to that of a boat or ship. Thus, it becomes difficult to approximate the structure of grass plants as a collection of simple canonical elements where the scattering is well known. Investigators have generally modeled these elements as circular cylinders, ellipsoids, or ellipse shaped discs [25, 29, 1, 34]. However, the accuracy of these models is at least open to question as neither considers curvature nor blade

shapes.

In addition, the stalk element adds even more significant problems when attempting to model grass canopies. Again comparing the problem to forests, the cylinders representing the branches of a tree are randomly distributed throughout a scattering layer which is much larger than the individual elements. Instead, as demonstrated by the illustration of Figure 1.2, the stalk element begins at the bottom of the scattering layer and traverses vertically to the top. In the vertical direction, these structures are barely random in the vertical dimension, and certainly not random over a distance equal to the canopy height. Although often treated as such[34, 25, 29], modeling these elements as random over the canopy height actually reflects the case demonstrated in Figure 1.3.

It is more strictly correct to define the locations of scatterers by their local reference, so in the case of long stalks the scattering layer could be defined as a thin band in the center of the scattering layer (Figure 1.4), providing that the local reference is defined as the center of the stalk element. However, the local reference is completely arbitrary and thus the other illustration of Figure 1.4 is equally valid. The problem thus occurs when attempting to applying radiative transfer to this definition. The intensity of the incident wave on the stalks as determined by radiative transfer would be far greater in case (b) than in case (a), as for case (b) the attenuation due to the vegetation would not be considered. Thus, for radiative transfer, or any model where the stalk elements are considered as point scatterers, the solution is dependent on the arbitrary definition of the stalk reference. If the constituent elements of a scattering layer are small in comparison to the scattering layer, this ambiguity causes little problem, as the intensity of the incident wave is approximately constant over the scattering element. However, for elements such as the stalk, the coherent wave

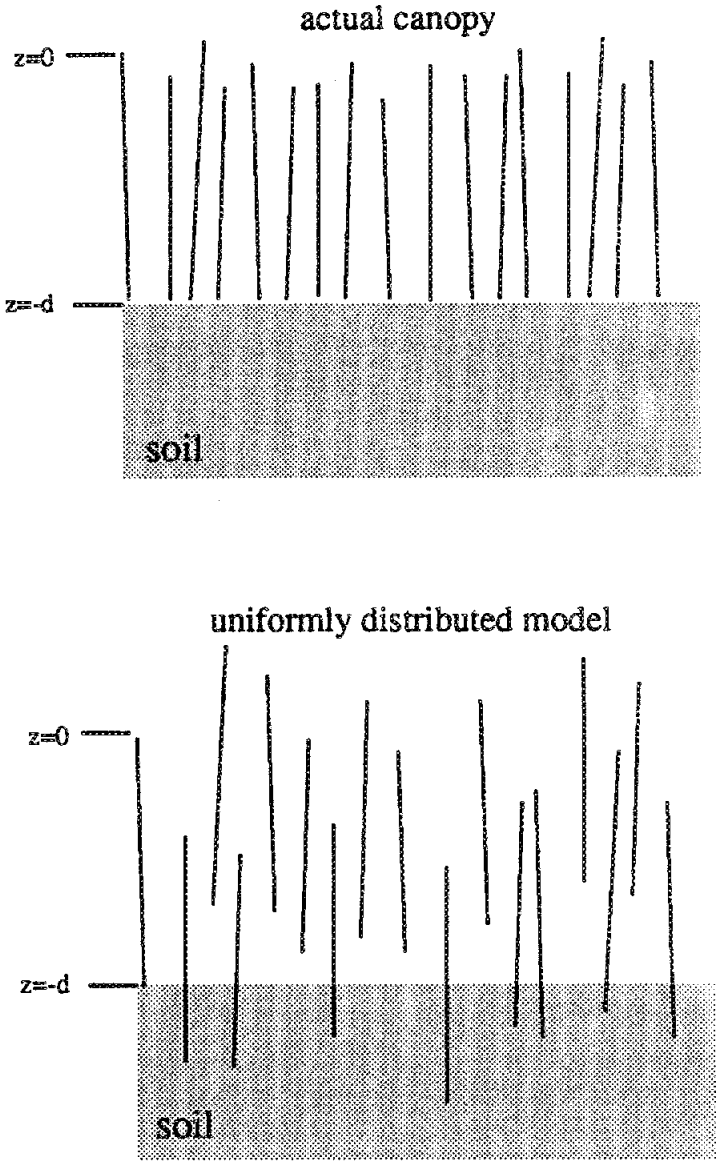

Figure 1.3: Illustration showing the structure of a grass canopy, as compared to the structure actually modeled if a uniform distribution is applied over the canopy height.

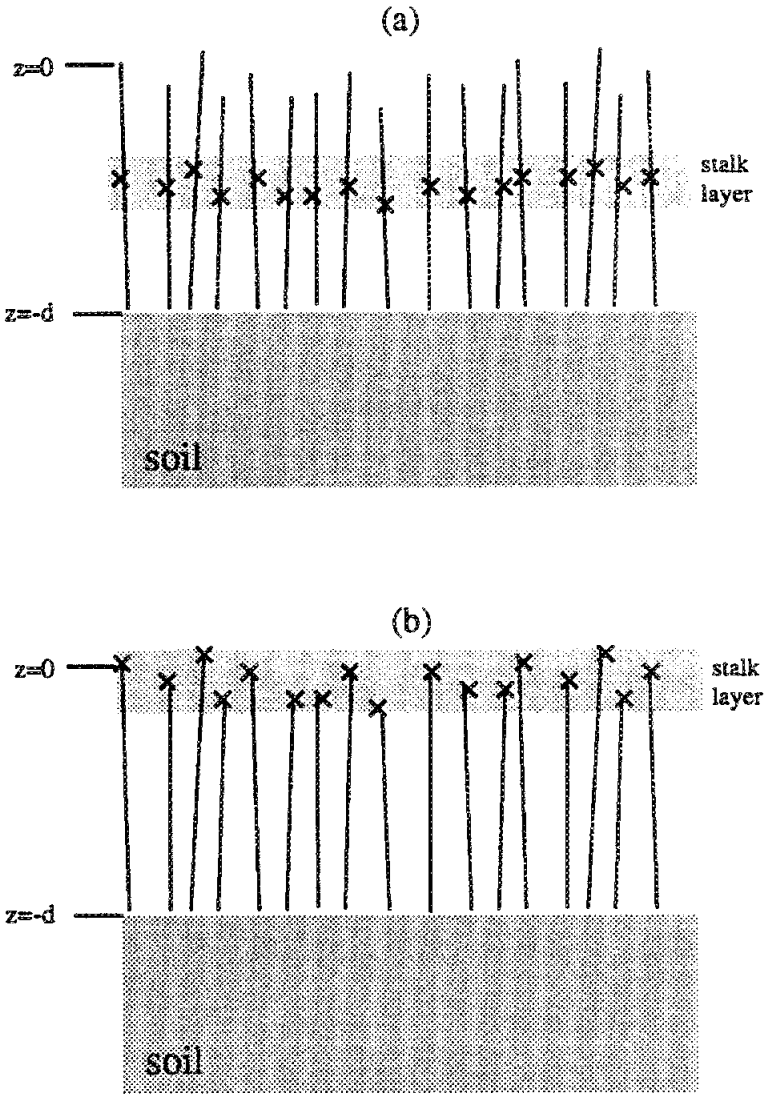

Figure 1.4: Illustration showing how the stalk layer is dependent on the arbitrary definition of the local scattering reference. Figure (a) shows the layer if the reference is at the center; (b) where the reference is defined at the top of the stalk.

intensity can change markedly from the top of the stalk to the bottom.

This leads the the next problem associated with grassland scattering, that of the non-uniform illumination of grassland elements. A long thin element of a grassland canopy, such as the stalk or even the leaf, can extend from the top of the vegetation to near the bottom. Since vegetation attenuates the incident wave (with both absorption and scattering), the coherent wave illuminating the element is non-uniform, that is the intensity of the wave illuminating the element varies over the scattering element. Moreover, this variation is a function of the overall canopy description (i.e. the parameters which influence extinction), as well as the position and orientation of the element within the layer. Thus, the concept of a scattering matrix element is eliminated, as the scattering from the element is dependent on more than just the parameters *of* the element, and the incident wave on the particle is not a uniform plane wave, but instead is arbitrary. A scattering matrix can be defined for the overall system; an element with a specific location and orientation in a specific attenuating layer, but not for the particle itself. Note that the scattering from an long element within this layer is not simply an attenuated version of the scattering in free-space, the arbitrary illumination will modify the form, as well as the magnitude of the induced currents, thus modifying the overall form of the bistatic scattering pattern.

Another problem associated with the large length of grass elements as compared to the canopy height is revealed when developing a formulation for extinction. The extinction through a canopy is generally determined by evaluating the energy lost (both absorption an scattering) when the coherent wave encounters a particle within the layer. A problem occurs when applying this logic to elements such as stalks, where the coherent wave propagating through a given distance of the canopy layer encounters not multiple particles, but merely a fraction of the entire element. In other words,

the difficulty lies in determining the extinction due to propagation, for example, 25, 50, or 75 percent down the stalk length. This problem is further complicated by the fact that the optical theorem, commonly used to evaluate particle extinction, is found from the *far-field* forward scattered field, whereas the propagation path through the vegetation is often far shorter than the far-field distance of the vertical stalks.

Finally, perhaps the most significant problem when dealing with grass canopies is due to potential for the scattered fields from dissimilar elements to be correlated. Even at the lowest frequencies of the microwave region, the size of forest vegetation is generally on the order of multiple wavelengths. This electrically large scattering volume, coupled with the complex and random nature of tree structures, lead to a case where the scattered fields from dissimilar scattering elements are virtually uncorrelated. However, both the stature and the structure of grassland elements lead to a case where field correlation can occur. The small stature of grasses can result in an electrically small scattering volume in the microwave region, and the simple structure of grass plants can lead to significant physical correlations between dissimilar elements (i.e. the grain is always at the apex of the stalk). As a result, the total scattering power cannot be reduced to a summation of the scattering power from each separate plant element, the plant structure as a whole must be considered.

To illustrate this, consider two scatterers lying in an arbitrary scattering V volume. Assuming no coupling between the elements, the scattering from the volume can be written as:

$$S_V = S_1 e^{ik_0 \hat{k} \cdot \bar{r}_1} + S_2 e^{ik_0 \hat{k} \cdot \bar{r}_2} \tag{1.2}$$

where S_1 represents the scattering from the first element relative to its local coordi-

nate system, and the complex exponential term represents the relative phase of the scatterer lying at location $\bar{r}_1$. Now assume that size, shape, orientation and location of the two scatterers are random variables with know statistics, and the *average* scattering power from the volume is thus:

$$\langle |S_V|^2 \rangle = \langle |S_1|^2 \rangle + \langle |S_2|^2 \rangle + 2Re\Big\{ \langle S_1 \rangle \langle S_2^* \rangle \langle e^{\imath k_0 \hat{k} \cdot (\bar{r}_1 - \bar{r}_2)} \rangle \Big\} \tag{1.3}$$

where it is assumed that the size,shape, and orientation parameters are independent of location and the other scatterer. The first two terms of the above equation are simply the average scattered power of each element individually. The remaining term is the inner product or coherent term, since it involves the relative phases between the two elements. If, as is often the case, the locations of the two scatterers are independent, the phase term $\langle \exp[\imath k_0 \hat{k} \cdot (\bar{r}_1 - \bar{r}_2)] \rangle$ can be separated such that the term equals $\langle \exp[\imath k_0 \hat{k} \cdot \bar{r}_1] \rangle \langle \exp[-\imath k_0 \hat{k} \cdot \bar{r}_2] \rangle$. If the location of each scatterer is uniformly distributed throughout the volume, and the scattering volume has significant electrical size (greater than a wavelength) in all dimensions, the value of $\langle \exp[-\imath k_0 \hat{k} \cdot \bar{r}_2] \rangle$ will be very small, and the coherent term of (1.3) will be insignificant when compared to the other two terms. These two terms can be considered as the incoherent scattering power, as the relative phases of the two scattering elements do not contribute to the solution, only the absolute scattering power of the elements are relevant. Thus, for this case, incoherent scattering formulations such as radiative transfer are applicable. However, if the scattering volume is electrically small, or the elements are physically correlated, the coherent term of (1.3) can be a significant portion of the total scattered power.

1.4 Research Goals

The goal of this study is to therefore develop a microwave scattering model which resolves these problems and accurately predicts the polarimetric microwave backscattering of grassland vegetation. More specifically, this study will focus on developing a scattering model with three main attributes, *fidelity*, *accuracy*, and *utility*.

1.4.1 Model Fidelity

The attribute of fidelity refers to the modeling of the grass structure, the physical analog to which the electromagnetic scattering theory is applied. This attribute is arguably the weakest trait of many scattering models for natural targets. The formulation for the electromagnetic scattering from a layer of cylinders and discs may be nearly perfect, but the relevance of a layer of cylinders and discs to the natural target might be questionable. This fidelity not only includes the physical structure of the elements, but the statistical description of the medium as well. Therefore, a goal of this investigation is to accurately model the structure and statistics of grassland vegetation. Examples of this include the blade shaped cross-section of the stalk or leaf elements, the complex curvature of the leaf elements, the distribution of plants within the scattering layer, the physical correlation of the elements of a grass plant, and the physical correlation of the grass plants in a canopy.

1.4.2 Model Accuracy

The attribute of accuracy corresponds to the electromagnetic scattering formulation which will be applied to the physical analog. The initial problem arises from the complexity of this analog. The scattering from circular cylinders and discs is known,

however, the evaluation of scattering from a leaf blade, a structure with both complex cross-section and curvature, does not appear in the literature and thus its formulation must be derived. Additionally, these elements can be illuminated by an non-uniform wave, and an accurate scattering formulation for this situation must be determined.

As discussed in the previous section, coherent effects can be significant for microwave scattering from grasslands. Thus, a formulation for these terms must be developed and accurately implemented. To accomplish this, the overall canopy scattering formulation must be coherent, i.e. fields rather than power must be used, and thus a discrete elements scattering approach will be taken. This introduces the a new set of problems, as the coherent model requires that phase be used and accurately evaluated. Finally, the extinction of the coherent wave as it propagates through the scattering layer must be properly evaluated, a difficult problem as the elements the grassland canopy are often of the same size as the vegetation layer.

1.4.3 Model Utility

One reason that greater accuracy and fidelity is not often added to vegetation scattering models is the fear of reducing model *utility*. The attribute of utility is defined as any characteristic which increases the usefulness of the scattering model. A chief characteristic is computational speed; the usefulness of a model is dependent on the volume of information produced by a model in a given time, as well as its accuracy. By adding fidelity and accuracy to the model, the computation time will inevitably suffer. However, the trade may be worthwhile if the improvement in model accuracy outweighs the reduction in speed. A model which instantaneously produces erroneous data is no more useful than a model which takes forever to calculate a perfect solution. Thus, solutions will be sought which increase computational speed

while minimizing the impact to model accuracy and utility.

Another aspect to the model utility is the parameterization of the model. That is, how many input parameters are required to specify vegetation scattering. For example, to define the structure of a straight circular cylinder, only two parameters are required, diameter and length. However, how many parameters are required to define the arbitrary curvature and cross-section of a leaf element? Clearly a method must be determined to parameterize a leaf element with just a few parameters while still preserving the information about the structure of the leaf. The approach will thus be to add fidelity and accuracy first, and then seek methods to increase utility while minimizing its impact on fidelity and accuracy.

1.5 Dissertation Outline

This dissertation consists of six major chapters. Chapter 2 provides a scattering formulation for the long thin dielectric elements found in grassland vegetation, a formulation which is valid for elements with axial curvature and non-circular cross-section. This solution will likewise be modified to handle to case of a non-uniform incident wave.

Chapter 3 uses the formulation of Chapter 2 to solve for the specific case of blade shape elements. A general blade shape is defined and parameterized, and a polynomial relationship is determined between these blade parameters and the corresponding numeric solutions using the formulation of Chapter 2. In this way, the utility of the formulation is increased while preserving the fidelity and accuracy.

Chapter 4 provides the scattering solution for a long thin cylinder in an extinction layer over a dielectric half-space. Using the formulation of Chapter 2, a coherent

solution is determined for the propagation and scattering in this layer, accounting for four first-order scattering mechanisms. Additionally, the complex extinction of a layer of long, thin elements is determined.

Chapter 5 utilizes the results of Chapter 4 to construct a scattering formulation for the grass plant of Figure 1.1. The scattering covariance terms are presented, as well as the correlation terms of the dissimilar elements of the grass plant. A scattering formulation for an entire grass canopy is then presented, including a coherent model for the row structures associated with cultural grasses.

Chapter 6 presents the data collected during an experiment which observed the growth of a wheat field with a multi-frequency polarimetric scatterometer. Both scattering and ground truth data is presented, along with the methods and procedures for collecting each.

Chapter 7 validates the scattering model by comparing the results of its software implementation with the measured data of Chapter 6. The accuracy of the model over frequency, polarization, and incidence angle is examined, and the effect of the coherent terms is quantified. Additionally, the extinction predictions are compared with measured data from other sources, and the effect of structural parameters such as cross-section and curvature is examined.

CHAPTER II

A SCATTERING MODEL FOR THIN DIELECTRIC CYLINDERS OF ARBITRARY CROSS-SECTION AND ELECTRICAL LENGTH

The initial problem which must be solved in regards to grassland scattering, is to determine the scattering behavior of a single element within the canopy. Aside from the grain element, the grassland constituents can be described generally as long, thin dielectric cylinders of arbitrary cross-section. In the microwave region, the radius of these cylinders are usually very small compared to the incident wavelength, whereas the electrical length may take any value. This generality in structure precludes the implementation of specific scattering solutions. The arbitrary value of electrical length $k\ell$ eliminates asymptotic solutions such as Rayleigh ($k\ell << 1$) or Physical Optics ($k\ell >> 1$), and the generally non-canonical cross-sections leave inapplicable solutions for circular and elliptical structures. Thus, a scattering solution is required which accurately comprehends these arbitrary particles, and additionally, a solution which is applicable to cylinders with axial curvature.

One relevant analysis is that of Sarabandi and Senior [21], who explicitly derived the scattering solution of an electrically thin but *infinitely* long dielectric cylinder

of arbitrary cross-section. This work provides a general solution for the internal electric fields, and demonstrates that the far-field scattering can be expressed in terms of a dipole moment per unit length. Using the high frequency approximation, the scattering from a *finite* but electrically long ($k\ell >> 1$) cylinder can be approximated by truncating the solution of the equivalent infinite length case. Although this solution is correct for arbitrary cross-sections, its validity can apparently be justified only for cylinders of large electrical length $k\ell$.

A solution which is often employed to model *circular* cylinders of smaller $k\ell$ is the Generalized Rayleigh-Gans approximation (GRG) introduced by Schiffer and Thielheim [26]. In this approximation, terms of the Borne (or Rayleigh-Gans) approximation are modified by the Rayleigh solution of a long thin spheroidal particle. The GRG approximation is said to be valid for electrically small, circular dielectric cylinders, provided that their normalized length ℓ/a is very large. No constraint is explicitly placed on electrical length $k\ell$. The GRG approximation was presented by first hypothesizing the solution and then successfully comparing the results to the asymptotic solutions known for both the long ($k\ell << 1$) and short ($k\ell >> 1$) wavelength cases. On this basis, it was inferred that GRG validity is independent of electrical length. Whereas this presentation provides evidence as to the accuracy of the GRG approximation, it does not *prove* its general validity; the scattering from objects with dimensions on the order of a wavelength is often quite different from either the short or long wavelength cases. In addition, the analysis does not address the issue of cylinder cross-section, only circular cylinders were considered.

In this paper, a scattering solution for the general case of an electrically thin dielectric cylinder of arbitrary cross-section and electrical length will be presented. The solution will be explicitly shown to be the unique asymptotic solution to the

scattering problem as the electrical radius ka converges to zero. A moment-method solution will likewise be implemented to quantify the convergence of this asymptotic solution.

2.1 An Analysis of Thin Cylinder Scattering

Consider an *infinite* length dielectric cylinder lying along the z-axis. This cylinder is illuminated by a uniform plane wave given as:

$$\mathbf{E}^i(\bar{r}) = \hat{e}\, e^{ik_0 \hat{k}^i \cdot \bar{r}} \tag{2.1}$$

where $\hat{e} \cdot \hat{k}^i = 0$, $\hat{e} = e_x\hat{x} + e_y\hat{y} + e_z\hat{z}$, and $\hat{k}^i$ is the propagation direction vector:

$$\hat{k}^i = \sin\beta\cos\phi\ \hat{x} + \sin\beta\sin\phi\ \hat{y} + \cos\beta\ \hat{z} \tag{2.2}$$

If the maximum radius of this cylinder(a) is small compared to a wavelength ($ka << 1$), then the total electric field in the interior of the cylinder can be written as [21]:

$$\mathbf{E}(\bar{r}) = \left(e_x\ \mathbf{E}_1(\bar{\rho}) + e_y\ \mathbf{E}_2(\bar{\rho}) + e_z\ \hat{z}\right)\ e^{ik_0\cos\beta\ z} \tag{2.3}$$

The terms $\mathbf{E}_1(\bar{\rho})$ and $\mathbf{E}_2(\bar{\rho})$ are Rayleigh scattering solutions describing the electric fields transverse to the z-axis. The first expression $\mathbf{E}_1(\bar{\rho})$, is the interior field induced by a unit amplitude, x-directed incident field ($\mathbf{E}^i = \hat{x}$), while the second solution is induced by similar y-directed field. In general, $\mathbf{E}_1(\bar{\rho})$ and $\mathbf{E}_2(\bar{\rho})$ contain both $\hat{x}$ and $\hat{y}$ components, with the total transverse field, as shown in equation(2.3), consisting of the superposition of the two solutions, weighted by the amplitude of the relevant

incident field component. Since the Rayleigh scattering formulation is essentially an electrostatic problem over the cylinder cross-section, its solution can be expressed in the form of an electro-static potential:

$$\mathbf{E}_1(\bar{\rho}) = -\nabla_t \Phi_1(\bar{\rho}) \quad \text{and} \quad \mathbf{E}_2(\bar{\rho}) = -\nabla_t \Phi_2(\bar{\rho}) \tag{2.4}$$

where the transverse gradient operator ∇_t is defined as:

$$\nabla_t = \hat{x}\frac{\partial}{\partial x} + \hat{y}\frac{\partial}{\partial y} \tag{2.5}$$

The potentials $\Phi_1(\bar{\rho})$ and $\Phi_2(\bar{\rho})$ are specified by Sarabandi and Senior as the solution to the following integral equations [21]:

$$\begin{aligned} \Phi_1(\overline{\rho}) + x + b_1 &= \frac{(\epsilon_r - 1)}{2\pi} \int_A \nabla_t' \Phi_1(\overline{\rho}') \cdot \nabla_t' \ln|\overline{\rho} - \overline{\rho}'| \, dA' \\ \Phi_2(\overline{\rho}) + y + b_2 &= \frac{(\epsilon_r - 1)}{2\pi} \int_A \nabla_t' \Phi_2(\overline{\rho}') \cdot \nabla_t' \ln|\overline{\rho} - \overline{\rho}'| \, dA' \end{aligned} \tag{2.6}$$

where b_1 and b_2 are arbitrary constants and A defines the cylinder cross section. Equation(2.3) can thus be written as:

$$\mathbb{E}(\bar{r}) = \Big(- e_x \, \nabla\Phi_1(\bar{\rho}) - e_y \, \nabla\Phi_2(\bar{\rho}) + e_z \, \hat{z} \Big) e^{\imath k_0 \cos\beta z} \tag{2.7}$$

Using the integral equations of (2.6), an analytical solution for a circular cross-section can be found:

$$-\nabla\Phi_1(\bar{\rho}) \; = \; -\nabla\Phi_2(\bar{\rho}) \; = \; \frac{2}{(\epsilon_r + 1)} \tag{2.8}$$

This solution is identical to the solution for a spheroidal Rayleigh particle as its normalized length ℓ/a converges to infinity [26]. As such, equation (2.7) for a circular cylinder is identical to that provided by the GRG approximation, namely

$$\mathbf{E}(\bar{r}) = \left(e_x \frac{2}{(\epsilon_r + 1)} + e_y \frac{2}{(\epsilon_r + 1)} + e_z \hat{z}\right) e^{\imath k_0 \cos\beta z} \tag{2.9}$$

Although the formulations for both approximations agree (for a circular cylinder), the general validity regions are in conflict. The GRG approximation claims that the above expression is valid for all electrical lengths $k\ell$, whereas the infinite cylinder approximation has only a high-frequency justification when $k\ell >> 1$. The requirement for the normalized cylinder length ($\ell/a >> 1$) is implied in the infinite cylinder approximation (since $ka << 1$, $k\ell/ka >> 1$), and explicitly required by GRG.

If the assertions of the GRG approximation are correct, it suggests that the validity limits placed on the truncated infinite cylinder solution are too restrictive. That is, in addition to the high-frequency limit ($k\ell >> 1$), the infinite cylinder solution could likewise be applied to finite cylinders with electrical lengths in the resonance ($kl \approx 1$) and Rayleigh ($kl << 1$) regions. However, given the heuristic nature of the GRG approximation, this is strictly conjecture, particularly with regard to non-circular cross-sections. Thus, we seek to determine under what conditions equations (2.3) and (2.6) define a valid scattering solution for thin, finite dielectric cylinders. Are they valid only for electrically long cylinders, or does the validity extend to cylinders of other $k\ell$? If so, is this true only for circular cylinders, or is the solution generally valid for all cross-sections?

If a formulation $\mathbf{E}(\bar{r})$ is a valid electromagnetic solution, then it will uniquely satisfy the integral equation which describes the scattering problem, $\mathbf{E}(\bar{r}) = \mathbf{E}^i(\bar{r}) +$

$\mathbf{E}^s(\bar{r})$, where the scattered field $\mathbf{E}^s(\bar{r})$ is given as:

$$\mathbf{E}^s(\bar{r}) = \left[k_0^2 + \nabla\nabla\cdot\right] \int_V (\epsilon_r - 1)\, \mathbf{E}(\bar{r}')\, g_0(|\bar{r} - \bar{r}'|)\, dv' \tag{2.10}$$

and $g_0(|\bar{r} - \bar{r}'|)$ is the free space Green's function. For a given type of scatterer (e.g. thin cylinders), a function $\mathbf{E}(\bar{r})$ may in general satisfy the integral equation, or perhaps satisfy only under specific conditions, such as a circular cross-section or infinite electrical length. Therefore, to determine the validity of the truncated infinite cylinder solution, equations (2.3) and (2.6) will be inserted into the integral equation for a thin finite cylinder and evaluated. The conditions under which the integral equation is satisfied will then be determined, thus defining the validity regions of this solution.

To begin, the electric field scattered from any dielectric body can be represented in terms of Hertz potentials as:

$$\mathbf{E}^s(\bar{r}) = \nabla\nabla\cdot\mathbf{\Pi}^e(\bar{r}) + k_0^2\, \mathbf{\Pi}^e(\bar{r}) \tag{2.11}$$

where $\mathbf{\Pi}^e(\bar{r})$ is the electric Hertz potential, defined as:

$$\mathbf{\Pi}^e(\bar{r}) = \frac{\imath Z_0}{k_0} \int_V \mathbf{J}(\bar{r}')\, G_0(|\bar{r} - \bar{r}'|)\, dv' \tag{2.12}$$

and $G_0(|\bar{r}-\bar{r}'|)$ is the free space Green's function. Since a dielectric body is considered, the current $\mathbf{J}(\bar{r})$ is the polarization current induced in the body:

$$\mathbf{J}(\bar{r}) = -\imath k_0 Y_0 (\epsilon_r - 1)\mathbf{E}(\bar{r}) \tag{2.13}$$

Combining (2.11), (2.12) and (2.13), the scattered field field expression can be written as:

$$\mathbf{E}^s(\bar{r}) = \nabla\nabla\cdot\int_V(\epsilon_r-1)\,\mathbf{E}(\bar{r}')\,G_0(|\bar{r}-\bar{r}'|)\,dv' + k_0^2\int_V(\epsilon_r-1)\,\mathbf{E}(\bar{r}')\,G_0(|\bar{r}-\bar{r}'|)\,dv' \quad (2.14)$$

The first term can be re-written using the identity:

$$\begin{aligned}\nabla\cdot[\mathbf{E}(\bar{r}')\,G_0(|\bar{r}-\bar{r}'|)] &= \mathbf{E}(\bar{r}')\cdot\nabla G_0(|\bar{r}-\bar{r}'|)\\ &= -\mathbf{E}(\bar{r}')\cdot\nabla' G_0(|\bar{r}-\bar{r}'|)\\ &= G_0(|\bar{r}-\bar{r}'|)\,\nabla'\cdot\mathbf{E}(\bar{r}') - \nabla'\cdot[\mathbf{E}(\bar{r}')\,G_0(|\bar{r}-\bar{r}'|)] \quad (2.15)\end{aligned}$$

However, given that the divergence of the electric field is zero, this reduces to:

$$\nabla\cdot[\mathbf{E}(\bar{r}')\,G_0(|\bar{r}-\bar{r}'|)] = -\nabla'\cdot[\mathbf{E}(\bar{r}')\,G_0(|\bar{r}-\bar{r}'|)] \quad (2.16)$$

The scattered field can thus be written as:

$$\mathbf{E}^s(\bar{r}) = -(\epsilon_r-1)\nabla\int_V\nabla'\cdot[\mathbf{E}(\bar{r}')\,G_0(|\bar{r}-\bar{r}'|)]\,dv' + (\epsilon_r-1)k_0^2\int_V\mathbf{E}(\bar{r}')\,G_0(|\bar{r}-\bar{r}'|)\,dv' \quad (2.17)$$

Implementing the divergence theorem, the first volume integral can be represented as as surface integral:

$$\mathbf{E}^s(\bar{r}) = -(\epsilon_r-1)\,\nabla\int_S\hat{n}'\cdot\mathbf{E}(\bar{r}')\,G_0(|\bar{r}-\bar{r}'|)\,ds' + (\epsilon_r-1)\,k_0^2\int_V\mathbf{E}(\bar{r}')\,G_0(|\bar{r}-\bar{r}'|)\,dv' \quad (2.18)$$

Likewise, moving the gradient operator into the integral to operate on $G_0(|\bar{r}-\bar{r}'|)$ gives:

$$\nabla \int_S \hat{n}' \cdot \mathbf{E}(\bar{r}')\, G_0(|\bar{r}-\bar{r}'|)\, ds' = \int_S \hat{n}' \cdot \mathbf{E}(\bar{r}')\, \nabla G_0(|\bar{r}-\bar{r}'|)\, ds'$$
$$= -\int_S \hat{n}' \cdot \mathbf{E}(\bar{r}')\, \nabla' G_0(|\bar{r}-\bar{r}'|)\, ds' \tag{2.19}$$

However,

$$\nabla' G_0(|\bar{r}-\bar{r}'|) = \frac{\partial G_0(|\bar{r}-\bar{r}'|)}{\partial|\bar{r}-\bar{r}'|}\ \nabla'|\bar{r}-\bar{r}'|$$
$$= \left(\imath k_0 - \frac{1}{|\bar{r}-\bar{r}'|}\right) G_0(|\bar{r}-\bar{r}'|)\, \nabla'|\bar{r}-\bar{r}'| \tag{2.20}$$

Since

$$\nabla'|\bar{r}-\bar{r}'| = \frac{-(\bar{r}-\bar{r}')}{|\bar{r}-\bar{r}'|} \tag{2.21}$$

the gradient of the free space Green's function can be written as:

$$\nabla' G_0(|\bar{r}-\bar{r}'|) = \frac{-\imath k_0\, G_0(|\bar{r}-\bar{r}'|)\,[\bar{r}-\bar{r}']}{|\bar{r}-\bar{r}'|} + \frac{G_0(|\bar{r}-\bar{r}'|)\,[\bar{r}-\bar{r}']}{|\bar{r}-\bar{r}'|^2} \tag{2.22}$$

Evaluating the derivatives and applying the divergence theorem, the previous

expression is presented as:

$$\begin{aligned}\mathbf{E}^s(\bar{r}) = &\frac{k_0^2(\epsilon_r-1)}{4\pi}\int_V \mathbf{E}(\bar{r}')\,\frac{e^{\imath k_0|\bar{r}-\bar{r}'|}}{|\bar{r}-\bar{r}'|}\,dv' \\ &- \frac{\imath k_0(\epsilon_r-1)}{4\pi}\int_S \hat{n}'\cdot\mathbf{E}(\bar{r}')\,\frac{e^{\imath k_0|\bar{r}-\bar{r}'|}}{|\bar{r}-\bar{r}'|^2}[\bar{r}-\bar{r}']\,ds' \\ &+ \frac{(\epsilon_r-1)}{4\pi}\int_S \hat{n}'\cdot\mathbf{E}(\bar{r}')\,\frac{e^{\imath k_0|\bar{r}-\bar{r}'|}}{|\bar{r}-\bar{r}'|^3}[\bar{r}-\bar{r}']\,ds'\end{aligned} \tag{2.23}$$

where S defines the surface of the cylinder. To emphasize the dependence of electrical size on scattering, the variables kx, ky, and kz are substituted for the quantities k_0x, k_0y, and k_0z. The integral can therefore be equivalently written as:

$$\begin{aligned}\mathbf{E}^s(\overline{kr}/k_0) = &\frac{(\epsilon_r-1)}{4\pi}\int_{k^3V} \mathbf{E}(\overline{kr}'/k_0)\,\frac{e^{\imath|\overline{kr}-\overline{kr}'|}}{|\overline{kr}-\overline{kr}'|}\,dk^3v' \\ &- \frac{\imath(\epsilon_r-1)}{4\pi}\int_{k^2S} \hat{n}'\cdot\mathbf{E}(\overline{kr}'/k_0)\,\frac{e^{\imath|\overline{kr}-\overline{kr}'|}}{|\overline{kr}-\overline{kr}'|^2}\left(\overline{kr}-\overline{kr}'\right)\,dk^2s' \\ &+ \frac{(\epsilon_r-1)}{4\pi}\int_{k^2S} \hat{n}'\cdot\mathbf{E}(\overline{kr}'/k_0)\,\frac{e^{\imath|\overline{kr}-\overline{kr}'|}}{|\overline{kr}-\overline{kr}'|^3}\left(\overline{kr}-\overline{kr}'\right)\,dk^2s'\end{aligned} \tag{2.24}$$

2.1.1 TE Solution

For a cylinder lying along the z-axis, an incident plane wave with an electric field transverse to the cylinder axis can be described within the thin cylinder as:

$$\begin{aligned}\mathbf{E}^i(\bar{r}) &= -\left(\sin\phi_i\,\hat{x} - \cos\phi_i\,\hat{y}\right)e^{\imath k_0\hat{k}^i\cdot\bar{r}} \\ &\approx -\left(\sin\phi_i\,\hat{x} - \cos\phi_i\,\hat{y}\right)e^{\imath k_0 z\cos\beta}\end{aligned} \tag{2.25}$$

within the thin cylinder. Comparing equations (2.25) and (2.1), the hypothesized internal field (2.7) becomes:

$$\mathbf{E}(\overline{r}) = \Big(\sin\phi_i \; \nabla_t \Phi_1(\overline{\rho}) - \cos\phi_i \; \nabla_t \Phi_2(\overline{\rho}) \Big) e^{\imath k_0 z \cos\beta} \tag{2.26}$$

Again performing the substitution $\overline{kr} = k_0 \, \overline{r}$, the above expression can be equivalently rewritten as:

$$\mathbf{E}^{2d}(\overline{r}) = \Big(\sin\phi_i \; \nabla_{kt} \Phi_1(\overline{k\rho}/k_0) - \cos\phi_i \; \nabla_{kt} \Phi_2(\overline{k\rho}/k_0) \Big) e^{\imath kz \cos\beta} \tag{2.27}$$

The operator ∇_{kt} is a result of the variable substitution implemented on ∇_t, and is defined as:

$$\nabla_{kt} = \hat{x} \frac{k_0 \partial}{\partial kx} + \hat{y} \frac{k_0 \partial}{\partial ky} \tag{2.28}$$

Without any loss in generality, ϕ_i is assumed to be $-\pi/2$, thus inserting equation (2.26) into (2.24) gives:

$$\begin{aligned}
\mathbf{E}^s(\overline{kr}/k_0) = & -\frac{(\epsilon_r - 1)}{4\pi} \int_{k^2 A} \nabla_{kt} \Phi_1(\overline{k\rho}'/k_0) \int_{k\ell} \frac{e^{\imath kz' \cos\beta} \; e^{\imath |\overline{kr} - \overline{kr}'|}}{|\overline{kr} - \overline{kr}'|} dkz' dk^2{}_{A'} \\
& + \frac{\imath(\epsilon_r - 1)}{4\pi} \int_{kC} \hat{n}' \cdot \nabla_{kt} \Phi_1(\overline{k\rho}'/k_0) \int_{k\ell} \frac{e^{\imath kz' \cos\beta} \; e^{\imath |\overline{kr} - \overline{kr}'|}}{|\overline{kr} - \overline{kr}'|^2} \left(\overline{kr} - \overline{kr}' \right) dkz' \, dkc' \\
& - \frac{(\epsilon_r - 1)}{4\pi} \int_{kC} \hat{n}' \cdot \nabla_{kt} \Phi_1(\overline{k\rho}'/k_0) \int_{k\ell} \frac{e^{\imath kz' \cos\beta} \; e^{\imath |\overline{kr} - \overline{kr}'|}}{|\overline{kr} - \overline{kr}'|^3} \left(\overline{kr} - \overline{kr}' \right) dkz' \, dkc'
\end{aligned} \tag{2.29}$$

To evaluate each integral over kz, the phase functions are first re-written as:

$$e^{\imath kz'\cos\beta}\, e^{\imath\sqrt{|\overline{k\rho}-\overline{k\rho}'|^2+(kz-kz')^2}} = e^{\imath kz\cos\beta}\, e^{-\imath kz\cos\beta}\, e^{\imath kz'\cos\beta}\, e^{\imath\sqrt{|\overline{k\rho}-\overline{k\rho}'|^2+(kz-kz')^2}}$$
$$= e^{\imath kz\cos\beta}\, e^{\imath\sqrt{|\overline{k\rho}-\overline{k\rho}'|^2+(kz-kz')^2}-\imath(kz-kz')\cos\beta} \quad (2.30)$$

Evaluation of the first integral over a cylinder length ℓ is therefore:

$$\begin{aligned}
& e^{\imath kz\cos\beta}\int_{-k\ell/2}^{k\ell/2}\frac{e^{\imath\sqrt{|\overline{k\rho}-\overline{k\rho}'|^2+(kz-kz')^2}-\imath(kz-kz')\cos\beta}}{\sqrt{|\overline{k\rho}-\overline{k\rho}'|^2+(kz-kz')^2}}\,dkz' \\
&= e^{\imath kz\cos\beta}\int_{kz}^{k\ell/2}\frac{e^{\imath\sqrt{|\overline{k\rho}-\overline{k\rho}'|^2+(kz'-kz)^2}+\imath(kz'-kz)\cos\beta}}{\sqrt{|\overline{k\rho}-\overline{k\rho}'|^2+(kz'-kz)^2}}\,dkz' \\
&+ e^{\imath kz\cos\beta}\int_{-k\ell/2}^{kz}\frac{e^{\imath\sqrt{|\overline{k\rho}-\overline{k\rho}'|^2+(kz-kz')^2}-\imath(kz-kz')\cos\beta}}{\sqrt{|\overline{k\rho}-\overline{k\rho}'|^2+(kz-kz')^2}}\,dkz' \\
&= e^{\imath kz\cos\beta}\int_{0}^{k\ell/2-kz}\frac{e^{\imath\sqrt{|\overline{k\rho}-\overline{k\rho}'|^2+(kz'')^2}+\imath(kz'')\cos\beta}}{\sqrt{|\overline{k\rho}-\overline{k\rho}'|^2+(kz'')^2}}\,dkz'' \\
&+ e^{\imath kz\cos\beta}\int_{0}^{k\ell/2+kz}\frac{e^{\imath\sqrt{|\overline{k\rho}-\overline{k\rho}'|^2+(kz'')^2}-\imath(kz'')\cos\beta}}{\sqrt{|\overline{k\rho}-\overline{k\rho}'|^2+(kz'')^2}}\,dkz''
\end{aligned} \quad (2.31)$$

The integrals of kz' cannot be evaluated. However, since the integration is over a finite region $k\ell$, the exponential term can be approximated in the region $k\ell/2 < kz < -k\ell/2$ by:

$$e^{\imath|\overline{kr}-\overline{kr}'|+\imath kz'\cos\beta} \approx \sum_{n=0}^{N}\frac{\left(\imath|\overline{kr}-\overline{kr}'|+\imath kz'\cos\beta\right)^n}{n!} \quad (2.32)$$

As N approaches infinity, the error associated with this approximation becomes arbitrarily small. Since both N and $k\ell$ are finite, the order of integration and summation can be interchanged. Performing the integration on each term results in a series whose

coefficients are in terms of $|\overline{k}\rho - \overline{k}\rho'|$. For example, the kz integral from the first term of equation (2.29) can be approximated as:

$$\int_0^{k\ell/2-kz} \frac{e^{\imath\sqrt{|\overline{k}\rho-\overline{k}\rho'|^2+(kz'')^2}+\imath(kz'')\cos\beta}}{\sqrt{|\overline{k}\rho-\overline{k}\rho'|^2+(kz'')^2}}dkz'' = \sum_{n=0}^{N}\int_0^{k\ell/2-kz} \frac{\left(\imath\sqrt{|\overline{k}\rho-\overline{k}\rho'|^2+(kz'')^2}+\imath kz''\cos\beta\right)^n}{n!\sqrt{|\overline{k}\rho-\overline{k}\rho'|^2+(kz'')^2}} \quad (2.33)$$

Performing the integration on each term results in a series whose coefficients are in terms of $|\overline{k}\rho - \overline{k}\rho'|$. Eliminating the terms of first order and above, an approximation to the integral when the cylinder diameter is small can be found.

$$\int_0^{k\ell/2-kz} \frac{e^{\imath\sqrt{|\overline{k}\rho-\overline{k}\rho'|^2+(kz'')^2}+\imath(kz'')\cos\beta}}{\sqrt{|\overline{k}\rho-\overline{k}\rho'|^2+(kz'')^2}}dkz'' \approx -\ln\left[|\overline{k\rho}-\overline{k\rho'}|\right]+\ln\left[2(k\ell/2-kz)\right]-\sum_{n=1}^{N}\frac{\left(\imath c_1(k\ell/2-kz)\right)^n}{n(n!)} \quad (2.34)$$

where $c_1 = 1+\cos\beta$.Similarly,

$$\int_0^{k\ell/2+kz} \frac{e^{\imath\sqrt{|\overline{k}\rho-\overline{k}\rho'|^2+(kz'')^2}-\imath(kz'')\cos\beta}}{\sqrt{|\overline{k}\rho-\overline{k}\rho'|^2+(kz'')^2}}dkz'' \approx -\ln\left[|\overline{k\rho}-\overline{k\rho'}|\right]+\ln\left[2(k\ell/2+kz)\right]-\sum_{n=1}^{N}\frac{\left(\imath c_2(k\ell/2+kz)\right)^n}{n(n!)} \quad (2.35)$$

where $c_2 = 1-\cos\beta$. These equations can likewise be written in terms of the exponential integral function $\mathrm{Ei}[x]$, where:

$$\mathrm{Ei}[x] \doteq -\int_{-x}^{\infty}\frac{e^{-t}}{t}dt \quad (2.36)$$

Since

$$\sum_{n=1}^{\infty} \frac{(\imath x)^n}{n(n!)} = \mathrm{Ei}[\imath x] - \gamma\frac{\imath\pi}{2} - \ln[x] \tag{2.37}$$

where γ is Euler's constant, the sum of equations (2.34) and (2.35) can be written as:

$$\begin{aligned}\int_{k\ell} \frac{e^{\imath|\overline{kr}-\overline{kr}'|+\imath kz'\cos\beta}}{|\overline{kr}-\overline{kr}'|}dkz' &= \sum_{n=0}^{N}\int_{k\ell}\frac{\left(\imath|\overline{kr}-\overline{kr}'|+\imath kz'\cos\beta\right)^n dkz'}{n!|\overline{kr}-\overline{kr}'|} \\ &\approx e^{\imath kz\cos\beta}\Big(\mathrm{Ei}\Big[\imath c_1(kl/2-kz)\Big]+\mathrm{Ei}\Big[\imath c_2(kl/2+kz)\Big]-2(\gamma+\imath\pi/2) \\ &\quad -2\ln\Big[\sin\beta|\overline{k\rho}-\overline{k\rho}'|/2\Big]\Big)+O\Big(\overline{k\rho}-\overline{k\rho}'\Big)\end{aligned} \tag{2.38}$$

where γ is Euler's constant, $c_1 = 1+\cos\beta$, $c_2 = 1-\cos\beta$ and $\mathrm{Ei}[x]$ is the exponential integral function defined as:

$$\mathrm{Ei}[x] = -\int_{-x}^{\infty}\frac{e^{-t}}{t}dt \tag{2.39}$$

Discarding the higher order elements $O\left(\overline{k\rho}-\overline{k\rho}'\right)$, equation(2.39) provides an accurate analytic approximation to the integral if $1 >> ka > |\overline{k\rho}-\overline{k\rho}'|$. Figure(2.1) graphically displays this, showing both the approximation and the numerical solution to the integral. Combining the second and third terms of (2.29), the resulting integral over kz can be divided into two parts, a component with the axial coefficient $\hat{z}$ and a component with the transverse coefficients $\hat{x}$ and $\hat{y}$. Expanding as before and

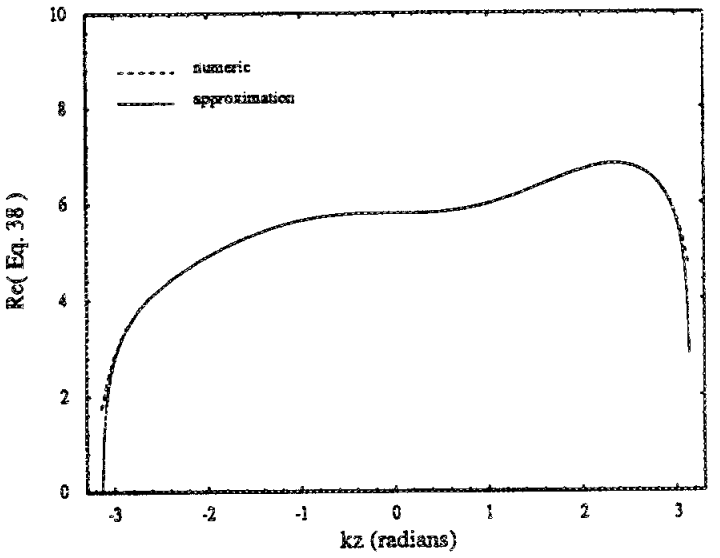

(a)

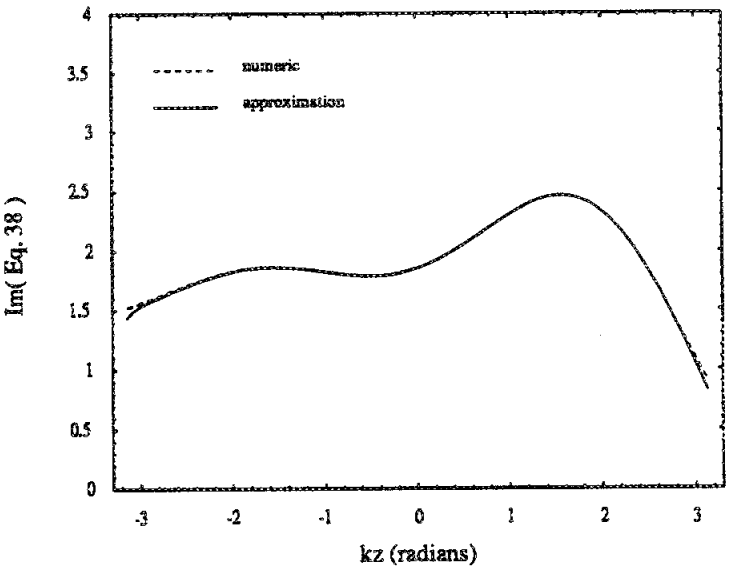

(b)

Figure 2.1: The real (a)and imaginary (b) parts of equation (2.38), both the exact numerical evaluation and the analytic approximation.($ka = 0.1$, $k\ell = 2\pi$, $\epsilon_r = 10$)

discarding the higher order terms, the transverse component can be approximated as:

$$\int_{-k\ell/2}^{k\ell/2} e^{\imath|\overline{kr}-\overline{kr'}|+\imath kz'\cos\beta}\left(\frac{-\imath}{|\overline{kr}-\overline{kr'}|^2}+\frac{1}{|\overline{kr}-\overline{kr'}|^3}\right)dkz'$$
$$\approx e^{\imath kz\cos\beta}\left(\frac{2}{|\overline{k\rho}-\overline{k\rho'}|^2}+\frac{\imath c_2 e^{\imath c_1(kl/2-kz)}}{2(kl/2-kz)}+\frac{\imath c_1 e^{\imath c_2(kl/2+kz)}}{2(kl/2+kz)}-\frac{e^{\imath c_1(kl/2-kz)}}{2(kl/2-kz)^2}\right.$$
$$\left.-\frac{e^{\imath c_2(kl/2+kz)}}{2(kl/2+kz)^2}\right)+\sin^2\beta\, e^{\imath kz\cos\beta}\left(-\ln\left[\sin\beta|\overline{k\rho}-\overline{k\rho'}|/2\right]+\frac{(1-2\gamma)}{2}\right.$$
$$\left.-\frac{\imath\pi}{2}+\frac{\mathrm{Ei}\left[\imath c_1(kl/2-kz)\right]}{2}+\frac{\mathrm{Ei}\left[\imath c_2(kl/2+kz)\right]}{2}\right) \quad (2.40)$$

Likewise, the axial component can be written as:

$$\int_{-k\ell/2}^{k\ell/2} e^{\imath|\overline{kr}-\overline{kr'}|+\imath kz'\cos\beta}\left(\frac{-\imath(kz-kz')}{|\overline{kr}-\overline{kr'}|^2}+\frac{(kz-kz')}{|\overline{kr}-\overline{kr'}|^3}\right)dkz'$$
$$\approx e^{\imath kz\cos\beta}\left(\cos\beta\left(\imath 2\ln\left[\sin\beta|\overline{k\rho}-\overline{k\rho'}|/2\right]+(\imath 2\gamma-\pi)-\imath\mathrm{Ei}\left[\imath c_1(kl/2-kz)\right]\right.\right.$$
$$\left.\left.-\imath\mathrm{Ei}\left[\imath c_2(kl/2+kz)\right]\right)+\frac{e^{\imath c_1(kl/2-kz)}}{kl/2-kz}-\frac{e^{\imath c_2(kl/2+kz)}}{kl/2+kz}\right) \quad (2.41)$$

Inserting the approximation of equations (2.38), (2.40), and (2.41) into (2.29), the scattered electric field is expressed as integrals over the cylinder circumference and the cylinder area only. As the electrical size of the cylinder cross-section reduces to zero, the integration involving higher order terms of $(\overline{k\rho}-\overline{k\rho'})$ likewise reduce to zero, providing that the interior field is non-singular throughout the region of integration. In fact only a single term, the first term of equation (2.40) $(2/|\overline{k\rho}-\overline{k\rho'}|^2)$, converges to a non-zero value after integration. Thus, the scattered field expression of (2.40)

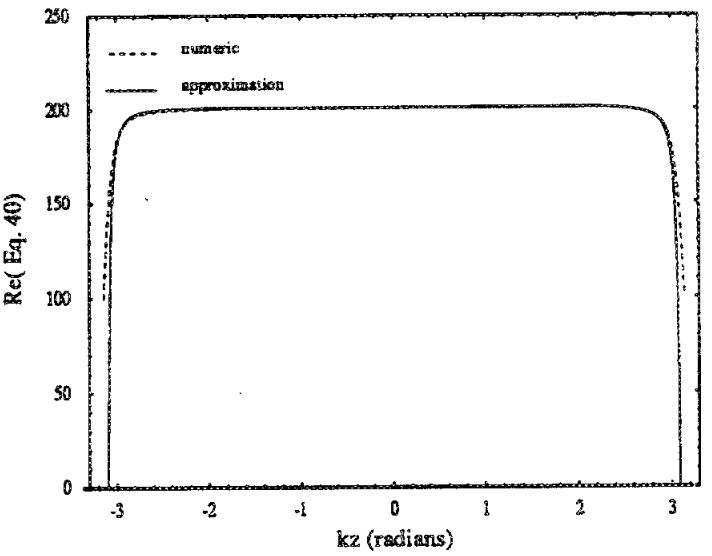

(a)

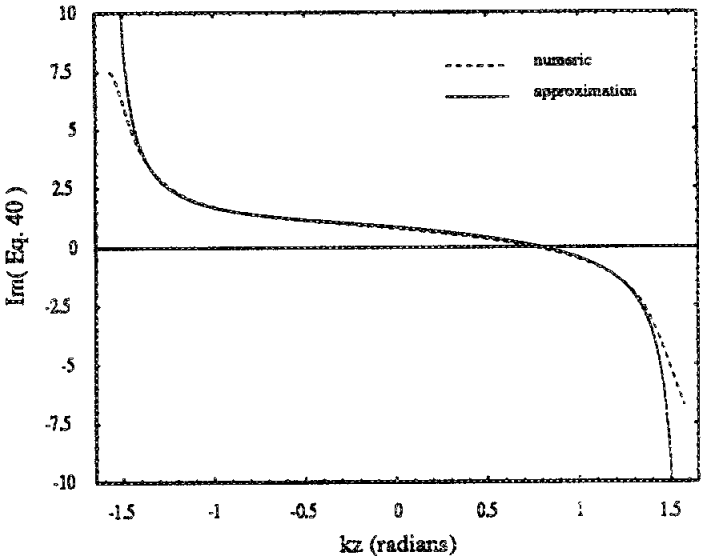

(b)

Figure 2.2: The real (a)and imaginary (b) parts of equation (2.40), both the exact numerical evaluation and the analytic approximation.($ka = 0.1$, $k\ell = 2\pi$, $\epsilon_r = 10$)

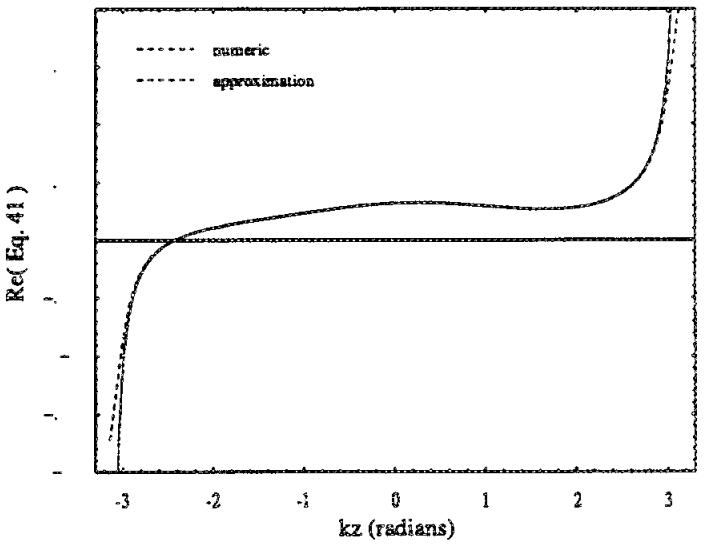

(a)

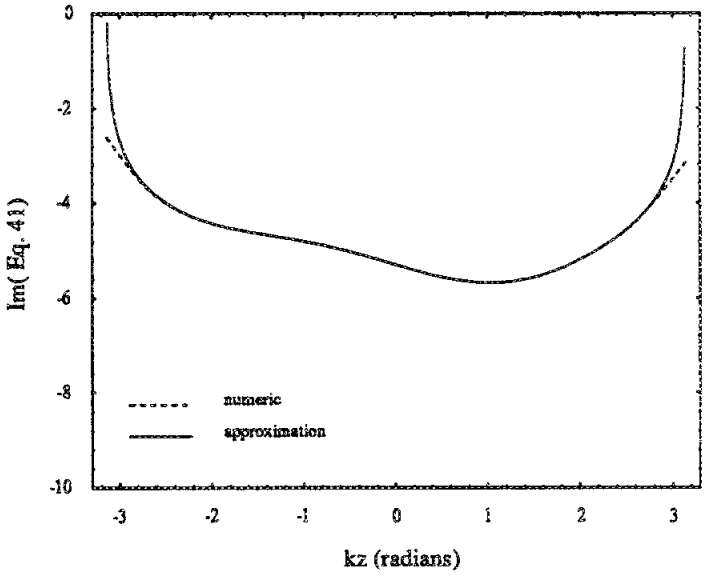

(b)

Figure 2.3: The real (a)and imaginary (b) parts of equation (2.41), both the exact numerical evaluation and the analytic approximation.($ka = 0.1$, $k\ell = 2\pi$, $\epsilon_r = 10$)

converges to an expression involving this single term as $ka \rightarrow 0$:

$$\begin{aligned}\lim_{kd\rightarrow 0} \mathbf{E}^s(\overline{r}) &= -\frac{(\epsilon_r - 1)}{4\pi}\, e^{ik_0 z\cos\beta} \int_{kc} \hat{n}' \cdot \nabla'_{kt}\Phi_1(\overline{k\rho}'/k_0)\, \frac{2(\overline{k\rho} - \overline{k\rho}')}{|\overline{k\rho} - \overline{k\rho}'|^2}\, dkc' \\ &= -\frac{(\epsilon_r - 1)}{4\pi}\, e^{ik_0 z\cos\beta} \int_{c} \hat{n}' \cdot \nabla'_t\Phi_1(\overline{\rho}')\, \frac{2(\overline{\rho} - \overline{\rho}')}{|\overline{\rho} - \overline{\rho}'|^2}\, dc'\end{aligned} \tag{2.42}$$

However, the question remains whether this expression is a valid solution the equation $\mathbf{E}(\overline{r}) = \mathbf{E}^i(\overline{r}) + \mathbf{E}^s(\overline{r})$. To determine this, we first recognize that:

$$\frac{\overline{\rho} - \overline{\rho}'}{|\overline{\rho} - \overline{\rho}'|^2} = \nabla_t \ln|\overline{\rho} - \overline{\rho}'| \tag{2.43}$$

Therefore the scattered field can be expressed as:

$$\begin{aligned}\mathbf{E}^s(\overline{r}) &= -\frac{(\epsilon_r - 1)}{2\pi}\, e^{ik_0 z\cos\beta} \int_C \hat{n}' \cdot \nabla'_t\Phi_1(\overline{\rho}')\, \nabla_t \ln|\overline{\rho} - \overline{\rho}'|\, dc' \\ &= -\frac{(\epsilon_r - 1)}{2\pi}\, e^{ik_0 z\cos\beta}\, \nabla_t \int_C \hat{n}' \cdot \nabla'_t\Phi_1(\overline{\rho}')\, \ln|\overline{\rho} - \overline{\rho}'|\, dc' \\ &= -\frac{(\epsilon_r - 1)}{2\pi}\, e^{ik_0 z\cos\beta}\, \nabla_t \int_A \nabla'_t \cdot (\ln|\overline{\rho} - \overline{\rho}'|\, \nabla'_t\Phi_1(\overline{\rho}'))\, dA' \\ &= -\frac{(\epsilon_r - 1)}{2\pi}\, e^{ik_0 z\cos\beta}\, \nabla_t \int_A \Big[\nabla'_t\Phi_1(\overline{\rho}') \cdot \nabla'_t \ln|\overline{\rho} - \overline{\rho}'| + \\ &\quad \ln|\overline{\rho} - \overline{\rho}'|\, \nabla'_t \cdot \nabla'_t\Phi_1(\overline{\rho}')\Big]\, dA' \\ &= -\frac{(\epsilon_r - 1)}{2\pi}\, e^{ik_0 z\cos\beta}\, \nabla_t \int_A \nabla'_t\Phi_1(\overline{\rho}') \cdot \nabla'_t \ln|\overline{\rho} - \overline{\rho}'|\, dA'\end{aligned} \tag{2.44}$$

But, from equation (2.6) it is known that $\Phi_1(\overline{\rho})$ is the solution to the equation:

$$\int_A \nabla'_t\Phi_1(\overline{\rho}') \cdot \nabla'_t \ln|\overline{\rho} - \overline{\rho}'|dA' = \frac{2\pi}{(\epsilon_r - 1)}\Big(\Phi_1(\overline{\rho}) + x + b_1\Big) \tag{2.45}$$

Using the above equation in (2.44), the scattered field reduces to:

$$\begin{aligned}\mathbf{E}^s(\overline{r}) &= -\nabla_t\Big(\Phi_1(\overline{\rho}) + x + b_1\Big)\, e^{\imath k_0 z\cos\beta} \\ &= -\Big(\nabla_t\Phi_1(\overline{\rho}) + \hat{x}\Big)\, e^{\imath k_0 z\cos\beta}\end{aligned} \tag{2.46}$$

The total field is the sum of the incident and scattered fields,

$$\begin{aligned}\mathbf{E}(\overline{r}) &= \mathbf{E}^i(\overline{r}) + \mathbf{E}^s(\overline{r}) \\ &= e^{\imath k_0 z\cos\beta}\,\hat{x} - \Big(\nabla_t\Phi_1(\overline{\rho}) + \hat{x}\Big)\, e^{\imath kz\cos\beta} \\ &= -e^{\imath k_0 z\cos\beta}\,\nabla_t\Phi_1(\overline{\rho}) \\ &= \mathbf{E}(\overline{r})\end{aligned} \tag{2.47}$$

the original hypothesized total field. Thus, for the incident field of (2.25) we have explicitly shown that the scattering solution for a finite dielectric cylinder converges to infinite cylinder solution of equation (2.7) as its electrical radius approaches zero. No constraint was placed on cross-section or electrical length $k\ell$, the solution is equally valid for cylinders of all electrical lengths and cross-sections.

2.1.2 TM Solution

If the magnetic field of the incident wave is transverse to the cylinder, then the incident electric field within the thin cylinder is given as:

$$\mathbf{E}^i(\overline{r}) = \Big(\cos\phi\cos\beta\,\hat{x} + \sin\phi\cos\beta\,\hat{y} - \sin\beta\,\hat{z}\Big)\, e^{\imath k_0 z\cos\beta} \tag{2.48}$$

The infinite cylinder solution thus leads to the following hypothesized internal field:

$$\mathbf{E}(\bar{r}) = \Big(-\cos\phi\cos\beta\ \nabla_t\Phi_1(\bar{\rho}) - \sin\phi\cos\beta\ \nabla_t\Phi_2(\bar{\rho}) - \ \sin\beta\hat{z}\Big)\ e^{\imath k_0\cos\beta z} \tag{2.49}$$

The previous section has demonstrated the validity of the transverse solution. For the axial component z, the hypothesized solution is just the $\hat{z}$ component of the incident field $\mathbf{E}^i(\bar{r})$. It was shown in the previous section that the transverse components of the incident field do not produce axial components in the limit as $ka \to 0$, thus we can consider only the z component of hypothesized field, $\hat{z}\exp[\imath k_0\cos\beta z]$ The divergence of this term is non-zero, thus additional terms will be generated by equation (2.14). Adding these terms, the expression for the scattered field is written as:

$$\begin{aligned}
\mathbf{E}^s(\bar{r}) = & \frac{k_0^2(\epsilon_r-1)}{4\pi}\int_V \mathbf{E}(\bar{r}')\,\frac{e^{\imath k_0|\bar{r}-\bar{r}'|}}{|\bar{r}-\bar{r}'|}\,dv' \\
& - \frac{\imath k_0(\epsilon_r-1)}{4\pi}\int_S \hat{n}'\cdot\mathbf{E}(\bar{r}')\,\frac{e^{\imath k_0|\bar{r}-\bar{r}'|}}{|\bar{r}-\bar{r}'|^2}\,[\bar{r}-\bar{r}']\,ds' \\
& + \frac{(\epsilon_r-1)}{4\pi}\int_S \hat{n}'\cdot\mathbf{E}(\bar{r}')\,\frac{e^{\imath k_0|\bar{r}-\bar{r}'|}}{|\bar{r}-\bar{r}'|^3}\,[\bar{r}-\bar{r}']\,ds' \\
& + \frac{\imath k_0(\epsilon_r-1)}{4\pi}\int_V \nabla'\cdot\mathbf{E}(\bar{r}')\,\frac{e^{\imath k_0|\bar{r}-\bar{r}'|}}{|\bar{r}-\bar{r}'|^2}\,[\bar{r}-\bar{r}']\,dv' \\
& - \frac{(\epsilon_r-1)}{4\pi}\int_V \nabla'\cdot\mathbf{E}(\bar{r}')\,\frac{e^{\imath k_0|\bar{r}-\bar{r}'|}}{|\bar{r}-\bar{r}'|^3}\,[\bar{r}-\bar{r}']\,dv'
\end{aligned} \tag{2.50}$$

Inserting the axial component of (2.49), the scattered field becomes

$$\begin{aligned}
\mathbf{E}^s(\overline{kr}/k_0) = & \frac{(\epsilon_r - 1)}{4\pi} \int_{k^3V} \hat{z}\, e^{\imath kz' \cos\beta}\, \frac{e^{\imath|\overline{kr}-\overline{kr}'|}}{|\overline{kr}-\overline{kr}'|}\, dk^3v' \\
& - \frac{\imath(\epsilon_r - 1)}{4\pi} \int_{k^2S} \hat{n}' \cdot \hat{z}\, e^{\imath kz' \cos\beta}\, \frac{e^{\imath|\overline{kr}-\overline{kr}'|}}{|\overline{kr}-\overline{kr}'|^2} \left(\overline{kr}-\overline{kr}'\right) dk^2s' \\
& + \frac{(\epsilon_r - 1)}{4\pi} \int_{k^2S} \hat{n}' \cdot \hat{z}\, e^{\imath kz' \cos\beta}\, \frac{e^{\imath|\overline{kr}-\overline{kr}'|}}{|\overline{kr}-\overline{kr}'|^3} \left(\overline{kr}-\overline{kr}'\right) dk^2s' \\
& - \frac{\cos\beta(\epsilon_r - 1)}{4\pi} \int_{k^3V} e^{\imath kz' \cos\beta}\, \frac{e^{\imath|\overline{kr}-\overline{kr}'|}}{|\overline{kr}-\overline{kr}'|^2} \left(\overline{kr}-\overline{kr}'\right) dk^3v' \\
& - \frac{\imath\cos\beta(\epsilon_r - 1)}{4\pi} \int_{k^3V} e^{\imath kz' \cos\beta}\, \frac{e^{\imath|\overline{kr}-\overline{kr}'|}}{|\overline{kr}-\overline{kr}'|^3} \left(\overline{kr}-\overline{kr}'\right) dk^3v'
\end{aligned} \tag{2.51}$$

The surface integrals reduce to integration over the end caps of the cylinder evaluated at $kz = \pm k\ell/2$:

$$\begin{aligned}
\mathbf{E}^s(\overline{kr}/k_0) = & \frac{(\epsilon_r - 1)}{4\pi} \int_{k^2A} \int_{k\ell} \frac{e^{\imath kz' \cos\beta} e^{\imath|\overline{kr}-\overline{kr}'|}}{|\overline{kr}-\overline{kr}'|}\, dkz'\, dk^2{}_A' \\
& - \frac{\imath(\epsilon_r - 1)}{4\pi} \int_{k^2A} \Big|_{-k\ell/2}^{k\ell/2} \frac{e^{\imath kz' \cos\beta} e^{\imath|\overline{kr}-\overline{kr}'|}}{|\overline{kr}-\overline{kr}'|^2} \left(\overline{kr}-\overline{kr}'\right) dk^2{}_A' \\
& + \frac{(\epsilon_r - 1)}{4\pi} \int_{k^2A} \Big|_{-k\ell/2}^{k\ell/2} \frac{e^{\imath kz' \cos\beta} e^{\imath|\overline{kr}-\overline{kr}'|}}{|\overline{kr}-\overline{kr}'|^3} \left(\overline{kr}-\overline{kr}'\right) dk^2{}_A' \\
& - \frac{\cos\beta(\epsilon_r - 1)}{4\pi} \int_{k^2A} \int_{-k\ell/2}^{k\ell/2} \frac{e^{\imath kz' \cos\beta} e^{\imath|\overline{kr}-\overline{kr}'|}}{|\overline{kr}-\overline{kr}'|^2} \left(\overline{kr}-\overline{kr}'\right) dkz'\, dk^2{}_A' \\
& - \frac{\imath\cos\beta(\epsilon_r - 1)}{4\pi} \int_{k^2A} \int_{-k\ell/2}^{k\ell/2} \frac{e^{\imath kz' \cos\beta} e^{\imath|\overline{kr}-\overline{kr}'|}}{|\overline{kr}-\overline{kr}'|^3} \left(\overline{kr}-\overline{kr}'\right) dkz'\, dk^2{}_A'
\end{aligned} \tag{2.52}$$

The integrals involving kz' are those examined in the previous section and therefore the approximations derived for thin cylinders (equations (2.38) to (2.41)) can be

implemented in (2.52). Again integrating and taking the limit as $ka \rightarrow 0$, we find that for this case that *every* $(\overline{k\rho} - \overline{k\rho'})$ term reduces to zero, not a single non-zero term remains. The scattered field equation thus reduces to:

$$\lim_{ka\rightarrow 0}\mathbf{E}^s(\overline{kr}/k_0) = \frac{-\imath(\epsilon_r - 1)}{4\pi}\int_{k^2S}\Big|_{-k\ell/2}^{k\ell/2}\frac{e^{\imath kz'\cos\beta}e^{\imath|\overline{kr}-\overline{kr'}|}}{|\overline{kr}-\overline{kr'}|^2}\left(\overline{kr}-\overline{kr'}\right)dk^2{}_{A'}$$
$$+\frac{(\epsilon_r - 1)}{4\pi}\int_{k^2S}\Big|_{-k\ell/2}^{k\ell/2}\frac{e^{\imath kz'\cos\beta}e^{\imath|\overline{kr}-\overline{kr'}|}}{|\overline{kr}-\overline{kr'}|^3}\left(\overline{kr}-\overline{kr'}\right)dk^2{}_{A'} \tag{2.53}$$

The above equation represents charges lying at each end of the dielectric cylinder, generating scattered fields which fall off rapidly as kz becomes a few ka distances removed from $\pm k\ell/2$. This region is insignificant if ka is small, and the value of $\mathbf{E}^s(kz)$ approaches zero at all $kz \neq \pm k\ell/2$ in the limit as $ka \rightarrow$. Thus, the scattered field $\mathbf{E}^s$ converges to zero as ka becomes small, resulting in neither an axial term nor transverse terms. Again notice that no assumption is made nor constraint placed on electrical length $k\ell$. Therefore, the total scattered field resulting from the incident wave of equation (2.48) contains no axial component, and the transverse solutions, using equation (2.46), lead to a scattered field expression:

$$\mathbf{E}^s(\overline{r}) = -\Big(\ \cos\phi\cos\beta(\nabla_t\Phi_1(\overline{\rho}) + \hat{x})\ +\ \sin\phi\cos\beta(\nabla_t\Phi_2(\overline{\rho}) + \hat{y})\ \Big)e^{\imath k_0\cos\beta z} \tag{2.54}$$

Adding the scattered field to the incident field, the equation for the total field is determined:

$$\mathbf{E}(\bar{r}) = \Big(-\cos\phi\cos\beta\ \nabla_t\Phi_1(\bar{\rho}) \ -\ \sin\phi\cos\beta\ \nabla_t\Phi_2(\bar{\rho}) \ -\ \sin\beta\ \hat{z}\Big)\ e^{\imath k_0 \cos\beta z} \tag{2.55}$$

This expression is again equal to the original hypothesis of (2.49), the infinite cylinder solution.

Thus, it has been explicitly demonstrated that scattering solution of a finite dielectric cylinder converges to the infinite cylinder solution as $ka \to 0$, a result independent of either cross-section or electrical length $k\ell$. It should be noted that for any finite $k\ell$, as ka approaches zero the normalized length $k\ell/ka = \ell/a$ converges to infinity, in fact $\ell/a \to \infty$ and $ka \to 0$ are equivalent statements for a fixed $k\ell$. Therefore, the infinite cylinder solution is valid for finite cylinders only if both $ka << 1$ and $ka << k\ell$. Since this approximation is independent of $k\ell$, it is likewise valid for Rayleigh cylinders where $k\ell << 1$. Thus, the electrostatic solutions $\Phi(\bar{\rho})$ derived for infinite cylinders (2.6) are the asymptotic solutions for a Rayleigh cylinder as $\ell/a \to \infty$. The GRG approximation, which considers circular cylinders, is therefore a specific case of the more general approximation defined by equations (2.6) and (2.7). As such, the validity regions of the GRG approximation, being identical to the requirements stated above ($ka << 1$, $ka << k\ell$ for all $k\ell$), have been explicitly proven by the analysis of this section.

2.2 Asymptotic Error Evaluation

As this solution is asymptotic, it will exhibit a finite error which becomes diminishingly small as $ka \rightarrow 0$. In order for the solution to be useful in modeling physical structures, this error must converge to insignificance at reasonable values of $k\ell$, ka, and ϵ_r. To evaluate this asymptotic error, we can compare the solution to formulations of higher fidelity which approach the "exact" scattering solution for the cylinder. To this end, a general moment-method solution was constructed to accurately model thin ($ka << 1$), circular cylinders of both arbitrary $k\ell$ and ℓ/a.

Ideally, a general three-dimensional numeric scattering formulation would be used to provide this "exact" solution. However, the extreme conditions of the problem, such as $ka << 1$ and $\ell >> a$, make generation of an accurate, high fidelity solution of $\mathbf{E}(\bar{r})$ problematic. Instead, we note that for the infinite case, each component $E(\bar{r})$ can be separated into functions of z and $\bar{\rho}$ ($E(\bar{r}) = -\nabla\Phi(\bar{\rho})\ \exp[\imath k_0 z \cos\beta]$). We then assume that for finite cylinders the terms are likewise separable, and that the form of the ρ function is the Rayleigh solution for $\ell >> a$. Thus, for a circular cylinder, the internal electric field can be represented as:

$$\mathbf{E}(\bar{r}) = \hat{x}\,\frac{2\,f_x(z)}{(\epsilon_r+1)} + \hat{y}\,\frac{2\,f_y(z)}{(\epsilon_r+1)} + \hat{z}\,f_z(z) \tag{2.56}$$

The expressions $f_x(z)$, $f_y(z)$, and $f_z(z)$ are unknown complex scalar functions which are dependent on the spatial variable z only. Comparing the above equation with (2.7), the values of the functions $f(z)$ predicted by the infinite cylinder approximation

are:

$$\begin{aligned} f_x(z) &= e_x\, e^{\imath k_0 \cos\beta z} = E_x^i \\ f_y(z) &= e_y\, e^{\imath k_0 \cos\beta z} = E_y^i \\ f_z(z) &= e_z\, e^{\imath k_0 \cos\beta z} = E_z^i \end{aligned} \tag{2.57}$$

Thus, the vector $\mathbf{F}(z)$, defined as $\mathbf{F}(z) = \hat{x} f_x(z) + \hat{y} f_y(z) + \hat{z} f_z(z)$, will equal the incident field axis if no approximation error is exhibited.

The ability of the moment-method solution to accurately reflect the exact scattering solution depends on the general validity of equation (2.56). To test this accuracy, the moment method code was used to determine the vector $\mathbf{F}(z)$ for Rayleigh cylinders ($k\ell >> 1$) at a variety of dielectrics and normalized lengths ℓ/a. Since the solution $\mathbf{E}(\bar{r})$ is independent of ρ, the polarizability tensor elements can be calculated as [21]:

$$\begin{aligned} \frac{P_{ww}}{(\epsilon_r - 1)\, V} &= \frac{1}{V} \int_V \frac{E_w(\bar{r})}{e_w}\, dv \\ &= \frac{1}{\ell} \int_{-\ell/2}^{\ell/2} \frac{E_w(z)}{e_w}\, dz \end{aligned} \tag{2.58}$$

where $w \in \{x, y, z\}$. The polarizability tensor of a circular cylinder is know [21], and thus can be directly compared to the tensor elements determined from the moment method solutions. Figure(2.4) displays the results of this exercise, both for the axial element P_{zz} and a transverse element P_{xx}. The moment method solution matches the exact values reasonably well over all dielectrics and normalized lengths ℓ/a, thus

providing evidence as to the accuracy of (2.56).

2.2.1 Transverse Moment-Method Solution

Due to the symmetry of a circular cylinder, the solutions for both transverse components $f_x(z)$ and $f_y(z)$ identical. The x directed term $F - x(z)$ was arbitrarily selected for this analysis, with the results applying directly to $f_y(z)$. To facilitate a moment-method solution, the unknown expression $J_x(z)$ is first approximated as a summation of pulse basis functions, given as:

$$f_x(z) \approx f_x(z = z_n) = f_x(z_n) \quad \text{from} \quad (z_n - \Delta) < z < (z_n + \Delta)$$

thus,

$$E_x(z) \approx \frac{2}{(\epsilon_r + 1)} \sum_n^N f_x(z_n) \tag{2.59}$$

Inserting this approximation into equation(2.24), the scattered field resulting from a single element n $(z'_n - \Delta < z' < z'_n + \Delta)$, as observed along the z axis $(\rho = 0)$, is

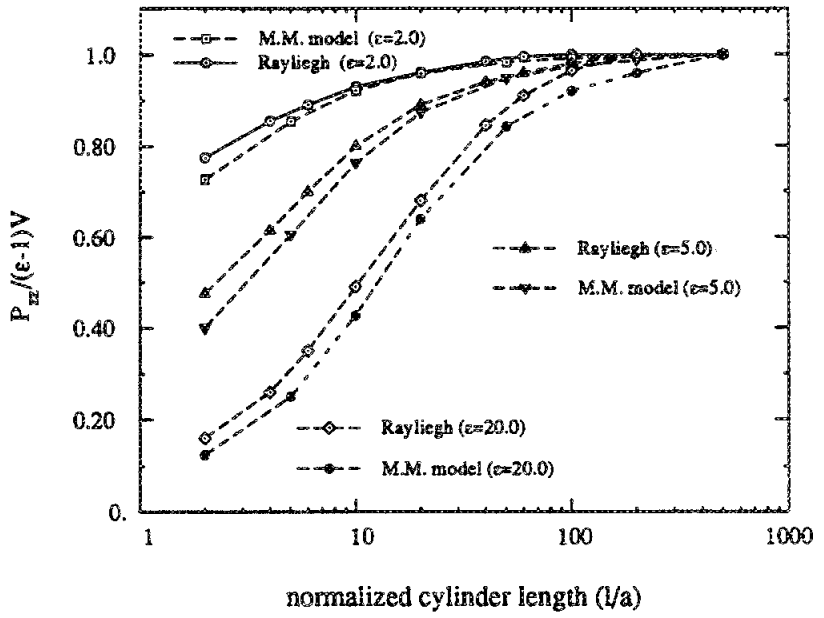

(a)

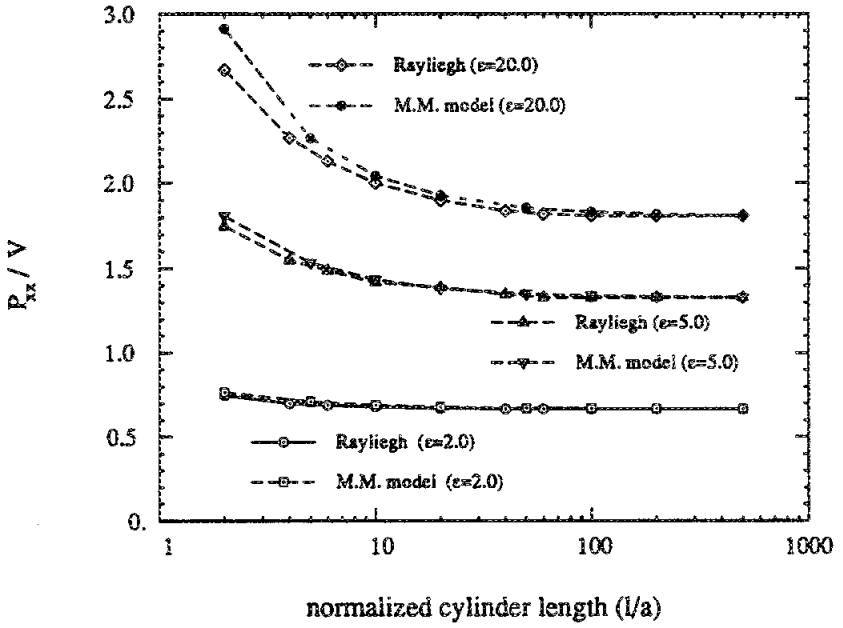

(b)

Figure 2.4: The axial (a) and transverse (b) normalized polarizability tensor elements of a circular cylinder, both the exact values and those determined using the MM model.

derived.

$$
\begin{aligned}
&\mathbf{E}_n^s(\bar{r}) = \\
&\frac{(\epsilon_r - 1)}{4\pi} f(z_n) \int_{-k\Delta\ell}^{k\Delta\ell} \int_0^{2\pi} \int_0^{ka} \frac{\hat{x}2}{(\epsilon_r + 1)} \frac{e^{\imath\sqrt{k\rho'^2 + (ku - k\delta)^2}}}{\sqrt{k\rho'^2 + (ku - k\delta)^2}} \, dk\rho' \, d\phi' \, dk\delta' \\
&-\imath\frac{(\epsilon_r - 1)}{4\pi} f(z_n) \int_{-k\Delta\ell}^{k\Delta\ell} \int_0^{2\pi} (\cos\phi'\hat{x} + \sin\phi'\hat{y}) \cdot \frac{\hat{x}2}{(\epsilon_r + 1)} \frac{e^{\imath\sqrt{k\rho'^2 + (ku - k\delta)^2}}}{(\sqrt{k\rho'^2 + (ku - k\delta)^2})^2} \\
&\Big(- ka\cos\phi'\hat{x} - ka\sin\phi'\hat{y} + (ku - k\delta')\hat{z} \Big) \, ka \, d\phi' \, dk\delta' \\
&+\frac{(\epsilon_r - 1)}{4\pi} f(z_n) \int_{-k\Delta\ell}^{k\Delta\ell} \int_0^{2\pi} (\cos\phi'\hat{x} + \sin\phi'\hat{y}) \cdot \frac{\hat{x}2}{(\epsilon_r + 1)} \frac{e^{\imath\sqrt{k\rho'^2 + (ku - k\delta)^3}}}{(\sqrt{k\rho'^2 + (ku - k\delta)^2})^3} \\
&\Big(- ka\cos\phi'\hat{x} - ka\sin\phi'\hat{y} + (ku - k\delta')\hat{z} \Big) \, ka \, d\phi' \, dk\delta'
\end{aligned}
\tag{2.60}
$$

In the above expression, $ku = kz - kz_n$ and $k\delta = kz' - kz_n$ so that $kz - kz' = ku - k\delta$. In addition, the direction vector normal to the cylinder surface is given as $\hat{n} = \cos\phi'\hat{x} + \sin\phi'\hat{y}$.

Performing the integration over the cylinder cross-section leaves an expression for the scattered field which is non-zero for the $\hat{x}$ component only:

$$
\begin{aligned}
\mathbf{E}_n^s(\bar{r}) = \; & \imath\frac{(\epsilon_r - 1)}{(\epsilon_r + 1)} f(z_n) \int_{-k\Delta\ell}^{k\Delta\ell} e^{\imath\sqrt{(ku - k\delta)^2}} - e^{\imath\sqrt{k\rho'^2 + (ku - k\delta)^2}} \, dk\delta' \\
& + \imath \, ka^2 \frac{(\epsilon_r - 1)}{(\epsilon_r + 1)} \frac{f(z_n)}{2} \int_{-k\Delta\ell}^{k\Delta\ell} \frac{e^{\imath\sqrt{ka^2 + (ku - k\delta)^2}}}{(\sqrt{ka^2 + (ku - k\delta)^2})^2} \, dk\delta' \\
& - ka^2 \frac{(\epsilon_r - 1)}{(\epsilon_r + 1)} \frac{f(z_n)}{2} \int_{-k\Delta\ell}^{k\Delta\ell} \frac{e^{\imath\sqrt{ka^2 + (ku - k\delta)^2}}}{(\sqrt{ka^2 + (ku - k\delta)^2})^3} \, dk\delta'
\end{aligned}
\tag{2.61}
$$

Thus, the scattered field from a transverse ($\hat{x}$) source component does not couple

into either of the other directional components $(\hat{y}, \hat{z})$. The scattered field can thus be re-written in terms of an integration over the variable $k\delta$.

$$\mathbf{E}_n^s(\bar{r}) = \hat{x}\,\frac{(\epsilon_r-1)}{(\epsilon_r+1)}\,f(z_n)\int_{-k\Delta\ell}^{k\Delta\ell}\left(\imath e^{\imath\sqrt{(ku-k\delta)^2}} - \imath e^{\imath\sqrt{ka^2+(ku-k\delta)^2}} + \frac{\imath ka^2}{2}\,\frac{e^{\imath\sqrt{ka^2+(ku-k\delta)^2}}}{(\sqrt{ka^2+(ku-k\delta)^2})^2} - \frac{ka^2}{2}\,\frac{e^{\imath\sqrt{ka^2+(ku-k\delta)^2}}}{(\sqrt{ka^2+(ku-k\delta)^2})^3}\right)dk\delta' \quad (2.62)$$

To evaluate this expression, we first consider the off-cell case wherein $ku = kz - kz_n > k\Delta$. Assuming that $k\Delta << 1$, the first term of the above equation can be approximated by expanding the integrand around $k\delta$, then integrating and keeping both the first and second order terms. In addition, the second and third terms of the above expression can be directly evaluated, provided that the phase term is approximated as:

$$e^{\imath\sqrt{ka^2+(ku-k\delta)^2}} \approx e^{\imath\sqrt{ka^2+ku^2}} \quad (2.63)$$

Again, a valid approximation provided that $k\Delta << 1$ The resulting expression for the off cell scattering term is therefore:

$$\begin{aligned}\mathbf{E}_n^s(\bar{r}) = \hat{x}\,\frac{(\epsilon_r-1)}{(\epsilon_r+1)}\,f(z_n)\Bigg\{ & \imath 2k\Delta\left(e^{\sqrt{ku^2}} - e^{\imath\sqrt{ka^2+ku^2}}\right) \\ & - \frac{\imath ka^2k\Delta^3}{3}\,\frac{e^{\imath\sqrt{ka^2+ku^2}}}{(\sqrt{ka^2+ku^2})^2} + \frac{ka^2\,k\Delta^3}{3}\,\frac{e^{\imath\sqrt{ka^2+ku^2}}}{(\sqrt{ka^2+ku^2})^3} \\ & + \frac{\imath ka}{2}\,e^{\imath\sqrt{ka^2+ku^2}}\left[\tan^{-1}\left(\frac{k\Delta-ku}{ka}\right)+\tan^{-1}\left(\frac{k\Delta+ku}{ka}\right)\right] \\ & - \frac{1}{2}e^{\imath\sqrt{ka^2+ku^2}}\left(\frac{k\Delta-ku}{\sqrt{ka^2+(k\Delta-ku)^2}} + \frac{k\Delta+ku}{\sqrt{ka^2+(k\Delta+ku)^2}}\right)\Bigg\} \quad (2.64)\end{aligned}$$

Considering now the self-cell case, wherein $kz - kz_n = ku < k\Delta$, the expression for the scattered field can likewise be evaluated by implementing the proper approximations.

The first term of equation(2.62) can be approximated as:

$$\imath\, e^{\imath\sqrt{(ku-k\delta)^2}} - \imath\, e^{\imath\sqrt{ka^2+(ku-k\delta)^2}} \approx \imath\, e^{\imath\,|ku|} - \imath\, e^{\imath\sqrt{ka^2+ku^2}} + k\delta\left(e^{\imath\,|ku|} - \frac{e^{\imath\sqrt{ka^2+ku^2}}\,ku}{\sqrt{ka^2+ku^2}}\right) + \frac{k\delta^2\,ka^2}{2}\,e^{\imath\sqrt{ka^2+ku^2}}\left(\frac{-\imath}{(\sqrt{ka^2+ku^2})^2} + \frac{1}{(\sqrt{ka^2+ku^2})^3}\right) \quad (2.65)$$

since $\sqrt{ka^2+kd^2} << 1$ in the self-cell region of an electrically thin cylinder.

As with the off-cell case, the second and third terms of equation(2.62) can be directly evaluated by recognizing that the phase term is approximately unity when $\sqrt{ka^2+kd^2} << 1$. The self-cell expression is therefore:

$$\mathbf{E}_n^s(\bar{r}) = \hat{x}\,\frac{(\epsilon_r-1)}{(\epsilon_r+1)}\,f(z_n)\left(k\Delta\,\sqrt{ka^2+k\Delta^2} - k\Delta^2 - \frac{k\Delta}{\sqrt{ka^2+k\Delta^2}} + \frac{\imath 2\,ka^2\,k\Delta}{3}\right) \quad (2.66)$$

2.2.2 Axial Moment-Method Solution

The scattered field resulting from an axial or z directed source can likewise determined with using the pulse basis approximation where:

$$E_z(z) \approx \sum_n^N f_z(z_n) \quad (2.67)$$

Thus, the scattered field resulting from an arbitrary cell centered at z_n can be determined by inserting equation(2.67) into equation(2.50).

$$\begin{aligned}
\mathbf{E}_n^s(\bar{r}) =& \frac{(\epsilon_r - 1)}{4\pi} f(z_n) \int_{-k\Delta\ell}^{k\Delta\ell} \int_0^{2\pi} \int_0^{ka} \hat{z} \, \frac{e^{\imath\sqrt{k\rho'^2 + (ku - k\delta)^2}}}{\sqrt{k\rho'^2 + (ku - k\delta)^2}} \, dk\rho' \, d\phi' \, dk\delta' \\
& - \imath \, \frac{(\epsilon_r - 1)}{4\pi} f(z_n) \Big|_{-k\Delta}^{k\Delta} \int_0^{ka} \int_0^{2\pi} \hat{z} \cdot \hat{z} \, \frac{e^{\imath\sqrt{k\rho'^2 + (ku - k\delta)^2}}}{(\sqrt{k\rho'^2 + (ku - k\delta)^2})^2} \\
& (-k\rho' \cos\phi' \hat{x} - k\rho' \sin\phi' + (ku - k\delta')\hat{z}) \, k\rho' \, d\phi' \\
& + \frac{(\epsilon_r - 1)}{4\pi} f(z_n) \Big|_{-k\Delta}^{k\Delta} \int_0^{ka} \int_0^{2\pi} \hat{z} \cdot \hat{z} \, \frac{e^{\imath\sqrt{k\rho'^2 + (ku - k\delta)^2}}}{(\sqrt{k\rho'^2 + (ku - k\delta)^2})^3} \\
& \Big(- k\rho' \cos\phi' \hat{x} - k\rho' \sin\phi' \hat{y} + (ku - k\delta')\hat{z} \Big) \, k\rho' \, d\phi'
\end{aligned} \tag{2.68}$$

The surface integrals for the axial case require integration over the top and bottom surfaces of the cylindrical cell, where $k\delta = \pm k\Delta$. In this case the normal vector is $\hat{n} = \hat{z}$ for the top surface of the cylindrical cell, and $\hat{n} = -\hat{z}$ for the bottom surface.

Performing the the cell cross-section, the previous expression reduces to:

$$\begin{aligned}
\mathbf{E}_n^s(\bar{r}) = \; & \hat{z} \frac{(\epsilon_r - 1)}{2} f(z_n) \left(\int_{-k\Delta}^{k\Delta} \imath \, e^{\imath\sqrt{(ku - k\delta)^2}} - \imath \, e^{\imath\sqrt{ka^2 + (ku - k\delta)^2}} \, dk\delta \right. \\
& \left. + \Big|_{-k\Delta}^{k\Delta} \frac{e^{\imath|ku - k\delta|} \, (ku - k\delta)}{|ku - k\delta|} - \Big|_{-k\Delta}^{k\Delta} \frac{e^{\imath\sqrt{ka^2 + (ku - k\delta)^2}} \, (ku - k\delta)}{\sqrt{ka^2 + (ku - k\delta)^2}} \right)
\end{aligned} \tag{2.69}$$

As with the transverse case, there is no coupling of the $\hat{z}$ directed source into the other (transverse) directional components, the scattered field expression is a coefficient of $\hat{z}$ only.

In contrast to the transverse case, the evaluation of only one integral is required. Although there is no analytical solution to the integral of equation(2.69), an approx-

imation to the integral can be derived for the off-cell case where $ku > k\delta$. Expanding the integrand around $k\delta$ and then integrating, an approximation to the integral is given as:

$$\int_{-k\Delta}^{k\Delta} \imath e^{\sqrt{(ku-k\delta)^2}} - \imath e^{\imath\sqrt{ka^2+(ku-k\delta)^2}}\, dk\delta$$
$$\approx \imath\, 2\, k\Delta \left(e^{\imath|ku|} - e^{\imath\sqrt{ka^2+ku^2}} + \frac{ka^2\, k\Delta^3}{3} \frac{e^{\imath\sqrt{ka^2+ku^2}}}{\sqrt{ka^2+ku^2}^3} \right) \tag{2.70}$$

Note that this is a second order approximation in $k\delta$, an improvement of the first order approximation normally used in moment-method solutions. This additionally fidelity was added to provide excellent accuracy for predicting the near-cell $kz = kz_n + 2k\Delta$ scattering over a wide range of values for ka and $k\Delta$. The scattered field for the off-cell case is thus given as:

$$\begin{aligned}
\mathbf{E}_n^s(\bar{r}) \;=\; \hat{z}\, \frac{(\epsilon_r - 1)}{2}\, f(z_n) \Bigg[& \imath 2\, k\Delta \left(e^{\imath|ku|} - e^{\imath\sqrt{ka^2+ku^2}} \right) \\
& - \frac{\imath ka^2\, k\Delta^3}{3} \frac{e^{\imath\sqrt{ka^2+ku^2}}}{(\sqrt{ka^2+ku^2})^2} + \frac{ka^2\, k\Delta^3}{3} \frac{e^{\imath\sqrt{ka^2+ku^2}}}{(\sqrt{ka^2+ku^2})^3} \\
& + \frac{e^{\imath|ku-k\Delta|}\,(ku-k\Delta)}{|ku-k\Delta|} - \frac{e^{\imath\sqrt{ka^2+(ku-k\Delta)^2}}\,(ku-k\Delta)}{\sqrt{ka^2+(ku-k\Delta)^2}} \\
& - \frac{e^{\imath|ku+k\Delta|}\,(ku+k\Delta)}{|ku+k\Delta|} + \frac{e^{\imath\sqrt{ka^2+(ku+k\Delta)^2}}\,(ku+k\Delta)}{\sqrt{ka^2+(ku+k\Delta)^2}} \Bigg]
\end{aligned} \tag{2.71}$$

For the self-cell condition $ku = 0$, since $\sqrt{ka^2+k\delta^2} << 1$, the integral can be approximated as:

$$\imath\, e^{\sqrt{(ku-k\delta)^2}} - \imath\, e^{\imath\sqrt{ka^2+(ku-k\delta)^2}} \approx \frac{\imath\, ka^2}{2} + \sqrt{ka^2+k\delta^2} - |k\delta| \tag{2.72}$$

$$\int_{-k\Delta}^{k\Delta} \imath\, e^{\sqrt{(ku-k\delta)^2}} - \imath\, e^{\imath\sqrt{ka^2+(ku-k\delta)^2}}\, dk\delta \;\approx\; \imath\, ka^2\, k\Delta$$
$$+\; k\Delta\,(\sqrt{ka^2+k\Delta^2}\;-\;k\Delta) + \frac{ka^2}{2}\,\ln\left[\sqrt{ka^2+k\Delta^2}+k\Delta\right]$$
$$-\;\frac{ka^2}{2}\,\ln\left[\sqrt{ka^2+k\Delta^2}-k\Delta\right] \quad (2.73)$$

The scattering expression for the self-cell case is therefore:

$$\mathbf{E}_n^s(\bar{r}) \;=\; \hat{z}\, f(z_n)\,\frac{(\epsilon_r-1)}{2}\left(\imath\, ka^2\, k\Delta \;+\; k\Delta(\sqrt{ka^2+k\Delta^2}-k\Delta)\right.$$
$$+\;\frac{ka^2}{2}\,\ln\left[\sqrt{ka^2+k\Delta^2}+k\Delta\right] \;-\; \frac{ka^2}{2}\,\ln\left[\sqrt{ka^2+k\Delta^2}-k\Delta\right]$$
$$\left.-\;2e^{\imath k\Delta} \;+\; 2\,\frac{e^{\imath\sqrt{ka^2+k\Delta^2}}\,k\Delta}{\sqrt{ka^2+k\Delta^2}}\right) \quad (2.74)$$

The evaluation delineated above does not predict any coupling of the source direction into another directional component. A z directed source will produce only z directed field along the cylinder axis; an x directed source will similarly produce an x directed filed. Because of this, the solutions for $f_x(z)$, $f_y(z)$ and $f_z(z)$, can be found independently of each other. Provided that the point matching is accomplished at the center of each cell($z = z_m$ such that $z_m = z_n$ for $m = n$), the elements of the impedance matrix are given as:

$$Z_{mn} = \begin{cases} -E^s(z=z_m)/f(z_n) & \text{if } m \neq n, \\ 1 - E^s(z=z_m)/f(z_n) & \text{if } m = n. \end{cases}$$

where $w \in \{x, y, z\}$

(2.75)

Using this formulation, the total electric field for a thin, circular dielectric cylinder

can be determined for arbitrary values of incidence angle, dielectric ϵ_r normalized physical length ℓ/a and electrical length $k\ell$ (providing ka remains small). The results af this analysis can then be used to determine the validity of the GRG approximation across these parameters.

2.2.3 Numeric Error Evaluation

The proof provided in section(2.1) is independent of cylinder electrical length, thus implying that the infinite cylinder approximation is valid for all $k\ell$. We seek first to verify this assertion with the moment-method model, as well as examine the relative accuracy of the infinite cylinder approximation as a function of $k\ell$. The physical length of the cylinder ℓ/a, is set at a large and constant value, and the MM solution is then determined for various values of $k\ell$. The electrical radius ka will likewise vary so that $k\ell/ka$ remains constant; essentially we are fixing the geometry of the cylinder and changing the wavelength. The results of this analysis are displayed in Figure(2.5), and confirm the results of section(2.1). The the infinite cylinder approximation ($|f(z)| = 1$) matches the MM solution very well, with the exception occurring at the very ends of the cylinder where a perturbation occurs. Interestingly, this error is also apparently independent of electrical length $k\ell$.

The analysis is now reversed, fixing $k\ell$ at a constant value and evaluating the MM solution for various normalized lengths ℓ/a. In contrast to the response as a function $k\ell$, the scattering solution exhibits a strong dependence as function of ℓ/a (Figure(2.6)). The result is a conformation of the requirement that the normalized length ℓ/a be large to ensure a valid approximation. As the normalized length becomes smaller the MM solution diverges from the infinite cylinder approximation of $|f(z)| = 1$. To examine the behavior of MM solution, the same data is again plotted

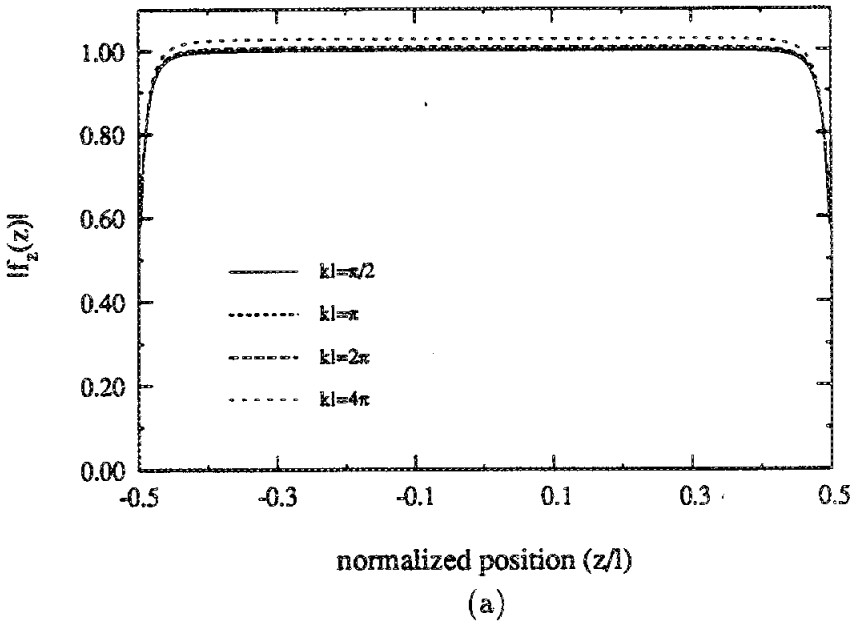

(a)

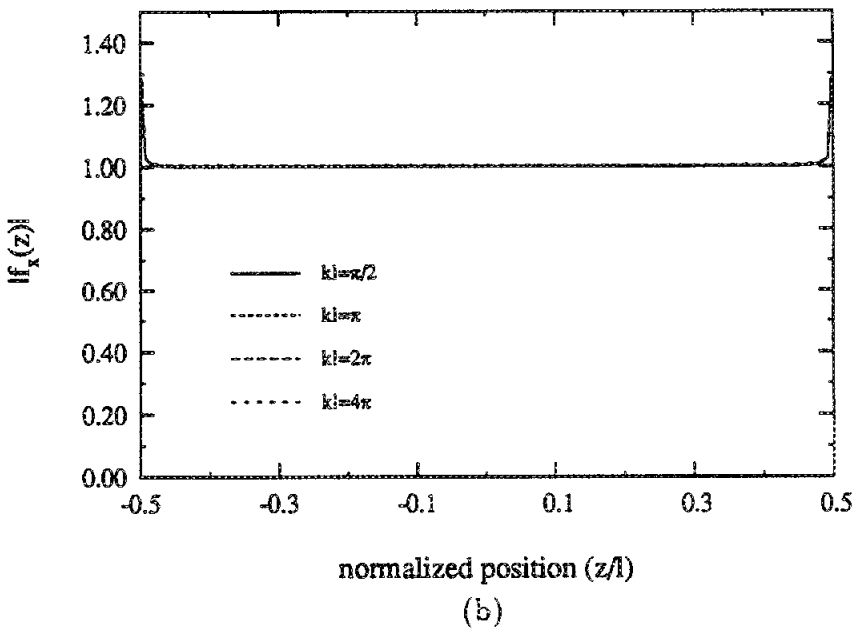

(b)

Figure 2.5: The axial (a) and transverse (b) components of the internal electric field in a thin circular cylinder for various electrical lengths. ($\ell/a = 200$, $\epsilon_r = 5.0$)

in Figure(2.7), this time as a function of $(\ell/2 - z)/a$. In this figure, it is apparent that the perturbation at the end of the cylinders is a function dependent only on the distance away from the cylinder ends, as normalized to the cylinder radius. Thus, changing the normalized length ℓ/a does not effect the behavior of $E_z(z)$ at the ends of the cylinder. As a result, as ℓ/a becomes smaller, the region where $E_z(z)$ diverges from the infinite cylinder approximation, while remaining a constant length (as normalized to a), becomes a significant portion of the entire cylinder length. At this point, the infinite cylinder approximation no longer provides an accurate representation of scattering behavior. From this data, it is apparent that the scattering phenomenon is very localized. The scattered field is the same for all points on the cylinder, except for the points too close (a few radius distances) to the end-caps of the cylinder. This is true for *all* cylinder lengths ℓ, from very long to very short.

To further examine its performance, the accuracy of the infinite cylinder approximation is examined as a function of both incidence angle and dielectric constant. Figure(2.8) displays the MM solution calculated for an oblique incidence angle ($\beta = \pi/8$). Although the solution $f(z)$, is dependent on incidence angle β, almost no sensitivity to this parameter was detected in regards to approximation accuracy; the errors exhibited at the ends of the cylinder remain constant regardless of incidence angle. Conversely, accuracy is greatly influenced by dielectric constant ϵ_r. Figure(2.9) displays the MM method solution for various dielectric constants. It is quite evident that as the value of ϵ_r is increased, so to does the region of significant error at either end of the cylinder. Thus, for larger values of ϵ_r, the constraint on the smallest physical length ℓ/a required to ensure accurate implementation (2.7) will likewise increase. This sensitivity to dielectric constant is observed almost entirely for the axial component $f_z(z)$; the transverse components displays only a slight sensitivity to ϵ_r.

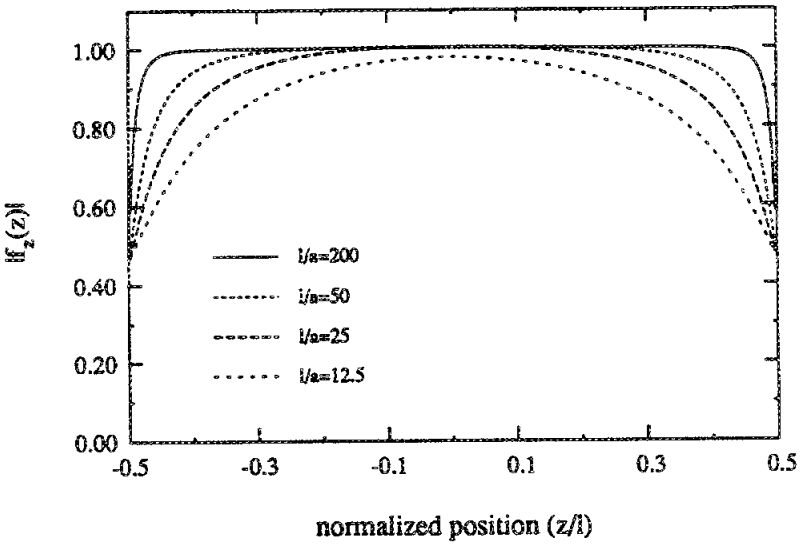

(a)

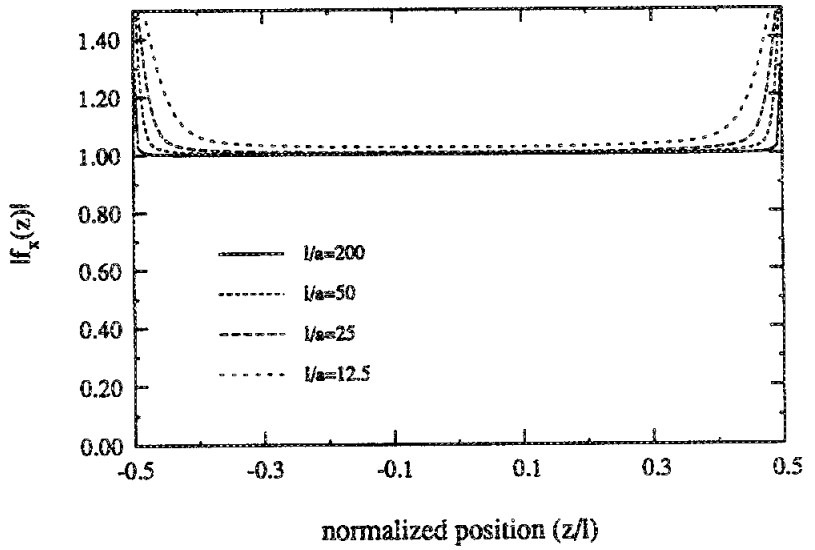

(b)

Figure 2.6: The axial (a) and transverse (b) components of the internal electric field in a thin circular cylinder for various normalized lengths. ($k\ell = \pi/2$, $\epsilon_r = 5.0$)

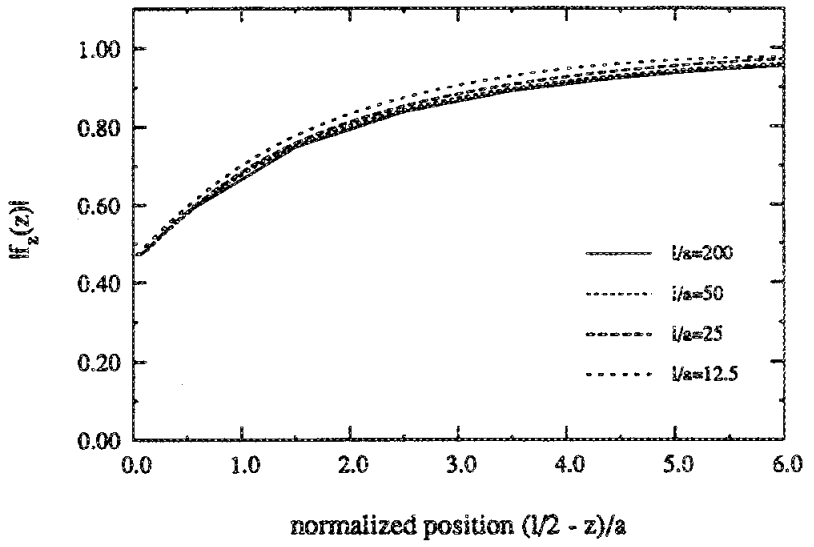

(a)

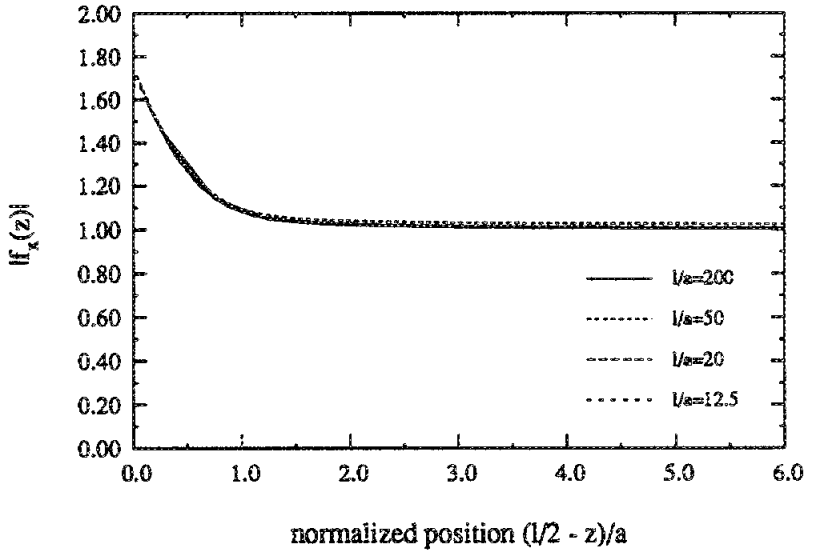

(b)

Figure 2.7: The axial (a) and transverse (b) components of the internal electric field in a thin circular cylinder for various normalized lengths, plotted as function of radius values from the cylinder end. ($k\ell = \pi/2$, $\epsilon_r = 5.0$)

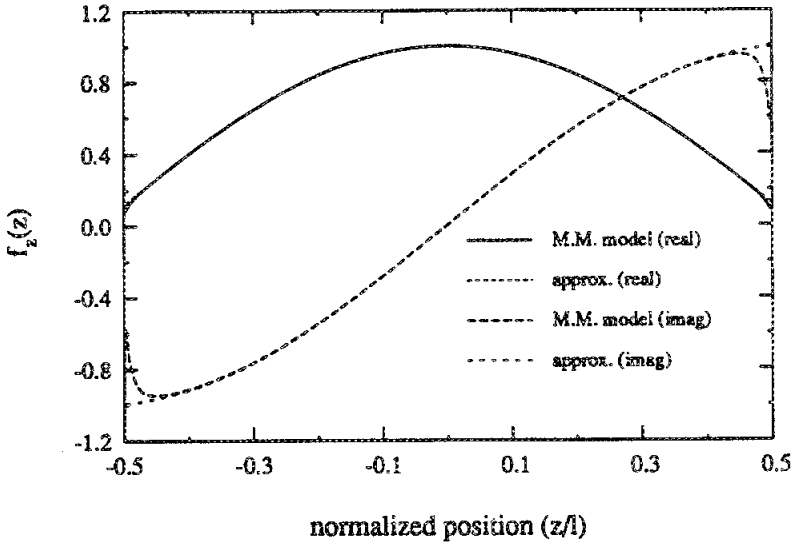

(a)

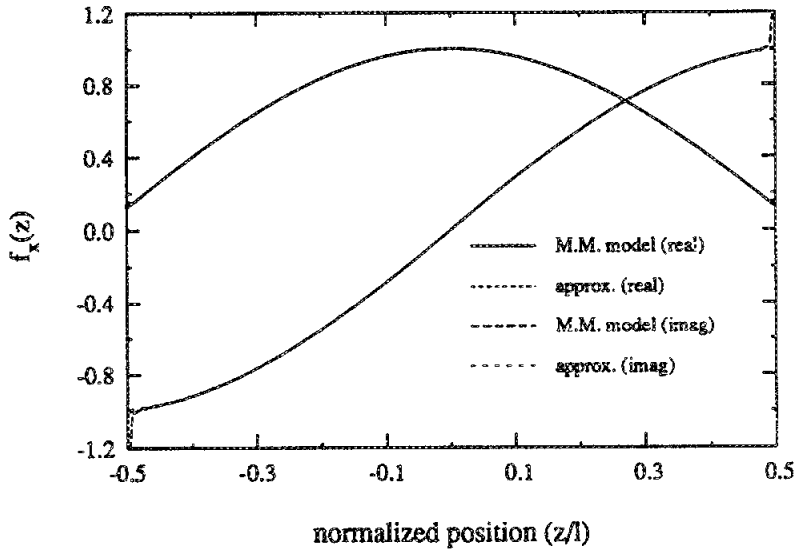

(b) .

Figure 2.8: The axial (a) and transverse (b) components of the internal electric field in a thin circular cylinder for an oblique incidence angle (β = 22.5). Both the MM model and the infinite cylinder approximation are plotted.($k\ell = \pi$, ℓ/a=200)

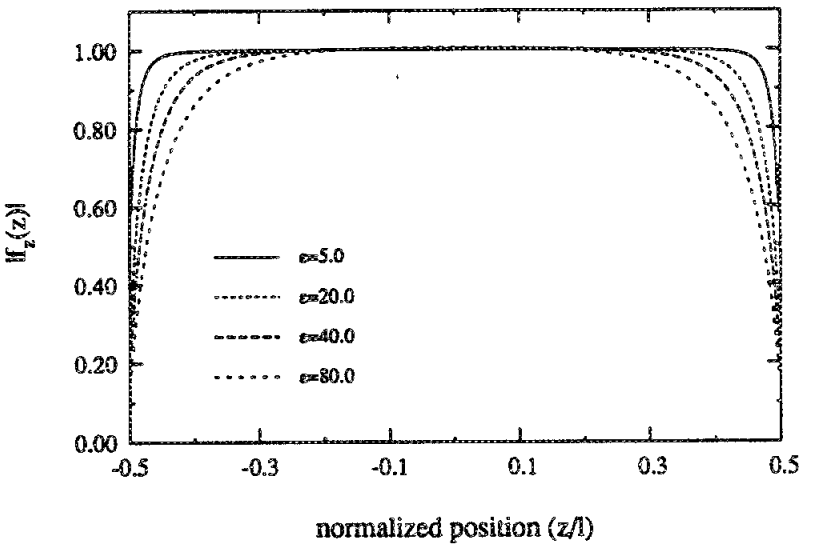

(a)

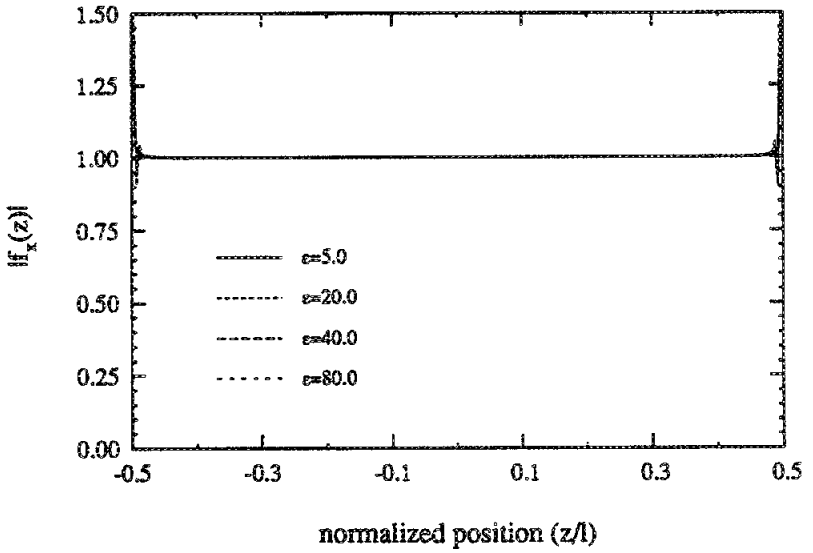

(b)

Figure 2.9: The axial (a) and transverse (b) components of the internal electric field in a thin circular cylinder for various dielectric values.($k\ell = \pi/2$, $\ell/a = 200$)

By comparison to a moment-method solution, we can conclude that the accuracy of the infinite cylinder approximation is dependent largely on the physical length ℓ/a and dielectric ϵ_r, but only slightly on incidence angle β and electrical length $k\ell$.

For a given criteria, the numerical results of the MM solution can be used to define the validity limits of the infinite cylinder approximation. The upper bound on ka is determined by the error of the Rayleigh approximation, a topic which has been addressed previously and therefore will not be examined here [11, 28]. Since approximation error is independent of $k\ell$, the remaining cylinder parameters, normalized length ℓ/a and dielectric ϵ_r, will define the validity region. The MM solution demonstrated that for all conditions the axial component $\hat{z}$ exhibited significantly greater error than the transverse component. Therefore, the axial solution will be used to define the limits on ℓ/a and ϵ_r.

The far-field scattering is a function of the total internal field $\mathbf{E}(\bar{r})$ convolved with the free-space Green's function. Therefore, the metric selected to define model accuracy is the average internal field, determined by integrating its magnitude over the cylinder length:

$$m = \frac{1}{\ell} \int_{-\ell/2}^{\ell/2} \left| \frac{E_z(z)}{e_z} \right| dz \tag{2.76}$$

This definition takes on a special significance when the electrical length of the cylinder is small ($k\ell << 1$), and thus entirely in the Rayleigh region. The value $E_z(z)/e_z$ is

entirely real, and the and the metric is equal to the normalized polarizability tensor:

$$\begin{aligned} m &= \frac{1}{\ell} \int_{-\ell/2}^{\ell/2} \left| \frac{E_z(z)}{e_z} \right| dz \\ &= \left| \frac{1}{\ell} \int_{-\ell/2}^{\ell/2} \frac{E_z(z)}{e_z}\, dz \right| \\ &= \left| \frac{1}{V} \int_{V} \frac{E_z(\bar{r})}{e_z}\, dv \right| \\ &= \left| \frac{P_{zz}}{(\epsilon_r - 1)\, V} \right| \end{aligned} \tag{2.77}$$

Inserting equation(2.7) into (2.76), we find that the infinite cylinder approximation results $m = 1.0$, regardless of the cylinder parameters.

If the form of $|E_z(z)|$ is independent of $k\ell$, the metric given by equation(2.76) should likewise be independent of electrical length. Figure(2.10) demonstrates this fact, plotting m as a function ℓ/a for various values of $k\ell$, with the constraint that $k\ell/(\ell/a) = ka << 1$. Since the metric m is independent of $k\ell$, from (2.77) it can be concluded that for all $k\ell$ and ϵ_r, the metric m is numerically equal to the value $|P_{zz}/(\epsilon_r - 1)V|$ for an equivalent Rayleigh particle. As a result, the polarizability tensor P_{zz} is a sufficient parameter for determining when the infinite cylinder approximation ($(m = 1.0)$ diverges from the exact solution, as defined by the metric m. For a circular cylinder, a validity requirement can thus be inferred for equation (2.7), as a function of the relevant parameters ℓ/a and ϵ_r. If a maximum error of 5% is arbitrarily placed on m, the infinite cylinder approximation will satisfy this criteria only if:

$$\ell/a > 20\sqrt{|\epsilon_r|} \tag{2.78}$$

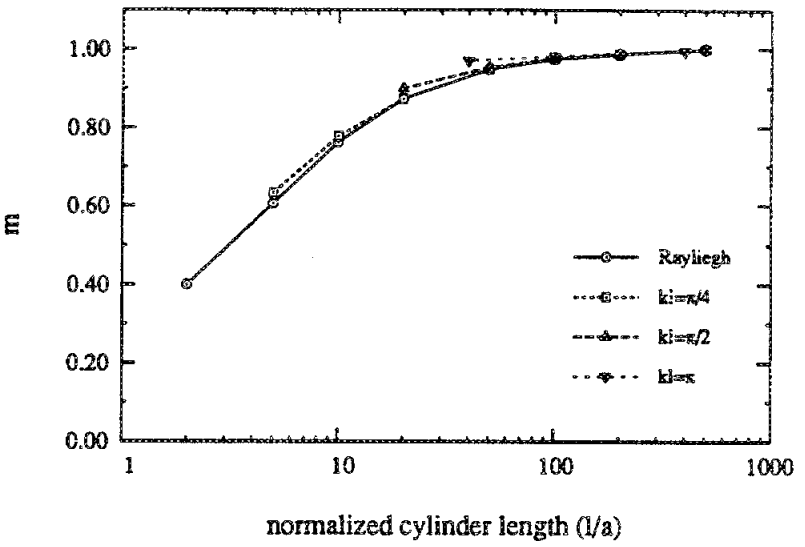

Figure 2.10: The metric m as a function of ℓ/a for various electrical lengths. ($\epsilon_r = 20$)

2.2.4 First-Order Solution

Returning to section(2.1), where the GRG approximation was shown to be correct in the limit as ka approached zero, we can see by observing equations (2.29) to (2.52) that as consequence of proving GRG validity that an analytic, first order solution to the scattering from a thin cylinder was generated. That is, if the lowest order solution is considered to be the GRG approximation given as equation(2.7), the first order solution can be found as:

$$\mathbf{E}_1 = \mathbf{E}^i + \mathbf{E}_1^s(\mathbf{E}_0) \tag{2.79}$$

where $\mathbf{E}_0$ is the GRG approximation, and $\mathbf{E}_1^s(\mathbf{E}_0)$ is the scattered field due assuming the GRG approximation. Often, although not always, a first oder scattering solution is a more accurate scattering solution than the lower (or "zeroth") order solution. From the MM solution, we have determined that the GRG approximation breaks down at the end of the cylinders for the axial polarization case. Perhaps a first order solution can provide a better analytic approximation for the cylinder current, particularly for physically short cylinders where ℓ/a is not large. To determine its accuracy, a first-order solution was constructed by inserting equation(2.40) and equation(2.41) into equation(2.52) to find $\mathbf{E}_1^s(\mathbf{E}_0)$. The results of this first-order solution are demonstrated in Figures(2.11). In the middle of a cylinder, where $(\ell/2 - |z|)/a$ is large, all three formulations, GRG, moment-method, and first order solutions, provide nearly identical answers. However, as $|z|$ approaches $\ell/2$, the GRG and first-order solutions diverge, with the first order formulation continuing to match the MM solution. Thus, in this region, the first-order solution meets or exceeds the accuracy of the GRG approximation, while still providing a strictly analytical formulation. However, for regions of the cylinder very near to the end (a few radius distances), the first order solution quickly diverges from the MM solution. This divergence is so great as to result in a huge error at the ends of the cylinder. Thus, when integrating over the cylinder length, the GRG provides a better match to the MM solution than the first-order approximation, with the exception of tenuous cylinders where ϵ_r is small.

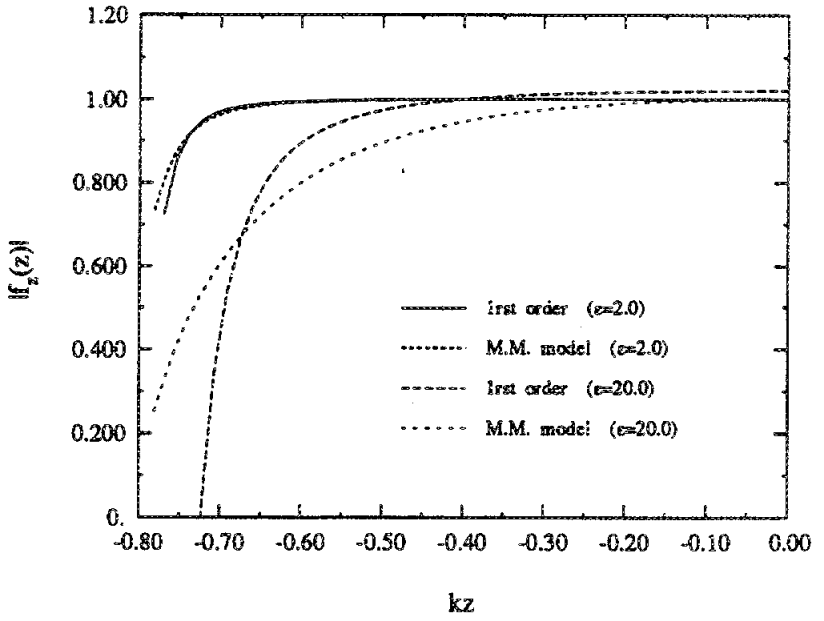

Figure 2.11: A comparison of the first-order and MM models.

2.3 Far-field Scattering from Thin Cylinders

The far-field scattering from a long thin dielectric cylinder can be determined by using the familiar far-field scattering equation [28]:

$$\mathbf{E}^s = -k_0^2\, \hat{k}^s \times \hat{k}^s \times \mathbf{\Pi}^e(\bar{r}) \tag{2.80}$$

where $\mathbf{\Pi}^e(\bar{r})$ is the electric Hertz potential vector. This potential vector can likewise be approximated in the far field:

$$\mathbf{\Pi}^e(\bar{r}) = \frac{e^{\imath k_0 r}}{r} \frac{\imath Z_0}{4\pi k_0} \int_V \mathbf{J}(\bar{r}') e^{-\imath k_0 \hat{k}^s \cdot \bar{r}'} dv' \tag{2.81}$$

The current density $\mathbf{J}(\bar{r})$ for a dielectric is the polarization current induced by the interior field ($\mathbf{J}(\bar{r}) = \imath k_0 Y_0(\epsilon_r - 1)\mathbf{E}(\bar{r})$), therefore the Hertz potential can be written

in terms of the interior field as:

$$\mathbf{\Pi}^e(\bar{r}) = -\frac{e^{\imath k_0 r}}{r}\frac{(\epsilon_r - 1)}{4\pi}\int_V \mathbf{E}(\bar{r}')\, e^{-\imath k_0 \hat{k}^s \cdot \bar{r}'} dv' \tag{2.82}$$

Since the cylinder is electrically thin, the phase kernel $\exp(\imath k_0 \hat{k}^s \cdot \bar{r}')$ is approximated as $\exp(\imath k_z^s z')$. Thus, inserting the infinite solution of equation(2.7), the electric Hertz potential is:

$$\mathbf{\Pi}^e(\bar{r}) = \frac{e^{\imath k_0 r}}{r}\frac{1}{4\pi}\int_\ell \int_A \Big(- e_x\, \nabla\Phi_1(\bar{\rho}) - e_y\, \nabla\Phi_2(\bar{\rho}) + e_z\, \hat{z}\Big) e^{-\imath(k_z^s - k_0\cos\beta)z'} dz' \tag{2.83}$$

Using a form of the divergence theorem:

$$\int_A \nabla_t \Phi(\bar{\rho})\, d_A = \int_C \Phi(\bar{\rho})\, \hat{n}\, dc \tag{2.84}$$

this equation can be re-written in terms of the polarizability tensor elements:

$$\mathbf{\Pi}^e(\bar{r}) = \frac{e^{\imath k_0 r}}{r}\frac{1}{4\pi}\int_\ell \Big(a_x(P_{xx}^{2d}\hat{x} + P_{yx}^{2d}\hat{y}) + a_y(P_{xy}^{2d}\hat{x} + P_{yy}^{2d}\hat{y}) + P_{zz}^{2d}\hat{z}\Big) e^{-\imath(k_z^s - k_0\cos\beta)z'} dz' \tag{2.85}$$

The coefficients P^{2d} are defined as the polarizability tensor elements per unit length of the thin cylinder, defined as [21]:

$$\begin{aligned}
P_{xx}^{2d} &= -(\epsilon_r - 1) \int_C \Phi_1 \, \hat{n} \cdot \hat{x} \, dc' \\
P_{xy}^{2d} &= -(\epsilon_r - 1) \int_C \Phi_2 \, \hat{n} \cdot \hat{x} \, dc' \\
P_{yx}^{2d} &= -(\epsilon_r - 1) \int_C \Phi_1 \, \hat{n} \cdot \hat{y} \, dc' \\
P_{yy}^{2d} &= -(\epsilon_r - 1) \int_C \Phi_2 \, \hat{n} \cdot \hat{y} \, dc' \\
P_{zz}^{2d} &= (\epsilon_r - 1) \int_A dA' \\
0 = P_{xz}^{2d} &= P_{zx}^{2d} = P_{yz}^{2d} = P_{zy}^{2d}
\end{aligned} \tag{2.86}$$

Equation(2.85) can therefore be succinctly written in terms of the polarizability tensor $\mathcal{P}^{2d}$.

$$\mathbf{\Pi}^e(\bar{r}) = \frac{e^{\imath k_0 r}}{4\pi r} \int_\ell \mathcal{P}^{2d} \cdot \hat{a} \; e^{-\imath(k_z^s - k_0 \cos\beta)z'} dz' \tag{2.87}$$

and from (2.80) the scattered field is computed as by evaluating the integral of length ℓ:

$$\mathbf{E}(\bar{r}) = -k_0^2 \frac{e^{\imath k_0 r}}{4\pi r} \hat{k}^s \times \hat{k}^s \times \mathcal{P}^{2d} \cdot \hat{a} \int_\ell e^{-\imath(k_z^s - k_0 \cos\beta)z'} dz' \tag{2.88}$$

$$= -k_0^2 \frac{e^{\imath k_0 r}}{4\pi r} \hat{k}^s \times \hat{k}^s \times \ell \mathcal{P}^{2d} \cdot \hat{a} \, \frac{\sin U}{U} \tag{2.89}$$

where the value U is the expression $U = \frac{k_0 \ell}{2}(\hat{k}^s \cdot \hat{z} - \cos\beta)$. From this expression, the elements of the scattering matrix can be expressed as [21]:

$$S_{\chi\psi} = \frac{k_0^2}{4\pi}\hat{\chi} \cdot \mathcal{P}^{2d} \cdot \hat{\psi} \int_\ell e^{-\imath(k_z^s - k_0 \cos\beta)z'} dz' \tag{2.90}$$

$$= \frac{k_0^2}{4\pi}\hat{\chi} \cdot \ell\mathcal{P}^{2d} \cdot \hat{\psi}\, \frac{\sin U}{U} \tag{2.91}$$

A definite physical interpretation can be can attached to this formulation. The scattering from a thin dielectric cylinder can be attributed to electric dipoles lying along the cylinder axis. The total scattering from the cylinder can be thought of as a coherent addition of the scattering from elemental or incremental dipoles, each with a dipole moment described as $\mathbf{p}^{2d}dz = \epsilon_0 \mathcal{P}^{2d} dz \cdot \hat{a}$, lying along the cylinder axis. The scattering from an incremental dipoles at a given location is a function the cross-section and dielectric the cylinder at that location, as well as the incident electric field at that location. It is important to note however, that the dipole moment of a short thin cylinder, length Δz, with identical shape and cross-section is not $\mathbf{p}^{2d}\Delta z$ as the end-caps of the short cylinder will dramatically effect polarizability. Thus, the incremental dipole of moment $\mathbf{p}^{2d}dz$ is merely a construct to describe the scattering from a long, thin structure, denoted hereafter as a line-dipole element.Like the Dirac delta function, polarizability tensor $\mathcal{P}^{2d}dz$ has no physical meaning, it must appear only in an operator in an integration.

The reason that the concept of a polarizability tensor can be implemented for thin cylinders is that the scattering solution is essentially an quasi-static solution. As this chapter demonstrated, the solution for small ka is not a function of the higher orders of k_0, hence its independence on electrical length $k\ell$. It was also shown that the solution given by equations (2.6) and (2.7) is the result of a very localized phenomenon, as the

moment-method and first-order models demonstrated that the solution is valid for all locations along the cylinder except at the very ends (a few radius lengths) , where the end-caps perturb the solution. Equations (2.6) and (2.7) provide an accurate solution for the internal electric field that is independent of total cylinder length ℓ. The field at an arbitrary point on the cylinder is dependent only on the incident field at that point and the dielectric material immediately surrounding it. The remainder of the cylinder may be very long, or relatively short, the field solution is unaffected. Returning to the incremental dipole concept, this means that the incremental dipole elements do not couple; that elements can be added or subtracted from the cylinder without perturbing the others.

If the fields at a point on a thin cylinder is unaffected by the scattering from regions of the cylinder outside its immediate vicinity, then it could logically inferred that perturbing slightly the scattering from these distant regions would likewise have no effect at the observation point. These perturbations could reflect a change in the shape, dielectric, or even *orientation* of the cylinder region (i.e. the incremental dipole moment). Thus, the solution of (2.6) and (2.7) can likewise be applied to cylinders with axial *curvature*, provided that the cylinder is locally straight throughout an axial region of several radius lengths. Thus, equation (2.91) can be modified to reflect a general curved cylinder:

$$S_{\chi\psi} = \frac{k_0^2}{4\pi} \int_L \hat{\chi} \cdot \mathcal{P}^{2d}(\bar{r}') \cdot \hat{\psi}\, e^{-\imath k_0 (\hat{k}^s - \hat{k}^i)\cdot \bar{r}'} d\ell' \tag{2.92}$$

where L defines the contour of the curved cylinder. Likewise, the scattering from a distant location of the cylinder can be perturbed by changing the incident field at that point. Thus, the incident field must only locally be a uniform plane wave, in

general the phase term of (2.92) can be more represented as an arbitrary propagation function $\Phi(\bar{r})$ so that:

$$S_{x\psi} = \frac{k_0^2}{4\pi} \int_L \hat{\chi} \cdot \mathcal{P}^{2d}(\bar{r}') \cdot \hat{\psi}\, \Phi(\bar{r}') d\ell' \tag{2.93}$$

This approximation is analogous to the Kirchoff or tangent-plane approximation in rough surface scattering, where the scattering from a given location is determined as if the surface at that point uniformly extends into infinity.

2.4 Conclusion

The preceding analysis has provided a scattering solution for long, thin dielectric cylinders of arbitrary electrical length. The truncated solution of a thin, infinite length dielectric cylinder is shown to be valid provided that the normalized cylinder length ℓ/a is large. Although this is an obvious result for electrically long cylinders ($k\ell >> 1$), the solution is explicitly shown to be asymptotically correct as $ka \rightarrow 0$, regardless of electrical length $k\ell$. As such, the formulation is likewise a valid Rayleigh scattering solution for particles whose length ℓ far exceeds their radius a. The generalized Rayleigh-Gans approximation, as applied to a circular cylinder, is thus a specific case of the infinite cylinder approximation. As a result, the assertion of GRG validity for all $k\ell$ was equivalently demonstrated by the analysis this chapter.

The moment-method solution provided a numeric tool for analyzing the accuracy of the infinite cylinder approximation. The infinite cylinder solution exhibits significant error only as the cylinder ends are approached. This error is apparently dependent on only the distance from the cylinder ends, as normalized to the cylinder radius. Thus, the normalized cylinder length ℓ/a, must be large for this error to reside

in an insignificant portion of the cylinder length. Although independent of electrical length, the magnitude of this error is strongly dependent on dielectric, enlarging as the dielectric value is increased.

Finally, it was shown that the scattering from thin cylinders can be attributed to dipoles on the cylinder axis, and thus the structure was defined as a line-dipole element consisting of incremental dipole elements. From the results of this chapter, it is evident that the scattering from these incremental dipoles are uncoupled, thus the solution can be extended to cylinders with moderate curvature such that all regions of the cylinder are locally straight.

CHAPTER III

A SCATTERING MODEL FOR THIN CYLINDERS WITH BLADE SHAPED CROSS-SECTIONS

The scattering model of the last chapter provided a microwave scattering model of arbitrary cross-section. The relation between cross-section and cylinder scattering is revealed in the integral equations of (2.6), which specifies the radial component of the cylinder electric field. These equations contain and integration over a region defining the cross-section of the cylinder. This region is completely arbitrary, and the the scattering solution is dependent on the cross-section shapes of the cylinder. As was demonstrated in in section 2.3, the effect this solution in regards to far-field scattering can be comprehended in terms of a polarizability tensor per unit length $\mathcal{P}^{2d}$, a parameter which therefore is also dependent on cylinder cross-section. The exception being the tensor element P_{zz}^{2d}, which is dependent on total cross-section area but not on shape (2.86).

The practical problem with this formulation is that analytical solutions for equation (2.6) is limited to canonical cross-sections such as circles and ellipses. Other more complex cross-sections require that the integral equations be solved using nu-

merical methods. This presents a conflict between two of the stated goals for the model. To preserve the fidelity of the physical analog, the complex blade shapes encountered in grassland vegetation should be accurately modeled. However, to do this would require solving numerically the integral equations, a procedure which requires significant computational overhead, thus reducing the utility of the scattering.

However, whereas the blade cross-sections of grasses may be complex and random, they are not arbitrary. The term "blade" refers to a generally "V" shaped cross-section, a thus a set of parameters could perhaps be defined to describe a family of these shapes. Additionally, this blade description parameter space can be numerically limited, constrained to the values which are involved in nature. Defining the problem in this manner greatly reduces the complexity of the problem. If the polarizability tensor elements are numerically evaluated at a significant number of sample points throughout the constrained parameter space, then perhaps a relationship between the parameters describing blade shape and the corresponding polarizability tensor can be inferred. If an analytic approximation is the result, then both goals of fidelity and utility can be satisfied. The complex shapes of grass blades can be accurately reflected in the model, while the resulting scattering (in terms of polarizability tensor) can be swiftly computed.

3.1 Grass Blade Geometry

The fine geometry exhibited by most grass blades occurring in nature can be approximated by a set of five description parameters as shown in Figure 3.1. These five parameters, thickness t, width w, blade angle θ, radius of curvature r, and blade length l can be combined to produce five new independent parameters, two of which

parameter	symbol	expression
Area	A	$\approx 2tw$
Length	l	l
Aspect Ratio	a	$t/(2w)$
Curvature	v	w/r
Blade Angle	θ	θ

Table 3.1: The five parameters describing blade geometry, including two parameters (length l, and area A) which specify blade size, and three dimensionless parameters (aspect ratio a, curvature v, and blade angle θ) which specify shape.

describe the size of the blade while the other three describe its shape. The first two of these parameters, as shown in Table 3.1, are the cross-sectional area A and blade length l, which together specify the blade size. The three remaining parameters are dimensionless quantities, and thus specify only the blade shape. The first, aspect ratio a, is defined as the ratio of blade thickness to blade width. The second parameter, curvature v, is the arc angle in radians of the arc formed by the curvature of the blade on either side of the center rib. The final parameter, blade angle θ, is the angle formed by the vector normal to the grass blade surface at the center rib, and the vector tangent to the blade curvature at the center rib. In addition, for purposes of the scattering formulation, the grass blades are assumed to be both long and thin, such that $2w << \lambda$ and $l >> w$.

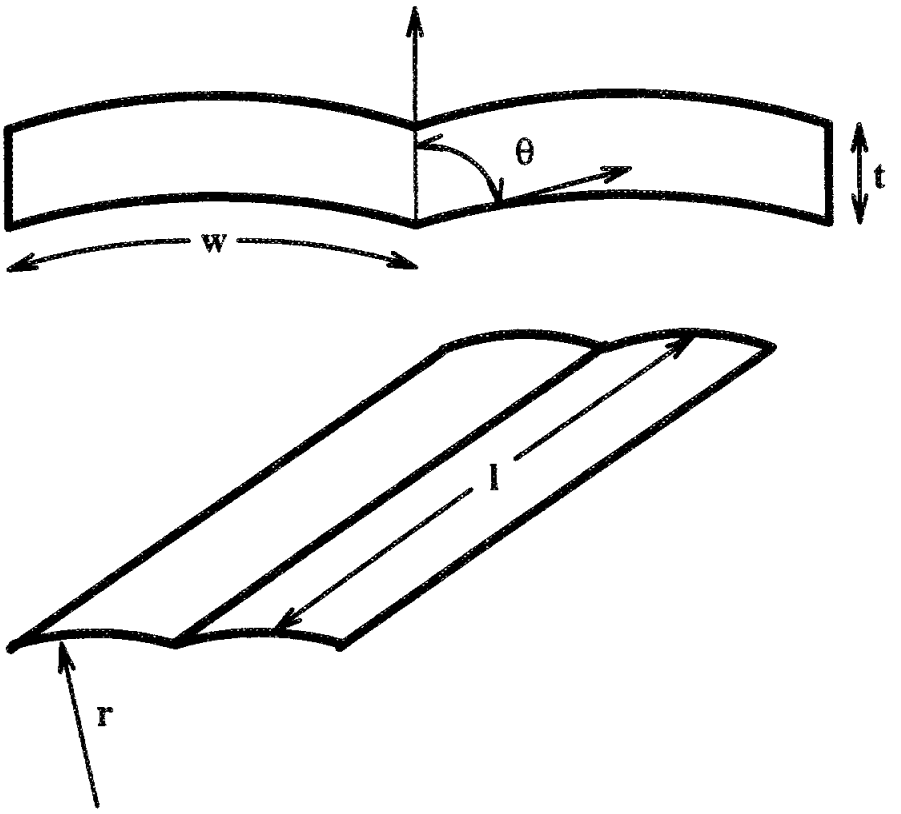

Figure 3.1: Diagram of grass blade geometry including blade cross-section (showing width w, thickness t, and blade angle θ) and overhead view (showing radius of curvature r and length l).

3.2 Polarizability Tensor Evaluation

A moment-method solution to the integral equations of (2.6) was likewise provided by Sarabandi and Senior []. This solution was implemented in computer code so that the polarizability tensor elements of grass blade cross-sections could be numerically evaluated. The parameter of interest in this case is the normalized polarizability tensor $\mathcal{P}^{2d}/A$. Each element of the polarizability tensor is directly proportional to the total cross-section area A, thus the normalized polarizability tensor $\mathcal{P}^{2d}/A$ is independent of area. Therefore, $\mathcal{P}^{2d}/A$ is a function of only the dielectric constant and the shape, as described by the dimensionless shape parameters, curvature v, aspect ratio a, and blade angle θ. For cylinders with symmetric cross-sections, the off-diagonal tensor elements P_{xy}^{2d} and P_{xy}^{2d} are both zero, providing the local coordinate system is aligned with the axis of symmetry. Since the blade shapes introduced in the previous section are of this type, the polarizability tensor is diagonal with the elements P_{xx}^{2d} and P_{yy}^{2d} dependent on shape. In general, the elements P_{xx}^{2d} and P_{yy}^{2d} are respectively proportional to the projected area of the blade shape onto the (x, z) and (y, z) planes. Thus, the parameter which most affects the normalized polarizability tensor elements is aspect ratio, followed by blade angle and then blade curvature. Figure 3.2 demonstrates this dependence, showing the effect of aspect ratio and blade angle on the real part of P_{xx}^{2d}/A for both a relatively flat and a relatively curved grass blade geometry.

Although these figures demonstrate the dependence of polarizability tensor, and hence scattering on blade geometry, the larger question of whether these shape parameters significantly affect scattering from an entire grassland target can not be inferred. Therefore, a radiative transfer scattering model [31, 13, 30] was implemented which modeled a layer of scatterers consisting of cylinders of a given length

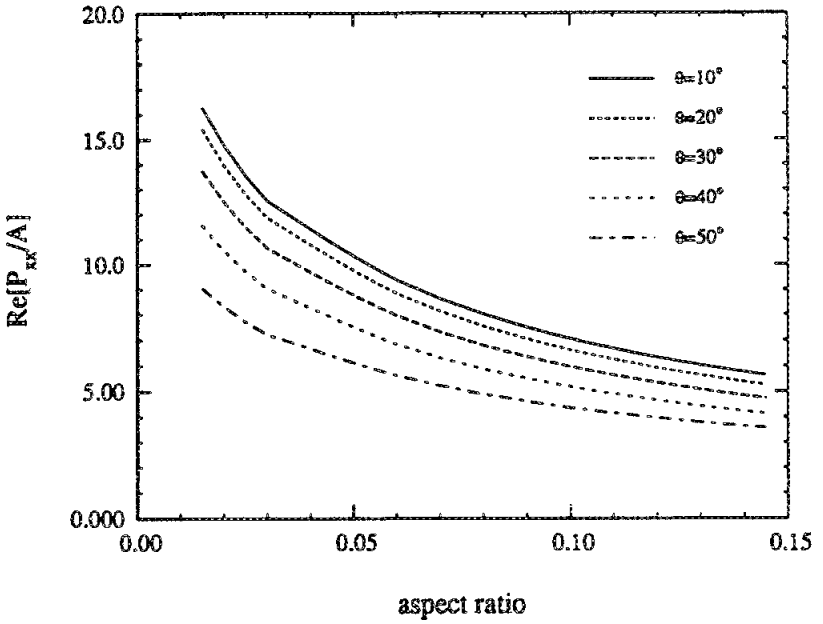

(a)

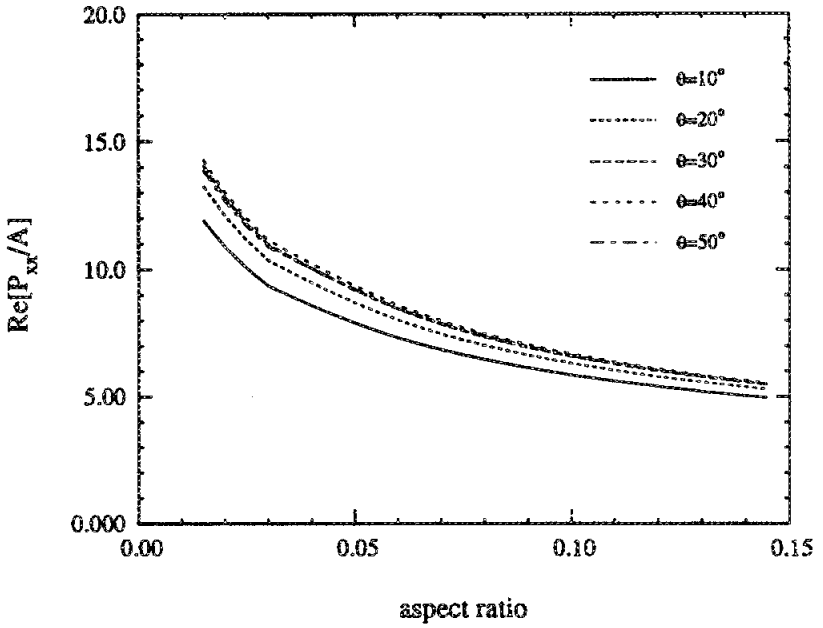

(b)

Figure 3.2: The real portion of the normalized polarizability tensor element P_{xx}^{2d}/A as a function of aspect ratio a and blade angle θ for blade curvature $v = 0.2$ (a) and 1.5 (b) ($\epsilon = 30 + j9$).

and cross-sectional area. Two cases were examined; in the first case, the cylinders were of circular cross-section, while in the other a blade shaped cross-section ($a = 0.045,\ \theta = 0,\ \upsilon = 0.01$) of identical area was implemented. Figure 3.3 displays the results of this model at two frequencies for two dielectric constants and three incidence angles. The difference in the cross-section shape results in a difference of as much as 5 dB in the value of σ°_{hh}. This contrast is largest at lower frequencies and for drier grass blades. Although this data represents a limited test case, it does show that for electrically small cross-sections, blade shape, in addition to blade size, *can* significantly affect the observed scattering from grassland targets.

3.3 Algebraic Model

For a cylinder of circular cross-section, an exact analytic solution to the integral equations of (2.6) exists, thus leading to an exact solution of the normalized polarizability tensor elements as a function of the complex dielectric constant [21, 28]:

$$\frac{P_{xx}}{A} = \frac{P_{yy}}{A} = 2\frac{\epsilon - 1}{\epsilon + 1} \tag{3.1}$$

As shown by Sarabandi and Senior [21], this equation can be modified to provide an approximate algebraic solution for cylinders of semi-circular, triangular, and square cross-sections which, although not an exact solution to the integral equations, matches the numeric solution with exceptional accuracy. This modified expression is given as:

$$\frac{P(\epsilon)}{A} = c_0\frac{\epsilon - 1}{\epsilon + 1} \cdot \frac{\epsilon + c_1}{\epsilon + c_2} \tag{3.2}$$

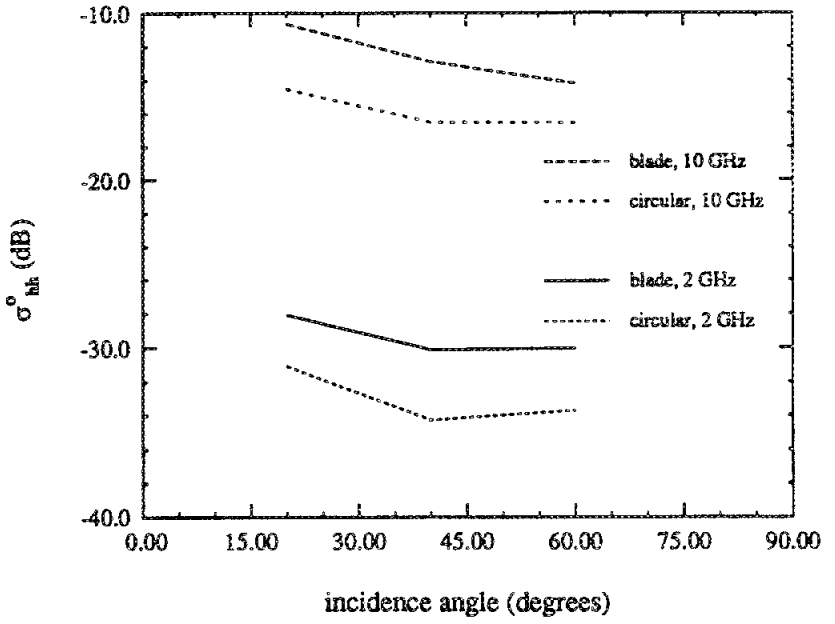

(a)

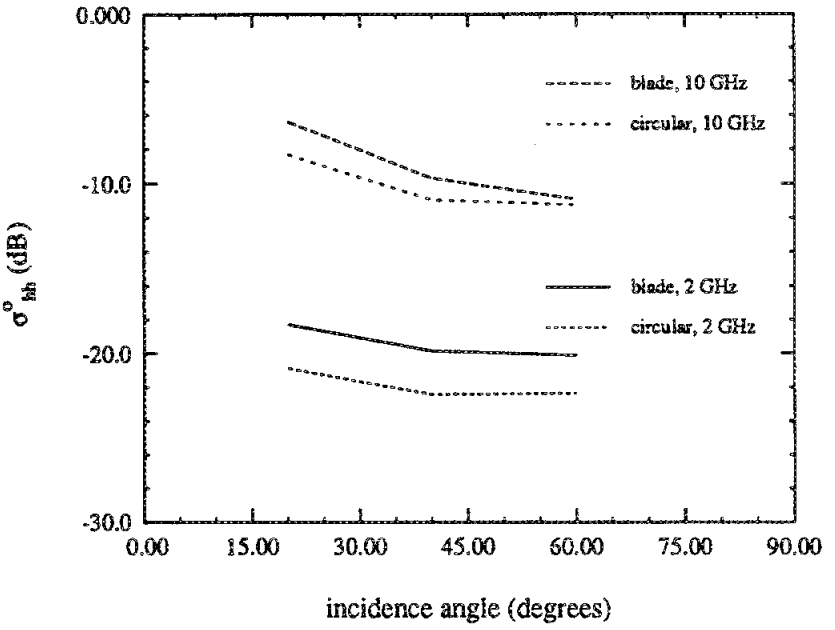

(b)

Figure 3.3: σ°_{hh} for dry (a) and moist (b) vegetation as predicted by a radiative transfer based grassland model for blades of both grass blade and circular shaped cross-sections ($a = 0.45$, $\theta = 0$, $v = 0.01$, $N = 2500/\ \mathrm{m}^3, l = .5\ \mathrm{m}, A = .03\ \mathrm{cm}^2, M_g = 0.3$ (a) and 0.9 (b)).

where the values of constants c_0, c_1, and c_2 are unique for each of the three cross-sections. This expression is valid for both P_{xx}^{2d}/A and P_{yy}^{2d}/A, although the three constants are of course different for non-symmetric cross-sections (semi-circular and triangular).

To determine if the validity of this expression extends to grass blade shapes, data was generated with the numerical model for a given blade geometry across a wide range of complex dielectric constants. Three constants c_1, c_2, and c_3 were then selected in an attempt to match (3.2) to the generated numerical data. As shown in Figure 3.4, constants were found which provided a match with good accuracy between the approximation of (3.2) and the numerical data. Thus, equation (3.2) appears to be valid for not only simple geometrical cross-sections, but for more general cross-sections (grass blades) as well. The constants c_0, c_1, and c_2, denoted as vector $\mathbf{c}$, can therefore be selected to relate the dielectric constant to the polarizability tensor for a given blade geometry. Since these constants are dependent only on cross-section geometry, and since cross-section geometry for a grass blade has been defined by the three shape parameters v, a, and θ, a more general algebraic approximation relating grass blade geometry, in addition to the dielectric constant, can be hypothesized:

$$\frac{P_{xx}^{2d}}{A} = c_0(\theta, a, v)\frac{\epsilon - 1}{\epsilon + 1} \cdot \frac{\epsilon + c_1(\theta, a, v)}{\epsilon + c_2(\theta, a, v)} \tag{3.3}$$

The expressions relating $\mathbf{c}$ to the shape parameters v, a, and θ must therefore be determined.

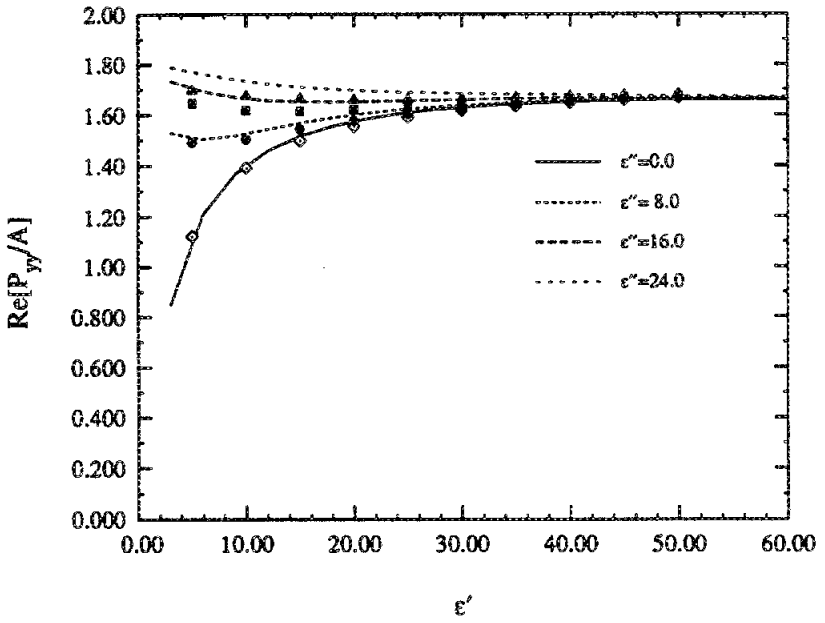

Figure 3.4: Comparison of the predicted dependence of $\mathrm{Re}[P_{yy}^{2d}/A]$ on dielectric constant for both the numerical scattering model (lines) and the algebraic approximation (marks) of (13) ($a = 0.1$, $\theta = 28°$, $v = 0.01$, $c_0 = 1.753$, $c_1 = 9.703$, and $c_2 = 10.297$).

3.4 Coefficient Estimation

To determine these relationships, the numerical model was used to determine the normalized polarizability tensor $\mathcal{P}^{2d}/A$ for various dielectrics for each of 512 separate blade geometries. These 512 geometries were uniformly selected from the parameter space shown in Table 3.2, describing the limited domain of geometries and dielectrics which, in general, are observed for grass blades. For a given geometry, six constants c_n must be determined, three for each P^{2d}_{xx}/A and P^{2d}_{yy}/A. Using the results of the numerical model at three distinct dielectric constants, a non-linear system of three equations $(\mathcal{P}^{2d}(\epsilon_1)/A,\ \mathcal{P}^{2d}(\epsilon_2)/A,\ \mathcal{P}^{2d}(\epsilon_3)/A)$ with three unknowns $(c_1,\ c_2,\ c_3)$ is formed using (3.2). Thus, nonlinear inversion techniques can be used to determine the three elements of $\mathbf{c}$ [18, ch. 9]. However, because (3.2) is merely an approximation, and not an exact solution for $\mathcal{P}^{2d}/A$, inversion techniques may lead to erroneous results. Inversion techniques force a solution which produces zero error at each of the three data points $\mathcal{P}^{2d}(\epsilon_1)/A$, $\mathcal{P}^{2d}(\epsilon_2)/A$, and $\mathcal{P}^{2d}(\epsilon_3)/A$, however in so doing may severely affect the accuracy of the approximation at other dielectric constant values.

As an alternative solution, the polarizability tensor elements were numerically computed at additional dielectric constants (six were found to be sufficient), and the three coefficients of $\mathbf{c}$ were then determined by locating those values which minimized the sum of the squared errors between (3.2) and the numerical data at these six dielectric values. Although the resulting algebraic approximation may exhibit non-zero error at all six dielectric values, the solution does match the numerical model results across the entire range of dielectric values. To determine an optimum selection of the vector $\mathbf{c}$, the conjugate gradient technique [18, ch. 10] was implemented which iteratively converges to the values of c_1, c_2, and c_3 that minimize the total squared

parameter	min.	max.
aspect ratio (a)	0.015	0.12
blade angle (θ)	0.0	50.0
curvature (v)	0.01	2.0
dielectric constant (ϵ')	5.0	45.0
dielectric constant (ϵ'')	2	25

Table 3.2: Model input parameter space estimating those values generally observed in nature.

error equation:

$$\sum_{n=1}^{6} \left(P_{num}^{2d}(\epsilon_n)/A - c_0 \frac{\epsilon_n - 1}{\epsilon_n + 1} \cdot \frac{\epsilon_n + c_1}{\epsilon_n + c_2} \right)^2, \tag{3.4}$$

where $P_{num}^{2d}(\epsilon_n)/A$ is the polarizability tensor element of a specified blade geometry with dielectric ϵ_n, as determined by the numerical model. Figure 3.5 contrasts the difference in the solutions obtained by using both an inversion and a minimization technique on the same set of numerical data. The minimization (conjugate gradient) technique selects coefficients $\mathbf{c}$ which result in a model matching all the numeric data points, whereas the inversion (Newton - Raphson) method results in a range of dielectric constants where (3.2) produces erroneous values for $\mathcal{P}^{2d}/A$.

Therefore, the conjugate gradient method was implemented on the selected 512 geometries to provide two sets of vector $\mathbf{c}$ (one set for each P_{xx}^{2d}/A and P_{yy}^{2d}/A) for

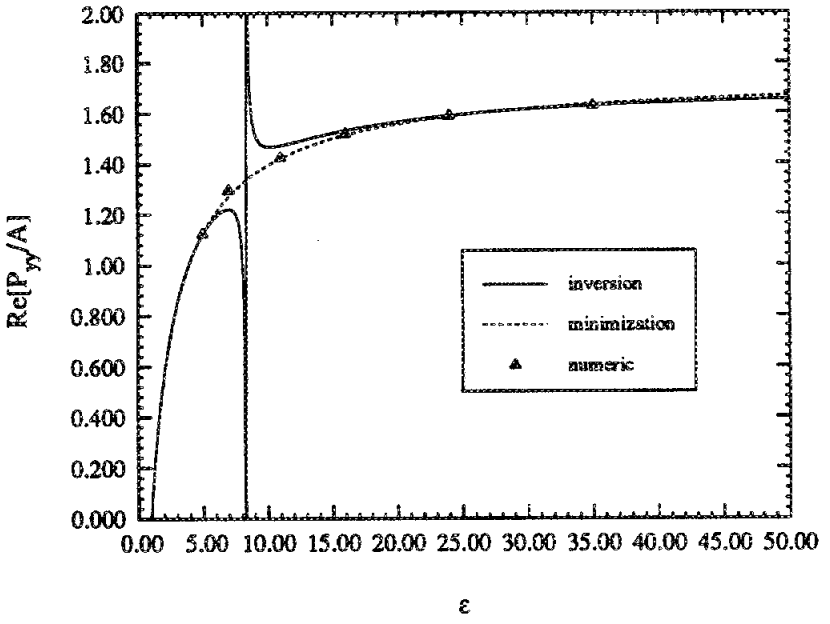

Figure 3.5: $\mathrm{Re}[P_{yy}^{2d}/A]$ versus ϵ as predicted by (13) using coefficients $\mathbf{c}$ determined by both inversion and error minimization methods. The inversion method results in large errors for some values of ϵ.

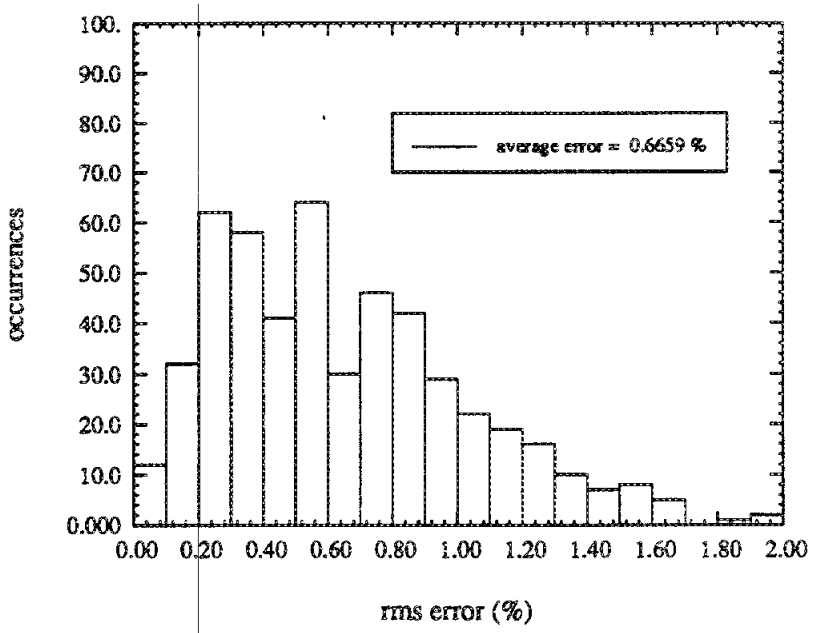

Figure 3.6: Histogram showing the distribution of the average rms error resulting from the approximation of (13) determined at 512 test geometries. The coefficients **c** were selected using a conjugate gradient error minimization technique.

each of the 512 cases. Figure 3.6 shows a histogram over the 512 geometries of the average rms error between the numerical model and the analytic approximation, using the coefficients as selected by the conjugate gradient technique. The average error for P_{xx}^{2d}/A was 0.07 %, whereas the average error for P_{yy}^{2d}/A was determined to be approximately 0.7 %. For each of the 512 geometries, a set of constants was found which provided an accurate model of the relationship between the dielectric constant and the polarizability tensor.

The conjugate gradient method converges to a set of coefficients **c** which provide a model with a minimum total squared error. However, this minimum may not be the global minimum, as the conjugate gradient may converge to any number of local minima, depending on the initial value of **c** used by the conjugate gradient

routine. These minima can be thought of as different "modes", with each mode producing a slightly different curve for (3.2), each matching the six numerical data points ($P^{2d}_{num}(\epsilon_n)/A$) in a slightly different fashion. For instance, one mode may result in a model which slightly underestimates the first three data points $P^{2d}(\epsilon)/A$ and slightly overestimates the last three, whereas for another mode the reverse may be true. Many of these modes may produce acceptable accuracy, but the desired solution is the mode associated with the smallest error (the global minimum). However, the mode associated with the global minimum at one geometry may not be the mode corresponding to the global minimum at another. Since we are ultimately seeking an expression relating c_1, c_2, and c_3 to the shape parameters v, a, and θ, a solution involving a single mode is required to avoid discontinuities in $\mathbf{c}$ across the domain of Table 3.2. For example, Figure 3.7(a) shows a solution for constant c_1 versus aspect ratio for various blade angle values. For blade angle values from $\theta = 0°$ to $\theta = 35°$, the minimum is associated with a single mode, however for $\theta = 42°$ and $49°$ the conjugate gradient algorithm converges to a different minimum, resulting in significantly different data and a large discontinuity in c_1 versus θ. Figure 3.7(b) shows the single-mode solution, a solution which is well behaved and continuous across both aspect ratio and blade angle.

If, for various regions of the blade shape parameter space (Table 3.2), the global minimum is associated with separate modes, then the selection of the "optimum" mode becomes a compromise between minimizing the average error across the parameter space and minimizing the maximum error occurring at any given point. In addition, forcing the conjugate gradient routine to converge to the same mode for all blade geometries may also prove to be difficult, as mode selection is determined only by the initial value of $\mathbf{c}$ of the conjugate gradient algorithm. This initial value

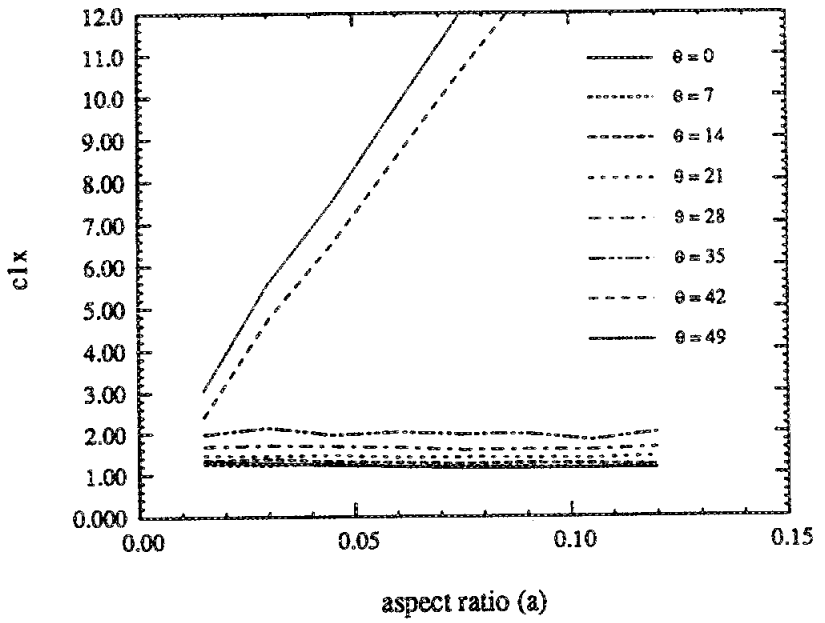

(a)

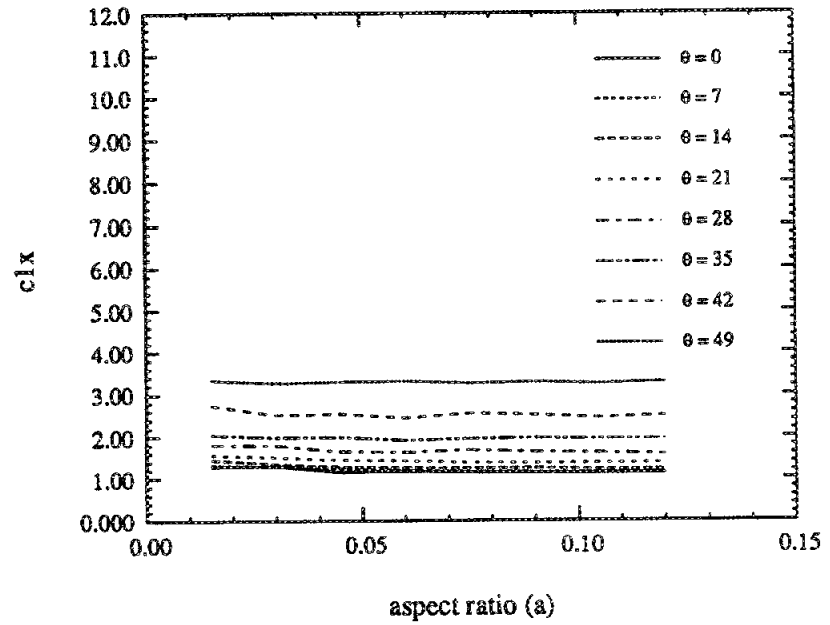

(b)

Figure 3.7: Two valid solutions for constant c_1 (of P_{xx}^{2d}/A) versus aspect ratio and blade angle; a dual-mode solution (a) resulting in a discontinuous function of c_1 versus θ, and a single-mode solution (b) resulting in a continuous function of c_1.

must be "close" enough to the correct solution for the conjugate gradient method to converge to that minimum rather than to another. Since the correct solution is unknown, selection of the initial values of $\mathbf{c}$ for a given geometry is problematic. Often several trials were required to force the conjugate gradient to converge to the correct mode. However, as $\mathbf{c}$ was determined for a significant number of blade geometries, an approximate relationship between the elements of $\mathbf{c}$ and the shape parameters v, a, and θ was inferred, and then used to properly determine an initial value for a given geometry.

3.5 Polynomial Fit

Once a single-mode solution for $\mathbf{c}$ for both P_{xx}^{2d} and P_{yy}^{2d} was determined for all 512 sample geometries, the mapping between $\mathbf{c}$ and the shape parameters v, a, and θ, could be replaced with a polynomial expression used to estimate the values of $\mathbf{c}$ across the domain of Table 3.2. These polynomials can then be used in (3.3) to provide a complete algebraic approximation of the numerical scattering formulation of Section 3.

To match a polynomial approximation to the data $\mathbf{c}$, a solution is assumed which is a linear combination of M basis functions, each basis function being an expression involving the parameters v, a, and θ. The number of basis functions is a compromise between the complexity and accuracy of the polynomial approximation, and for this application a third order expansion consisting of 20 basis functions was chosen. For the polynomials associated with the normalized polarizability tensor P_{xx}^{2d}/A, the basis functions (as determined by trial and error) are expansions of the parameters v, $(1/a)$,

and $\cos\theta$; the general polynomial approximations for $\mathbf{c}$ are therefore given as:

$$c_n = \sum_{i=0}^{3}\sum_{j=0}^{3}\sum_{k=0}^{3} b_m \frac{\mathrm{v}^i \cos^j\theta}{\mathrm{a}^k} \tag{3.5}$$

such that $i+j+k \leq 3$, $m = 1, 20$, and $n = 1, 3$. For the polynomials of P_{vy}^{2d}/A, the chosen basis functions are an expansion of the parameters v, $(1/a)$, and $\sec\theta$, thus the polynomials are given as:

$$c_n = \sum_{i=0}^{3}\sum_{j=0}^{3}\sum_{k=0}^{3} b_m \frac{\mathrm{v}^i \sec^j\theta}{\mathrm{a}^k}, \tag{3.6}$$

such that $i+j+k \leq 3$, $m = 1, 20$, and $n = 1, 3$.

Using orthogonality principles, the values of the coefficients b_m are determined by solving the linear estimation equation [18, ch. 14]

$$(\mathbf{X}^T \cdot \mathbf{X}) \cdot \mathbf{b} = \mathbf{X}^T \cdot \mathbf{C} \tag{3.7}$$

where $\mathbf{b}$ is a 20 element vector containing the polynomial coefficients, $\mathbf{C}$ is a 512 element vector containing the conjugate gradient estimate of c_n at the 512 test geometries, and $\mathbf{X}$ is a 512 x 20 matrix containing rows of the 20 basis functions evaluated at the 512 test geometries. The coefficients $\mathbf{b}$ determined by this computation are given in Table 3.3. Thus, (3.3), (3.5), and (3.6), along with the coefficients listed in Table 3.3, provide a fast algebraic approximation to the slower numerical model of Section 3.

	$\mathcal{P}_{xx}^{2d}/A$			$\mathcal{P}_{yy}^{2d}/A$		
b_n	c_0	c_1	c_2	c_0	c_1	c_2
b_1	-11.18	13.29	17.82	-12.94	28.02	-9.268
b_2	-0.8747	-3.469E-02	1.769	0.2781	9.4470E-03	-0.2167
b_3	-1.307E-02	-3.569E-05	-1.466E-02	-1.768E-03	2.574E-03	-4.961E-03
b_4	1.031E-04	-1.287E-06	1.108E-04	1.253E-05	-1.111E-05	5.296E-05
b_5	50.81	-24.15	-49.43	16.92	-16.94	21.39
b_6	3.444	9.537E-02	-1.197	-0.491	-5.920E-02	0.595
b_7	5.384E-04	1.068E-04	8.748E-04	4.137E-04	-1.204E-03	-1.098E-03
b_8	-85.25	15.15	44.45	-0.9688	-2.717	-4.099
b_9	-1.611	-5.654E-02	0.5463	0.2635	-2.507E-02	-0.1640
b_{10}	46.74	-3.199	-13.91	-2.435	3.558	-1.006
b_{11}	-10.16	-0.3726	-7.273	24.61	-38.03	38.43
b_{12}	0.5911	2.250E-02	-0.3542	0.1876	-0.2218	6.614E-02
b_{13}	6.520E-04	-4.893E-06	5.482E-04	-1.720E-04	7.368E-04	1.796E-04
b_{14}	42.69	-8.406	-1.913	-37.74	55.67	-54.33
b_{15}	-0.6183	-2.045E-02	0.2870	-0.1915	0.1518	-5.175E-02
b_{16}	-31.18	8.512	10.01	12.74	-16.36	15.16
b_{17}	-3.462	0.6613	6.350	-0.5466	1.895	-1.887
b_{18}	-6.594E-02	-3.032E-03	5.077E-02	3.487E-02	-1.413E-02	-2.532E-03
b_{19}	2.133	-5.807E-02	-4.617	1.855	-4.746	5.115
b_{20}	0.2449	4.645E-02	-0.5782	-0.3788	0.7839	-0.9007

Table 3.3: Values of the 20 coefficients b_n for each of the six expansions of $\mathbf{c}$, as given by (17) and (18).

3.6 Results

To test the accuracy of this algebraic approximation, 3125 test points, covering the range of shape parameters and complex dielectric constants found in Table 3.2, were selected and used to determine the complex elements of the polarizability tensor with both the numerical model and the algebraic approximation. The magnitude of the vector formed by P_{xx}^{2d} and P_{yy}^{2d}, defined as:

$$|P^{2d}| = \sqrt{P_{xx}^{2d} P_{xx}^{*2d} + P_{yy}^{*2d} P_{yy}^{2d}}, \tag{3.8}$$

was calculated for both models, and this data was used to build the histogram of Figure 3.8, showing the percent error of the algebraic approximation of $|P^{2d}|$ as compared to the numerical model. As estimated from 3125 test cases, the algebraic approximation exhibited little bias, with a mean error of 0.2 %, in addition to producing an acceptable rms error of 2.5 %. Figure 3.9 shows the accuracy typical of the approximation, displaying the predictions of both the numeric and algebraic models for $\mathrm{Re}[P_{xx}^{2d}/A]$ versus aspect ratio at a number of blade angle values.

3.7 Conclusions

Using a numerical solution to solve the scattering problem of cylinders with arbitrary cross-sections, it was determined that blade shape, in addition to blade size, can significantly affect the scattering solution for a long, thin grass blade structure. Likewise, a simple radiative-transfer model demonstrates that the calculated backscattering coefficients for grassland target can also be significantly affected. The numerical scattering model is required for characterizing scattering by complex grass

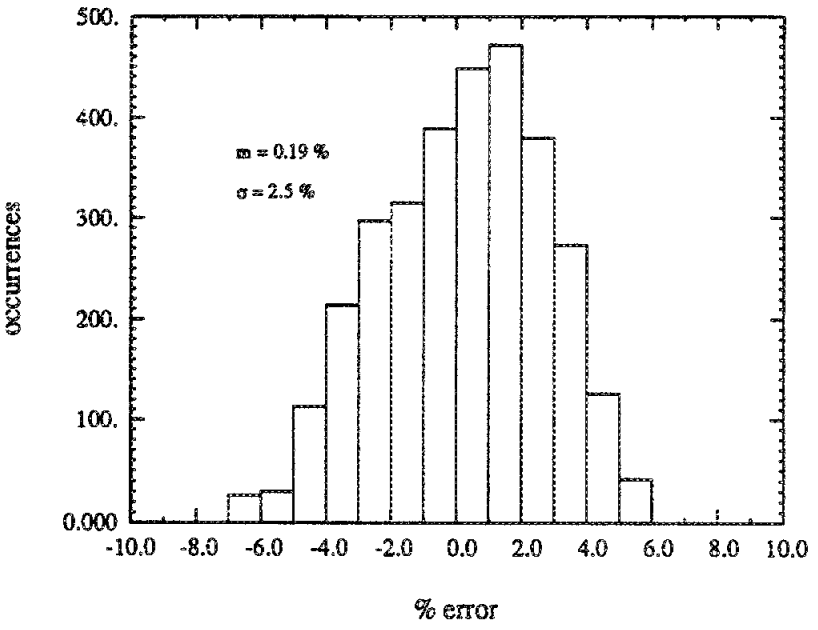

Figure 3.8: Histogram showing the distribution of the error resulting from the approximation given by (14), as determined using 3125 test cases covering the range of parameters given in Table 2.

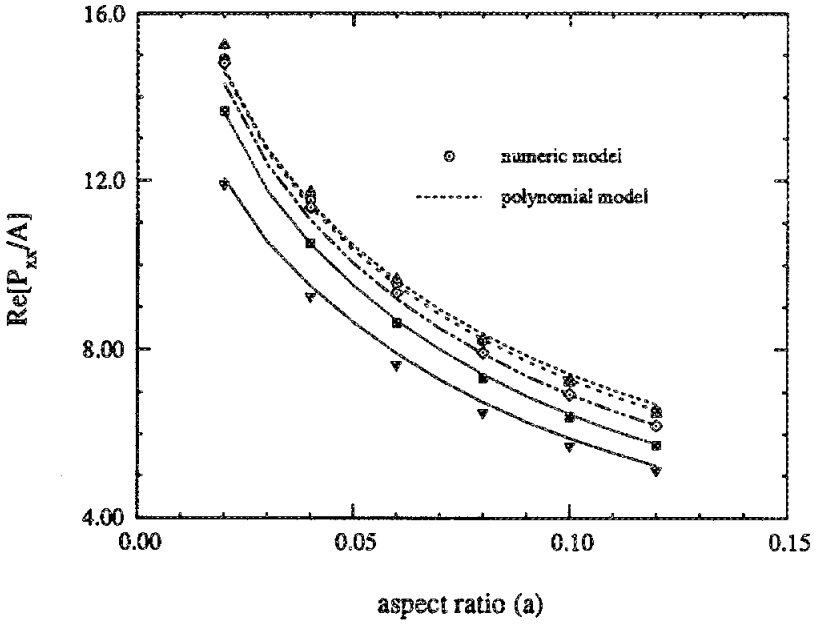

Figure 3.9: Comparison of the polynomial approximation to the numerical model predictions for $\mathrm{Re}[P_{xx}^{2d}/A]$ versus aspect ratio at various blade angles.

blade shapes. However, direct implementation of this numerical model into a larger radiative-transfer solution for grassland targets can result in a model of unacceptable computation time and complexity, especially when the radiative-transfer model is used in an inversion algorithm.

Although the complexity of the numerical model is necessary to describe a cylinder of arbitrary cross-section, the cross-sections associated with grass blades are not arbitrary but are instead limited to those described by parameters a, v, and θ, and by the domain of Table 3.2. These limits greatly reduce the information requirement of the numerical scattering model, thereby allowing for its replacement by a relatively simple analytical approximation. By combining the relationship of $\mathcal{P}^{2d}/A$ with ϵ (3.2) and the relationship of $\mathbf{c}$ versus a, v, and θ inferred from a small but representative sample of numeric solutions (3.5,3.6), an analytic approximation was developed that can predict the scattering response of blade shaped cylinders both rapidly and accurately.

CHAPTER IV

SCATTERING FROM THIN CYLINDERS IN AN ATTENUATING LAYER ABOVE A DIELECTRIC HALF SPACE

Chapter II examined the scattering of a thin dielectric cylinder in free space, demonstrating that the result is a coherent addition of incremental or line dipoles along its axis. We now seek to implement this knowledge to determine the scattering from typical structures found in grassland media. However, the long thin elements found in grassland differ from the elements analyzed in Chapter II in two respects. First, the structures are not residing in free space but instead are embeded in an attenuating vegetation layer. As a result, the elements are not illuminated by a uniform plane wave. The effective propagation constant of the coherent or average wave within the vegetation is complex, thus a long element may be illuminated with an incident wave of varying amplitude at each point along the element. The second difference is the presence of a soil boundary beneath the surface, a dielectric interface which results in additional scattering from the energy reflected at the surface.

In formulations such as radiative transfer, the free-space scattering of a single particle is used to determine the scattering and propagating intensities of a random

collection of these particles. In this chapter, the concept of an incremental line dipole will be used to directly determine the far-field scattering of a thin dielectric element, buried in an attenuating layer over dielectric half-space. As such, the solution will depend not only on the size, shape, and orientation of the element, but on its location in the layer as well. To determine this solution, the scattered fields from the various scattering mechanisms must be added in a coherent fashion, carefully accounting for the relative phase of each.

Once the scattering from an element has been determined, expressions for the average scattered power and average scattered field can be directly determined for a thin structure with random parameters such as shape, size, orientation and location. Additionally, the extinction due to this element can be determined, both for scattering and absorption loss.

4.1 The General Solution

The reflected energy from the dielectric soil boundary creates backscattered energy in addition to that scattered directly form the plant. This formulation will consider only the first order scattering mechanisms, that is the scattering terms which interact with the vegetation just a single time. For sparse media such as vegetation, these first-order mechanisms dominate and have been shown to be sufficient in predicting the scattering[13]. There are four of these mechanisms, a direct scattering term, two ground bounce terms, and a double bounce term (Figure 4.1). The total scattered field is therefore the coherent summation of these four terms. Because vegetation is a relatively sparse random media, the effective propagation constant is not significantly different from that of free space. Additionally, the air-vegetation interface is a diffuse

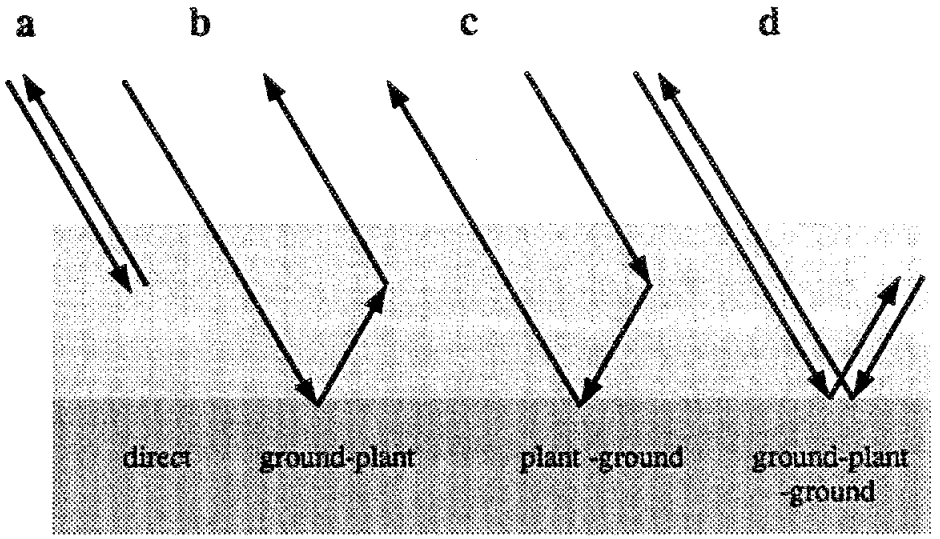

Figure 4.1: The four first-order scattering mechanisms considered in this formulation: (a) the direct propagation path, (b) the ground-plant path,(c) the plant-ground path, and (d) the ground-plant-ground path.

boundary, and therefore for these reasons refraction is neglected in this formulation.

4.1.1 Propagation Paths

To correctly determine this value, each of the four scattering mechanisms must be referenced to a single equi-phase plane. The propagation by each of the four scattering mechanisms can be modeled as a sum of two complex propagation paths, the direct path and the reflected or image path. Figure 4.2 shows the geometry of the direct path, denoted Φ_1, where the equi-phase plane is arbitrarily taken to pass through the origin. Using ray optics, the propagation from the equi-phase plane directly to the

particle is therefore:

$$\begin{aligned}\Phi_1(\bar{r}') =&(\bar{r}_1 - \bar{r}_p)\cdot\bar{k}_0 + (\bar{r}' - \bar{r}_1)\cdot\bar{k}_1 \\ =&\bar{r}_1\cdot\bar{k}_0 + (\bar{r}' - \bar{r}_1)\cdot\bar{k}_1 \end{aligned} \tag{4.1}$$

where $\bar{r}_1$ defines the location where the ray intersects the top of the vegetation layer, and $\bar{r}_p$ defines the location where the ray intersects the equi-phase plane. The vector $\bar{k}_0$ specifies the propagating wave in free space, and is defined as:

$$\bar{k}_0 = k_0^x\hat{x} + k_0^y\hat{y} + k_0^z\hat{z} \tag{4.2}$$

where $k_0^x = k_0\cos\phi\sin\theta$, $k_0^y = k_0\sin\phi\sin\theta$, and $k_0^z = k_0\cos\theta$. Note that $\bar{k}_0\cdot\bar{r}_p = 0$, which leads to the second equation of (4.1). The propagation vector $\bar{k}_1$, specifying the propagation through the attenuating layer, is given as the same form as equation (4.2), with the real propagation constant k_0 being replaced with the complex effective constant k_1. The two terms of (4.1) have an obvious physical interpretation; the second term represents the complex propagation through the layer, whereas the first term shifts the relative phase to the equi-phase plane.

To determine $\Phi_1(\bar{r}')$, the vector $\bar{r}_1 = x\hat{x} + y\hat{y}$ must be specified in terms of the location of the scatterer $\bar{r}' = x'\hat{x} + y'\hat{y} + z'\hat{z}$. To determine this, we observe that $\bar{r}_1$ is uniquely defined as the vector which makes $\bar{r}' - \bar{r}_1$ perpendicular to the equi-phase plane. Thus, if vector $\bar{r}_{ep}$ is any arbitrary vector lying on the equi-phase plane, then $\bar{r}_{ep}\cdot(\bar{r}' - \bar{r}_1) = 0$. An expression for vector $\bar{r}_{ep} = x\hat{x} + y\hat{y} + z\hat{z}$ can be found by likewise noting that $\hat{k}_0\cdot\bar{r}_{ep} = 0$. Therefore,

$$0 = \cos\phi\sin\theta x + \sin\phi\sin\theta y + \cos\theta z \tag{4.3}$$

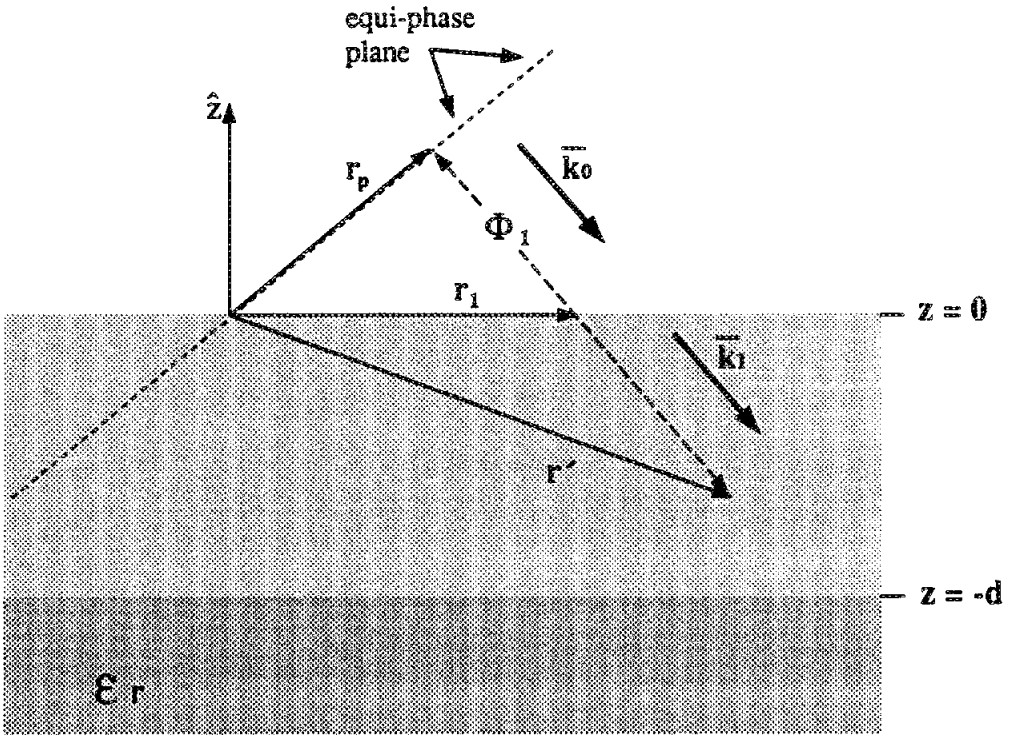

Figure 4.2: The propagation geometry for the direct scattering path Φ_1. The propagation in the media with effective dielectric k_1 ($\bar{r}_1$ to $\bar{r}'$) is shown, along with the propagation path in free-space ($\bar{r}_p$ to $\bar{r}_1$) from an arbitrary equi-phase plane.

Using the above expression to define z, the vector $\bar{r}_{ep}$ is written in terms of the arbitrary variables x, y as:

$$\bar{r}_{ep} = x\hat{x} + y\hat{y} - (\cos\phi\tan\theta x + \sin\phi\tan\theta y)\hat{z} \tag{4.4}$$

The vector $\bar{r}_1$ can now be found by enforcing the condition $\bar{r}_{ep} \cdot (\bar{r}' - \bar{r}_1) = 0$. Thus, if x and y are defined by $\bar{r}_1 = x\hat{x} + y\hat{y}$:

$$\begin{aligned} \bar{r}_1 \cdot \bar{r}_{ep} &= \bar{r}' \cdot \bar{r}_{ep} \\ x^2 + y^2 &= x(x' - z'\cos\phi\tan\theta) + y(y' - z'\sin\phi\tan\theta) \end{aligned} \tag{4.5}$$

Solving for x and y, vector $\bar{r}_1$ can be written in terms of $\bar{r}'$ as:

$$\bar{r}_1 = (x' - z'\cos\phi\tan\theta)\hat{x} + (y' - z'\sin\phi\tan\theta)\hat{y} \tag{4.6}$$

Thus, the term $\bar{r}_1 \cdot \bar{k}_0$ can now be evaluated:

$$\begin{aligned} \bar{r}_1 \cdot \bar{k}_0 &= k_0^x(x' - z'\cos\phi\tan\theta) + k_0^y(y' - z'\sin\phi\tan\theta) \\ &= k_0^x x' + k_0^y y' - \frac{z'}{\cos\theta}(k_0^x\cos\phi\sin\theta + k_0^y\sin\phi\sin\theta) \\ &= k_0^x x' + k_0^y y' - \frac{z'k_\rho^2}{k_0\cos\theta} \end{aligned} \tag{4.7}$$

Additionally, the second term of (4.1) can be derived:

$$\begin{aligned}(\bar{r}' - \bar{r}_1) \cdot \bar{k}_1 =& k_1^x(x' - x' + z'\cos\phi\tan\theta) + k_1^y(y' - y' + z'\sin\phi\tan\theta) + k_1^z z' \\ =& k_1^x z'\cos\phi\tan\theta + k_1^y z'\sin\phi\tan\theta + k_1^z z' \\ =& \frac{(k_1^x)^2 z'}{\cos\theta k_1} + \frac{(k_1^y)^2 z'}{\cos\theta k_1} + \frac{(k_1^z)^2 z'}{\cos\theta k_1} \\ =& \frac{k_1 z'}{\cos\theta}\end{aligned} \tag{4.8}$$

Thus, equation (4.1) is given as:

$$\Phi_1(\bar{r}') = k_0^x x' + k_0^y y' - \frac{k_\rho^2 z'}{k_0\cos\theta} + \frac{k_1 z'}{\cos\theta} \tag{4.9}$$

The second propagation path includes a reflection from the soil surface, and is most easily determined by considering the image of the scatterer, as represented in Figure 4.3. Equation (4.1) is still valid for this propagation path, however the location vector $\bar{r}'$ is now given as:

$$\bar{r}' = x'\hat{x} + y'\hat{y} - (z' + 2d)\hat{z} \tag{4.10}$$

where the $\hat{z}$ is modified to account for the additional propagation length of this path. Note the same physical interpretation can be given to equation (4.1) as before; the second term considers the complex propagation through the vegetation layer and the first term adjusts the phase to the equi-phase plane.

Using the same sequence of steps as shown for Φ_1, the image term is determined

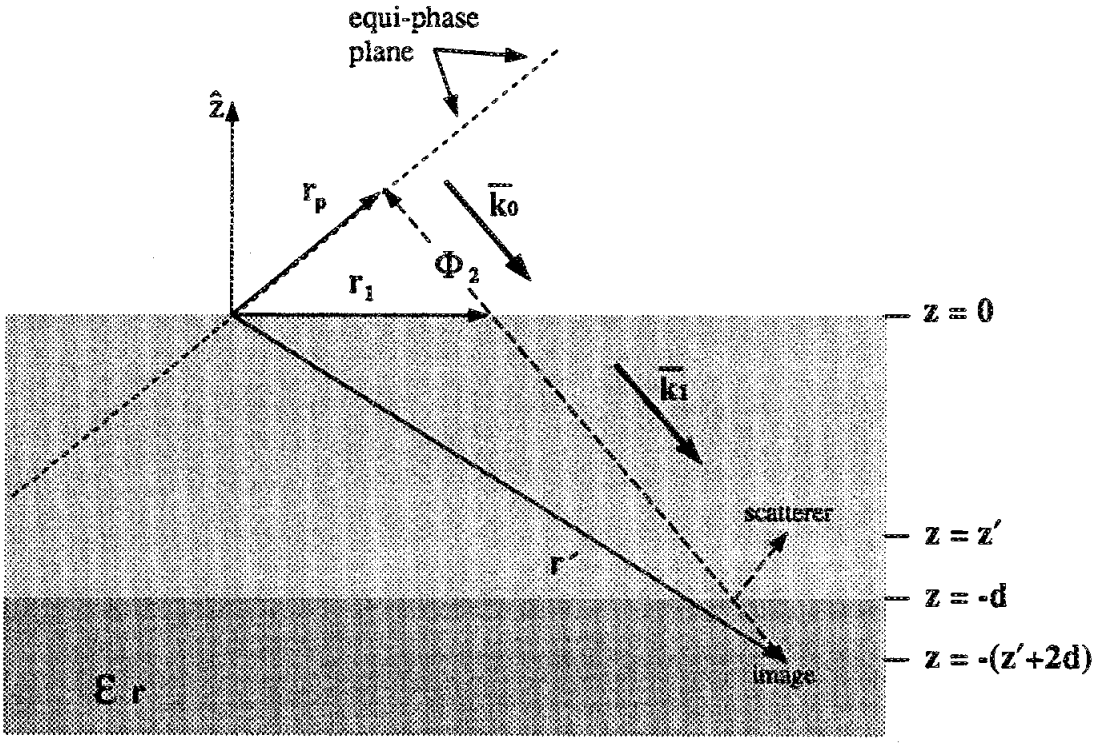

Figure 4.3: The propagation geometry for the ground-bounce scattering path Φ_2. The geometry more easily determined by considering the image of the scatterer below the dielectric surface.

to be:

$$\Phi_2(\bar{r}') = k_0^x x' + k_0^y y' + \frac{k_\rho^2(z'+2d)}{k_0\cos\theta} - \frac{k_1(z'+2d)}{\cos\theta} \tag{4.11}$$

The coherent wave at $\bar{r}'$ after propagating through path 1 is given as:

$$\begin{aligned} E(\bar{r}') &= E_0 \exp[\imath\Phi_1(\bar{r}')] \\ &= E_0 \exp\Big[\imath\Big(k_0^x x' + k_0^y y' - \frac{k_\rho^2 z'}{k_0\cos\theta}\Big)\Big] \exp\Big[\imath\Big(\frac{k_1 z'}{\cos\theta}\Big)\Big] \end{aligned} \tag{4.12}$$

where E_0 is the coherent wave at the equi-phase reference.

For the second, or ground bounce propagation path, the coherent wave is likewise modified by the reflection off the dielectric half space. Denoting the complex reflection coefficient as R, the coherent field at $\bar{r}'$ after propagating through path 2 is given as:

$$\begin{aligned} E(\bar{r}') &= E_0 R \exp[\imath\Phi_2(\bar{r}')] \\ &= E_0 \exp\Big[\imath\Big(k_0^x x' + k_0^y y' + \frac{k_\rho^2(z'+2d)}{k_0\cos\theta}\Big)\Big] \exp\Big[-\imath\Big(\frac{k_1 d}{\cos\theta}\Big)\Big] R \exp\Big[-\imath\Big(\frac{k_1(z'+d)}{\cos\theta}\Big)\Big] \end{aligned} \tag{4.13}$$

The preceding equation was written to explicitly show the propagation through the attenuation layer to the dielectric boundary at $z = -d$, the reflection off the dielectric boundary (R), and the upward propagation to the scatterer ($-k_1(z+d)\sec\theta$).

Up to this point, nothing has been stated about the general form of k_1 and R. Certainly these parameters are dependent on the polarization of the coherent wave. Additionally, however, propagation may be sufficiently complex that k_1 and R may not be accurately represented in scalar form. If the polarization state of the coherent wave is modified as it propagates from the equi-phase plane to $\bar{r}'$, then k_1 and R

must represent not only the propagation of two orthogonal polarization states but the coupling between the two as well.

For example, if the orthogonal polarizations are denoted as m and n, the general propagation of a wave through and electrically anisotropic layer is described by the following coupled differential equations [30, p. 461]:

$$\frac{dE_m}{ds} = \imath k^{mm} E_m + \imath k^{mn} E_n \tag{4.14}$$

$$\frac{dE_n}{ds} = \imath k^{nn} E_n + \imath k^{nm} E_m \tag{4.15}$$

where $\hat{s}$ is the direction of propagation. Making the following definitions,

$$\mathbf{E} = \begin{bmatrix} E_m \\ E_n \end{bmatrix} \qquad \mathcal{K} = \begin{bmatrix} \imath k^{mm} & \imath k^{mn} \\ \imath k^{nm} & \imath k^{nn} \end{bmatrix} \tag{4.16}$$

the differential equations can be re-written as:

$$\frac{d\mathbf{E}}{ds} = \mathcal{K}\mathbf{E} \tag{4.17}$$

The solution to this equation is of the form:

$$\mathbf{E}(s) = \mathbf{E}(s=0)\exp[\mathcal{K}s] \tag{4.18}$$

Comparing this solution with equations (4.12) and (4.13), it is evident that k_1 is in its most general form a 2×2 complex matrix.

Although though the above solution is mathematically concise, it is in a form which cannot directly be evaluated. To express (4.17) in a form which can be evaluated, we first determine the eigenvectors ($\hat{v}_1$, $\hat{v}_2$) and eigenvalues (λ_1, λ_2) of $\mathcal{K}$, and then

rewrite this propagation matrix in the following form:

$$\begin{aligned}\mathcal{K} =& \left[\hat{v}_1, \hat{v}_2\right]^{-1} \begin{bmatrix} \lambda_1 & 0 \\ 0 & \lambda_2 \end{bmatrix} \left[\hat{v}_1, \hat{v}_2\right] \\ =& \mathcal{Q}^{-1}\mathcal{D}\mathcal{Q} \end{aligned} \tag{4.19}$$

Multiplying $\mathcal{Q}$ by (4.17), and defining $\mathbf{Y} = \mathcal{Q}\mathbf{E}$, the differential equation can now be written as:

$$\frac{d\mathbf{Y}}{ds} = \mathcal{D}\mathbf{Y} \tag{4.20}$$

Since $\mathcal{D}$ is a diagonal matrix, the differential equations decouple and the solution is easily determined:

$$\mathbf{Y} = \begin{bmatrix} e^{\lambda_1 s} & 0 \\ 0 & e^{\lambda_2 s} \end{bmatrix} \begin{bmatrix} c_1 \\ c_2 \end{bmatrix} = \mathcal{L}(s)\mathbf{C} \tag{4.21}$$

From the definition of vector $\mathbf{Y}$, an expression for the coherent electric field can be determined:

$$\mathbf{E}(s) = \mathcal{Q}^{-1}\mathcal{L}(s)\mathbf{C} \tag{4.22}$$

Both $\mathcal{Q}^{-1}$ and $\mathcal{L}(s)$ are determined from the eigen analysis of propagation matrix $\mathcal{K}$. However, the value of vector $\mathbf{C}$ remains unsolved. To determine $\mathbf{C}$, we set $s = 0$ so that $\mathcal{L}(s = 0)$ is equal to the identity matrix $\mathcal{I}$. The vector $\mathbf{C}$ is therefore equal to

$\mathcal{Q}\mathbf{E}(s=0)$, and the coherent electric field is thus determined to be:

$$\begin{aligned}\mathbf{E}(s) &= \mathcal{Q}^{-1}\mathcal{L}(s)\mathcal{Q}\mathbf{E}(s=0) \\ &= e^{\kappa s}\mathbf{E}(s=0)\end{aligned} \tag{4.23}$$

As with the propagation, the specular reflection from the dielectric half-space must be expressed in a general polarimetric form, specifically:

$$\mathbf{E}^s = \mathcal{R}\mathbf{E}^i \tag{4.24}$$

where $\mathbf{E}^i$ represent the polarization state of the wave incident to the dielectric, $\mathbf{E}^s$ similarly represents the specular wave reflected from the boundary, and $\mathcal{R}$ is a 2×2 complex matrix which specifies the boundary reflection in a general, polarimetric form.

Denoting the free-space phase term as:

$$\Phi(\hat{k}; z) = \exp\left[\imath\left(k^x x + k^y y - \frac{k_\rho^2 z}{k_0 \cos\theta}\right)\right] \tag{4.25}$$

where the dependence on x, y is implicit, equations (4.12) and (4.13) can likewise be written in a general polarimetric form:

$$\mathbf{E}(\bar{r}') = \Phi(\hat{k}_0; z')\mathcal{Q}^{-1}\mathcal{L}(z' \sec\theta)\mathcal{Q}\mathbf{E}^i \tag{4.26}$$

for path 1, and for path 2:

$$\mathbf{E}(\bar{r}') = \Phi(\hat{k}_0; -(z' + 2d))\mathcal{Q}^{-1}\mathcal{L}(-d\sec\theta)\mathcal{Q}\mathcal{R}\mathcal{Q}^{-1}\mathcal{L}(-(z' + d)\sec\theta)\mathcal{Q}\mathbf{E}^{\mathrm{i}} \tag{4.27}$$

For sparse random media such as vegetation, where the volume fraction of the material is typically < 0.01, Foldy's approximation is most often employed to determine the elements of the propagation matrix $\mathcal{K}$. These elements are given as[30, p. 461]:

$$\begin{aligned} k^{mm} &= \imath k_0 - \imath M_{mm} \qquad & k^{mn} &= -\imath M_{mn} \\ k^{nn} &= \imath k_0 - \imath M_{nn} \qquad & k^{nm} &= -\imath M_{nm} \end{aligned} \tag{4.28}$$

where the M is a complex value related to the average forward scattering of the constituents of the media:

$$M_{\chi\psi}(\hat{k}_0^i) = \frac{\imath 2\pi n_o}{k_0}\langle S_{\chi\psi}(k_0^s = k_0^i)\rangle \tag{4.29}$$

where $\langle S_{\chi\psi}(k_0^s = k_0^i)\rangle$ is the average forward scattering of the constituents for the polarization pair $\chi\psi$, and n_o is the number density of the constituents. Using the results of (4.28), an eigen analysis of $\mathcal{K}$ can be performed to provide explicit forms of eigenvalues λ_1 and λ_2,

$$\lambda_1 = \imath k_0 + \frac{M_{mm} + M_{nn} - r}{2} \qquad \lambda_2 = \imath k_0 + \frac{M_{mm} + M_{nn} + r}{2} \tag{4.30}$$

as well as matrix $\mathcal{Q}$

$$\mathcal{Q} = \begin{bmatrix} \frac{M_{mm}-M_{nn}-r}{2M_{nm}} & 0 \\ 0 & \frac{M_{mm}-M_{nn}+r}{2M_{nm}} \end{bmatrix} \tag{4.31}$$

and its inverse:

$$\mathcal{Q}^{-1} = \begin{bmatrix} \frac{-M_{nm}}{r} & \frac{M_{mm}-M_{nn}+r}{2r} \\ \frac{M_{nm}}{r} & \frac{M_{mm}-M_{nn}+r}{2r} \end{bmatrix} \tag{4.32}$$

where r is:

$$r = \sqrt{(M_{vv} - M_{hh})^2 + 4M_{mn}M_{nm}} \tag{4.33}$$

4.1.2 Dipole Scattering

The previous section examined the propagation to a point within an attenuating layer above a dielectric half-space. This section will examine the scattering which occurs at this point. Chapter II demonstrated that the scattering from thin dielectric structures such as those found in grassland canopies can be attributed to line dipoles along the length of the structure. Accordingly, the concept of an incremental dipole moment $\mathbf{p}^{2d}d\ell$ and a line dipole element was introduced. Therefore, the scattering from arbitrary dipole elements will be examined in this section.

A scattering matrix element for a dipole element with polarizability $\mathcal{P}$ is given as:

$$S_{\chi\psi} = \frac{k_0^2}{4\pi}\hat{\chi}_s \cdot \mathcal{P} \cdot \hat{\psi}_i \tag{4.34}$$

where S is an element of the scattering matrix for receive/transmit polarizations

χ, ψ, and P is the complex 3×3 polarizability tensor which completely defines the scattering of a dipole element. The entire scattering matrix $\mathcal{S}$ can thus be written as:

$$\mathcal{S} = \frac{k_0^2}{4\pi} \mathcal{A}\mathcal{P}\mathcal{B} \tag{4.35}$$

where matrix $\mathcal{A}$ is:

$$\mathcal{A} = \begin{bmatrix} \hat{m}^s \cdot \hat{x} & \hat{m}^s \cdot \hat{y} & \hat{m}^s \cdot \hat{z} \\ \hat{n}^s \cdot \hat{x} & \hat{n}^s \cdot \hat{y} & \hat{n}^s \cdot \hat{z} \end{bmatrix} \tag{4.36}$$

and $\mathcal{B}$ is likewise:

$$\mathcal{B} = \begin{bmatrix} \hat{m}^i \cdot \hat{x} & \hat{m}^i \cdot \hat{y} & \hat{m}^i \cdot \hat{z} \\ \hat{n}^i \cdot \hat{x} & \hat{n}^i \cdot \hat{y} & \hat{n}^i \cdot \hat{z} \end{bmatrix} \tag{4.37}$$

The polarizability tensor $\mathcal{P}$ is defined in global coordinate space x, y, z. However, the tensor is often the result of a well defined structure or element (such as an ellipsoid) oriented in arbitrary fashion. The polarizability tensor of the element ($\mathcal{P}'$) is most easily defined in the natural local coordinate system of the structure (x', y', z'), with the global tensor $\mathcal{P}$ then determined by translating the local coordinate coordinate system into the global system:

$$\mathcal{P} = \mathcal{T}^T \mathcal{P}' \mathcal{T} \tag{4.38}$$

In this case, $\mathcal{P}$ is a function of element parameters only, namely size, shape, and dielectric. Conversely, tensor $\mathcal{T}$ is a real, 3×3 matrix which is dependent on particle

orientation only.

$$\mathcal{T} = \begin{bmatrix} \hat{x}' \cdot \hat{x} & \hat{x}' \cdot \hat{y} & \hat{x}' \cdot \hat{z} \\ \hat{y}' \cdot \hat{x} & \hat{y}' \cdot \hat{y} & \hat{y}' \cdot \hat{z} \\ \hat{z}' \cdot \hat{x} & \hat{z}' \cdot \hat{y} & \hat{z}' \cdot \hat{z} \end{bmatrix} \tag{4.39}$$

If the rotation of the element from the global (unprimed) coordinate space to the local (primed) coordinate space is specified in terms of Eulerian angles α, β and γ, the translating matrix $\mathcal{T}$ is easily specified using the relations:

$$\hat{x}' = (\cos\gamma\cos\beta\cos\alpha - \sin\gamma\sin\alpha)\hat{x} + (\cos\gamma\cos\beta\sin\alpha + \sin\gamma\cos\alpha)\hat{y} - \cos\gamma\sin\beta\hat{z} \tag{4.40}$$

$$\hat{y}' = (-\sin\gamma\cos\beta\cos\alpha - \cos\gamma\sin\alpha)\hat{x} + (\cos\gamma\cos\alpha - \sin\gamma\cos\beta\sin\alpha)\hat{y} + \sin\gamma\sin\beta\hat{z} \tag{4.41}$$

$$\hat{z}' = \sin\beta\cos\alpha\hat{x} + \sin\beta\sin\alpha\hat{y} + \cos\beta\hat{z} \tag{4.42}$$

Collecting all of the above formulations, the bistatic scattering matrix for a dipole element is described as:

$$\mathcal{S} = \frac{k_0^2}{4\pi}\mathcal{A}\mathcal{T}^T\mathcal{P}'\mathcal{T}\mathcal{B} \tag{4.43}$$

4.1.3 Scattering Mechanisms

We have thus examined the propagation of a coherent wave to/from an element in an extinction layer, as well as determined the scattering for that element if it is an arbitrary dipole. The two will now be combined to provide a complete scattering solution for a thin dielectric element residing in an extinction layer over a dielectric

The total scattering from this dipole element is therefore just the coherent sum of these four terms:

$$\mathcal{S} = \sum_{mech=a}^{d} \mathcal{S}_{mech} \tag{4.48}$$

Similarly, if the scattering dipole described by polarizability tensor $\mathcal{P}'$ is in fact an elemental line dipole described by $\mathcal{P}^{2d}d\ell$, then the scattering for each mechanism from a complete line-dipole element can be determined by integrating the scattering from the incremental line dipoles along the length of the thin element, and the total scattering from a line dipole element is found by summing coherently the results of the four scattering mechanisms.

$$\mathcal{S} = \sum_{mech=a}^{d} \int_L \mathcal{S}_{mech}^{2d} d\ell \tag{4.49}$$

Several points should be emphasized about this formulation. The first is that this solution provides the coherent addition of the scattered *fields* for each of the four first-order scattering mechanisms, rather than the scattered *power*, the parameter most often evaluated. The importance of this can be seen when multiplying (4.49) by its complex conjugate. Sixteen terms will result, four of which represent the scattered power associated with each mechanism. The remaining twelve terms are the "inner product" values which can significantly increase or decrease the total scattering power. Thus, these terms must be considered if an accurate representation of scattered power is required.

Another important point about this solution is its completeness, This is not a solution for the scattering of a thin dielectric element, but instead of a dielectric element in an extinction layer over a dielectric half space. The effect of the extinction

extensive numerical evaluation is often required. Thus, in this section, the general solution will be applied to a specific and limited scattering problem, resulting in significant reductions in model complexity.

To begin, we shall limit the problem to backscattering only, setting $\hat{k}_s = -\hat{k}_i$. In addition, the formulation will be limited to scattering elements that are azimuthally symmetric, that is, the azimuthal orientation of the element (Eulerian angle α) is random and uniformly distributed over 2π radians. Finally, we choose the orthogonal polarizations to be the standard horizontal ($\hat{h}\cdot\hat{k} = \hat{h}\cdot\hat{z} = 0$) and vertical ($\hat{v}\cdot\hat{k} = \hat{v}\cdot\hat{h} = 0$) convention. From a polarimetric standpoint the choice of polarization basis vectors does not matter, as the response from any polarization can be synthesized from the final result. However, since the elements of the media are azimuthally symmetric, the choice of $\hat{v}$ and $\hat{h}$ as basis vectors will greatly simplify the evaluation of the wave propagation, as will be shown later.

4.2.1 Propagation Paths

The combination of an azimuthally symmetric media and $\hat{v}, \hat{h}$ polarization basic vectors lead to simple but significant result when determining the propagation through the media. For such situations, the average forward cross-pol scattering is zero ($\langle S_{hv}(k_0^s = k_0^i)\rangle = \langle S_{vh}(k_0^s = k_0^i)\rangle = 0$), therefore the terms M_{hv} and M_{vh} vanish. As a result, the propagation matrix $\mathcal{K}$ is diagonal, and the eigen analysis leads to the trivial solution $\mathcal{Q} = \mathcal{I}$, $\lambda_1 = \imath k_0 + M_{vv}$ and $\lambda_2 = \imath k_0 + M_{hh}$. The polarizations in effect decouple, each propagating independent of the other.

This leads to a physical interpretation of the eigen analysis of matrix $\mathcal{K}$. For a medium with an arbitrary propagation matrix $\mathcal{K}$, there exists two polarizations where the propagation decouples. That is, the propagation occurs without changing

where $m \in v, h$. Likewise, equation (4.27) can be similarly expressed as:

$$E^{\psi}(\bar{r}') = r_{\psi\psi} \exp\left[\imath\left(k_0^x x' + k_0^y y' - k_0^z(z'+2d)\right) - \frac{M_{\psi\psi}(z'+2d)}{\cos\theta}\right] E_0^{\psi} \tag{4.54}$$

The above equations are valid for homogeneous regions where the particle density n_0 is uniform. In random media such as vegetation, however, particle density is often a variable quantity dependent on vertical position z ($n_0 = n_0(z)$). To account for this variance, researchers often employ a layered model, determining the value $M_{\psi\psi}^n$ for each of N layers of size Δz_n. Using this approach, equation (4.53) becomes:

$$\begin{aligned} E^{\psi}(\bar{r}') &= \exp\left[\imath\left(k_0^x x' + k_0^y y' + k_0^z z'\right)\right] \prod_{n=0}^{N} \exp\left[\frac{M_{\psi\psi}^n \Delta z_n'}{\cos\theta}\right] E_0^{\psi} \\ &= \exp\left[\imath\left(k_0^x x' + k_0^y y' + k_0^z z'\right)\right] \exp\left[\sum_{n=0}^{N} \frac{M_{\psi\psi}^n \Delta z_n'}{\cos\theta}\right] E_0^{\psi} \end{aligned} \tag{4.55}$$

Therefore, as the layer thickness becomes incrementally small, the summation in the above equation can be replaced by an integration (denoted as $\tau(z)$) over the continuous function $M_{\psi\psi}(z)$:

$$\lim_{\Delta z \to 0} \sum_{n=0}^{N} M_{\psi\psi}^n \Delta z_n' = \int_0^z M_{\psi\psi}(z) dz \doteq \tau_{\psi}(z) \tag{4.56}$$

Expressions (4.53) can thus be rewritten as:

$$E^{\psi}(\bar{r}') = \exp\left[\imath\left(k_0^x x' + k_0^y y' + k_0^z z'\right) + \frac{\tau_{\psi}(z')}{\cos\theta}\right] E_0^{\psi} \tag{4.57}$$

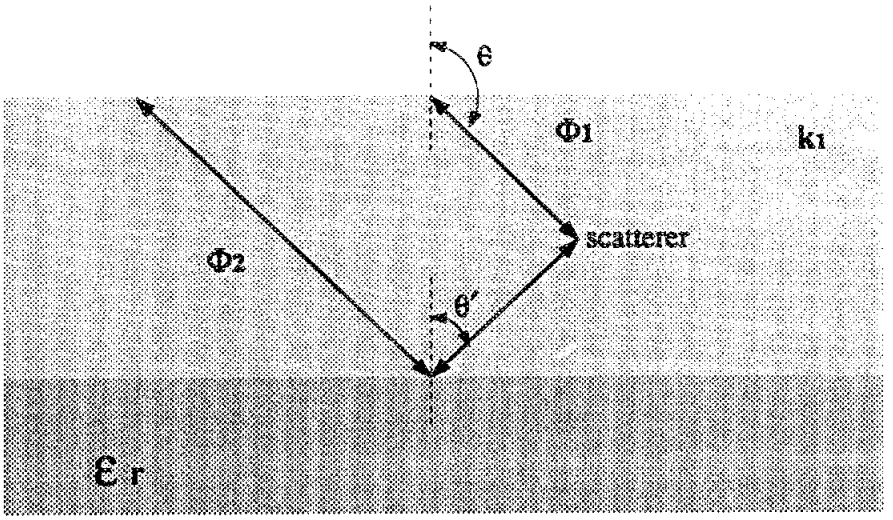

Figure 4.4: Diagram defining the direction of the propagation vectors at the scattering element. The vector associated with the ground-bounce path (θ', ϕ') is related incident direction of the direct path as $\phi' = \phi_i$ and $\theta' = \pi - \theta_i$.

as

$$\hat{v}_2 = \cos\phi' \cos\theta' \hat{x} + \sin\phi' \cos\theta' \hat{y} - \sin\theta' \hat{z} \tag{4.62}$$

$$\hat{h}_2 = -\sin\phi' \hat{x} + \cos\phi' \hat{y} \tag{4.63}$$

Again referring to Figure 4.4, the primed direction parameters can be related to the incident angles as $\phi' = \phi_i$ and $\theta' = \pi - \theta_i$. Using this in equation (4.61), $\mathcal{A}_2$ and $\mathcal{B}_2$ can be explicitly determined:

$$\mathcal{A}_2 = \mathcal{B}_2 = \begin{bmatrix} -\cos\phi_i \cos\theta_i & -\sin\phi_i \cos\theta_i & -\sin\theta_i \\ -\sin\phi_i & \cos\phi_i & 0 \end{bmatrix} \tag{4.64}$$

is found:

$$P_{xx} = \cos^2\alpha\cos^2\beta P'_{xx} + \sin^2\alpha P'_{yy} + \cos^2\alpha\sin^2\beta P'_{zz} \tag{4.66}$$

$$P_{xy} = P_{yx} = \cos\alpha\sin\alpha\cos^2\beta P'_{xx} - \cos\alpha\sin\alpha P'_{yy} + \cos\alpha\sin\alpha\sin^2\beta P'_{zz} \tag{4.67}$$

$$P_{xz} = P_{zx} = -\cos\alpha\cos\beta\sin\beta P'_{xx} + \cos\alpha\cos\beta\sin\beta P'_{zz} \tag{4.68}$$

$$P_{yy} = \sin^2\alpha\cos^2\beta P'_{xx} + \cos^2\alpha P'_{yy} + \sin^2\alpha\sin^2\beta P'_{zz} \tag{4.69}$$

$$P_{yz} = P_{zy} = -\sin\alpha\cos\beta\sin\beta P'_{xx} + \sin\alpha\cos\beta\sin\beta P'_{zz} \tag{4.70}$$

$$P_{zz} = \sin^2\beta P'_{xx} + \cos^2\beta P'_{zz} \tag{4.71}$$

As stated before, the scattering dipole in this formulation can be an incremental line dipoles with polarizability tensor $\mathcal{P} = \mathcal{P}_{2d}d\ell$. This incremental dipole lies along a contour defined by the larger element upon which dipole lies, as shown in Figure 4.5. Thus, the local (primed) coordinate system of the incremental dipole is dependent on the shape of this larger element, as well as its location $\bar{r}_\ell$ on structure. Thus, the Euler angles α and β, defining the local coordinate system, are a function of location $\bar{r}_\ell$. Since the total element scattering is determined by integrating along the contour L, the relationship of α and β with $\bar{r}_\ell$ must be determined.

At this point, an assumption about the shape of the scattering element defined by L must be applied. It is assumed that for all points along the element, there is a single plane in which both unit vector $\hat{z}$ and $\bar{r}_\ell$ reside. That is, the element curves only in two-dimensions, its general shape being able to be expressed as function of two single dimension variables (i.e. $z = f(x)$). This is shown in Figure 4.6, with the location of the plane containing the scattering element being specified by angle ϕ_e. The value of azimuthal angle α is therefore easily determined, being $\alpha = \phi_e$ for all

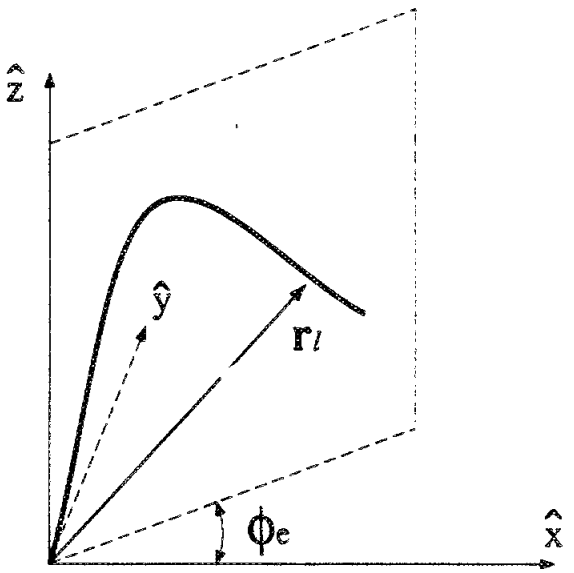

Figure 4.6: Geometry of a line-dipole element residing in a vertical plane defined by Φ_e. The vector $\bar{r}_\ell$ defining the element contour resides entirely in plane.

points defined by $\bar{r}_e$.

The remaining angle, β can be determined using differential geometry. If the shape of the element can be expressed as a function of cylindrical variable ρ as $z = f(\rho)$, and if the derivatives of $f(\rho)$ exist at every point along contour L, then $\cos\beta$ and $\sin\beta$ can be derived using the differential geometry shown in Figure 4.7:

$$\cos\beta = \frac{dz}{\sqrt{dz^2 + d\rho^2}} = \frac{\frac{dz}{d\rho}}{\sqrt{1 + (\frac{dz}{d\rho})^2}} \tag{4.72}$$

$$\sin\beta = \frac{d\rho}{\sqrt{dz^2 + d\rho^2}} = \frac{1}{\sqrt{1 + (\frac{dz}{d\rho})^2}} \tag{4.73}$$

where $dz/d\rho$ is the derivative of $z = f(\rho)$ with respect to ρ. If the element is instead expressed as a function of z ($\rho = f(z)$), a similar result is obtained. From the results

4.2.3 Scattering Mechanisms

The results of the previous two sections can again be used to determine the scattering from each mechanism shown in Figure 4.1. Combining equations (4.57) and (4.58), the propagation paths associated with each of the four scattering mechanisms can be expressed in terms of arbitrary polarization pair $\chi\psi = \{vv, hv, vh, hh\}$.

$$\Phi^a_{\chi\psi} = \exp\left[\imath 2\left(k^i_x x^\ell + k^i_y y^\ell + k^i_z z^\ell\right) + \frac{\tau_\chi(z^\ell) + \tau_\psi(z^\ell)}{\cos\theta}\right] \tag{4.76}$$

$$\Phi^b_{\chi\psi} = r_\psi \exp\left[\imath 2\left(k^i_x x^\ell + k^i_y y^\ell\right) + \frac{\tau_\chi(z^\ell) - \tau_\psi(z^\ell)}{\cos\theta}\right] \exp\left[-\imath 2k^i_z d + \frac{2\tau_\psi(-d)}{\cos\theta}\right] \tag{4.77}$$

$$\Phi^c_{\chi\psi} = r_\chi \exp\left[\imath 2\left(k^i_x x^\ell + k^i_y y^\ell\right) + \frac{\tau_\psi(z^\ell) - \tau_\chi(z^\ell)}{\cos\theta}\right] \exp\left[-\imath 2k^i_z d + \frac{2\tau_\psi(-d)}{\cos\theta}\right] \tag{4.78}$$

$$\Phi^d_{\chi\psi} = r_\chi r_\psi \exp\left[\imath 2\left(k^i_x x^\ell + k^i_y y^\ell - k^i_z z^\ell\right) - \frac{\tau_\chi(z^\ell) + \tau_\psi(z^\ell)}{\cos\theta}\right] \exp\left[-\imath 2k^i_z d + \frac{2\tau_\psi(-d)}{\cos\theta}\right] \tag{4.79}$$

the scattering matrix elements for a line dipole element can be expressed for each mechanism as:

$$S^a_{\chi\psi} = \frac{k_0^2}{4\pi}\int_L \hat{\chi}_1(\hat{k}^i)\cdot\mathcal{P}_{2d}(\bar{r}_\ell)\cdot\hat{\psi}_1(\hat{k}^i)\;\Phi^a_{\chi\psi}(\hat{k}^i;\bar{r}_\ell)d\ell \tag{4.80}$$

$$S^b_{\chi\psi} = \frac{k_0^2}{4\pi}\int_L \hat{\chi}_1(\hat{k}^i)\cdot\mathcal{P}_{2d}(\bar{r}_\ell)\cdot\hat{\psi}_2(\hat{k}^i)\;\Phi^b_{\chi\psi}(\hat{k}^i;\bar{r}_\ell)d\ell \tag{4.81}$$

$$S^c_{\chi\psi} = \frac{k_0^2}{4\pi}\int_L \hat{\chi}_2(\hat{k}^i)\cdot\mathcal{P}_{2d}(\bar{r}_\ell)\cdot\hat{\psi}_1(\hat{k}^i)\;\Phi^c_{\chi\psi}(\hat{k}^i;\bar{r}_\ell)d\ell \tag{4.82}$$

$$S^d_{\chi\psi} = \frac{k_0^2}{4\pi}\int_L \hat{\chi}_2(\hat{k}^i)\cdot\mathcal{P}_{2d}(\bar{r}_\ell)\cdot\hat{\psi}_2(\hat{k}^i)\;\Phi^d_{\chi\psi}(\hat{k}^i;\bar{r}_\ell)d\ell \tag{4.83}$$

pairs can be synthesized, either directly or more typically using other constructs, such as the real-valued Mueller matrix, which are obtained from the elements of the covariance matrix $\mathcal{C}$. Note the diagonal terms of $\mathcal{C}$ are real valued and represent the average scattered power for each of the four polarization states. Due to reciprocity, for the backscattering case the cross=polarizations are equal ($S_{hv} = S_{vh}$), resulting in the equality of the four center terms ($\langle|S_{hv}|^2\rangle = \langle|S_{vh}|^2\rangle = \langle S_{hv}S_{vh}^*\rangle = \langle S_{vh}S_{hv}^*\rangle$). Of the five independent terms remaining, it has been shown that only one is non-zero when backscattering is considered from a statistically azimuthally symmetric scatterer[22]. This term is $\langle S_{hh}S_{vv}^*\rangle$, a value which provides statistics about the co-polarized phase difference, defined as $\arg(\langle S_{hh}S_{vv}^*\rangle) = \phi_{hh} - \phi_{vv}$[22]. Thus, for the backscattering from a collection of azimuthally symmetric random scatterers, the polarimetric response is defined completely with just five real values, $\langle|S_{vv}|^2\rangle$, $\langle|S_{hh}|^2\rangle$, $\langle|S_{hv}|^2\rangle$, $\mathrm{Re}(\langle S_{hh}S_{vv}^*\rangle)$, and $\mathrm{Im}(\langle S_{hh}S_{vv}^*\rangle)$.

From equation (4.84), the average scattered power can be expressed as:

$$\langle|S_{\chi\psi}|^2\rangle = \sum_{mech=a}^{d}\sum_{mech'=a}^{d}\langle S_{\chi\psi}^{mech}S_{\chi\psi}^{*mech'}\rangle \tag{4.86}$$

There are thus sixteen terms required to determine the total power, four ($mech = mech'$) of which represent the "incoherent" power, the scattered power from each scattering mechanism considered independently. The remaining twelve inner product terms can either add to, or detract from, the incoherent power value, resulting in the total scattering power, where the correlation between the scattered fields of dissimilar scattering mechanisms is considered. For many cases, the correlation is small, and the twelve inner product terms are insignificant when compared to the incoherent power. However, this is true only for certain specific situations, and thus for this

Each of the sixteen scattering elements described in (4.80) to (4.83) can now be expressed explicitly for all receive/transmit polarizations $vv, hv, vh, h\dot{h}$ and scattering mechanisms a, b, c, d.

$$S^a_{vv} = \frac{k_0^2}{4\pi}\int_L \Phi^a_{vv}(\hat{k}^i;\bar{r}_\ell)\Big(\cos^2\theta_i P^{2d}_{xx}(\bar{r}_\ell) - 2\cos\theta_i\sin\theta_i P^{2d}_{xz}(\bar{r}_\ell) + \sin^2\theta_i P^{2d}_{zz}(\bar{r}_\ell)\Big)d\ell \tag{4.92}$$

$$S^b_{vv} = \frac{k_0^2}{4\pi}\int_L \Phi^b_{vv}(\hat{k}^i;\bar{r}_\ell)\Big(-\cos^2\theta_i P^{2d}_{xx}(\bar{r}_\ell) + \sin^2\theta_i P^{2d}_{zz}(\bar{r}_\ell)\Big)d\ell \tag{4.93}$$

$$S^c_{vv} = \frac{k_0^2}{4\pi}\int_L \Phi^c_{vv}(\hat{k}^i;\bar{r}_\ell)\Big(-\cos^2\theta_i P^{2d}_{xx}(\bar{r}_\ell) + \sin^2\theta_i P^{2d}_{zz}(\bar{r}_\ell)\Big)d\ell \tag{4.94}$$

$$S^d_{vv} = \frac{k_0^2}{4\pi}\int_L \Phi^d_{vv}(\hat{k}^i;\bar{r}_\ell)\Big(\cos^2\theta_i P^{2d}_{xx}(\bar{r}_\ell) + 2\cos\theta_i\sin\theta_i P^{2d}_{xz}(\bar{r}_\ell) + \sin^2\theta_i P^{2d}_{zz}(\bar{r}_\ell)\Big)d\ell \tag{4.95}$$

$$S^a_{hv} = \frac{k_0^2}{4\pi}\int_L \Phi^a_{hv}(\hat{k}^i;\bar{r}_\ell)\Big(\cos\theta_i P^{2d}_{yx}(\bar{r}_\ell) - \sin\theta_i P^{2d}_{yz}(\bar{r}_\ell)\Big)d\ell \tag{4.96}$$

$$S^b_{hv} = \frac{k_0^2}{4\pi}\int_L \Phi^b_{hv}(\hat{k}^i;\bar{r}_\ell)\Big(-\cos\theta_i P^{2d}_{yx}(\bar{r}_\ell) - \sin\theta_i P^{2d}_{yz}(\bar{r}_\ell)\Big)d\ell \tag{4.97}$$

$$S^c_{hv} = \frac{k_0^2}{4\pi}\int_L \Phi^c_{hv}(\hat{k}^i;\bar{r}_\ell)\Big(\cos\theta_i P^{2d}_{yx}(\bar{r}_\ell) - \sin\theta_i P^{2d}_{yz}(\bar{r}_\ell)\Big)d\ell \tag{4.98}$$

$$S^d_{hv} = \frac{k_0^2}{4\pi}\int_L \Phi^d_{hv}(\hat{k}^i;\bar{r}_\ell)\Big(-\cos\theta_i P^{2d}_{yx}(\bar{r}_\ell) - \sin\theta_i P^{2d}_{yz}(\bar{r}_\ell)\Big)d\ell \tag{4.99}$$

$$S^a_{vh} = \frac{k_0^2}{4\pi}\int_L \Phi^a_{vh}(\hat{k}^i;\bar{r}_\ell)\Big(\cos\theta_i P^{2d}_{yx}(\bar{r}_\ell) - \sin\theta_i P^{2d}_{yz}(\bar{r}_\ell)\Big)d\ell \tag{4.100}$$

$$S^b_{vh} = \frac{k_0^2}{4\pi}\int_L \Phi^b_{vh}(\hat{k}^i;\bar{r}_\ell)\Big(-\cos\theta_i P^{2d}_{yx}(\bar{r}_\ell) - \sin\theta_i P^{2d}_{yz}(\bar{r}_\ell)\Big)d\ell \tag{4.101}$$

$$S^c_{vh} = \frac{k_0^2}{4\pi}\int_L \Phi^c_{vh}(\hat{k}^i;\bar{r}_\ell)\Big(\cos\theta_i P^{2d}_{yx}(\bar{r}_\ell) - \sin\theta_i P^{2d}_{yz}(\bar{r}_\ell)\Big)d\ell \tag{4.102}$$

$$S^d_{vh} = \frac{k_0^2}{4\pi}\int_L \Phi^d_{vh}(\hat{k}^i;\bar{r}_\ell)\Big(-\cos\theta_i P^{2d}_{yx}(\bar{r}_\ell) - \sin\theta_i P^{2d}_{yz}(\bar{r}_\ell)\Big)\Big)d\ell \tag{4.103}$$

4.4.1 Scattering Loss from Rayleigh Elements

As a coherent wave propagates through a media consisting of random particles, the power of the wave is continually reduced. For a homogeneous medium, the relation between attenuation and propagation distance is expressed as $dP = -\kappa_e P ds$, the solution of which is:

$$\frac{P(s)}{P(s=0)} = e^{-\kappa_e s} \tag{4.108}$$

where $P(s)$ represents the power density of the wave at location s. The extinction coefficient κ_e defines the extinction of the layer, however this extinction is attributed to two separate physical phenomenon. The energy removed from the coherent wave is either absorbed by the lossy elements of the media (converted to heat), or scattered by the elements into other directions. Thus, the extinction coefficient can be represented by the sum of two separate coefficients, the absorption coefficient κ_a and the scattering coefficient κ_s ($\kappa_e = \kappa_a + \kappa_s$)[31, p. 212].

For a sparse collection of independent scatters, the extinction coefficient κ_e can be determined from the average extinction cross-section (σ_e) of a single particle as $\kappa_e = n_0\langle\sigma_e\rangle$. The extinction cross expresses the energy loss due to a single particle, and likewise can be expressed in terms of absorption and scattering loss, $\sigma_e = \sigma_a + \sigma_s$. The extinction cross-section of a scatterer can be determined by calculating its forward scattering and applying the optical theorem[30, [p.137]:

$$\sigma_e^{\psi} = \frac{4\pi}{k_0}\mathrm{Im}\left[S_{\psi\psi}(\hat{k}^i;\hat{k}^i)\right] \tag{4.109}$$

This equation is similar to that derived from Foldy's approximation (4.29) to

the extinction calculation is invalid. For both low absorption and larger electrical radiuses ka, the error of the Rayleigh solution is evident. Therefore, to accurately determine the extinction due to Rayleigh particles, the extinction due to scattering must separately and explicitly be determined.

4.4.2 Extinction of Incremental Dipole Elements

As explained in Chapter II, the scattering from a thin dielectric structure can be attributed to incremental dipoles with polarizability tensor $\mathcal{P}_{2d}d\ell$ lying along the structure contour L. This of course includes forward scattering, and since $\bar{k}^i - \bar{k}^s = 0$, equation (2.92) becomes:

$$S_{\chi\psi} = \int_L \frac{k_0^2}{4\pi} \hat{\chi} \cdot \mathcal{P}_{2d}(\ell) \cdot \hat{\psi} d\ell \tag{4.111}$$

Again to emphasize the concept of an incremental dipole element with polarizability $\mathcal{P} = \mathcal{P}_{2d}d\ell$ we consider a collection of N dipole elements with polarizability $\mathcal{P}_n = \mathcal{P}^n_{2d}\Delta z$, each located at an arbitrary position in space denoted by $\bar{r}_n$. The forward scattering for this collection is therefore:

$$\begin{aligned} S_{\chi\psi} &= \sum_{n=1}^{N} \frac{k_0^2}{4\pi} \hat{\chi} \cdot \mathcal{P}^n_{2d}\Delta z \cdot \hat{\psi}\, e^{\imath(\bar{k}^i - \bar{k}^s)\cdot\bar{r}_n} \\ &= \sum_{n=1}^{N} \frac{k_0^2}{4\pi} \hat{\chi} \cdot \mathcal{P}^n_{2d} \cdot \hat{\psi}\, \Delta z \end{aligned} \tag{4.112}$$

coefficient can be calculated as[9]:

$$\begin{aligned}\sigma_s^{\psi} &= \int_0^{2\pi}\int_0^{\pi}\left(S_{v\psi}\hat{v}+S_{h\psi}\hat{h}\right)\cdot\left(S_{v\psi}^{*}\hat{v}+S_{h\psi}^{*}\hat{h}\right)\sin\theta_s d\theta_s d\phi_s \\ &= \int_0^{2\pi}\int_0^{\pi}\left(|S_{v\psi}|^2+|S_{h\psi}|^2\right)\sin\theta_s d\theta_s d\phi_s \end{aligned} \tag{4.115}$$

If we consider a straight line dipole element lying along the $\hat{z}$ axis, the scattered field is found from (2.91) to be:

$$S_{\chi\psi} = \frac{k_0^2}{4\pi}\hat{\chi}\cdot\mathcal{P}_{2d}\ell\cdot\hat{\psi}\frac{\sin U}{U} \tag{4.116}$$

where value U is a phase term given as:

$$U = \frac{k\ell}{2}(\cos\theta_s - \cos\theta_i) \tag{4.117}$$

The scattered power $|S_{\chi\psi}|^2$ is therefore a function of $\sin^2 U/U^2$, which becomes very narrow with respect to θ_s as the electrical length of the cylinder becomes large, becoming a delta function as $k_0\ell$ approaches infinity.

$$\lim_{k\ell\to\infty}\frac{\sin^2 U}{U^2} = C\delta(U) \tag{4.118}$$

where C is a normalization constant. To determine the value of C we integrate (4.118) from $\theta_s = 0$ to $\theta_s = \pi$. Since $du = -(k_0\ell/2)\sin\theta_s d\theta_s$ we can write:

$$\begin{aligned} C &= \int_0^{\pi}\frac{\sin^2 U}{U^2}\,d\theta_s \\ &= \lim_{k_0\ell\to\infty}\frac{-2}{k_0\ell\sin\theta_s}\int_{k_0\ell}^{-k_0\ell}\frac{\sin^2 U}{U^2}\,dU \\ &= \frac{2\pi}{k_0\ell\sin\theta_s} \end{aligned} \tag{4.119}$$

section per unit length can be defined as $\sigma_s^{2d} = \sigma_s/\ell$. The extinction cross-section per unit length is thus $\sigma_e^{2d} = \sigma_a^{2d} + \sigma_s^{2d}$, and the extinction cross-section of an incremental dipole is $\sigma_e^{2d}dz$. Note this incremental cross-section has no direct physical meaning, it is merely a mathematical construct which has physical meaning only after application in a definite integral.

Using (4.114) and (4.124) to explicitly write the extinction coefficient, it is apparent that the expression can be conveyed in a more compact form:

$$\begin{aligned}
\sigma_e^{2d} =& \frac{4\pi}{k_0}\mathrm{Im}\left[\frac{k_0^2}{4\pi}\left(P_{xx}^{2d}(\hat{x}\cdot\hat{\psi})^2 + P_{yy}^{2d}(\hat{y}\cdot\hat{\psi})^2 + P_{zz}^{2d}(\hat{z}\cdot\hat{\psi})^2\right)\right] \\
&+\frac{k_0^3}{8}\left[(1+\cos^2\theta_i)|P_{xx}|^2(\hat{x}\cdot\hat{\psi})^2 + (1+\cos^2\theta_i)|P_{yy}|^2(\hat{y}\cdot\hat{\psi})^2 + 2\sin^2\theta_i|P_{zz}|^2(\hat{z}\cdot\hat{\psi})^2\right] \\
=& \frac{4\pi}{k_0}\mathrm{Im}\left[\frac{k_0^2}{4\pi}\left(P_{xx}^{\prime 2d}(\hat{x}\cdot\hat{\psi})^2 + P_{yy}^{\prime 2d}(\hat{y}\cdot\hat{\psi})^2 + P_{zz}^{\prime 2d}(\hat{z}\cdot\hat{\psi})^2\right)\right] \\
=& \frac{4\pi}{k_0}\mathrm{Im}\left[\frac{k_0^2}{4\pi}\hat{\psi}\cdot\mathcal{P}^{\prime 2d}\cdot\hat{\psi}\right]
\end{aligned} \tag{4.125}$$

where again $\psi \in \{v, h\}$, and the primed tensor elements are given as:

$$P_{xx}^{\prime 2d} = P_{xx}^{2d} + \frac{ik_0^2}{8}|P_{xx}^{2d}|^2(1+\cos^2\theta_i') \tag{4.126}$$

$$P_{yy}^{\prime 2d} = P_{yy}^{2d} + \frac{ik_0^2}{8}|P_{yy}^{2d}|^2(1+\cos^2\theta_i') \tag{4.127}$$

$$P_{zz}^{\prime 2d} = P_{zz}^{2d} + \frac{ik_0^2}{8}|P_{zz}^{2d}|^2 2\sin^2\theta_i' \tag{4.128}$$

Note that (4.125) provides an expression for σ_e^{2d} which is in the form of the optical theorem, with the only change being the introduction of the new primed polarizability tensor elements. Thus, equations(4.126) to (4.128) provide a new set of polarizability tensor elements, modified such that the optical theorem is valid when applied to the forward scattering solution. This modification is possible because the new primed tensors are independent of polarization ψ, although an addition complication arises

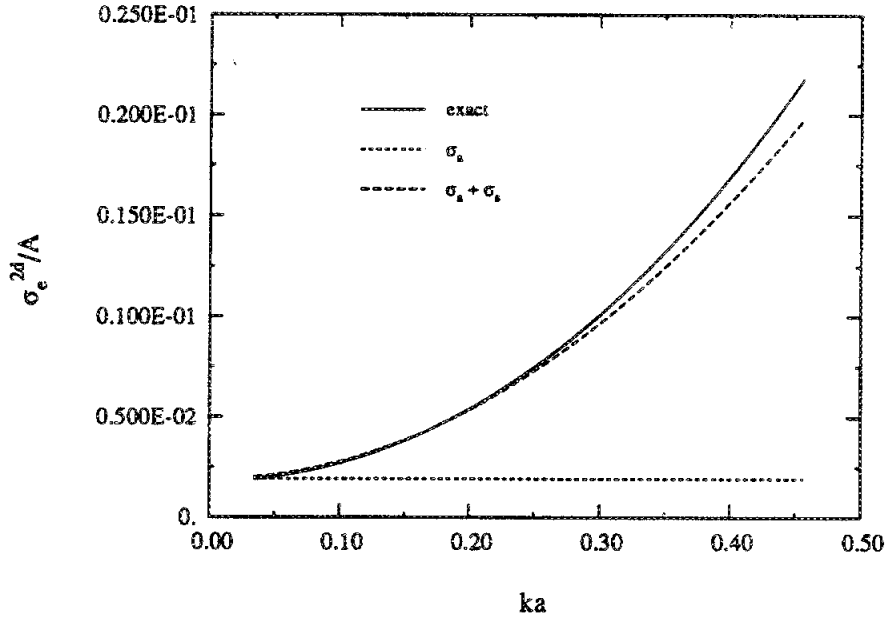

(a)

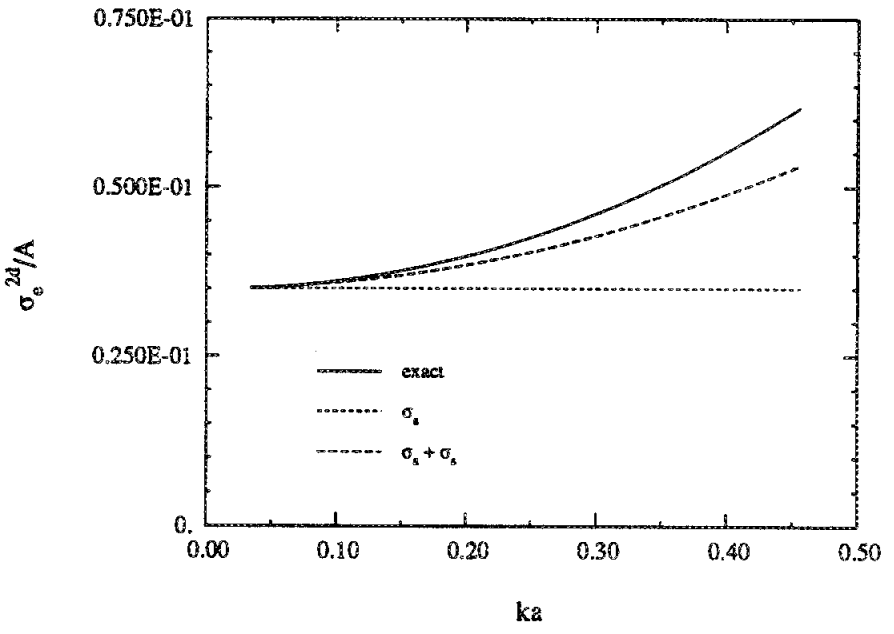

(b)

Figure 4.8: Plot displaying the normalized extinction cross-section (per unit length) of a circular dielectric cylinder. Shown are the exact solution, the Rayleigh solution (σ_a), and the solution of equation (4.125) ($\sigma_a + \sigma_s$). The dielectric for (a) is $\epsilon_r = 10 + \imath 0.1$ and for (b) $\epsilon_r = 10 + \imath 2$. Polarization is horizontal and $\theta_i = 45°$.

dependent on α and β, as well as incidence direction $\hat{k}^i$.

$$\begin{aligned}\cos\theta_i' =& \hat{k}^i \cdot \hat{z} \\ =& (\sin\theta_i\hat{x} + \cos\theta_i\hat{z}) \cdot (\sin\beta\cos\alpha\hat{x} + \sin\beta\sin\alpha\hat{y} + \cos\beta\hat{z}) \\ =& \sin\theta_i(\sin\beta\cos\alpha) + \cos\theta_i\cos\beta \end{aligned} \tag{4.129}$$

Again using the concept of an incremental dipole element, the effective propagation constant of a collection of line dipole elements can be computed. We first consider a layer of thickness Δz with a collection of line dipole elements passing completely through the layer, as shown in Figure 4.10. The section of each line dipole element passing through this layer can be considered an elemental dipole with polarizability tensor $\mathcal{P}^{2d}\Delta\ell$. The particle density of these elements, defined as n_0 particles per unit volume, is therefore $n_0 = N_{epa}\ \Delta z$, where N_{epa} is the average number of elements intersecting a unit area of the layer. Therefore, the propagation value $M_{\psi\psi}$ defined in equation (4.29) can be expressed as:

$$M_{\psi\psi}^{inc}(\hat{k}_0^i) = \frac{\imath N_{epa}k_0^3}{2\Delta z}\langle\hat{\psi}\cdot\mathcal{P}^{2d}\cdot\hat{\psi}\rangle\left(\frac{\Delta\ell}{\Delta z}\right)\Delta z \tag{4.130}$$

$$M_{\psi\psi}^{inc}(\hat{k}_0^i) = \frac{\imath N_{epa}k_0^3}{2}\langle\hat{\psi}\cdot\mathcal{P}^{2d}\cdot\hat{\psi}\rangle\left(\frac{\Delta\ell}{\Delta z}\right) \tag{4.131}$$

Likewise, the propagation value $\tau_\psi(\Delta z)$ given by (4.56) is equal to $M_{\psi\psi}^{inc}\Delta z$. If the layer described in Figure 4.10 is one of N sequential layers stacked upon each other, then $\tau_\psi(z)$ can be described as:

$$\tau_\psi(N\Delta z) = \sum_{n=1}^{N} M_{\psi\psi}^{inc\ n}\Delta z \tag{4.132}$$

If the value $d = N\Delta z$ is fixed, then taking the limit as Δz approaches zero ($N \to \infty$)

It should be emphasized that this propagation solution is only valid for layer structures as depicted in Figure 4.11 where the element length is of the order of the layer height and particles are located in the far-field of each other only in the two-dimensional sense. That is, in the region of the scattering layer, the propagation is basically a two-dimensional problem, with the scattered fields propagating as cylindrical waves, and the real power flow occurring primarily in the 2π space of the forward scattering cone. Thus, the two dimensional extinction solution of Section 4.4.2 is valid for determining the propagation of a wave in a layer of this type. However, if the scattering layer is of the type in depicted in Figure 4.12, the particles reside generally in the far-field of each other, and the scattered fields are therefore spherical within the layer. Even if the particles are line dipole elements, their scattering cross-sections cannot in general be modeled as $\sigma_s^{2d}\ell$. It must instead be explicitly be determined by integrating over 4π space, as given by equation (4.115). However, if the electrical length $k\ell$ is large, $\sigma_s^{2d}\ell$ is a good approximation for the scattering cross-section, as the power flow in this case is again primarily in the forward-scattering cone. Additionally, the absorption cross-section of (4.114) is also valid regardless of $k\ell$, as the value is directly proportional to length.

4.5 Comparison to Dielectric Slab Model

The propagation model derived above assumed a diffuse boundary between the extinction layer and free-space; the wave assumed to travel straight into the region using a ray-optics approach. Conversely, other examinations of scattering from random media have treated the layer as a dielectric slab, such that the coherent wave is refracted at the upper boundary. If sparse scattering media is considered, the effective

propagation constant is given from (4.28) as $k_1 = k_0 - \imath M$, and using the formulation of this chapter, the propagation to point $\bar{r}$ is expressed as $e^{\imath\Phi_A}$, where Φ_A is:

$$\Phi_A = \imath(k_0 \sin\theta_i x + k_0 \cos\theta_i z - \imath M \sec\theta_i z) \tag{4.136}$$

Whereas, if the layer is modeled as a dielectric slab, the propagation to $\bar{r}$ is $e^{\imath\Phi_B}$ where[12, p. 119]:

$$\begin{aligned}\Phi_B =& k_0 \sin\theta_i x + \sqrt{k_1^2 - k_0 \sin^2\theta_i} z \\ =& k_0 \sin\theta_i x + \sqrt{k_0^2 - \imath 2k_0 M - M^2 - k_0 \sin^2\theta_i} z \\ =& k_0 \sin\theta_i x + \sqrt{k_0^2 \cos^2\theta_i - \imath 2k_0 M - M^2} z\end{aligned} \tag{4.137}$$

These two equations appear disconcertingly different. However, if we recognize that for a sparse media the value M is small compared to k_0, an approximation to the square root term of (4.137) can be found by taking a Taylor series expansion:

$$\begin{aligned}\Phi_B =& k_0 \sin\theta_i x + \sqrt{k_0^2 \cos^2\theta_i - \imath 2k_0 M - M^2} z \\ \approx& k_0 \sin\theta_i x + k_0 \cos\theta_i z - \imath M \sec\theta_i z + \frac{\sec\theta_i \tan^2\theta_i M^2 z}{2k_0} \\ =& \Phi_A + \frac{\sec\theta_i \tan^2\theta_i M^2 z}{2k_0}\end{aligned} \tag{4.138}$$

Therefore, to the first order in M these two approaches provide identical results. This is significant because, as stated before, M is generally small compared to k_0 for sparse media.

mulation was used to determine the complex propagation of the coherent wave in the media as a general function of vertical location z. In Chapter II it was demonstrated that the scattering from thin dielectric elements of arbitrary cross-section could be modeled by a line dipole element. In Chapter II, the polarizability tensor elements for cylinders with grass plant cross-sections was determined. Adding to this the results of this chapter, the scattering and extinction of grassy vegetation can now be derived.

all dissimilar plant elements is now required .

Finally, the covariance terms for a complete grassland canopy will be derived, again including the coherent effects due to plant location. The effects are particularly significant for the case of the row structured canopies often found in cultural grasses. It should be noted that all these models include only first order scattering effects. It could be argued that a first order scattering model is insufficient for describing the scattering from long vertical stalks, as for all but the most sparse canopies the elements would reside in the near-field of each other and thus likely have stronger inter-element coupling. However, studies have demonstrated that the average scattered power for a collection of randomly located vertical scatters can be sufficiently modeled by considering only first order effect[20], although this is less true for the cross-polarized power than the co-polarized scattering.

5.1 Scattering from a Grass Plant

Implementing the definitions expressed above, the scattering from a single grass plant can be formulated. Using first-order discrete scattering theory (i.e. no constituent coupling), the scattered field from a grass plant can be expressed as the coherent sum of the scattering from its constituent elements:

$$S_{x\psi}^{plant} = S_{x\psi}^{grain} + S_{x\psi}^{stalk} + \sum_{n=1}^{N} S_{x\psi}^{leaf\ n} \tag{5.1}$$

essentially compute (5.2) as:

$$\langle S_{x\psi}^{plant} S_{\lambda\mu}^{*plant} \rangle =$$
$$\sum_{mech=a}^{d} \langle S_{x\psi\ mech}^{grain} S_{\lambda\mu\ mech}^{*grain} \rangle + \sum_{mech=a}^{d} \langle S_{x\psi\ mech}^{stalk} S_{\lambda\mu\ mech}^{*stalk} \rangle + \sum_{mech=a}^{d} \sum_{n=1}^{N} \langle S_{x\psi\ mech}^{leaf\ n} S_{\lambda\mu\ mech}^{*leaf\ n} \rangle \tag{5.4}$$

If the plant contains four leaves, then the number of terms in (5.4) totals 24. This is contrasted to the coherent formulation of (5.2) and (5.3), where $24^2 = 576$ terms, including the 24 of (5.4), are represented. If the covariance element is a real power value, then the 24 terms of (5.4) represent the incoherent scattered power. These incoherent terms generally the dominant terms of equation (5.2), and this fact is often used to justify using the simpler form of (5.4). However, the question is not whether the incoherent terms are dominant but whether the remaining 552 coherent terms are insignificant when taken in total. Perhaps the smallest coherent term is, for example, an order of magnitude larger than the largest coherent term. The coherent terms may still be significant as their quantity (552) is more than an order of magnitude greater ($552/24 = 23$). Theoretically, these coherent terms can reduce the total power to zero, or increase the total power to as much as 13.8 dB ($10 \log_{10} 24$) higher than the incoherent scattered power.

Both the stature and the structure of the grass plant may lead to conditions where the coherent terms are significant. As explained in Chapter I, the coherent scattering terms of two random scatterers will reduce to zero if the expected value of their phase difference is large. A situation where this occurs is when the position of the scatterers are independent and randomly distributed throughout an electrically large scattering volume. However, this is not always the case for grassland vegetation. Both the

tensor elements derived in Chapter III or the tensor elements of a circular cylinder given Sarabandi and Senior[21]. The other item requiring definition is the vector $\bar{r}_\ell$, which defines the contour of the scattering element. For a stalk element, the shape is modeled as $\rho = f(z) = a(z+d)$, so that $\bar{r}_{stalk}$ is:

$$\bar{r}_\ell = \bar{r}_{stalk} = \cos\phi_{stalk}\; a(z+d)\hat{x} + \sin\phi_{stalk}\; a(z+d)\hat{y} + z\hat{z} \qquad -d < z < z_0 \tag{5.5}$$

The transformation matrix $\mathcal{T}(z)$ from (4.65) can now be determined, explicitly writing the trigonometric terms of Euler angles α and β.

$$\cos\alpha = \cos\phi_{stalk} \qquad \sin\alpha = \sin\phi_{stalk} \tag{5.6}$$

$$\cos\beta = \frac{1}{\sqrt{1+a^2}} \qquad \sin\beta = \frac{a}{\sqrt{1+a^2}} \tag{5.7}$$

Therefore, the stalk is modeled as a straight element, originating at $-d\hat{z}$. Although straight, the element is tilted at an angle $\theta = \tan^{-1} a$ in the azimuthal direction ϕ_{stalk}. The length of the stalk element is thus $\sqrt{1+a^2}(z_0+d)$. Additionally, the diameter of the stalk is not constant, but instead tapers with height, so that its diameter can be generally represented as $dm(\ell)$, where ℓ is the distance along the stalk contour from its base ($z = -d$). For example, observation of natural elements leads to the following expression as a representative analog :

$$dm(z) = dm_0\left(1 - dm_{taper}\left[\frac{\ell(z)}{\ell(z=0)}\right]^4\right) \tag{5.8}$$

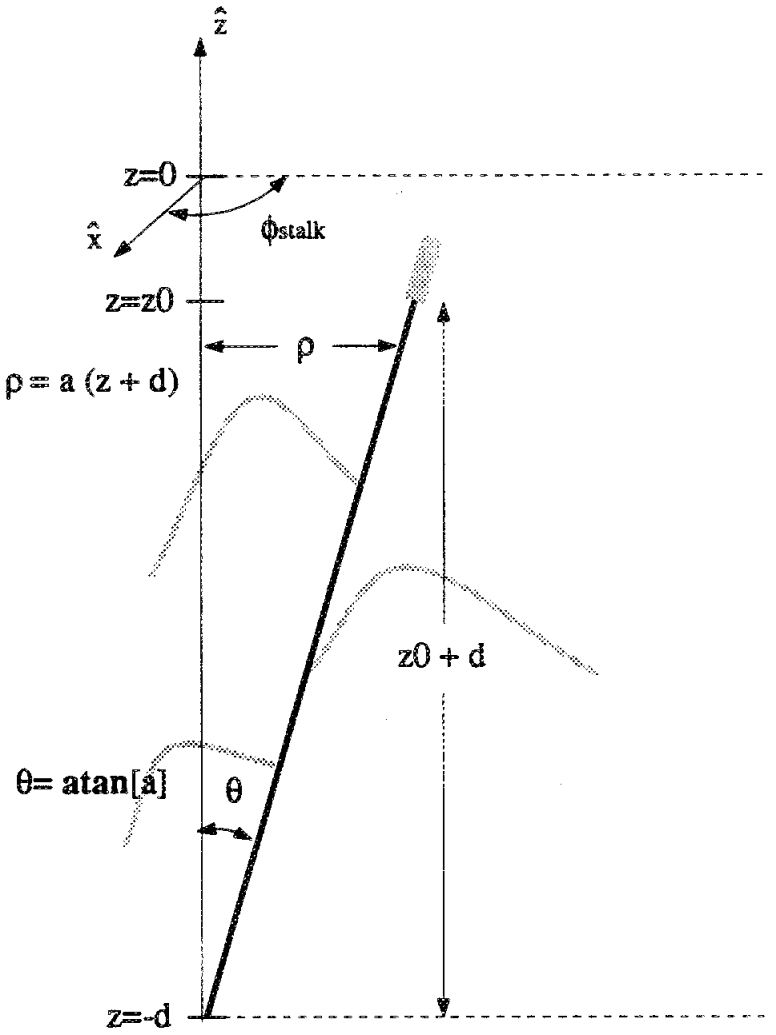

Figure 5.1: The geometry of the stalk model, demonstrating the variables z_0, a and ϕ_{stalk}

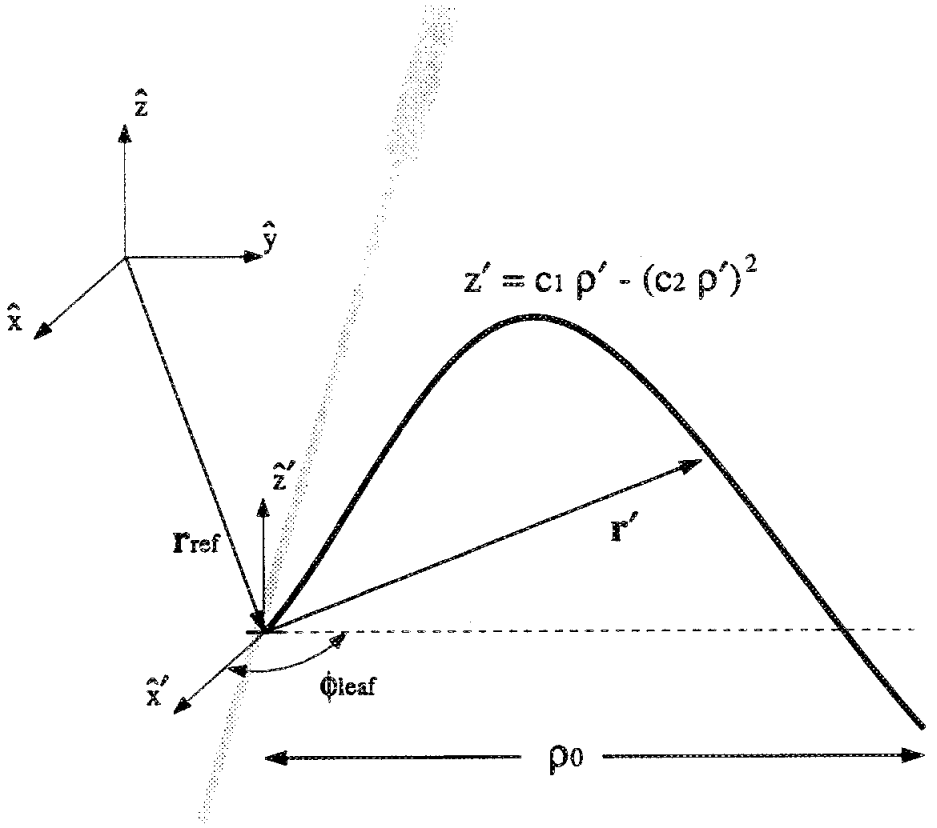

Figure 5.2: Geometry of leaf model, showing variables z_{ref}, ϕ_{leaf}, c_1, c_2 and ρ_0

transformation matrix $\mathcal{T}(\rho)$ can be determined using the following relations:

$$\begin{aligned} \cos\alpha &= \cos\phi_{leaf} & \sin\alpha &= \sin\phi_{leaf} \\ \cos\beta &= \frac{c_1 - 2c_2^2\rho}{\sqrt{1+(c_1-2c_2^2\rho)^2}} & \sin\beta &= \frac{1}{\sqrt{1+(c_1-2c_2^2\rho)^2}} \end{aligned} \tag{5.12}$$

However, the vector $\bar{r}_{leaf}$ does not equal the vector $\bar{r}_\ell$ of equation (4.74). From 5.5, it is apparent that the leaf originates ($\rho = 0$) at the global reference. However, the structure of the plant model indicates that the leaf originates from a location along the contour defined by equation (5.5); that is, from the stalk. The spatial variables of (5.12) are therefore defined in the local coordinate space of the leaf, located at its origin. The vector defining the leaf contour in global coordinate space, $\bar{r}_e$, can therefore be given as:

$$\begin{aligned} \bar{r}_\ell &= \bar{r}_{ref} + \bar{r}'_{leaf} \\ \bar{r}_\ell &= \cos\phi_{stalk}\, a(d+z_{ref})\hat{x} + \sin\phi_{stalk}\, a(d+z_{ref})\hat{y} + z_{ref}\hat{z} + \bar{r}'_{leaf} \end{aligned} \tag{5.13}$$

where $\bar{r}_{ref}$, more specifically z_{ref}, defines the location of the leaf along the stalk contour. The plant is modeled such that the leaves reside along a region of the stalk defined as $z_{lc} - \Delta_{leaf}/2 < z_{ref} < z_{lc} + \Delta_{leaf}/2$. Thus, the leaves reside in a layer of thickness Δ_{leaf}, with leaf center at $z = z_{lc}$. If the propagation value $M_\psi(z)$ is approximately constant throughout this leaf layer, then the integrated value $\tau_\psi(z)$ can be expressed for $z = z_{ref} + z'$ as:

$$\tau_\psi(z_{ref}+z') \approx \tau_\psi(z_{ref}) + M_\psi^{leaf} z' \tag{5.14}$$

with $\Psi_{\chi\psi}^{mech}(z')$ as:

$$\Psi_{\chi\psi}^{a}(z') = \exp\left[\imath 2\left(k_x^i \cos\phi_{leaf}\rho' + k_y^i \sin\phi_{stalk}\rho' + k_z^i z'\right) + \frac{M_\chi(z') + M_\psi(z')}{\cos\theta}\right] \tag{5.21}$$

$$\Psi_{\chi\psi}^{b}(z') = \exp\left[\imath 2\left(k_x^i \cos\phi_{stalk}\rho' + k_y^i \sin\phi_{stalk}\rho'\right) + \frac{M_\chi(z') - M_\psi(z')}{\cos\theta}\right] \tag{5.22}$$

$$\Psi_{\chi\psi}^{c}(z') = \exp\left[\imath 2\left(k_x^i \cos\phi_{stalk}\rho' + k_y^i \sin\phi_{stalk}\rho'\right) + \frac{M_\psi(z') - M_\chi(z')}{\cos\theta}\right] \tag{5.23}$$

$$\Psi_{\chi\psi}^{d}(z') = \exp\left[\imath 2\left(k_x^i \cos\phi_{stalk}\rho' + k_y^i \sin\phi_{stalk}\rho' - k_z^i z'\right) - \frac{M_\chi(z') + M_\psi(z')}{\cos\theta}\right] \tag{5.24}$$

and $z' = c_1\rho - c_2^2\rho^2$. Since $d\ell = \sqrt{1 + (c_1 - 2c_2^2\rho)^2}$, the scattering from a leaf element for an arbitrary mechanism *mech* can therefore be written as:

$$S_{\chi\psi}^{mech} = \Phi_{\chi\psi}^{mech}(z_{ref}) \int_0^{\rho_0} \hat{\chi}_{mech} \cdot \mathcal{P}_{2d}^{leaf}(\rho') \cdot \hat{\psi}_{mech}\ \Psi_{\chi\psi}^{mech}(\rho')\sqrt{1 + (c_1 - 2c_2^2\rho')^2}\, d\rho' \tag{5.25}$$

For the leaf model, the variables which are assumed to be random from leaf to leaf are ϕ_{leaf}, c_1, c_2, ρ_0 and z_{ref}; all other variables are assumed to be constant throughout the canopy layer. The leaf model, with five random variables, is implemented with two more random variables than the stalk model. The covariance terms (5.2) are determined by computing the expected value over these random variables, an evaluation which generally will be completed numerically. Since the time to numerically evaluate a N-fold integral increases roughly as the power of N, the value in limiting

matrix $\mathcal{C}$ can be written in terms of a diagonal matrix:

$$\mathcal{C} = \mathcal{Q}\mathcal{D}\mathcal{Q}^{-1} = \left[\mathbf{e}_1, \mathbf{e}_2, \mathbf{e}_3\right] \begin{bmatrix} \lambda_1 & 0 & 0 \\ 0 & \lambda_2 & 0 \\ 0 & 0 & \lambda_3 \end{bmatrix} \left[\mathbf{e}_1, \mathbf{e}_2, \mathbf{e}_3\right]^{-1} \tag{5.27}$$

where $\mathbf{e}_n$ and λ_n are the eigenvectors and eigenvalues of $\mathcal{C}$. The matrix $\mathcal{Q}$ represents a linear transformation of the parameter space $\mathbf{l}$ into a new parameter space denoted $\mathbf{v} = \{v_1, v_2, v_3\}$, such that $\mathbf{v} = \mathcal{Q}^{-1}\mathbf{l}$ and $\mathbf{l} = \mathcal{Q}\mathbf{v}$. Matrix $\mathcal{D}$ is thus the covariance matrix of $\mathbf{v}$ so, unlike the elements of $\mathbf{l}$, the elements of $\mathbf{v}$ are linearly independent ($\mathcal{D}$ is diagonal), and the value λ_n is therefore the variance of variable v_n. The leaf curvature can be equivalently expressed in either parameter space $\mathbf{l}$ or $\mathbf{v}$. However, in $\mathbf{v}$, the methodology for reducing the parameter set becomes apparent.

Essentially every parameter describing a leaf element is a random variable, as no two leaves of a given canopy are exactly alike. However, for many parameters this variation is small, and thus the variance is assumed to be zero. Only the parameters with large variances are considered random. Similarly, the two elements of $\mathbf{v}$ with the smallest eigen values (variances) can discarded, approximating their variances as zero. The variable with the largest eigen value (denoted v_e) will still be regarded as random, but the other two variables will be set at their mean value ($v = m_v = 0$). Thus, the total number of random variables in the leaf model is reduced from five to three $\phi_{leaf}, z_{ref}, v_e$. The variables c_1, c_2, and ρ_0 are now direct functions of v_e, found by translating from $\mathbf{v}$ back to $\mathbf{l}$ using matrix $\mathcal{Q}$. Since two of the elements of $\mathbf{v}$ are zero, this transformation is simply $\mathbf{l} = \mathcal{Q}\mathbf{v} = \mathbf{e}_e v_e$ where $\mathbf{e}_e$ is the eigenvector

c_1 mean	c_1 variance	c_2 mean	c_2 variance
ρ_0 mean	ρ_0 variance	c_1, c_2 covariance	c_1, ρ_0 covariance
ρ_0, c_2 covariance	cross-section	dielectric	blade width
blade angle	blade curvature	blade taper	blade thickness
leaf layer size	leaf layer location	leaves per plant	leaf spacing

Table 5.2: Leaf Model Parameter List

scattering model without adversely effecting computational speed.

Finally, we note that the cross-section of a leaf structure is not constant along its axial extent. Instead, its width w tapers to a point at the end of each leaf. The effect can be modeled with the following function:

$$w(\ell) = w_0\left(1 - \left[\frac{\ell(\rho)}{\ell(\rho_0)}\right]^4\right) \tag{5.31}$$

where w_0 is the leaf width at its base $\rho = 0$ and $\ell(\rho)$ is the distance along the leaf contour from its base to a point denoted by ρ

$$\ell(\rho) = \int_0^\rho d\ell = \frac{\delta z\ \delta\ell - c_1\sqrt{1+c_1^2} - \sinh^{-1}[c_1] + \sinh^{-1}[dz]}{-4c_2^2} \tag{5.32}$$

where $\delta z = c_1 - 2c_2^2\rho$ and $\delta\ell = \sqrt{1+dz^2}$. Similar to stalk taper, the leaf width w can be determined at each point along its length, and the appropriate local polarizability tensor $\mathcal{P}'_{2e}$ can be evaluated using the model of Chapter III. As with stalk taper, this calculation adversely effects computation speed, and its effect on accuracy is scenario dependent. Therefore the approximation $w(\ell) = w_0$ is used as the default model. The entire set of variables can now be defined for this leaf model, and are listed in Table 5.2.2.

where $\hat{v}'$ and $\hat{h}'$ are the polarization vectors determined using the local coordinate space:

$$\hat{h}^{i\prime} = \frac{\hat{z}' \times \hat{k}^i}{|\hat{z}' \times \hat{k}^i|} \qquad \hat{v}^{i\prime} = \hat{h}^{i\prime} \times \hat{k}^i \tag{5.35}$$

$$\hat{h}^{s\prime} = \frac{\hat{z}' \times \hat{k}^s}{|\hat{z}' \times \hat{k}^s|} \qquad \hat{v}^{s\prime} = \hat{h}^{s\prime} \times \hat{k}^s \tag{5.36}$$

Note that $\hat{v}' \neq \hat{v}$ and $\hat{v}' \neq \hat{v}$. To complete the solution, unit vector $\hat{z}'$ is represented in terms of grain orientation angles α and β.

$$\hat{z}' = \sin\beta\cos\alpha\hat{x} + \sin\beta\sin\alpha\hat{y} + \cos\beta\hat{z} \tag{5.37}$$

Unlike either the leaf or stalk, the relatively small stature of the grain element allows it to be accurately modeled as a point scatterer, illuminated by a uniform plane wave and occupying a single location in space. If the grain element resides therefore at location $\bar{r}_{grain}$ in an extinction layer above a dielectric half-space, the scattering for an arbitrary polarization ($\chi\psi$) and scattering mechanism ($mech$) is found using (5.34) and (4.64) as:

$$S^{grain}_{\chi\psi\ mech}(\hat{k}^i;\hat{k}^s;\alpha,\beta) = S^{cyl}_{\chi\psi\ mech}\Phi^{mech}_{\chi\psi}(\bar{r}_{grain}) \tag{5.38}$$

Of course, $\bar{r}_{grain}$ is not an arbitrary point, as the grain is modeled as resting at the apex ($z = z_0 + \cos\beta h_{grain}/2$) of the stalk structure. Furthermore, it is assumed that the grain lies directly along the stalk axis, that is the stalk and grain orientations are identical. Therefore, the Euler angles defining grain orientation can be defined in

h_{grain} mean dielectric	h_{grain} variance diameter	h_{grain} pdf

Table 5.3: Grain Model Parameter List

term of the previously examined stalk parameters:

$$\alpha = \phi_{stalk} \qquad \beta = \tan^{-1}[a] \tag{5.39}$$

and the vector $\bar{r}_{grain}$ can be derived from (5.5) by setting $z = z_0 + \cos\beta h_{grain}/2 \approx z_0 + h_{grain}/2$ so that:

$$\bar{r}_{grain} = \cos\phi_{stalk}\, a(z_0 + h_{grain}/2 + d)\hat{x} + \sin\phi_{stalk}\, a(z_0 + h_{grain}/2 + d)\hat{y} + (z_0 + h_{grain}/2)\hat{z} \tag{5.40}$$

where the extra $\cos\beta h_{grain}/2$ added to z_0 reflects the fact that the scattering origin in (5.34) is at the center, not the bottom of the grain structure. Since the tilt angle of the stalk/grain is generally small, $\cos\beta \approx 1$ and the approximation $\cos\beta h_{grain}/2 = h_{grain}/2$ introduces little error.

The parameters with significant variability in these structures are grain length h_{grain} and orientation angles α and β. Since the orientation angles are directly dependent on stalk random variables a and ϕ_{stalk}, only one new random variable, h_{grain} is added to the overall plant model. An entire list of the parameters defining grain structure is given in Table 5.2.3.

Sixteen terms must therefore be determined for each of the four required covariance elements $\langle|S_{vv}|^2\rangle$, $\langle|S_{hh}|^2\rangle$, $\langle|S_{hv}|^2\rangle$ and $\langle S_{hh}S_{vv}^*\rangle$. However, the total computation time can be significantly reduced by noticing that many of these terms are either equal to, or the conjugate of, other terms. This is particularly true for the two ground-bounce terms, as the propagation traverses the same path, albeit in opposite directions. The precise relationships are dependent on polarization and are given as:

$$\begin{aligned}
\langle S_{vv}^{mech} S_{vv}^{*mech'}\rangle &= \langle S_{vv}^{mech'} S_{vv}^{*mech}\rangle^* \qquad \langle S_{vv}^{b} S_{vv}^{*mech'}\rangle = \langle S_{vv}^{c} S_{vv}^{*mech}\rangle \\
\langle S_{hh}^{mech} S_{hh}^{*mech'}\rangle &= \langle S_{hh}^{mech'} S_{hh}^{*mech}\rangle^* \qquad \langle S_{hh}^{b} S_{hh}^{*mech'}\rangle = \langle S_{hh}^{c} S_{hh}^{*mech}\rangle \\
\langle S_{hv}^{mech} S_{hv}^{*mech'}\rangle &= \langle S_{hv}^{mech'} S_{hv}^{*mech}\rangle^* \qquad \langle S_{hh}^{b} S_{vv}^{*mech'}\rangle = \langle S_{hh}^{c} S_{vv}^{*mech}\rangle
\end{aligned} \tag{5.42}$$

These relations represent a reduction in the number of calculated terms from 64 to 31. Additionally, if the inner integral over z_0 is numerically evaluated, the computation time can be likewise reduced if the scattering element $S_{\chi\psi\ mech}^{stalk}$ is computed as:

$$\begin{aligned}
S_{\chi\psi\ mech}^{stalk} = &\int_{-d}^{m_{z_0}} \hat{\chi}_{mech} \cdot \mathcal{P}_{2d}^{stalk}(z) \cdot \hat{\psi}_{mech} \Phi_{\chi\psi}^{mech}(z)\sqrt{1\ + a^2}dz \\
&+ \int_{m_{z_0}}^{z_0} \hat{\chi}_{mech} \cdot \mathcal{P}_{2d}^{stalk}(z) \cdot \hat{\psi}_{mech} \Phi_{\chi\psi}^{mech}(z)\sqrt{1\ + a^2}dz
\end{aligned} \tag{5.43}$$

where m_{z_0} is the mean value of random variable z_0. The first term of the above equation is independent of z_0, and thus can be calculated just once for each iteration of a and ϕ_{stalk}. Since the value $z_0 - m_{z_0}$ will likely be significantly less than $z_0 + d$, the computation time in determining the second term will be much less than if numerically integrating over the entire length of the stalk.

can be directly evaluated. The $\Phi_{\chi\psi}^{mech}$ covariance term can thus be expressed as:

$$\begin{aligned}\langle \Phi_{\chi\psi}^{mech}(z_{ref}) \Phi_{\lambda\mu}^{*mech'}(z_{ref}) \rangle \\ &= \Phi_{\chi\psi}^{mech}(z_{lc}) \Phi_{\lambda\mu}^{*mech'}(z_{lc}) \frac{1}{\Delta_{leaf}} \int_{-\Delta_{leaf}/2}^{\Delta_{leaf}/2} e^{\Omega\zeta} d\zeta \\ &= \Phi_{\chi\psi}^{mechref}(z_{lc}) \Phi_{\lambda\mu}^{*mech'ref}(z_{lc}) \frac{e^{\Omega\Delta_{leaf}/2} - e^{-\Omega\Delta_{leaf}/2}}{\Omega\Delta_{leaf}}\end{aligned} \tag{5.45}$$

where the substitution $z_{ref} = z_{lc} + \zeta$ was made so that $\tau_\psi(z_{ref}) \approx \tau_\psi(z_{lc}) + M_\psi^{leaf}\zeta$. The term Ω is a complex constant dependent on the polarization and scattering mechanism of each of the two applicable scattered fields. It can be generally expressed as $\Omega = \omega(\chi\psi, mech)\, \omega^*(\lambda\mu, mech')$ where ω is

$$\omega(\chi\psi, mech = a) = \imath 2\hat{k}_z^i + (M_\chi^{leaf} + M_\psi^{leaf}) \sec\theta_i \tag{5.46}$$

$$\omega(\chi\psi, mech = b) = (M_\chi^{leaf} - M_\psi^{leaf}) \sec\theta_i \tag{5.47}$$

$$\omega(\chi\psi, mech = c) = (-M_\chi^{leaf} + M_\psi^{leaf}) \sec\theta_i \tag{5.48}$$

$$\omega(\chi\psi, mech = d) = -\imath 2\hat{k}_z^i - (M_\chi^{leaf} + M_\psi^{leaf}) \sec\theta_i \tag{5.49}$$

Finally, the equality relationship provided in equation(5.42) for stalks are likewise valid for the leaf and grain covariance elements, thus reducing significantly the total computation time.

5.3.3 Grain Covariance

The grain covariance calculation is similar to the leaf covariance calculation, as both are elements located on the contour defined by the stalk. The difference is that the grain location is denoted by z_0 rather than z_{ref}, and of course the unique

the terms of the stalk-leaf covariance can be written as:

$$\langle S^{stalk}_{\chi\psi\ mech} S^{*leaf}_{\lambda\mu\ mech'} \rangle =$$
$$\langle \int_{-d}^{z_0} \hat{\chi}_{mech} \cdot \mathcal{P}^{stalk}_{2d}(z) \cdot \hat{\psi}_{mech} \Phi^{mech}_{\chi\psi}(z) \sqrt{1+a^2}\, dz \;\; \Phi^{*mech'}_{\lambda\mu}(z_{ref}) \rangle_{z_{ref},a,\phi_{stalk},z_0}$$
$$\langle \int_{0}^{\rho_0} \hat{\chi}'_{mech} \cdot \mathcal{P}^{*\,leaf}_{2d}(\rho') \cdot \hat{\psi}'_{mech} \Psi^{*mech'}_{\chi\psi}(\rho') \sqrt{1+(c_1 - 2c_2^2\rho)^2}\, d\rho' \rangle_{\phi_{leaf},v_e,\rho_0} \quad (5.52)$$

The expression is written as the product of two expected value operations, the first over stalk variables ϕ_{stalk}, a and z_0, as well as leaf variable z_{ref}. Unlike the the cases examined in the previous two section, this term does not reduce further; all random variables are present and must be evaluated. However, the integration over z_{ref} can be evaluated as shown in equation (5.45), provided the requisite assumptions are valid. The second product of (5.52) is essentially the average scattered electric field of the leaf element without the propagation path represented by $\Phi^{mech}_{\chi\phi}(z_{ref})$. Note this is not, however, the average free-space scattered field, as the value M^{leaf} in $\Psi^{mech}_{\chi\phi}(\rho)$ modifies this field solution. Because of azimuthal symmetry, this average scattered field term is uniquely zero for cross-pol polarizations hv and vh.

A result equivalent to (5.52) is likewise derived for $\langle S^{leaf}_{\chi\psi} S^{*stalk}_{\lambda\mu} \rangle$, and given the fact that $S^{leaf}_{\chi\psi} S^{*stalk}_{\chi\phi} = (S^{stalk}_{\chi\psi} S^{*leaf}_{\chi\phi})^*$ it is apparent that only portion of the 32 terms required for each covariance of four covariance matrix elements are required. The

5.3.6 Leaf-Grain Covariance

Again, the scattering from the leaf and grain are both dependent on the stalk contour a and ϕ_{stalk}. Recalling that S^{leaf} is additionally dependent on v_e and z_{ref}, the required covariance terms can be written as:

$$\langle S^{leaf}_{\chi\psi\ mech} S^{*grain}_{\lambda\mu\ mech'} \rangle = \langle \langle S^{leaf}_{\chi\psi\ mech} \rangle_{v_e, z_{ref}, \phi_{leaf}, \rho_0} \langle S^{*grain}_{\lambda\mu\ mech'} \rangle_{z_0, h} \rangle_{a, \phi_{stalk}} \tag{5.55}$$

Since all of the random variables defined in the plant model are involved, this is the most computationally intensive scattering term. Conversely, because the grain-leaf element pair is the physically least correlated element pair, its numerical significance is questionable. Thus, the utility of adding this term to the plant scattering model is uncertain.

5.3.7 Leaf-Leaf Covariance

The formulation of Section 5.3.2 provides the covariance for the scattered fields from a single leaf. However, the grass plant model assumes that the plant may consist of more than one leaf element. The correlation between the scattered fields of dissimilar leaf elements will be considered here. Assuming the curvature v_e and azimuth angle ϕ_{leaf} of dissimilar elements are independent, the covariance terms can

$p(z_{ref}, z'_{ref}) = p(z'_{ref}|z_{ref})p(z_{ref})$ where the conditional density function is defined as:

$$p(z'_{ref}|z_{ref}) = \begin{cases} \frac{1}{\Delta_{leaf}-2\delta} & \text{for } \frac{z_{lc}-\Delta_{leaf}}{2} + \delta z_{ref} < \frac{z_{lc}+\Delta_{leaf}}{2} - \delta \\ & \text{and } \frac{z_{lc}-\Delta_{leaf}}{2} < z'_{ref} < z - \delta \\ \frac{1}{\Delta_{leaf}-2\delta} & \text{for } \frac{z_{lc}-\Delta_{leaf}}{2} + \delta z_{ref} < \frac{z_{lc}+\Delta_{leaf}}{2} - \delta \\ & \text{and } z + \delta < z'_{ref} < \frac{z_{lc}+\Delta_{leaf}}{2} \\ \frac{1}{\Delta_{leaf}/2+(z_{ref}+\delta)} & \text{for } \frac{z_{lc}+\Delta_{leaf}}{2} - \delta < z_{ref} < \frac{z_{lc}+\Delta_{leaf}}{2} \\ & \text{and } \frac{-\Delta_{leaf}}{2} < z'_{ref} < z - \delta \\ \frac{1}{\Delta_{leaf}/2-(z_{ref}+\delta)} & \text{for } \frac{z_{lc}-\Delta_{leaf}}{2} < z_{ref} < \frac{z_{lc}-\Delta_{leaf}}{2} + \delta \\ & \text{and } z + \delta < z'_{ref} < \frac{z_{lc}+\Delta_{leaf}}{2} \\ 0 & \text{elsewhere} \end{cases} \quad (5.57)$$

This expression states that for a leaf located at z_{ref}, the probability that another leaf at z'_{ref} is within distance δ from z_{ref} is zero, while the probability that z'_{ref} resides outside this region is uniformly distributed across the remainder of the stalk from $z_{lc} - \Delta_{leaf}$ to $z_{lc} + \Delta_{leaf}$. If z_{ref} is likewise uniformly distributed across the leaf layer $\left(p_z(z_{ref}) = \frac{1}{\Delta_{leaf}}\right)$ the expected value term $\langle \Phi^{mech}_{\chi\psi}(z_{ref}) \Phi^{*mech'}_{\lambda\mu}(z'_{ref}) \rangle_{zref,zref'}$ is

$$\nu(\chi\psi, mech = c) = \imath 2\hat{k}_z^i + (-M_\chi^{leaf} + M_\psi^{leaf}) \sec\theta_i \tag{5.64}$$

$$\nu(\chi\psi, mech = d) = -\imath 2(\hat{k}_x^i + \hat{k}_z^i) - (M_\chi^{leaf} + M_\psi^{leaf}) \sec\theta_i \tag{5.65}$$

and $\xi(\lambda\mu, mech') = \nu^*(\lambda\mu, mech')$. The expression of (5.61) is a function of both a and ϕ_{stalk}. Therefore, a two dimensional integration over these two random variables is still required to complete the evaluation of $\langle \Phi_{\chi\psi}^{mech}(z_{ref}) \Phi_{\lambda\mu}^{*mech'}(z'_{ref}) \rangle_{z_{ref}, z'_{ref}, a, \phi_{stalk}}$.

5.4 Scattering from Grassland Canopies

The preceding sections have provided a solution for the average scattering from a single plant residing in the vegetation layer. However, the desired solution is the average scattering from an entire grassland canopy, a random collection of individual plants. Similar to plant scattering, the scattering from a canopy can be modeled as the coherent sum of the scattering from individual plants. Consider planar area A containing N grass plants, the location of each denoted by vector $\bar{\rho}_{plant}^n$. The scattered electric field can be represented in the far-field as:

$$S_{\chi\psi}^{canopy} = \sum_{n=1}^{N} S_{\chi\psi\, n}^{plant} e^{\imath 2k_0 \hat{k}_\rho^i \cdot \bar{\rho}_{plant}^n} \Theta(\rho_{plant}^n) \tag{5.66}$$

where the term $S_{\chi\psi\, n}^{plant}$ is likewise the coherent sum of all four scattering mechanisms and $\Theta(\bar{\rho}_{plant}^n) = \exp[\imath 2k_0 \hat{k}_\rho^i \cdot \bar{\rho}_{plant}^n]$ is the relative phase of the plant. Note the propagation vector $\hat{k}_\rho^i = \cos\phi_i \sin\theta_i \hat{x} + \sin\phi_i \sin\theta_i \hat{y}$ is in its most general form, with ϕ_i as an arbitrary variable. Recall the assumption $\phi_i = 0$ was used in Chapter IV to simplify the derivations, although the results are equally valid for all ϕ_i, providing the plant is azimuthally symmetric. Thus, letting ϕ_i be an arbitrary value does not

5.4.1 Average Scattered Field

Appearing in equation (5.67) is the term $\langle S^{plant} \rangle$, the average scattered *field* of a grass plant; a value determined as:

$$\langle S^{plant}_{\chi\psi} \rangle = \langle S^{stalk}_{\chi\psi} \rangle + \langle S^{grain}_{\chi\psi} \rangle + N_{leaf} \langle S^{leaf}_{\chi\psi} \rangle \tag{5.69}$$

where the expected value operations are performed over the relevant random variables of each plant element. For electrically large and very random vegetation, the average field $\langle S^{plant} \rangle$ will likely be small and thus the coherent power can be disregarded. However, the small stature and simple structure of a grass plant can result in a significant average scattered field.

If the scattered field of a random particle over all states is represented as a phasor in the complex plane, it is apparent (Figure 5.5) that the average field will be approximately zero if the vectors are uniformly distributed over 2π radians. However, the average field will not be zero if the vectors are distributed over only a fraction of 2π or if the scattering from a single state dominates in magnitude the scattering from all other states. The first cases occurs if the scatterer is restricted or confined to a region which is electrically small in regards to propagation direction. The second can occur when a specular scattering point occurs within the domain of the expected value integration, or when a single point scatterer dominates.

Both situations are plausible scenarios when considering scattering from grass plants. At low frequencies, random variables such as z_0, z_{ref}, v_e and a, constrained to the relatively small volume of a grass plant, modify the propagation functions $\Phi^{elmt}_{\chi\psi\, mech}(\bar{r})$ functions only slightly if the resulting physical variation is small compared to a wavelength. Even at higher frequencies, if random variable a is approxi-

5.4.2 Scattering From Uniformly Distributed Plants

Assuming that the average scattered field $\langle S^{plant} \rangle$ is significant, the remaining portion of the coherent power term is the function $\langle \Theta(\bar{\rho}^n)\Theta^*(\bar{\rho}^m) \rangle$, the correlation of the relative phases of dissimilar plants due to their position on the planar surface A. Variables which effect this function include canopy structure (i.e. the distribution of the plants on the soil surface) and scattering area A (i.e. illumination spot size), neither of which effect the incoherent scattering term. Two cases will be examined, the first where the plants are uniformly distributed over the planar surface, with the second considering the problem of cultural grasses planted in row patterns.

If the location of two plants residing in area A are both independent and uniformly distributed, the relative phase term $\langle \Theta(\bar{\rho}^n_{plant})\Theta^*(\bar{\rho}^m_{plant}) \rangle$ can be expressed as

$$\langle \Theta(\bar{\rho}^n_{plant})\Theta^*(\bar{\rho}^m_{plant}) \rangle = \frac{1}{A}\int_A e^{\jmath 2k_0 \hat{k}^i_\rho \cdot \bar{\rho}^n_{plant}}\, d\bar{\rho}^n_{plant}\, \frac{1}{A}\int_A e^{-\jmath 2k_0 \hat{k}^i_\rho \cdot \bar{\rho}^m_{plant}}\, d\bar{\rho}^m_{plant} \tag{5.70}$$

For an area A electrically large in terms of the radial phase constant $k_\rho = k_0 \sin\theta_i$, the integrals in (5.70) are insignificant, and the total canopy scattering power is expressed in terms of the incoherent power only. However, the assumption of independence used in the above equation is approximately valid only for cases where the plants sparsely populate the region A. As with a forest canopy, grasslands are often continuously populated, with the area defining the location of one plant immediately adjoining the area of another. Again similar to forests, this does not mean that the scattering volume is dense, it merely reflects the fact that nature soon fills open spaces in the canopy with new plants. For this reality, the independent assumption is invalid, for in a well populated region independence would result in many instances of plants being

straight, periodic rows. The coherent scattering term can be greatly influenced by this structure, and thus the coherent solution for this distribution will be presented here. To begin, we first consider the scattering from a section of a single row, located at x=0 and extending from $y_{min} < y < y_{max}$. The plant locations are assumed to be uniformly distributed in y, with a gaussian distribution in x. The scattering covariance from this row section can be expressed as:

$$\langle S^{row}_{\chi\psi} S^{*row}_{\lambda\mu} \rangle = N_p \langle S^{plant}_{\chi\psi} S^{*plant}_{\lambda\mu} \rangle + N_p(N_p-1)\langle S^{plant}_{\chi\psi}\rangle\langle S^{*plant}_{\lambda\mu}\rangle\langle \exp[\imath 2k_0 \bar{k}_\rho \cdot (\bar{\rho}_n - \bar{\rho}_m)]\rangle_{n\neq m} \quad (5.74)$$

were the two term can again be interpreted as the incoherent and coherent scattering terms. Since the scattering from a single plant is independent of its location, the row structure will numerically effect only the phase function $\langle \exp[\imath 2k_0 \bar{k}_\rho \cdot (\bar{\rho}_n - \bar{\rho}_m)]\rangle_{n\neq m}$ Again assuming that the $\hat{x}$ and $\hat{y}$ components of $\bar{\rho}$ are independent, and that the plant locations are independent of each other, this phase term is evaluated as:

$$\begin{aligned}
&= \langle \exp[\imath 2k_0 \bar{k}_\rho \cdot (\bar{\rho}_n - \bar{\rho}_m)]\rangle_{n\neq m} \\
&= \left| \int_{y_{min}}^{y_{max}} e^{\imath 2k^i_y y} \frac{1}{y_{max}-y_{min}} dy \right|^2 \left| \int_{-\infty}^{\infty} e^{\imath 2k^i_x x} \frac{e^{-x^2/(2\sigma_x^2)}}{\sigma_x\sqrt{\pi}} dx \right|^2 \\
&= \left| \frac{\imath\left(e^{\imath 2k^i_y y_{max}} - e^{\imath 2k^i_y y_{min}}\right)}{k^i_y(y_{min}-y_{max})} \right|^2 \left| \sqrt{2} e^{-2(k^i_x\sigma_x)^2} \right|^2
\end{aligned} \quad (5.75)$$

This function, and thus the total scattering expressed by (5.74), is highly dependent on incidence angle and the statistics of the row section. If $k_0\sigma_x$ is small, then the collection of plants behave like a linear array of scatterers. If the illumination is perpendicular to the row direction ($\phi_i = 0$) then the plants along the row segment produce backscattered fields which are in-phase, so that (5.75) is nearly 1.0 and the

the rows generate a Bragg scattering phenomenon[12, pp. 515-525], with the average scattered field from each row constructively adding in phase at a set of specific incidence angles. If $\phi_i = 0$, then this occurs when $k_0 \sin\theta_i X_{row} = n\pi$, where $n \in \{\ldots, -2, -1, 0, 1, 2, \ldots\}$ and defines the Bragg scattering mode. Mode 0 occurs when $\theta_i = \pi$, the other modes are dependent on the frequency and row spacing. Note only a finite number of non-zero modes can occur between $\theta_i = \pi/2$ and $\theta_i = \pi$, and if $k_0 X_{rwo} < \pi$ then no non-zero modes occur. For large spot sizes, these coherent effects will be observed only at the incidence angle associated with the Bragg mode. As the spot size decreases and the number of illuminated rows N_{row} becomes small however, the scattering beam width associated with this effect will broaden. From equation (5.76), it is apparent that the effect of this Bragg scattering on the total scattering depends on the relative magnitude of $\langle S_{\chi\psi}^{caonpy} \rangle$. If the average scattered field of a single row is small, then no Bragg effects will be observable.

Equation (5.76) describes the scattering from an arbitrary collection of N_{row} row segments, each with arbitrary length $y_{max}^r - y_{min}^r$. This general equation can be made specific if a general form of the illuminating spot size, defining area A, is selected. In this case, a simple antenna model of a circular beam of uniform intensity will be assumed. As shown in Figure 5.6, the pattern subtends a circular area A at the target, and thus projects an ellipse with area $A\sec(\pi - \theta_i)$ onto the target plane, with the major ellipse of the target lying in the direction of propagation $\hat{k}_\rho^i$. The basic geometry of this problem is displayed in Figure 5.7, where $R = \sqrt{A/\pi}$. Thus, the problem is to determine from a given area A and propagation direction $\hat{k}^i$ the number of rows N_{row} intersecting the ellipse, as well as the beginning and ending points y_{min}, y_{max} for each.

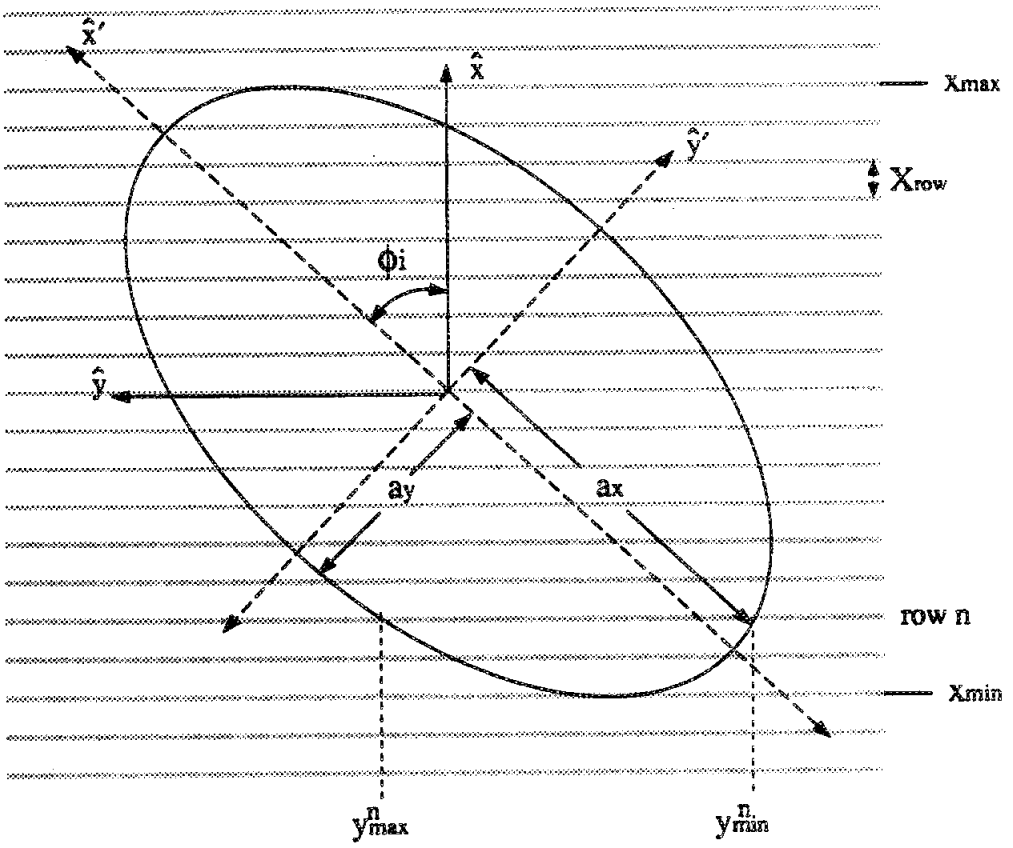

Figure 5.7: Geometry of the projected ellipse on the row pattern, demonstrating the values x_{max}, x_{min}, y^n_{min} and y^n_{max}.

canopy height (d)	plants/meter^2	plants/row meter
row spacing	row plant x-location variance	row plant x-location pdf

Table 5.4: Row Model Parameter List

5.5 Canopy Propagation

If the canopy is a uniformly distributed collection of plants, then the propagation through the canopy as expressed by $\tau_\psi(z)$ is determined in a straight-forward manner using the concepts introduced in Chapter IV. Since $\tau_\psi(z)$ is determined from calculating the forward scattering of the plant elements, where the relative phase $\imath(\bar{k}^i - \bar{k}^s)\cdot\bar{r}$ is equal to zero, coherent effects are not a consideration and the propagation in the canopy is simply the sum of propagation effects due to each element:

$$\tau_\psi^{canopy}(z) = \tau_\psi^{leaf}(z) + \tau_\psi^{stalk}(z) + \tau_\psi^{grain}(z) \tag{5.81}$$

For this model, both the grain and the leaves are considered point scatterers distributed vertically through the canopy layer. The particle density is determined as $n_0(z) = N_{ppa}N_{epp}p(z_{elmt})$ where N_{ppa} is the number of plants per unit area, N_{epp} the number of elements (such as leaves) per plant, and $p(z_{elmt})$ is the pdf of the element location in z (i.e. $p(z_{ref})$ for leaves). These values and thus $\tau_\psi(z)$ are then determined from equations (4.29) and (4.56). The stalks however, extending from the surface to the top of the scattering layer, are considered strictly as line dipole, with the formulation of Section 4.4.3 implemented to provide $\tau_\psi(z)$.

However, if the plants are not uniformly distributed over the surface, but are instead planted in row structures, determining the propagation value $\tau_\psi(z)$ is more

density over a single row period X_{row},

$$M_\psi(z) \approx \int_{-Xrow/2}^{Xrow/2} M_\psi(x,z)dx \tag{5.83}$$

and use this average to compute $\tau_\psi(z)$. If again no z dependence is assumed, this becomes the familiar function:

$$\tau(x=0,z)_\psi = \int_{-z\tan\theta_i\cos\phi_i}^{x=0} M_\psi \frac{dx}{\sin\theta_i\cos\phi_i} = \frac{M_\psi z}{\cos\theta_i} \tag{5.84}$$

Essentially, equation (5.83) models the row structured vegetation as a continuous canopy independent of variable x. Figure 5.5 demonstrates the validity of this approximation, using the example density function. This approximation greatly reduces the complexity in evaluating τ_ψ, as it can be considered as a one-dimensional function of just variable z only.

Finally, to provide an accurate representation of the incident intensity on a row of plants, a final problem must be addressed. Figure 5.9 represents a periodic structure consisting of stalk and grain elements. It demonstrates that the grain elements and the very top of stalks have a direct optical path to the radar. No extinction occurs before reaching this portion of the vegetation. However, Figure 5.5 shows non-zero extinction for all $z < 0$. This is due to the fact that half of the extinction due to propagation *through* the center row is applied to the coherent wave *at* the center row. That is, the coherent wave encounters a portion of half the center stalks before reaching the plane $x = 0$. Although this is a correct mathematical interpretation arising from the continuity of $\tau_\psi(z)$ (if $\tau_\psi(-\Delta) = 0$ and $\tau_\psi(\Delta) = 1$, then $\tau_\psi(0) = 0.5$), it is not a correct physical interpretation. The sparsely distributed elements of the linear row greatly effect the intensity of the wave illuminating the next row, but it is

physically suspect to assign half this effect at $x = 0$. For a layer with small extinction or at large incidence angles, this error is slight. But if the counter examples occur, then the effect is significant. A better model is to therefore consider the extinction at $x = 0$ to be a result of the adjacent row only.

The effect of this is that the extinction curve of Figure 5.8 is shifted to the right by an amount $-X_{row} \tan\theta_i \cos\phi_i/2$. This result has a physical interpretation; the zero value of $\tau_\psi(z, x = 0)$ for $0 < z < -X_{row} \tan\theta_i \cos\phi_i/2$ indicates that the top of the canopy is directly illuminated. At $z = -X_{row} \tan\theta_i \cos\phi_i/2$, the propagation begins to see the effect of the very top of the adjacent row. This effect is essentially that observed with an optical shadow, an effect illustrated in curve of Figure 5.9. This model is thus easily implemented by first computing the values $\tau_\psi^{'stalk}(z)$ and $\tau_\psi^{'grain}(z)$ and then shifting this value downward by making the substitution $\tau'_\psi(z) = \tau_\psi(z + X_{row} \tan\theta_i \cos\phi_i/2)$. With this substitution, the propagation equations will correctly account for this shadow for all four scattering mechanisms. Effectively, this model shortens the stalk layer depth by $-X_{row} \tan\theta_i \cos\phi_i/2$.

5.6 Conclusions

A microwave scattering model for a grassland canopy has thus been completed. This model is an improvement on early scattering models in that it includes the coherent scattering effects of a single plant, including the field covariances between dissimilar scattering mechanisms and dissimilar plant elements. It accounts for the non-uniform illumination of the plant elements, and accurately determines the scattering from elements which are curved an/or have non-circular cross-sections. It accurately determines the extinction in a layer of these long elements, including the

scattering loss often neglected in Rayleigh formulations. Finally, the solution accounts for the overall canopy structure, including the coherent effects of both row and uniformly distributed canopies. The effect of row structured canopies on the extinction calculation was also determined.

Although this results in a model of significantly improved accuracy, it will have little usefulness if the computation time increased proportionately. Therefore, significant effort was placed in increasing computational efficiency. Among these steps included reducing the number of dependent random variables by transforming them into a new parameter space were the "randomness" of the system could be adequately represented by a single random variable. With this method the fidelity of the structure model is preserved while its utility is increased. To determine the validity of this model, or any model, its must be compared with a robust set of measured data, collected over a wide sample of relevant grassland vegetation targets. The methodology for satisfying this requirement for the grassiand scattering model described in this Chapter will be discussed in the next.

the plant changes dramatically from the beginning to end, beginning as a lush, green plant and ending as a dry, brown structure. Thus, each measurement opportunity consisted of observing a canopy which was significantly and sometimes dramatically different than the previous measurement. Additionally, data diversity was achieved by utilizing multiple sensor parameters. Polarization, frequency, incidence angle, and azimuth look angle were all variables at which multiple data points were collected. This was facilitated by the use of the the University of Michigan's polarimetric radar test unit. This fully polarimetric scatterometer operates at L, C and X band, and is mounted on a hydraulic boom to allow for arbitrary incidence and look angles.

However, this diverse set of scattering data cannot alone satisfy the of this experiment. A thorough set of ancillary data, precisely describing the grass canopy is likewise required. Often ancillary, or ground-truth data is collected with an eye to the parameters that are of ultimate interest to the user of remotely sensed data, parameters which include soil moisture, biomass, and leaf area. Although important, these parameters would represent an insufficient set of data. Instead, all parameters which effect the microwave scattering must be evaluated and quantified, regardless of there ultimate significance to remote sensing users. For example, leaf curvature and cross-section may be of no ultimate interest, but must be quantified since they (presumably) effect plant scattering. Thus, each of these parameters was evaluated at every test session.

The results of this experiment are presented in this chapter. A description of the scatterometer and its calibration is discussed, along with the methodology of ancillary data collection and results. Finally, the backscattering data is presented, and a qualitative analysis of the results is provided, satisfying the second of the stated test goals. The first goal, that of validating the scattering model, will be presented

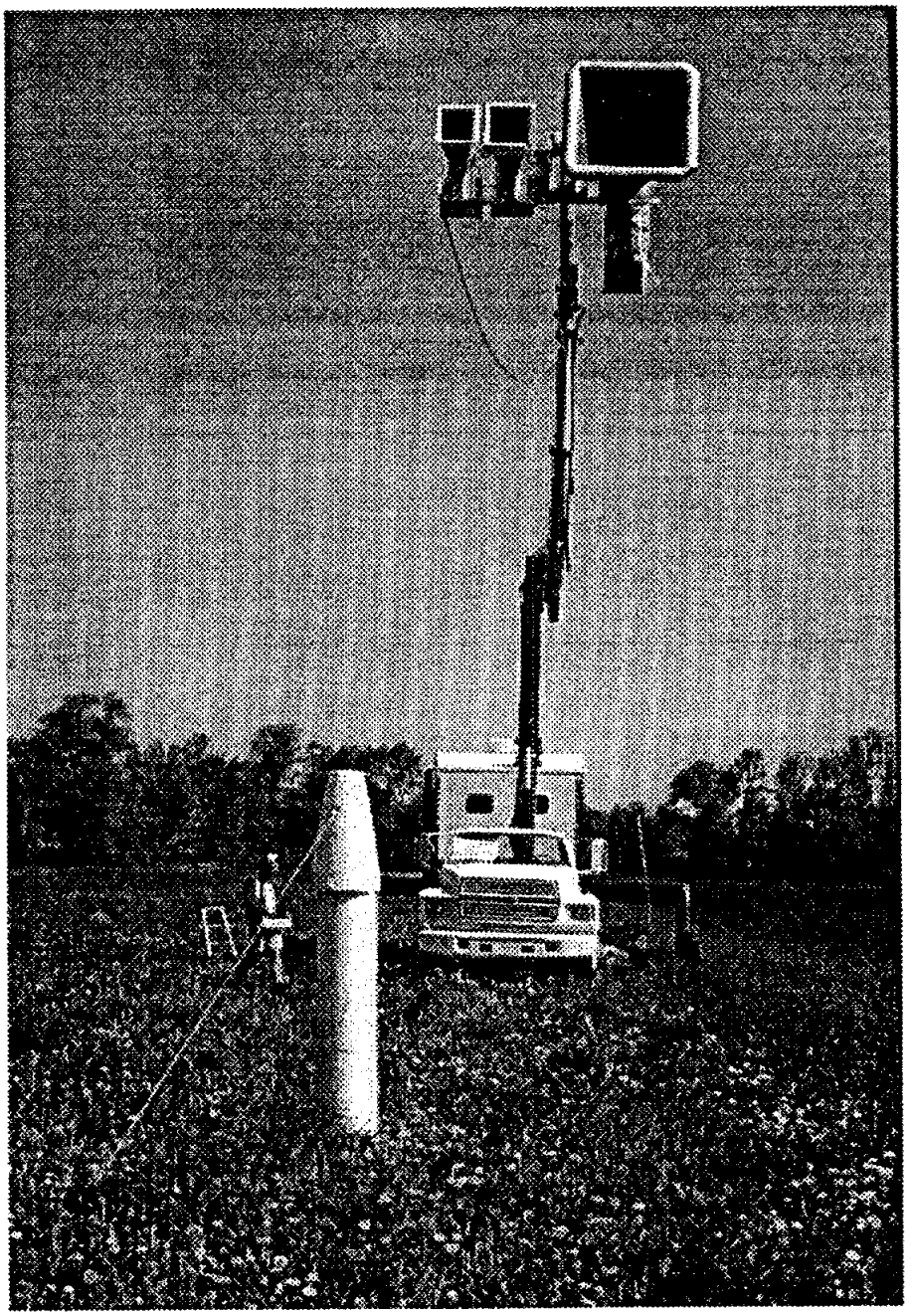

Figure 6.1: Photo of The University of Michigan's Microwave Polarimetric Scatterometer, including truck, boom, antennas (X,C,L), and calibration pedestal.

6.1.1 Calibration

The procedure which transforms a radar into a scatterometer is calibration. If correctly done, calibration maps the arbitrary magnitude and phase of the radar measurements into an accurate representation of the scattering matrix. Much has been written about this topic, but in regards to calibrating scatterometer measurements of distributed targets, the most complete work has been provided by Sarabandi [23, 24]. For a distributed target, the total backscattered energy is the a complex integration of the energy transmitted and received over the entire antenna pattern, not just the from the antenna boresight. In addition to the obvious variations in amplitude, the relative phase and polarization likewise varies over the antenna beam width. Since a full complex scattering matrix is desired, this variation must be accounted for. Thus, the antenna patterns for the Michigan scatterometer were measured, not only in terms of relative magnitude, but as a function of phase and polarization as well. Sarabandi shows how this antenna measurement can then be used in the calibration process to provide an accurate polarimetric scattering measurement, independent of antenna performance.

The amplitude and phase of the antenna pattern is provided relative to the boresight measurement. This relative measurement of the passive antenna element is assumed to be constant over time. However, the relative amplitude and phase of the radar measurement is of course not constant. The active devices, along with the long IF cable lengths traveling from the antenna front ends to the truck, make the radar a dynamic system, with the amplitude and electrical length of the transmit/receive path varying as a function of time. This problem is made all the more difficult by the four polarization states, each with unique (but not independent) paths. Add to the mix the problem of polarization coupling and the problem becomes quite difficult.

field, parallel to the row structures.

The testing began on May 10, 1993 and ended on July 22, when the test field was measured just after the wheat was harvested. Data was collected on a total of 15 test days, spaced any where from 3 to 7 days apart. The observed canopy was planted in the late fall of the previous year (i.e. winter wheat), where they grew a small amount ($\approx$ 4 to 5 cm) before going dormant as the winter set in. In the spring, as the weather grew warm, the plants emerged from there dormancy and began to grow again. A general description of the wheat growth during the test period, as referenced to the specific test day (date; day of year), is given below:

May 13; 133 Testing begins, the wheat plants are approximately 13 cm in height and are very green and lush. The plant consists of a single vertical stalk of circular cross-section, and protruding along its axis are 4 blade-shaped leaves.

May 28; 148 Plant still green and moist. Stalks are now averaging 43 cm in height. "Booting" begins, wherein the top of the stalk thickens as the grain begins to form inside.

June 4; 155 Grain emerges from stalk. Leaves at bottom of plant begin to turn brown.

June 10; 161 Plant growth ends. Average plant height is approximately 85 cm. Lowest leaf has completely dried.

June 18; 169 Grain begins to show signs of dryness.

June 25; 176 Grain element is "milky" when crushed.

July 7; 188 All leaves are nearly dried. Grain is completely brown; no longer milky but still soft. Stalk showing some dryness but appears green overall.

Parameter	Value	Units
Plant Density	427.4	plants/square meter
Row Density	82.7	plants/row meter
Row Spacing X_{row}	19.4	cm
x-deviation σ_x	1.2	cm

Table 6.2: Canopy Parameters

300 points was then determined, and from the square-root of the variance σ_x was determined. These values are presented in Table 6.2.1.

6.2.2 Soil Surface Data

Two parameters are sufficient to characterize the soil surface under the wheat canopy[16], the first being surface rms height σ_s. If the surface height $h(\rho)$ is modeled as a stationary random process, then σ_s is the square-root of the variance of this process. The statistics of a random process can be estimated from a sample process, and thus the surface height h was measured along a linear trace lying between, and running parallel to, the wheat rows. This was accomplished by use of a laser profilometer, a system using a modulated laser to measure a linear surface profile. This laser is mounted on a level rail approximately 10 cm above the soil surface. The laser is used to measure the vertical distance to the surface, and then a stepper motor precisely moves the laser along the rail a specified increment, where the height measurement is again repeated. The procedure is completely automated, including motor control and data logging. For this experiment, a height measurement was taken every 1 cm over five, 1 meter sections. One of these sample sections is plotted in Figure 6.2.

Parameter	Value	Units
RMS Height	0.31	cm
Bulk Density	1.34	g/cc
Soil Type	Sandy Loam	
Volumetric Moisture		na
5/13	0.089	
5/17	0.075	
5/20	0.090	
5/25	0.113	
5/28	0.095	
6/01	0.114	
6/04	0.093	
6/10	0.229	
6/15	0.134	
6/18	0.115	
6/22	0.236	
6/25	0.162	
6/29	0.223	
7/02	0.194	
7/07	0.145	
7/15	0.156	

Table 6.3: Soil Parameters

latter dried and weighed again to determine M_g^{soil}. If density is expressed in grams per milliliter, then because $\rho_{water} = 1.0$ the volumetric moisture can be expressed as $M_v^{soil} = M_g \rho_{soil}$.

For the scattering model however, the required parameter is not the soil moisture but the soil dielectric. This parameters are certainly related, and Hallikainen et al. [5] has defined this relationship as a function of specific soil type. This model was used to convert soil moisture to dielectric for the sandy loam of the test field. The complete set of soil surface ancillary data is presented in Table 6.2.2.

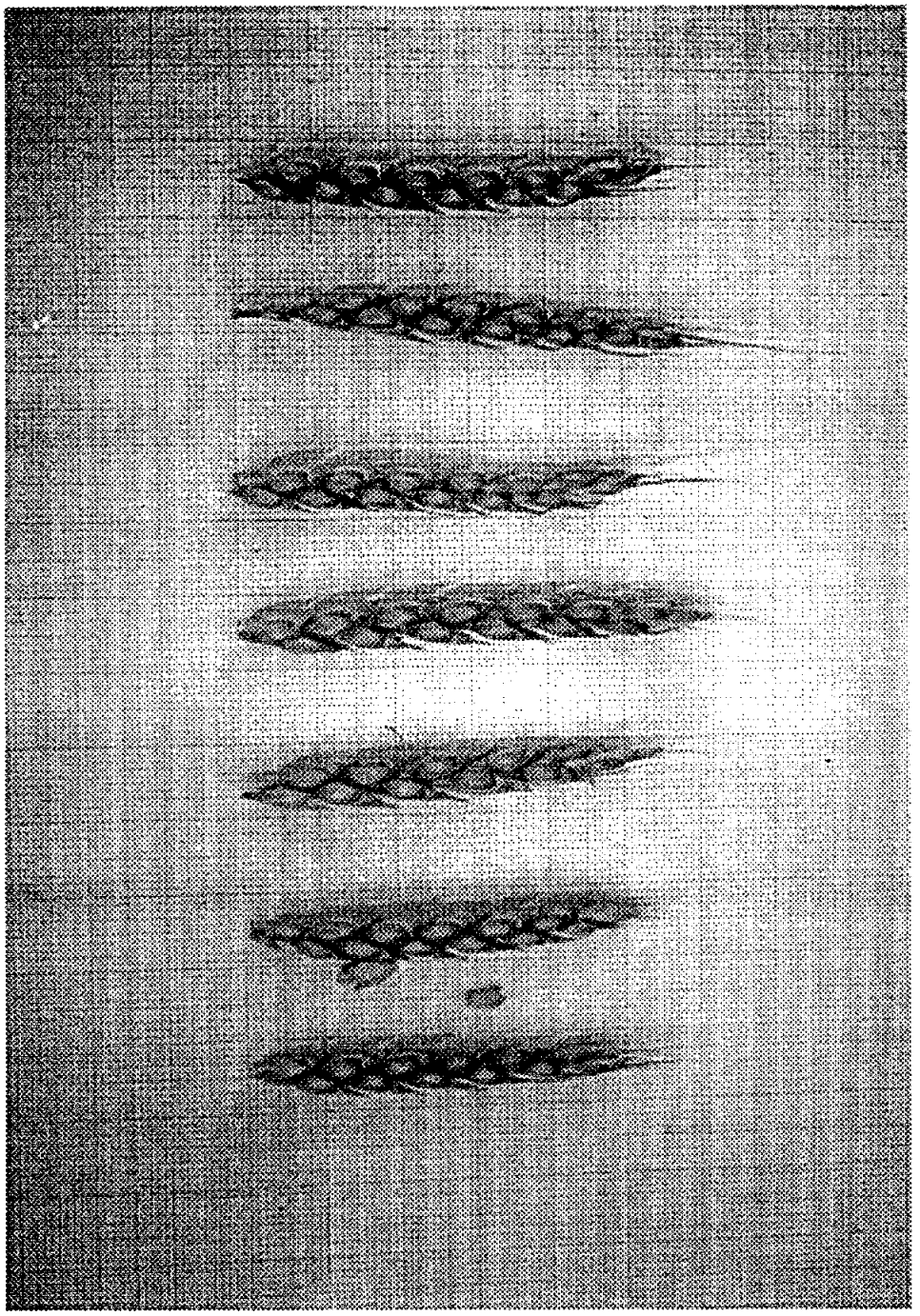

Figure 6.3: A photo wheat grain elements.

6.2.4 Leaf Data

Of the three plant elements, characterizing the wheat leaves were by far the most difficult. The structure of these elements, with a complex cross-section and axial curvature, lead to multiple, difficult measurements. Add to this the fact that there are multiple leaves on a given plant, and thus the distribution statistics of their location must be characterized.

In Chapter III, the scattering from thin cylinders with a blade shape cross-section was considered. The polarizability tensor elements where presented in terms of four shape parameters, aspect ratio a, curvature v, blade angle θ, and cross-section area A. Aspect ratio and cross-section are functions of leaf width w and thickness t. The average value of these parameters were found directly measuring a sample of wheat leaves from the plant canopy. These values were assigned to all wheat leaves, regardless of position. The remaining two parameters, curvature and blade angle, are harder to quantify. The leaves of a wheat plant are basically flat, exhibiting little of the curvature or angle that v and θ define. Thus, these values were estimated by a direct observation to approximate the basic shape of the leaf cross-section; no numerical data or estimate was used to determine these values.

From ChapterV, the parameters c_1, c_2, and ρ_0 where defined to specify the axial curvature of the leaf elements. As stated in that chapter, these random variables are correlated, and thus an entire 3×3 covariance matrix is required to specify curvature. To estimate this covariance, leaves in the wheat canopy were evaluated by measurement of the vector (angle and distance) from the base of a leaf element to three points spaced along this element, as shown in Figure 6.5. These three points were then converted to (ρ_n, z_n) pairs, and the values c_1 and c_2 defining the curvature

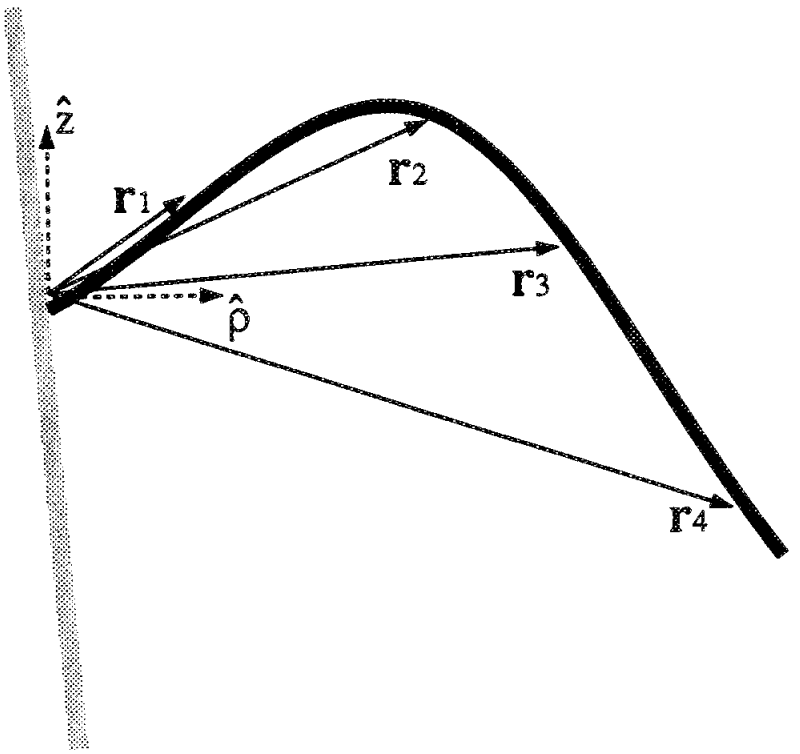

Figure 6.5: Illustration showing four vectors $\bar{r}$ which can be used to estimate curvature parameters c_1 and c_2.

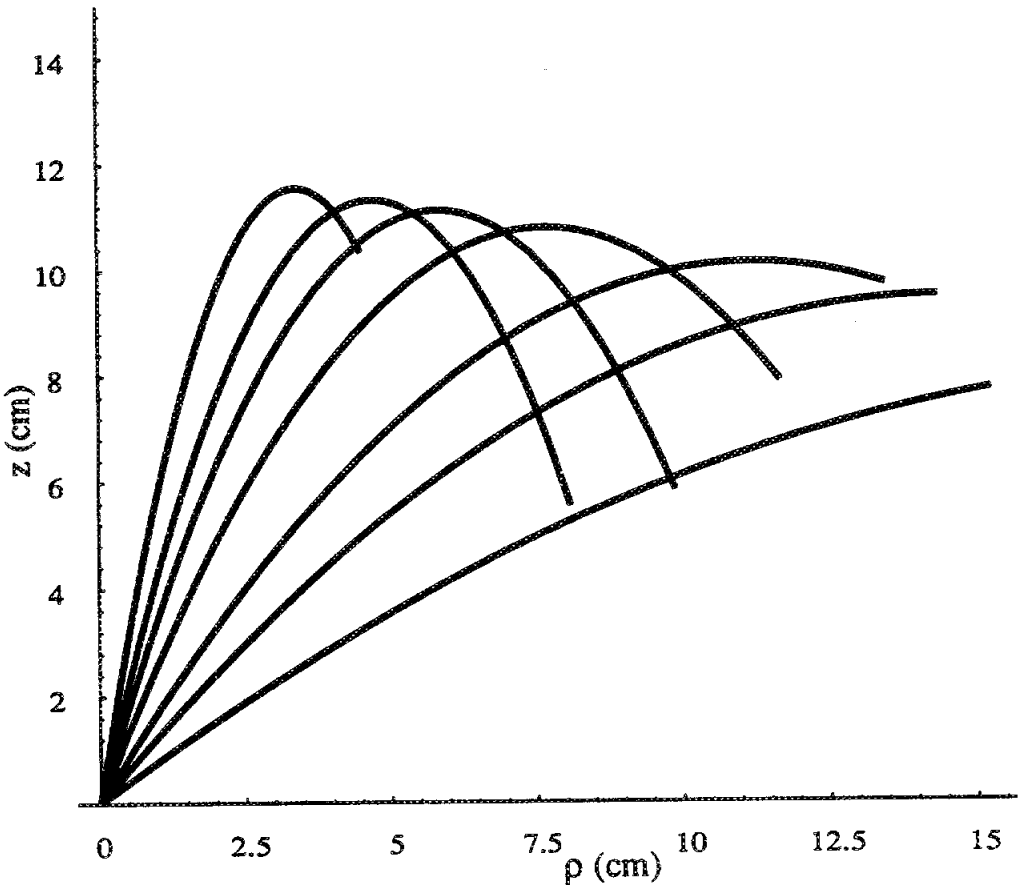

Figure 6.6: A collection of leaf models, each generated by a different value of v_e selected over the 3 σ range of the variable.

these include z_{lc} and Δ_{leaf}, which respectively define the position and size of the leaf layer; the hole-pair distribution parameter δ, which specifies the minimum distance between any two leaves of a wheat plant; and N_{leaf} which specifies the number of leaf elements residing on a given plant. To estimate these parameters, the height above the surface for each leaf on a collection of leaf plants was recorded for each test day. The heights of the lowest and highest leaf on each plant was then used to determine the average highest leaf location $\bar{h}_{high}$ and the average lowest leaf location $\bar{h}_{low}$. The leaf layer size can then be estimated as $\Delta_{leaf} = \bar{h}_{high} - \bar{h}_{low}$, and its location specified as $z_{lc} + d = (\bar{h}_{high} - \bar{h}_{low})$, where the soil surface is located at $z = -d$. The hole-pair value δ is defined as the minimum distance between leaf elements. Therefore, this value is estimated by simply using the minimum observed distance between any two leaves of the test sample. Finally, determining the the number of leaves per plant (N_{leaf}) is straightforward for wheat, as each plant contains 4 leafs (there is a small fifth leaf which is located at the base of the plant, but it quickly dies and thus is ignored). However, as the wheat plant matures, the leaves begin to die, starting from the bottom. When a leaf loses all significant moisture, it is ignored and the leaf count N_{leaf} is reduced (this also alters z_{lc} and Δ_{leaf}).

The final required parameter is again moisture content. Estimating the volumetric moisture content of wheat leaves, however, is accomplished in a manner sightly different than described for the grain. The difficulty arises in finding the density for leaf vegetation. Studies have shown that the dry density ρ_{dry}^{leaf} for vegetation of this type is approximately 0.33 grams/ml, and this value is assumed here[4]. Dry density differs from bulk density in that dry density is the ratio of the dry mass to *dry* volume, i.e. the volume of the leaf after drying. Since the leaf shrinks as it loses moisture, dry density is not equal to bulk density, which uses the wet volume as a basis. Using

6.2.5 Stalk Data

The parameters describing the position and density of the wheat stalks were provided in Section 5.2.1. The remaining stalk parameters deal with the structure and moisture of the stalks, parameters which vary dramatically throughout the experiment. The first parameter considered is stalk height $(z_0 - d)$ and its deviation σ_{z_0}. These were determined by simply measuring the height of a collection of plants each test day.

From equation (5.8), it is evident that two parameters are required to define the diameter of the stalk as a function of height. As stated earlier, the diameter of the stalk remains approximately constant over the length of the stalk until it tapers significantly at the very top. Value dm_0 specifies the diameter at the base of the stalk and dm_{taper} defines the taper. For a given stalk, these values were estimated by measuring the diameter at four points spaced over the stalk length, denoted $dm_{meas}(z_n)$ where $n \in \{1,2,3,4\}$. The values dm_0 and dm_{taper} were then found which minimized the squared error:

$$\sum_{n=1}^{N} \left\{ dm_{meas}(z_n) - dm_0\Big(1 - dm_{taper}[\ell(z)/\ell(z=0)]^4\Big)^2 \right\}^2 \tag{6.3}$$

By completing this procedure for a collection of stalks, the average value of dm_0 and dm_{taper} were determined for a given test day.

The final geometry value required to define the structure of the stalk is a_{stalk}, which defines the tilt in elevation of the stalk (Euler angle $\beta = \tan^{-1}[a_{stalk}]$) Recall the stalk is modeled as a straight element, although in reality the angle of the stalk with respect to the vertical axis $\hat{z}$ changes 3 or 4 times over the length of a stalk. This angle was measured at four stalk location for 20 stalks, and the average angle β_{ave}

was collected as shown in Figure 6.8, with the boom swept in azimuth from an angle of approximately -60 to 60 degrees. To insure independent scattering samples, while still maximizing the data collected in a single sweep, the antenna footprint was moved approximately one spot-size (L-band) radius between measurements, allowing for as many as 100 measurements in an single azimuth sweep. While illuminating a single spot a complete set of frequency and polarization data was collected. To provide additional independent samples, the radius of the boom was altered, and an azimuth sweep was again performed along a different arch. Typically 2 or 3 such sweeps were required to measure the the more than 120 independent spots illuminated for each frequency, polarization, and incidence angle. From these 120 measurement, as well as the calibration, estimates for $\langle|S_{\chi\psi}|^2\rangle$, and therefore backscattering coefficient $\sigma^0_{\chi\psi} = 4\pi\langle|S_{\chi\psi}|^2\rangle/A$ (A is illuminated area), was determined. Estimates for the complex term $\langle S_{hh}S^*_{vv}\rangle$ where not found however, as relative slowness of the network analyzer radar, coupled with the time-varying wheat target (due to the wind), made the coherent measurement between S_{hh} and S_{vv} unreliable.

6.4 L-Band Data

At the conclusion of this experiment, when the data began to be processed and analyzed, it became obvious that the L-band data was exhibiting surprising results. The variation that was being observed as a function of azimuth was dramatic, with significant changes from at least -40 to 40 degrees. An example of this is shown in Figure 6.9, displaying a more than 13 dB change from the peak at 0 degrees azimuth to where it flattens out at approximately 40 degrees. The variation is similar to a $\sin x/x$ pattern, and suggests a coherent effect in the data. Another interesting behavior is

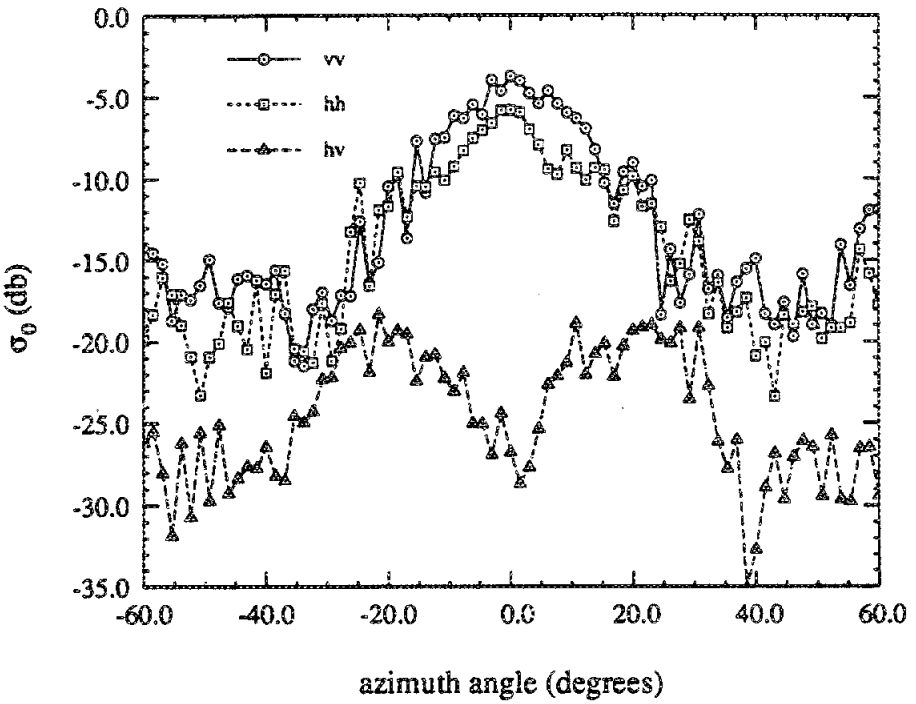

Figure 6.9: Azimuthal response of L-band backscattering, showing a large scattering lobe when the radar propagation direction is perpendicular to row direction.

the fact that the variation is quite dependent on elevation angle. The center "lobe" of the pattern is barely discernible at 70 degrees incidence, increases sharply (as much as 15 dB) to a maximum at 40 degrees, and then falls off slightly at 30 and 20 degrees incidence. This is shown clearly when plotting the backscattering at 0 degrees azimuth as a function of incidence angle, as shown in Figure 6.10. This provides even more evidence as to a coherent effect, as the first Bragg mode for a periodic scatterer of period $X_{row} = 19.4$ at the L-band center frequency is approximately 40 degrees.

At large azimuth angles such as 45 degrees, the scattered data is out of the center lobe and much less dependent on incidence angle. This is demonstrated in Figure 6.11, which shows how the backscattering decreases just a few dB from 30 to 70 degrees

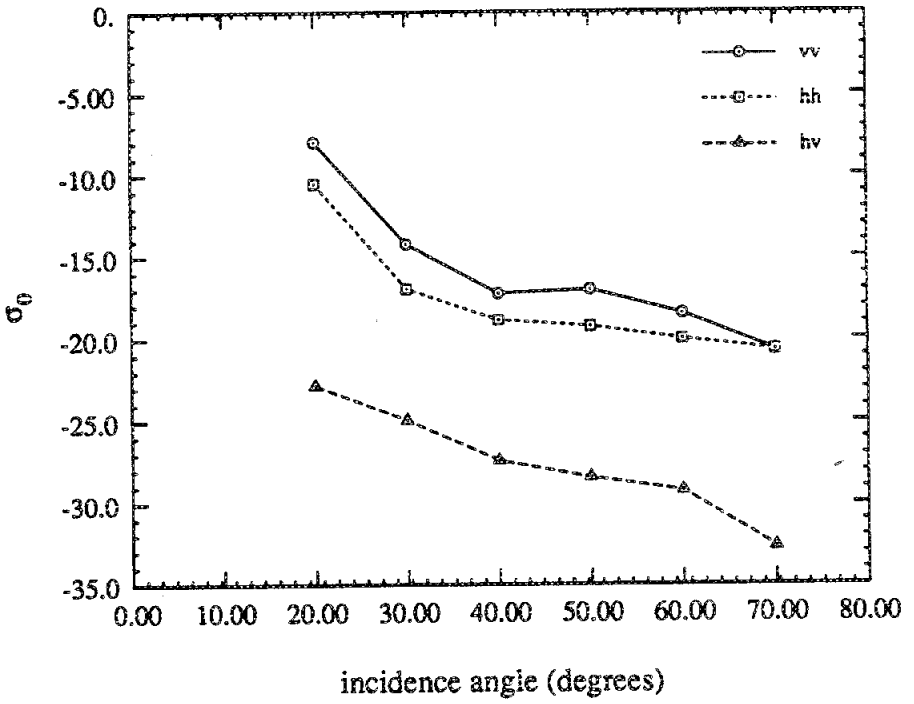

Figure 6.11: Backscattering versus incidence angle at $\phi_i = 45$, with no effect of Bragg scattering in evidence.

incidence, in definite contrast to the data of Figure 6.10. At the peak occurring at 0 degrees azimuth, σ_{vv} is generally larger than σ_{hh} for nearly all test days and incidence angles. The cross-pol value is significantly less than the co-pol coefficients, approaching 25 dB less for data at 40 degrees incidence angle. For data at 45 degrees, the co-polarized coefficients are closer to even, with the cross-pol on the order of 10 dB less

A result of the unexpected sensitivity in azimuth angle was that the number of data sets collected for L-band was less than the ideal quantity. One hundred twenty data points is more than sufficient for estimating a single value of σ^0, but for estimating an arbitrary function of azimuth angle $\sigma^0(\phi)$, multiple sweeps in ϕ are ideal, rather than

(a)

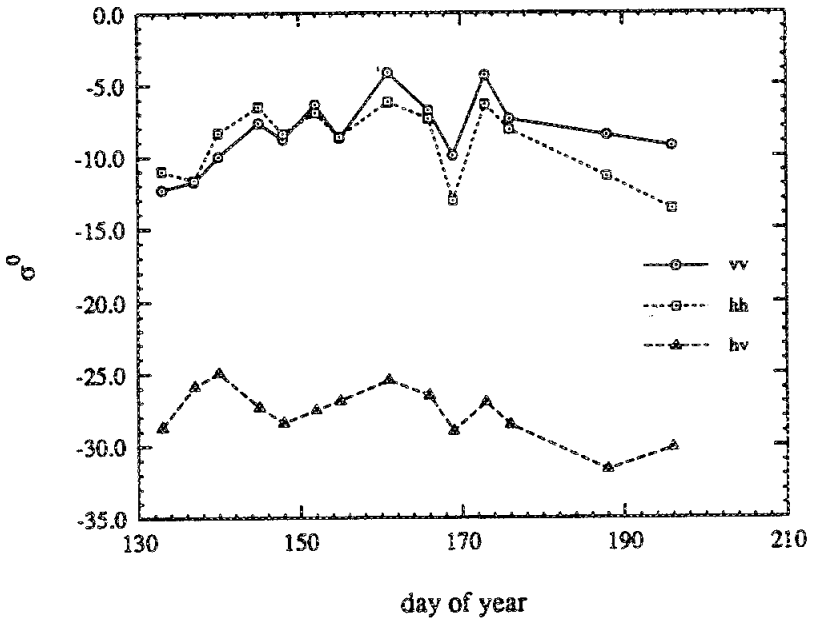

(b)

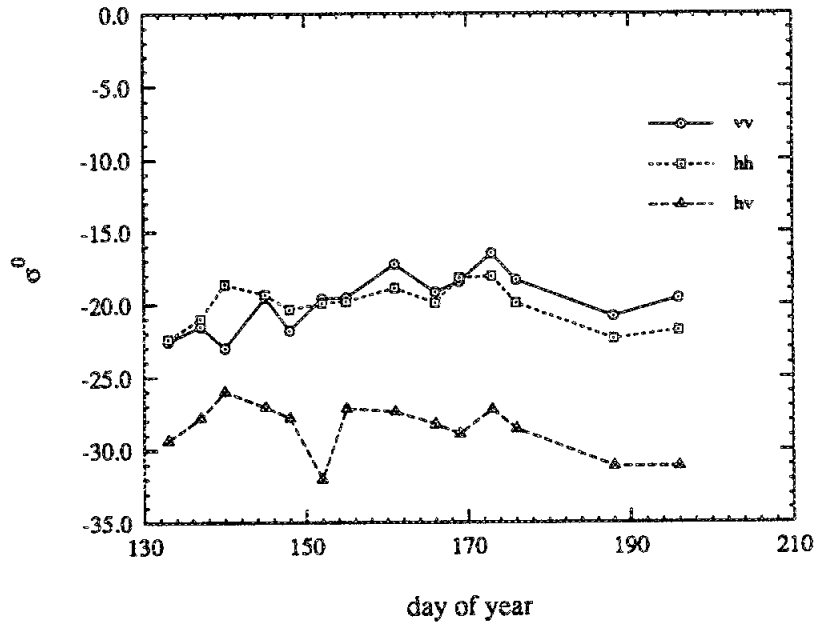

Figure 6.12: L-band data ($\theta_i = 40$) as a function of test day, displaying data at both $\phi_i = 0$ (a) and $\phi_i = 45$ (b) degrees.

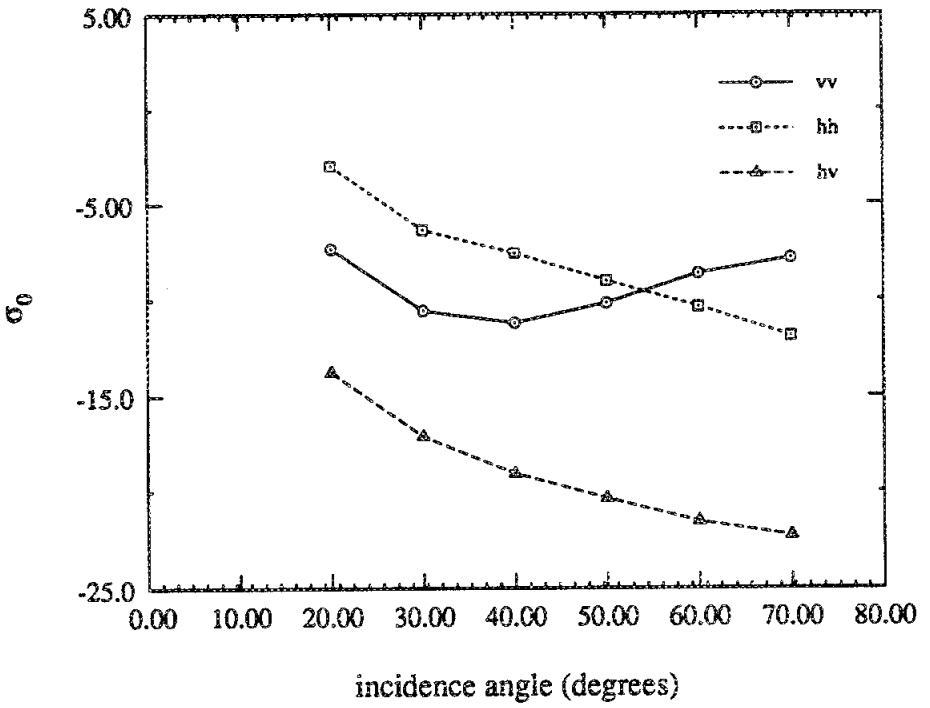

Figure 6.14: C-band data demonstrating the non-standard behavior of σ_{vv}.

greatly increased soil moisture and thus soil dielectric. By observing the scattering data, we note that the horizontal co-polarized backscattering coefficient has increased on the second day for every incidence angle. The vertical coefficient has likewise increased for small incidence angles, but at large angles σ^0_{vv} is nearly identical for both sets of test data. The inference derived from this data is that σ^0_{hh} is significantly effected by scattering mechanisms which involve scattering from the soil surface. Recall there are two such mechanisms, the direct scattering from the soil surface, and the ground bounce terms off the grass vegetation. It cannot be discerned from the data to what extent each of these soil terms contribute. The same is true for σ^0_{vv}, at small incidence angles, which likewise shows significant sensitivity to the change in soil moisture. However, at incidence angles of 40 degrees and above, the lack of sensitivity to soil moisture indicates that the scattering directly from the vegetation dominates in this region. Thus, the distinctive convex curve exhibited by the vertical data appears to be a result of separate scattering mechanisms; a mechanism which involves soil scattering for the decreasing portion of the curve and the direct scattering mechanism for the region increasing with incidence angle.

This interpretation is further enforced if the data is plotted as a function of test day. Figure 6.16 shows this data for 30 and 70 degrees incidence. Comparing this data with Figure 6.17, which displays soil moisture and wet biomass, the sensitivity to soil moisture is apparent for 30 degrees, and at 70 degrees incidence the sensitivity to biomass is equally apparent. This likewise is apparent when viewing the same data in terms of the co-polarized and depolarized ratios, as shown in Figure 6.18.

(a)

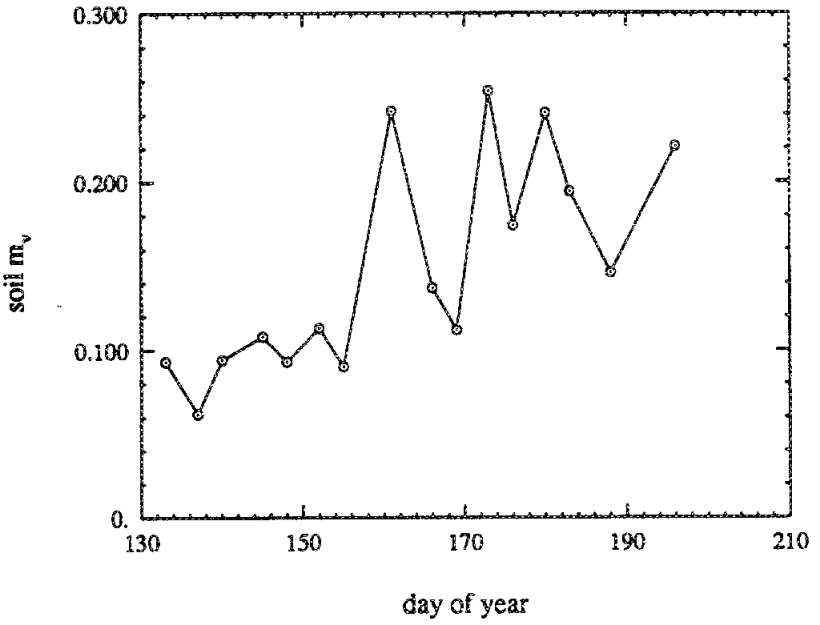

(b)

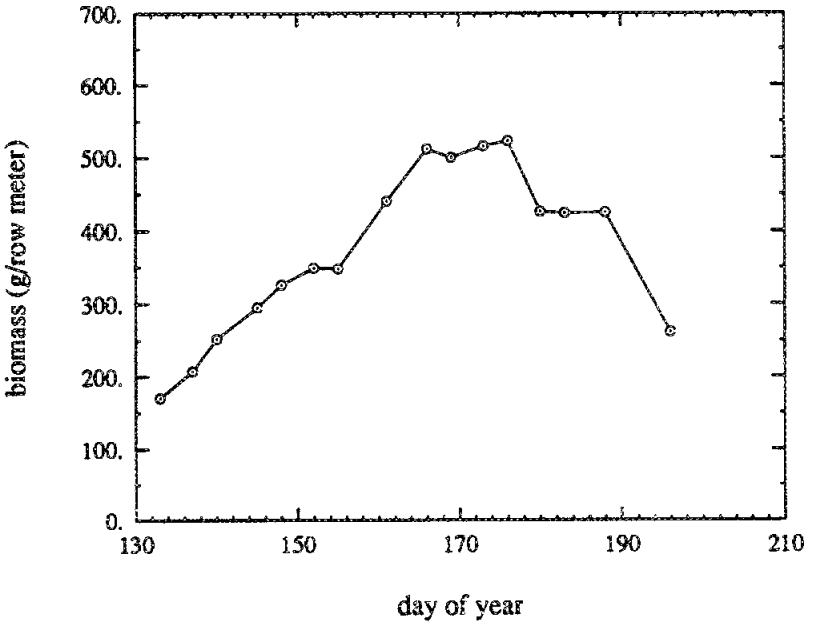

Figure 6.17: Soil moisture M_v (a) and biomass (b) for the test area as a function of test day.

6.5.1 X-Band Data

The description of the X-band data must be divided into two groups, the data prior to the grain head appearing and the data after the event. Prior to the grain arrival, the data is similar to that presented by Figure 6.19. Both co-polarized coefficients are approximately equal and approximately constant as a function of incidence angle, with the cross-pol data approximately 8 to 10 dB smaller. After the grain appears, the contrast in co-polarized data returns, with σ^0_{hh} as much as 5 dB larger. Initially, σ^0_{hh} still exhibits little variation with incidence angle, and σ^0_{vv} increases slightly with incidence angle in a response slightly resembling the C-band data (Figure 6.20). However, as the leaves begin to dry and die, the data begins even more to resemble the C-band data, with the horizontal decreasing and the vertical coefficient increasing significantly (5 to 10 dB) from 30 to 70 degrees incidence.

Plotting this data as a function of test day, the decrease in the co-polarized ratio $\sigma^0_{vv}/\sigma^0_{hh}$ as the wheat growth progresses is apparent, particularly for the smaller incidence angles(Figure 6.21). Again, significant sensitivity to the canopy parameters is detected, with the a given backscattering coefficient changing by as much as 10 dB over the test period. However, similar to the L-band data, is is difficult to make a direct correlation with a single canopy parameter. The exception to this is possibly σ^0_{hh} at low incidence angles, where a clear sensitivity to soil moisture is evident.

6.6 Conclusions

A significant result of this experiment is the behavior of L-band data as a function of azimuth look angle. Although it has long been reported that backscattering changes at specific incidence angles [31, ch. 21], this data is perhaps the first showing this

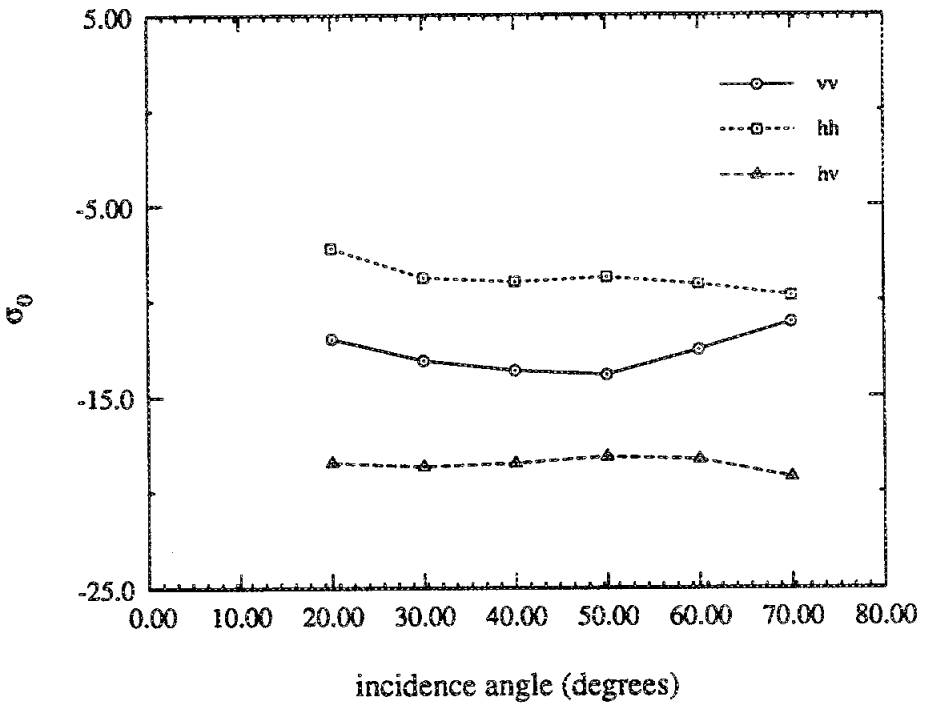

Figure 6.20: X-band backscattering data after the appearance of the grain element.

data as a general function of ϕ_i. The dramatic changes in backscattering with azimuth angle strongly suggests a coherent effect due to the row structure. This raises the question as to weather this phenomenon can be adequately predicted/modeled by the coherent formulation of Chapter V. It also leads to the question if the other coherent effects modeled in that chapter, such as dissimilar element correlation, are likewise significant in this scattering phenomenon.

The non-standard behavior of σ_{vv} in the C-band data has been reported by other researchers [2]. The data taken in this experiment suggests that the rise in backscattering with increasing incidence angle is a phenomenon which is insensitive to soil moisture. This could only be true if the response is due to the direct backscattering from the plants. Conversely, the data suggests that σ_{hh} is sensitive to soil moisture at all incidence angles, which would occur if the ground-bounce terms or the direct scattering from the soil is significant. The constant increase in ratio $\sigma^0_{hh}/\sigma^0_{vv}$ with plant growth is perhaps the most interesting artifact of the X-band data, interesting for its potential use as a potential determinant of plant maturity. The challenge now is to determine weather the model of Chapter V likewise predicts these results, and to infer from the model the specific mechanisms and scattering phenomenon which lead to their occurrence.

meric integration of a complex integrand. Add to these computations the evaluation of the propagation parameters, canopy scattering and programming overhead, and the final model required more than 20,000 lines of FORTRAN code to implement.

A major concern of any software code of this size, particularly one where multi-dimensional numeric integration is required, is computation speed. As stated in the introduction, the utility of this model is a major goal of this study, and the steps to reduce and simplify the computations have been related in the previous chapters. However, it is difficult to provide a general description of the general speed of the program. Using a SUN sparc20 workstation, the computation of a single term can take from a fraction of second to several days, depending on the term, incidence angle, frequency, polarization, and numerical tolerance. Generally speaking however, the terms which take the longest computation time are very small, and thus can be ignored without adversely effecting model accuracy. These terms are most often the inner product terms, where the correlation from dissimilar scattering mechanisms and/or elements are evaluated. Unlike the incoherent scattering terms, these inner product terms are complex, with the real and imaginary portions of the integrand changing in a sinusoidal fashion. If the relative phase of the scattered fields varies over multiples of 2π across the region of integration, then the integrand will exhibit a corresponding number of sinusoidal periods. Numerically integrating several periods of an oscillating function such as a sinusoid is computationally difficult, however, as discussed in Chapter I, a variation of several wavelengths will result in a small value for the integration. The inner product or coherent terms will be significant only in the computationally simple case where the phase changes only marginally in the integration region.

Thus, for efficient computation, the coherent terms were made optional in the

had doubled height, but still consisted of just leaves and stalks. On June 12 the wheat had nearly doubled in height again, and the grain head was now prominent. Finally, on July 7, the structure was identical to that of June 10, but the plant moisture had changed from green, lush condition of early June to the dry, brown condition of mature wheat. It should be stressed that the data provided here is determined from the original ancillary or ground truth data; no effort was made to "tweak" the ground truth to better match the scattering data.

7.2 L-Band Data

The data presented in the previous chapter demonstrated the unique scattering response exhibited by the L-band data as a function of azimuth look angle. The dramatic change in scattering with azimuth angle was attributed to the the coherent effects of the plant canopy, that is the coherent effect of the plants being planted in straight rows. In Chapter V, a formulation was presented which described the scattering from these canopy structures when illuminated by a finite antenna pattern. Thus, a major question of this section is whether this formulation can accurately predict the scattering observed in the experiment. However, the most important question of this section concerns the coherent terms of the plant. As the lowest of the three test frequencies, L-band should exhibit the largest coherent plant scattering terms. The question is whether these terms are significant in comparison to the incoherent power, and whether the model can accurately predict these incoherent terms.

(a)

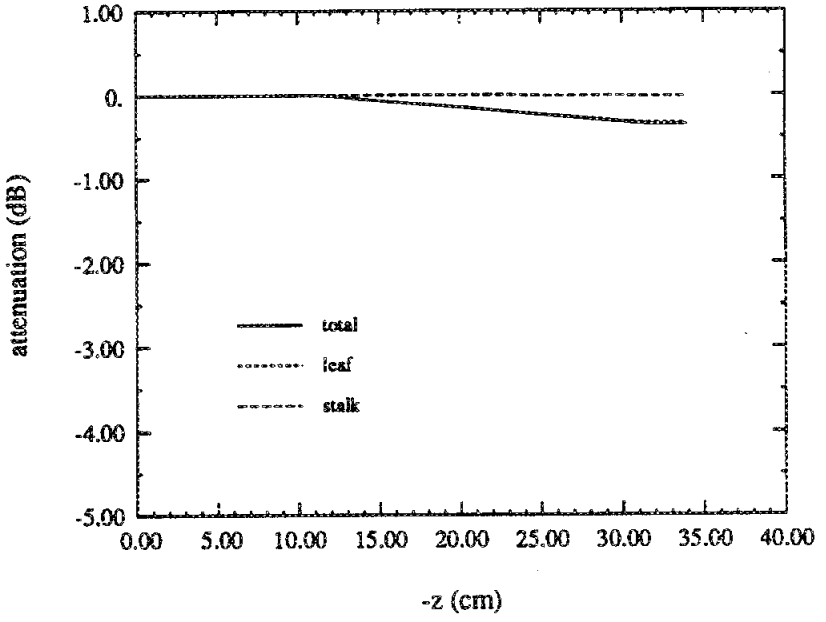

(b)

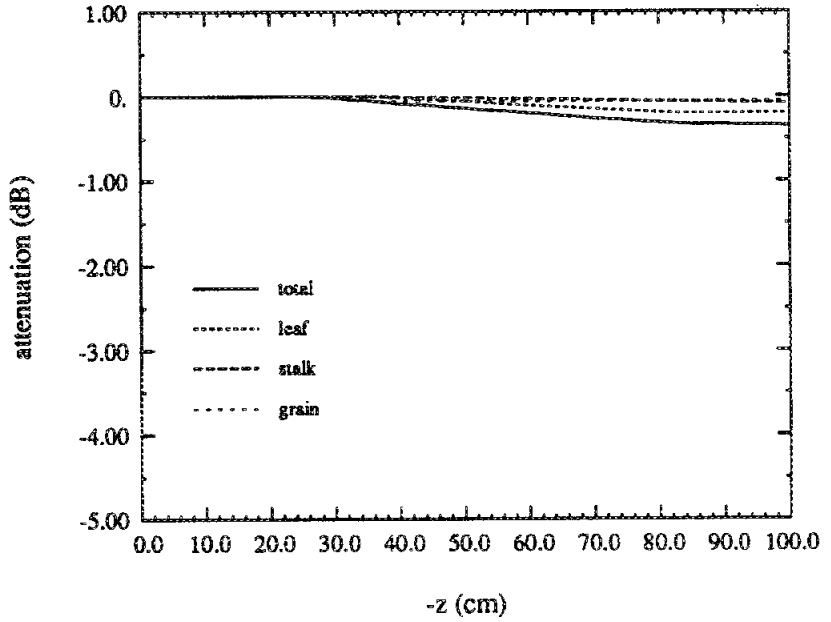

Figure 7.1: The attenuation in a wheat canopy as a function of vertical position z for horizontal polarization at L-band. Figure (a) is for May 17 and (b) for June 10.

(a)

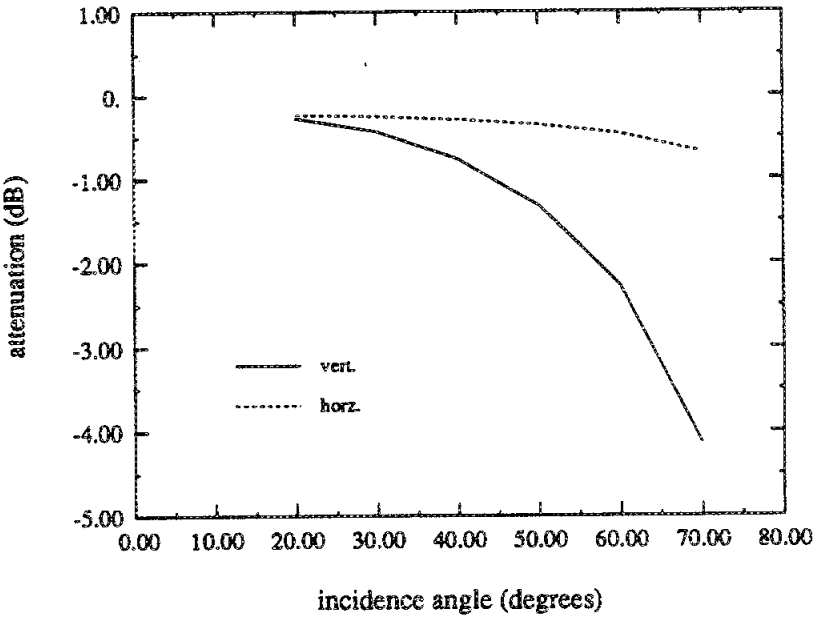

(b)

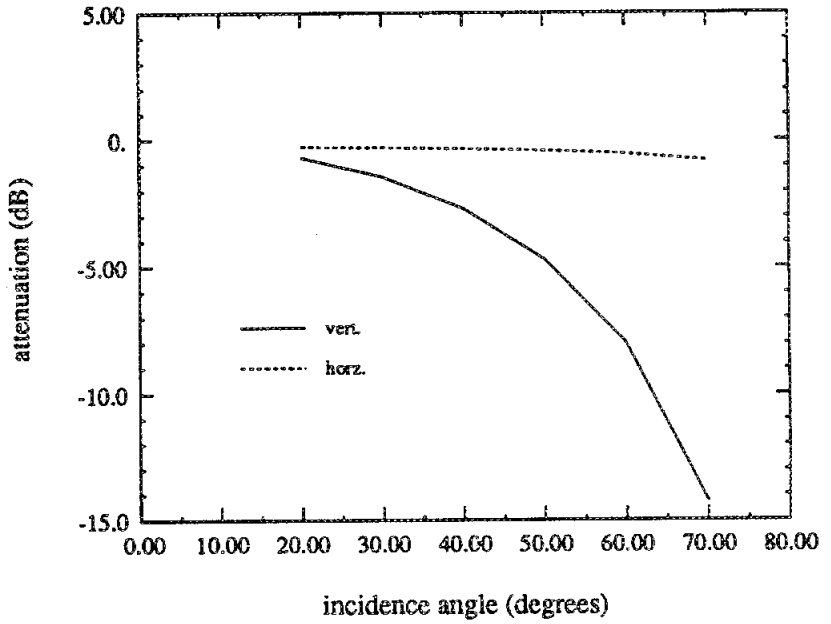

Figure 7.3: The total attenuation at L-band of the coherent wave at the soil surface ($z = -d$), as a function of incidence angle.

This value, however, includes all the inner product or coherent terms resulting from the correlation between dissimilar mechanisms or elements. The difference between this total plant power and the incoherent power is as much as 5 dB. Thus, the coherent scattering terms not only are significant, they actually are in aggregate greater than the incoherent power.

The scattering lobe exhibited by the L-band data centered at azimuth angle $\phi_i = 0$ is wider for the measured data than that predicted by the model. This indicates that the illumination spot-size used by the model is too large, resulting in a narrower scattering lobe. Recall from Chapter V that the illumination pattern of the row scattering formulation is a simple circular model, with uniform illumination within the pattern and no illumination outside the pattern. Of course, the actual scatterometer antenna pattern is a more complex function, and selecting the spot-size for the simple model is an arbitrary decision. The 3 dB beamwidth of the actual antenna pattern was used to determine the spot-size of the simple model, a selection which appears to provide too large a value. Figure 7.6 shows a solution for May 25 where the diameter of the spot size is reduced by half. The result is a widening of the lobe to better match the measured data.

To provide a better data match however, a formulation is required which uses the actual antenna pattern of the scatterometer. This leads to a major difficulty which arises from the coherent effects of the row structure. Specifically, the backscattering coefficient becomes a function of the measuring sensor. If the plants were uniformly distributed over the surface area, then the total scattered power from an illuminated area is proportional to the size of that area. Thus, the measured backscattering coefficient, which is the scattering cross-section of a distributed target normalized to unit area, will be identical for all sensors regardless of illuminated area. This

(a)

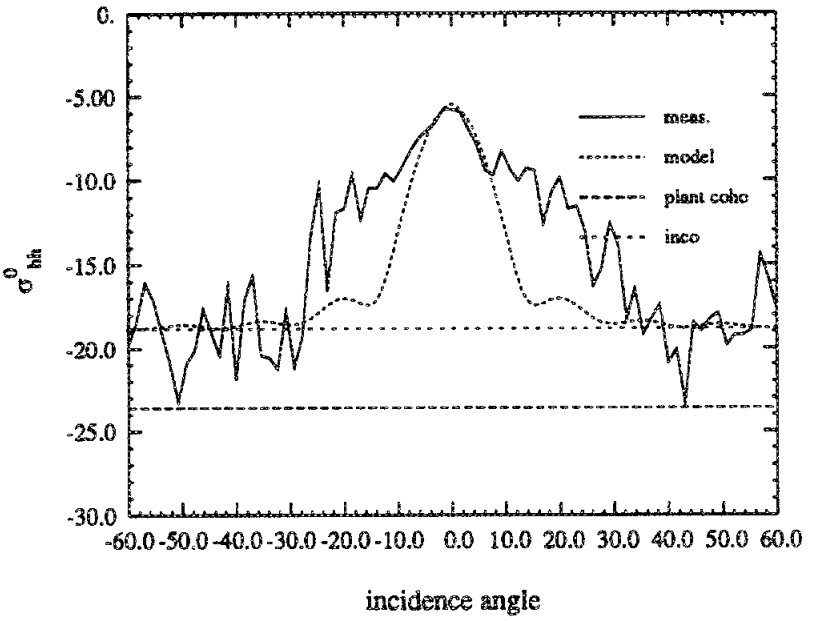

(b)

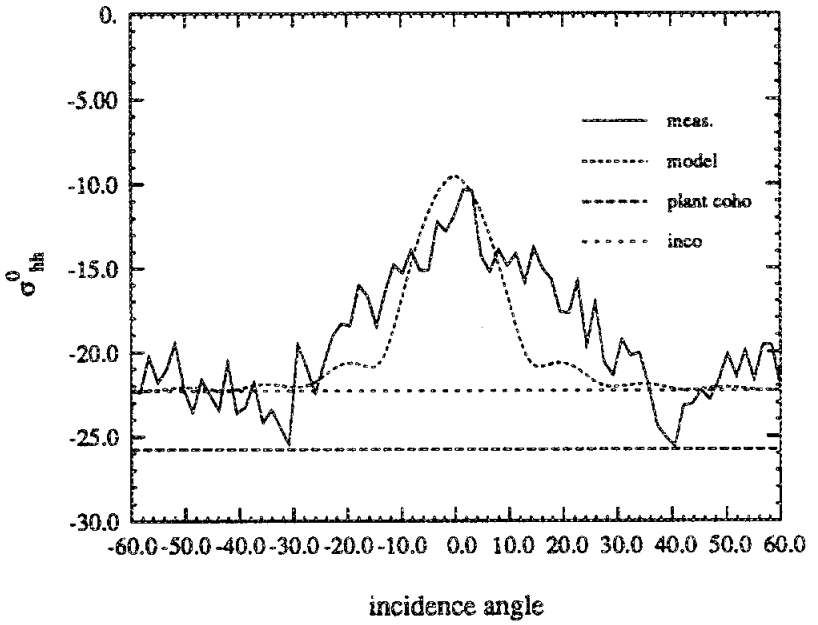

Figure 7.5: The measured and modeled backscattering coefficient σ^0_{hh} as a function of azimuth angle for (a) June 10 and (b) July 7.

of course is a requirement for remotely sensed data to be widely useful. However, for the coherent effect of the row structure, the scattering is not proportional to the illumination area, otherwise the results of Figure 7.4 and 7.6 would be identical. Thus, different sensors will measure different values when the row coherent effect is significant.

Examining the scattering as a function of incidence angle is difficult, as the response changes dramatically with azimuth look angle. Therefore, the response as a function of incidence angle was evaluated at two specific azimuth angles, 0 and 45 degrees. The 45 degree case is shown in Figures 7.7 and 7.8, and with the exception of May 17, shows good agreement with the measured data. These figures likewise show the contribution to the total scattered power for each of the scattering formulations. The lowest plot is again the incoherent power, with the next trace being the power with the correlation between dissimilar scattering mechanisms of single element added in. Note that these terms are a significant addition, increasing the power by as much as 2.5 dB. The next plot provides the total power with the correlation between dissimilar elements included, an addition which can increase the total scattered power by as much as 3 dB. The final trace shows the total scattered power, including coherent effects of the row structure. Note at 45 degrees, the contribution from this phenomenon is relatively small, although it can increase the scattered power another dB.

Figures 7.9 and 7.10 display the scattering as a function of incidence angle when the radar is looking perpendicular to the row structure ($\phi_i = 0$). Both co-polarized responses, hh and vv are presented in these figures. In this case, the coherent effect due to the row structure is the dominant scattering contributor in all but the largest incidence angles. The Bragg scattering effect is evident, peaking at 40 degrees and

(a)

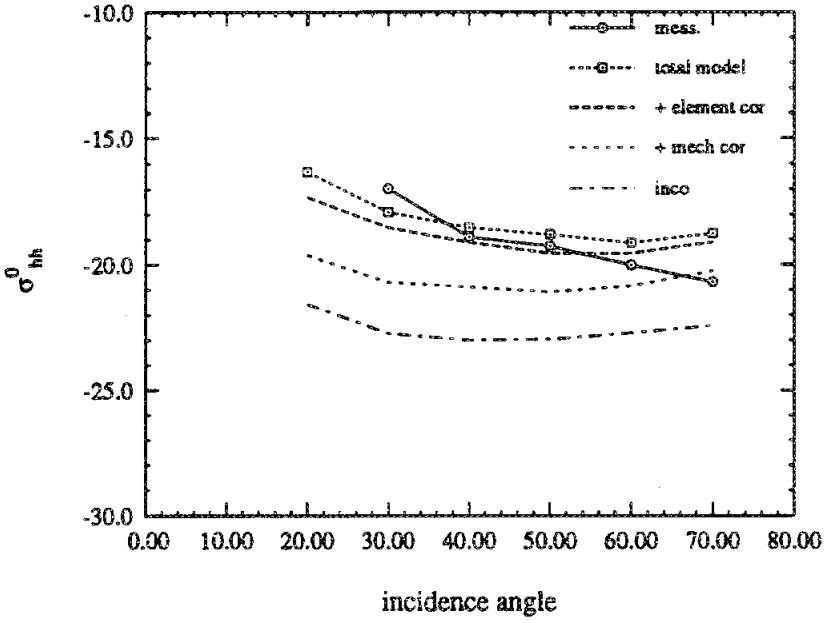

(b)

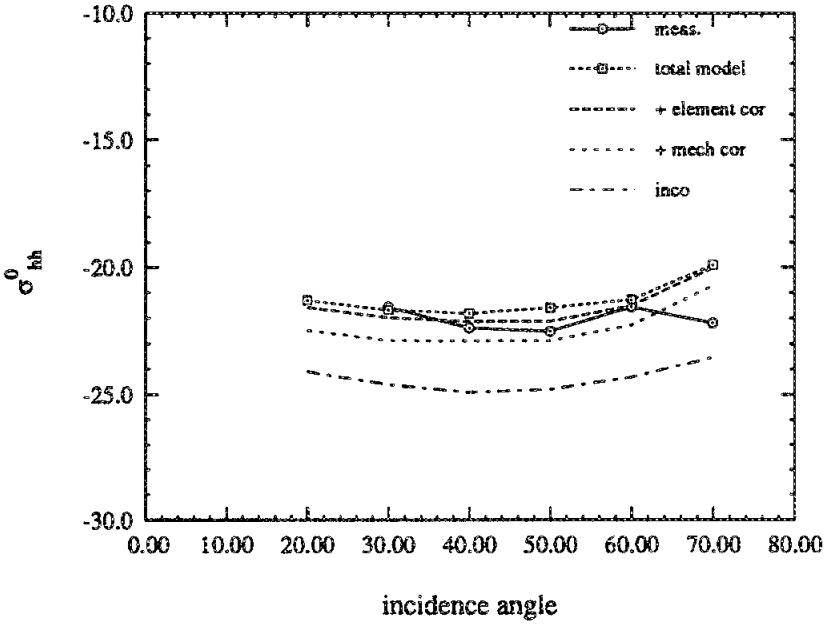

Figure 7.8: The measured and modeled backscattering coefficient σ^0_{hh} at 45 degrees azimuth, plotted as a function of incidence angle for (a) June 10 and (b) July 7.

(a)

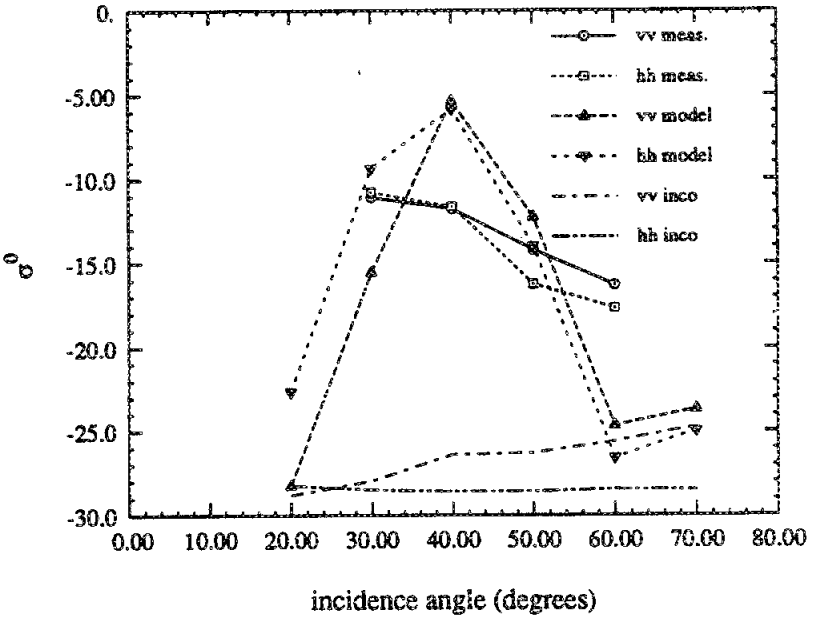

(b)

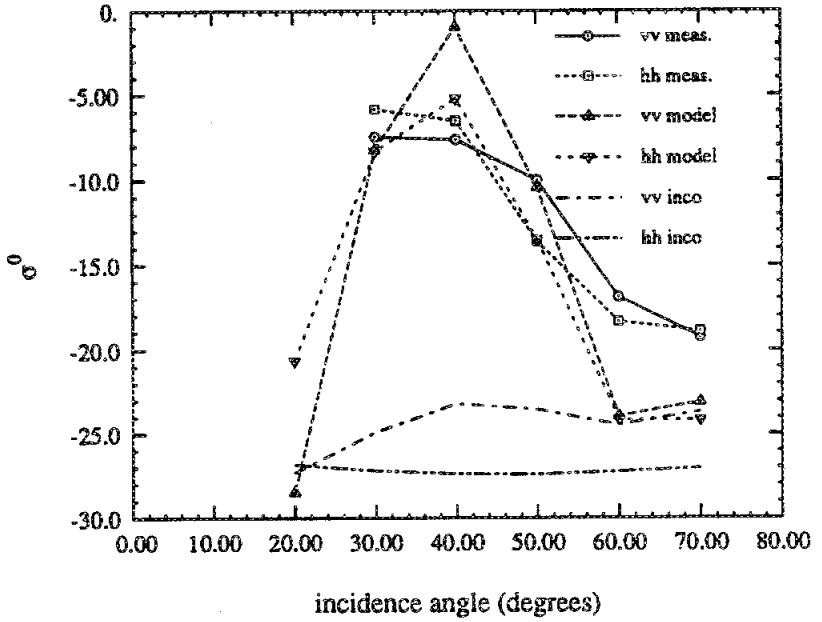

Figure 7.9: The measured and modeled backscattering coefficient at zero degrees azimuth, plotted as a function of incidence angle for (a) May 17 and (b) May 25.

(a)

	direct	ground-plant	plant-ground	ground-plant -ground
direct	-19.56	-31.00	-31.00	-39.43
ground-plant	-31.00	-19.30	-19.30	-34.77
plant-ground	-31.00	-19.30	-19.30	-34.77
ground-plant -ground	-39.43	-34.77	-34.77	-36.53

(b)

	direct	ground-plant	plant-ground	ground-plant -ground
direct	-16.48	-23.96	-23.96	-31.38
ground-plant	-23.96	-11.69	-11.69	-29.17
plant-ground	-23.96	-11.69	-11.69	-29.17
ground-plant -ground	-31.38	-29.17	-29.17	-27.41

Table 7.1: The radar cross-section (hh) of a single plant, listed in terms of the magnitude of the 16 covariance terms associated with the 4 scattering mechanisms. Table (a) corresponds to May 17, while (b) provides the June 10 data.

displays again the importance, if not dominance of the correlation terms between dissimilar elements, as compared to the incoherent power. For the June 10 data, the size of the leaf elements are essentially the same, and thus the scattering involving only the leaf elements are similar to the earlier data. However, the height of the stalk is nearly four times as large, and a grain element has appeared. Thus, the stalk and grain elements are the largest contributors to the plant scattering for this date. The coherent terms are again a major portion of the total scattered energy, although they are less dominant than for the May 17 canopy.

An interesting outcome of this analysis is that the model never predicts a significant contribution by the rough soil surface, even for small incidence angle and low-loss canopies. This is a very different result than many interpretations of grassland data [29]. Of course, it is very difficult to make a general pronouncement, as the soil observed in this experiment was relatively smooth and generally dry during the test period, and the grass vegetation was comparatively dense. However, the extremely small contribution of the soil surface scattering predicted from this data appears to be a departure from many other interpretations.

7.2.3 VV Polarization

The scattering power for the vv polarization pair ($\langle|S_{vv}|^2\rangle$) exhibits the same type of row coherent effect that was displayed for the horizontal co-polarized data. Figures 7.11 and 7.12 again display the scattering as a function of azimuth angle for an incidence angle of 40 degrees. The error for this polarization can likewise be reduced if the selected spot-size is made smaller, as shown in Figure 7.13. As before, the difference between the coherent effect of the row structure and the incoherent scattering power is great at azimuth angles near $\phi_i = 0$. However, the error of the

(a)

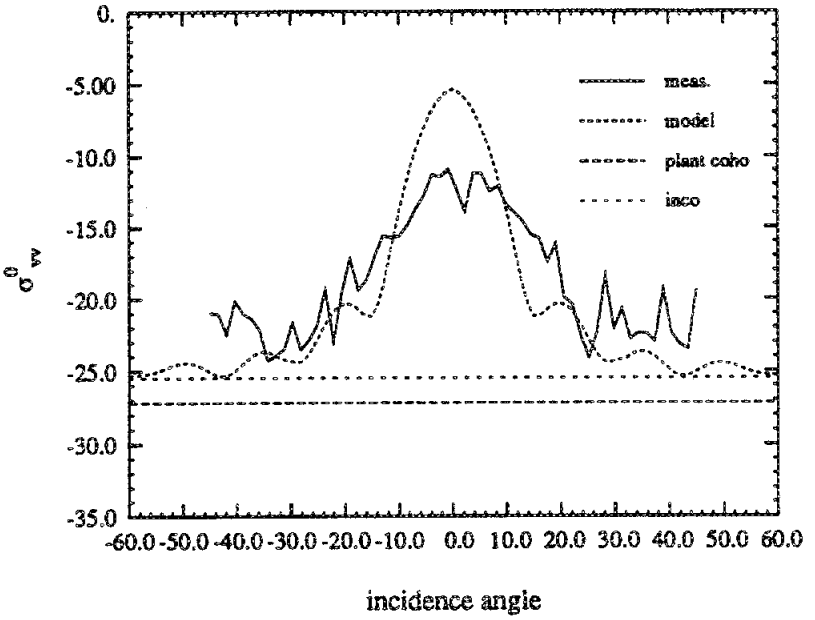

(b)

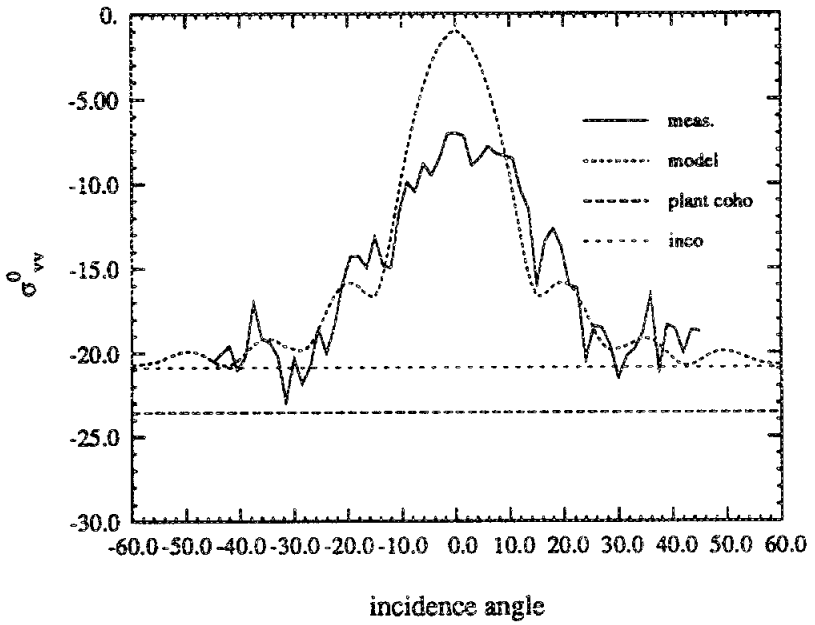

Figure 7.11: The measured and modeled backscattering coefficient σ^0_{vv} as a function of azimuth angle for (a) May17 and (b) May 25.

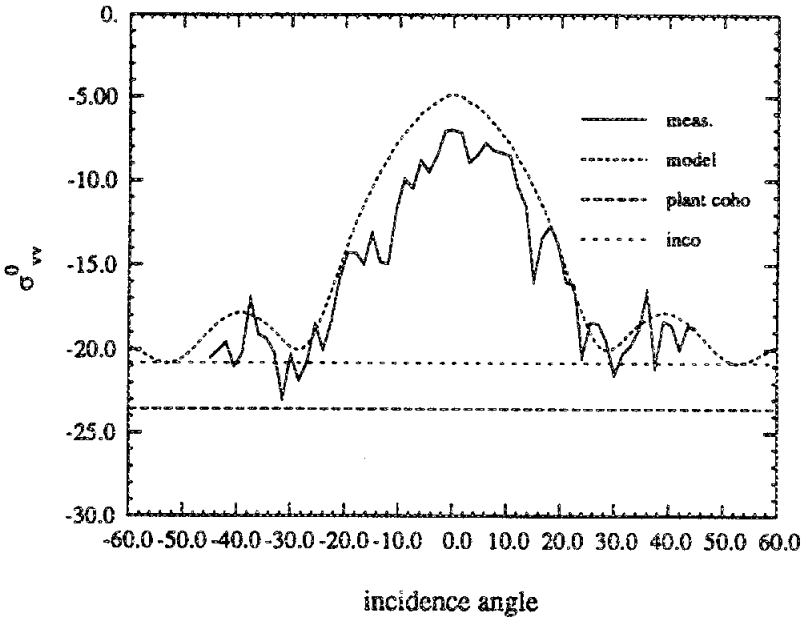

Figure 7.13: The measured and modeled backscattering coefficient σ^0_{vv} as a function of azimuth angle for May 25, as evaluated with a reduced illumination spot-size.

	May 17	June 10
total	-11.79	-2.35
leaf inco	-18.36	-21.21
leaf coho	-40.30	-37.29
stalk inco	-15.98	-6.83
stalk coho	-19.93	-7.11
grain inco		-10.32
grain coho		-17.86
stalk/leaf	-20.90	-14.5
grain/stalk		-12.23
leaf/leaf	-36.83	-30.3

Table 7.3: The rcs (vv) of a single plant, listed in terms of the magnitude of the various coherent and incoherent scattering terms.

(a)

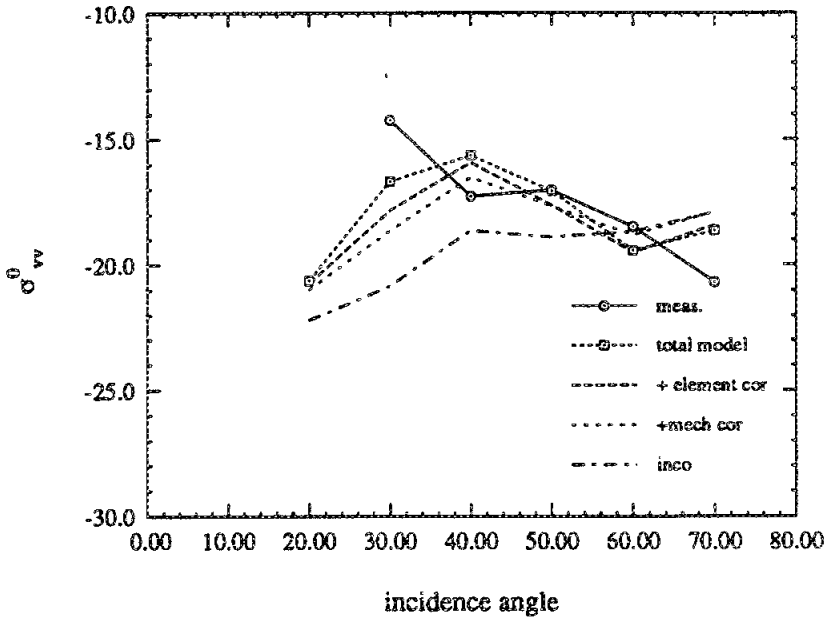

(b)

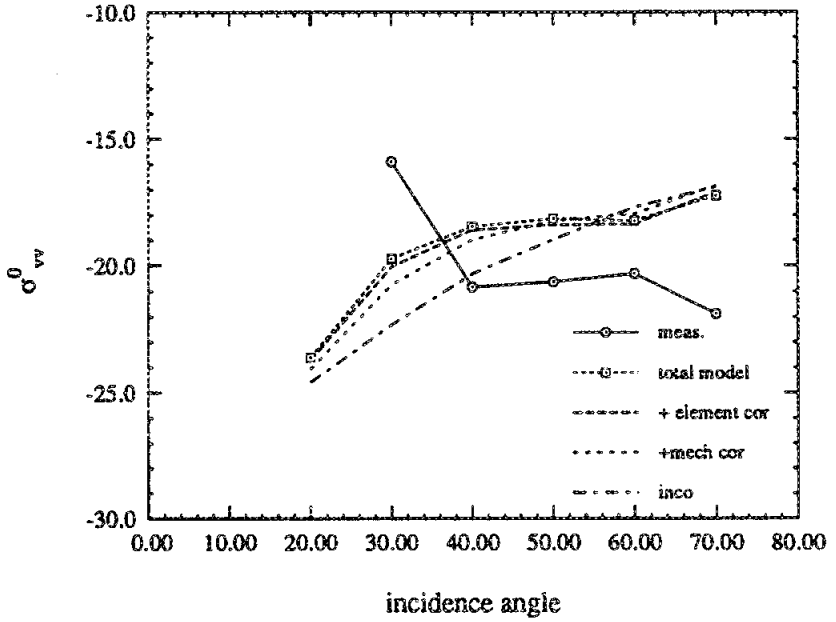

Figure 7.15: The measured and modeled backscattering coefficient σ^0_{vv} at 45 degrees azimuth, plotted as a function of incidence angle for (a) June 10 and (b) July 7.

(a)

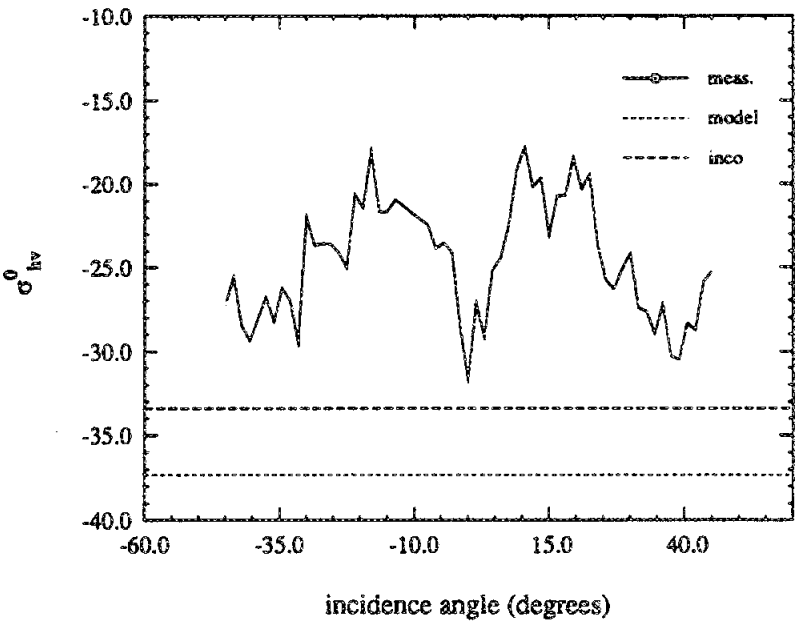

(b)

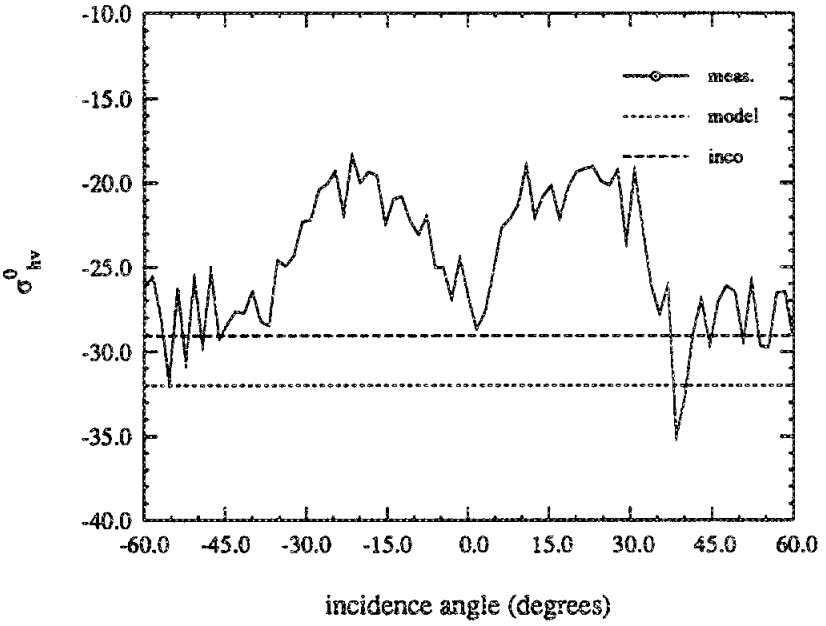

Figure 7.16: The measured and modeled backscattering coefficient σ^0_{hv} as a function of azimuth angle for (a) May 25 and (b) June10.

(a)

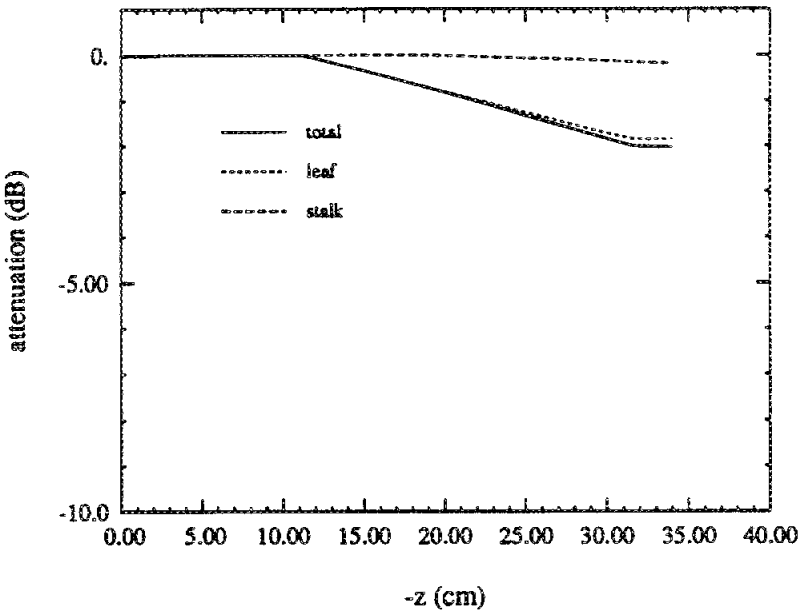

(b)

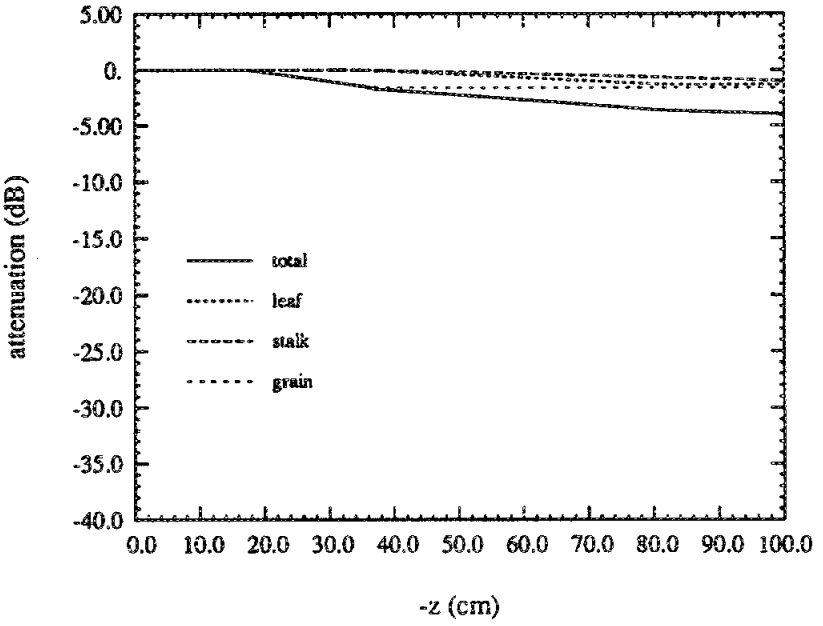

Figure 7.17: The attenuation in a wheat canopy as a function of vertical position z for horizontal polarization at C-band. Figure (a) is for May 17 and (b) for June 10.

(a)

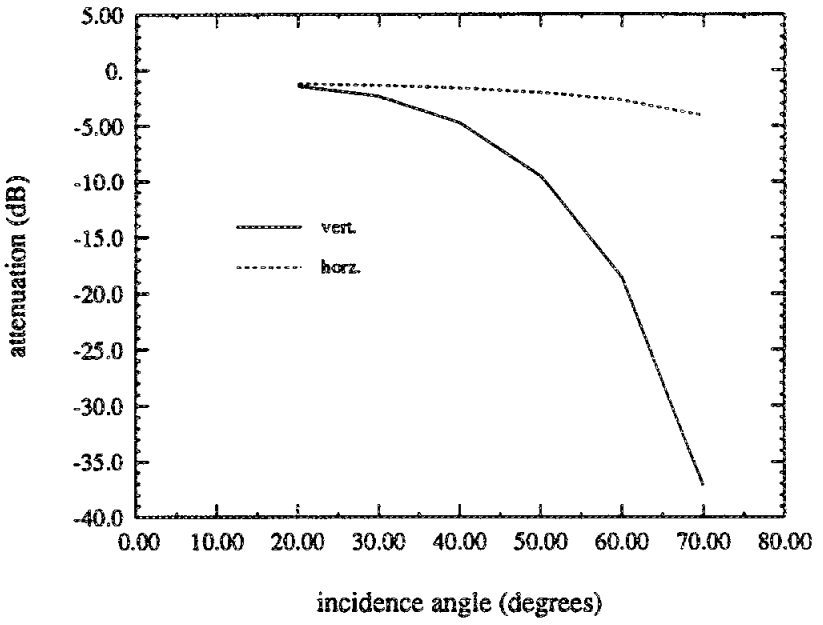

(b)

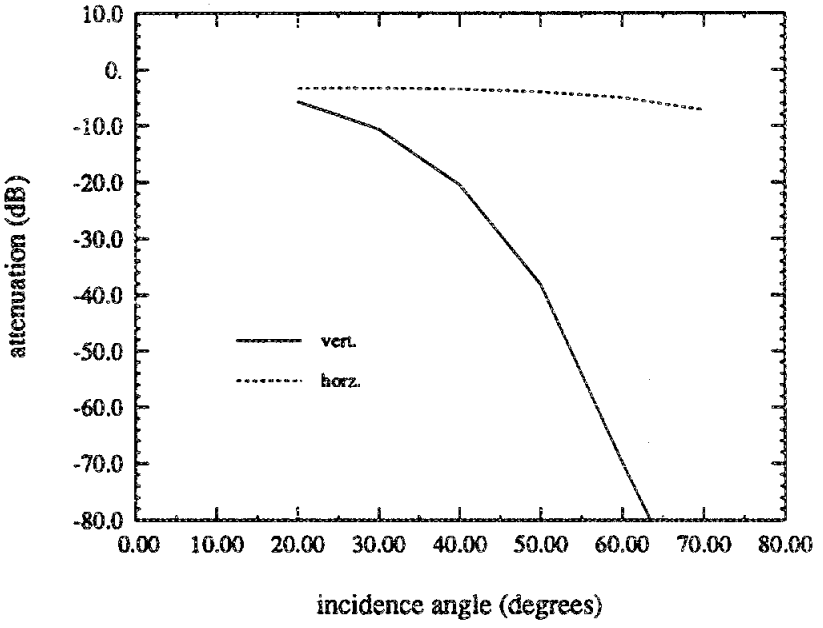

Figure 7.19: The total attenuation at C-band of the coherent wave at the soil surface ($z = -d$), as a function of incidence angle.

(a)

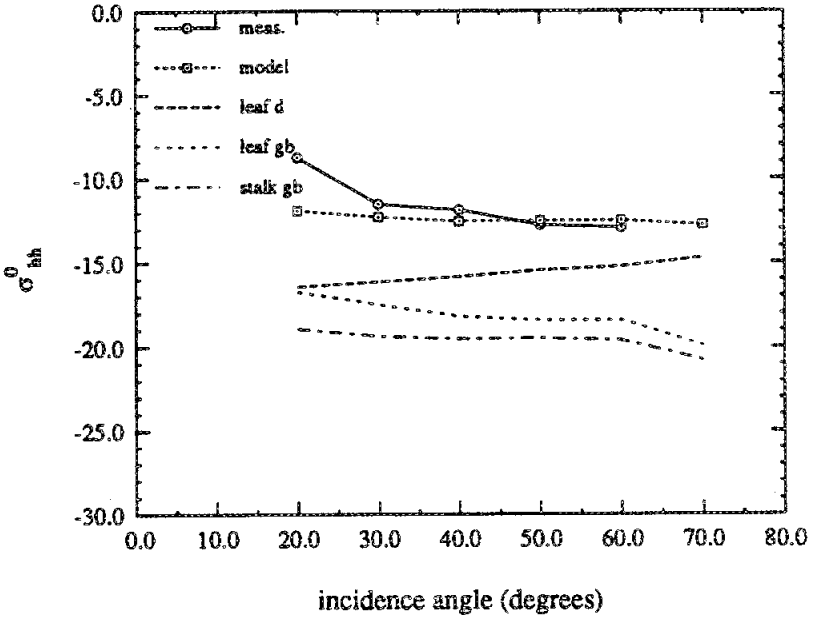

(b)

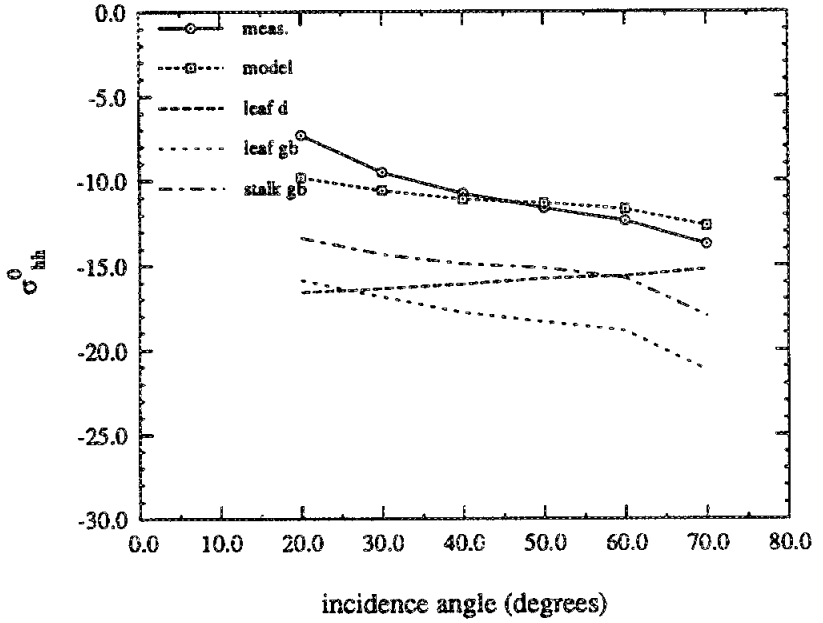

Figure 7.20: The measured and modeled backscattering coefficient σ^0_{hh} at C-band, plotted as a function of incidence angle for (a) May17 and (b) May 25.

extinction, which seems to be underestimated by the model. For the June 10 case, the extinction due to the leaves causes the ground-bounce mechanisms to decrease with incidence angle, as the increasing propagation path length attenuates the scattered energy. However, for the July 7 test day, the leaves are dead, and thus the grain ground-bounce mechanism is not sufficiently attenuated with increasing incidence angle, and the response stays erroneously flat with incidence angle.

The results of the model for *hh* polarization likewise confirm the general results observed in the measured data. The measurements suggested that the scattering is sensitive to soil moisture for all incidence angles. The dominance of the ground-bounce term for this polarization confirms this, as the ground-bounce scattering is directly proportional to the reflection coefficient of the soil surface. However, this value is likewise dependent on the size of the wheat vegetation, so that the scattering is essentially a reflection of both biomass and soil moisture.

Finally, recall that both the cross-section shape, as well as leaf curvature, are considered in the leaf scattering model. The model data of May 17 provides an excellent opportunity to test the importance of this added fidelity. The model data not only matches the measured data well for this date, but also shows that the leaf scattering is the major contributor to the response. Therefore, the data was again computed with leaves of the same cross-sectional area, average length, and angular distribution as before, however this time the cross-section was assumed to be circular, and the leaves to be straight. The results are provided in Figure 7.22, and graphically demonstrate the tremendous difference between the two cases. For the straight, circular model, the direct leaf scattering drops by as much as 25 dB, with the leaf ground-bounce term likewise reduced approximately 5 dB. Conversely, the stalk ground-bounce has increased 2 to 3 dB, and has thus been moved from the least significant scattering

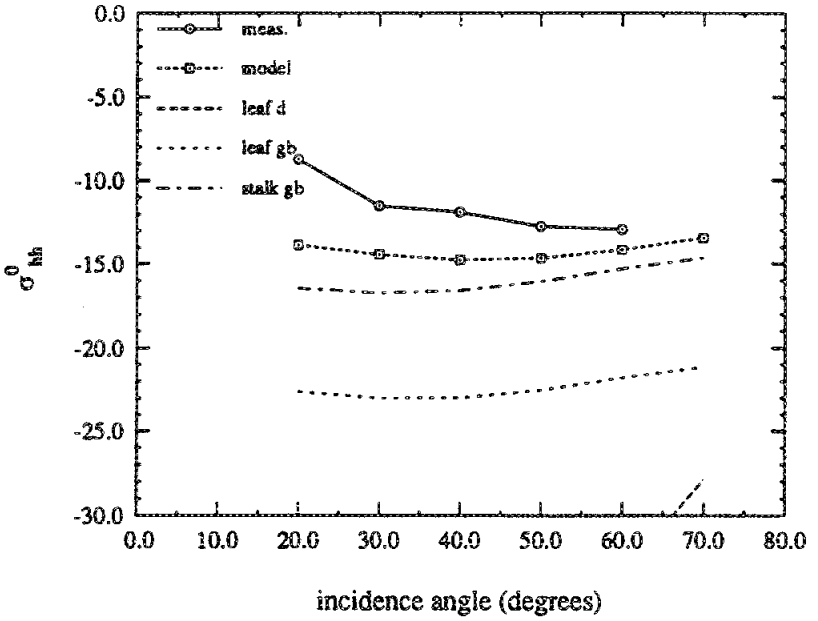

Figure 7.22: The measured and modeled backscattering coefficient σ^0_{hh} at C-band, evaluated with straight leaves of circular cross-section.

diminishes. For moderate incidence angles therefore, the scattering is attributed only to the direct leaf scattering. Then, as the incidence angle increases, the vertical polarization of the incident wave begins to couple more and more into the vertical wheat stalks, and the direct scattering from the stalk element begins to rise dramatically as the incidence angle approaches 60 and 70 degrees.

The importance of correctly modeling the non-uniform illumination of the stalk element is revealed in this data. If the amplitude of the incident wave on the stalk element was determined by its value at the stalk reference (center), then the extreme attenuation of the vegetation layer would result in little predicted direct scattering from the stalk. With the scattering model that correctly applies the intensity of the incident wave at each point along the stalk element, the model evaluates the scattering from the upper portion of the stalk element which is still significantly illuminated by

(a)

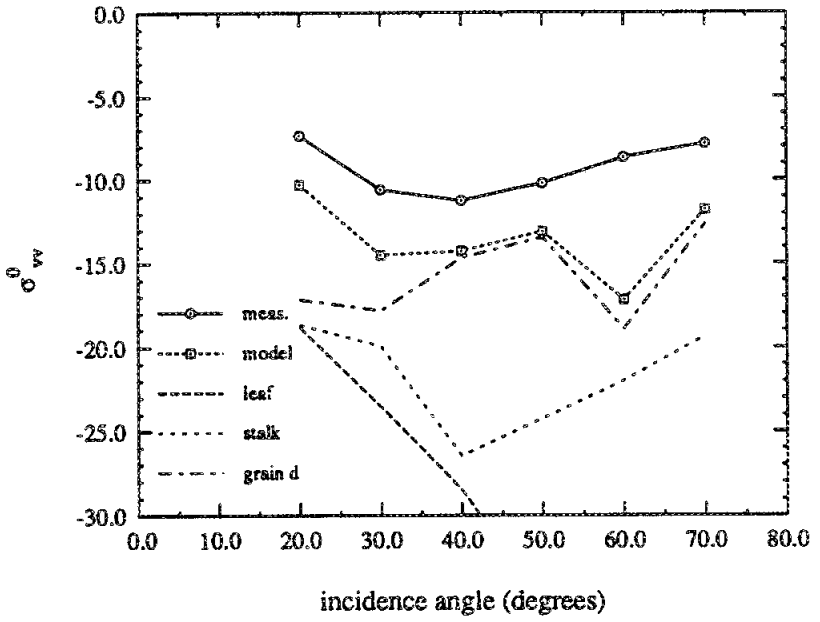

(b)

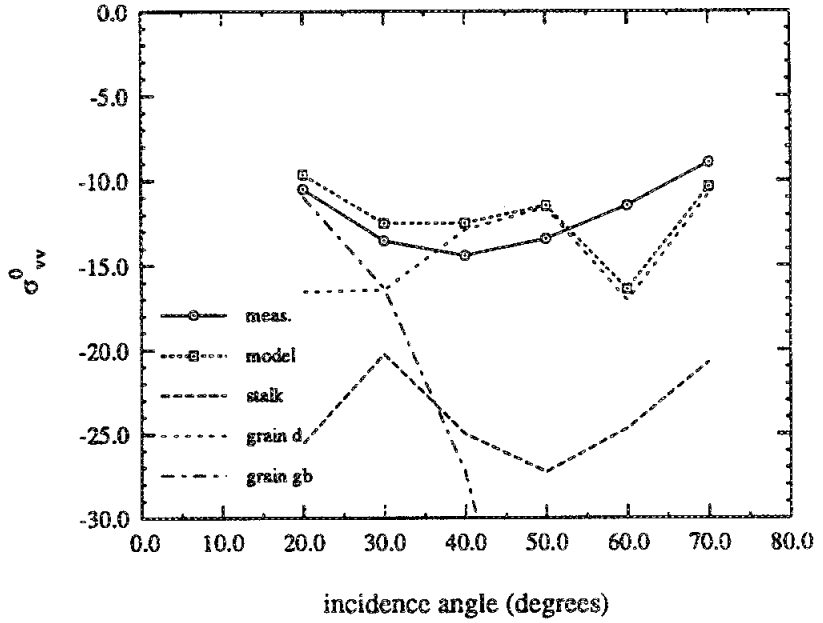

Figure 7.24: The measured and modeled backscattering coefficient σ^0_{vv} at C-band, plotted as a function of incidence angle for (a) June 10 and (b) July 7.

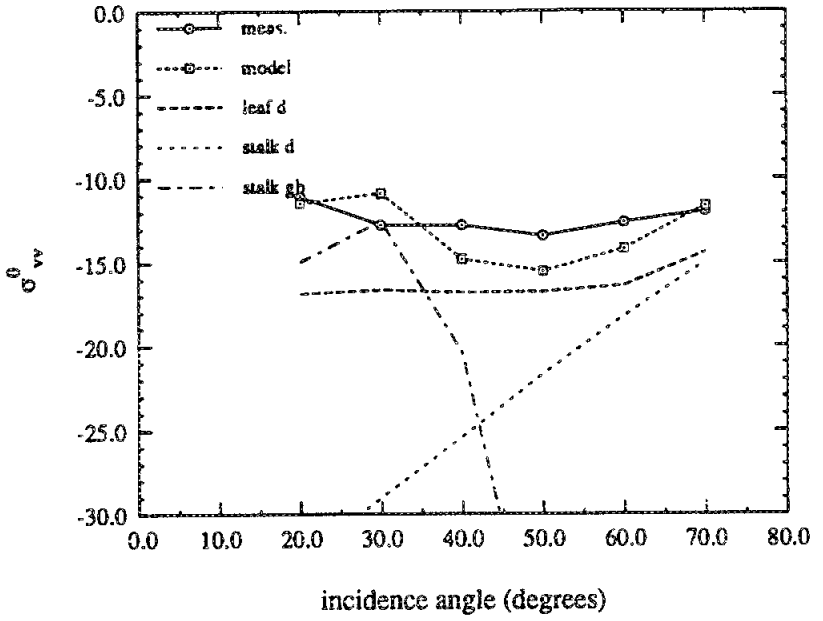

Figure 7.25: The measured and modeled backscattering coefficient σ^0_{vv} at C-band, evaluated when the leaf layer of May 25 is raised by 7 cm.

by observing where the leaf attaches to the stalk, although the leaf can extend above this value by several centimeters. In a high extinction environment, this seemingly insignificant ambiguity can make a significant difference. In Figure 7.25, the results are again presented for the data of May 25, this time with the leaf layer location increased by 7 cm. This increase, which essentially defines the leaf layer by the top of the leaf elements, significantly increases the direct leaf scattering while reducing the direct scattering from the stalk.

For the later test days where the grain head is evident, the general scattering response is well matched for most incidence angles, although the numeric error is large for the June 10 test day. The model shows that at small incidence angles, the scattering is due to three mechanisms, the ground-bounce terms of both the stalk and the grain head, and the direct scattering from the grain. The leaf scattering is not a

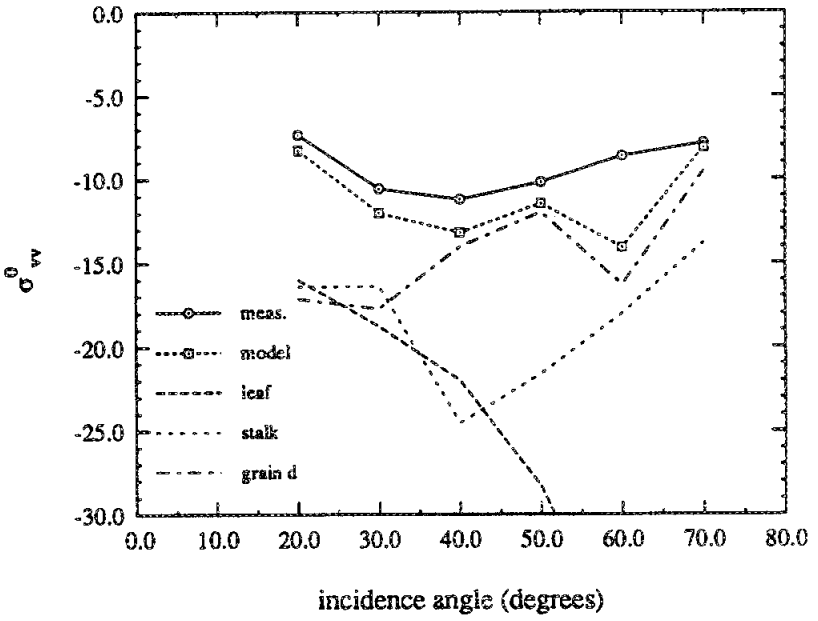

Figure 7.26: The measured and modeled backscattering coefficient σ^0_{vv} at C-band, evaluated for June 10 data with a lower shadow boundary.

To demonstrate the importance of correctly calculating the extinction, the shadow boundary, which defines the vertical boundary the where the extinction from a given row begins to effect an adjacent row (Figure 5.8), is changed from a value of $X_{row} \tan \theta_i/2$ to $X_{row} \tan \theta_i$. It could be argued that this is a more accurate approximation for the high extinction cases, and the resulting model data does indeed produce a better match to the measurements, as shown in Figure 7.26.

Finally, it should be noted that the model confirms the measured data presented by Figure 6.15. This data suggested that the scattering at C-band is sensitive to soil moisture at all incidence angles for σ^0_{hh}, but sensitive only at incidence angles of 20 and 30 degrees. As discussed earlier, the model confirmed the σ^0_{hh} behavior, and this section has likewise demonstrated this for the vertically polarized case. The model showed that the ground-bounce scattering mechanism is significant only at 20 and 30

(a)

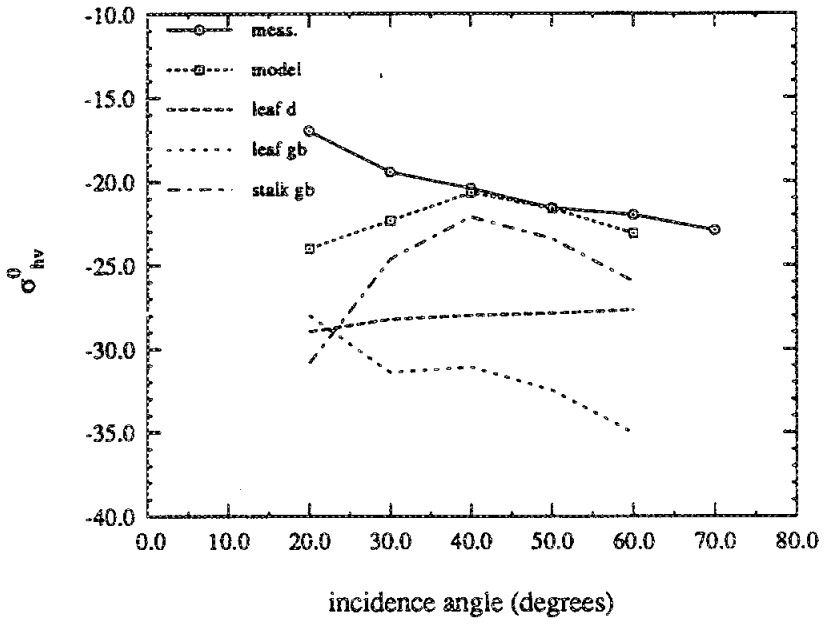

(b)

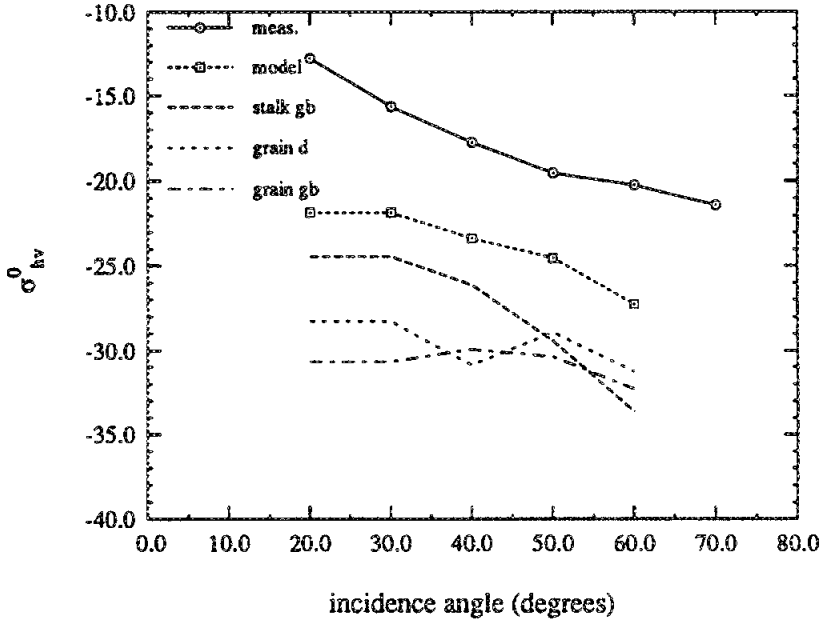

Figure 7.27: The measured and modeled backscattering coefficient σ^0_{hv} at C-band, plotted as a function of incidence angle for (a) May 25 and (b) June 10.

(a)

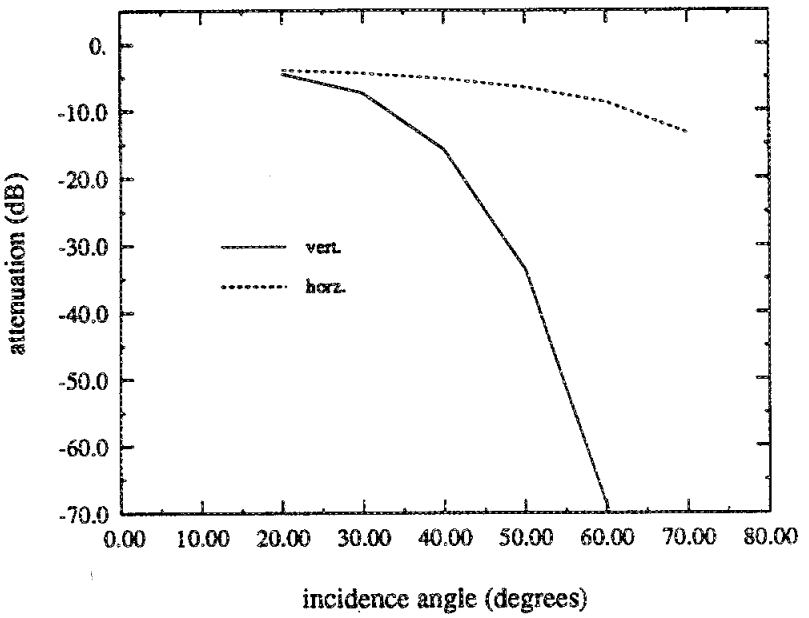

(b)

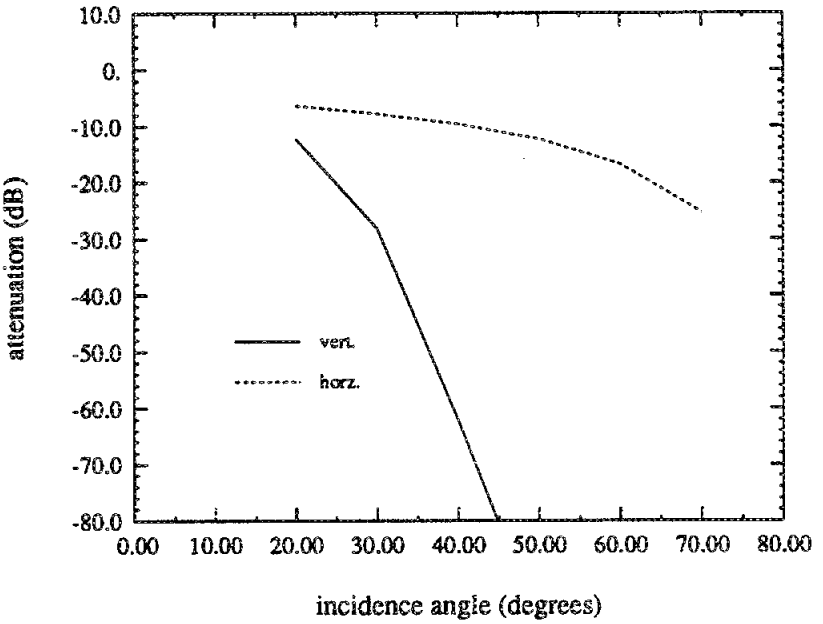

Figure 7.28: The total attenuation at X-band of the coherent wave at the soil surface ($z = -d$), as a function of incidence angle.

(a)

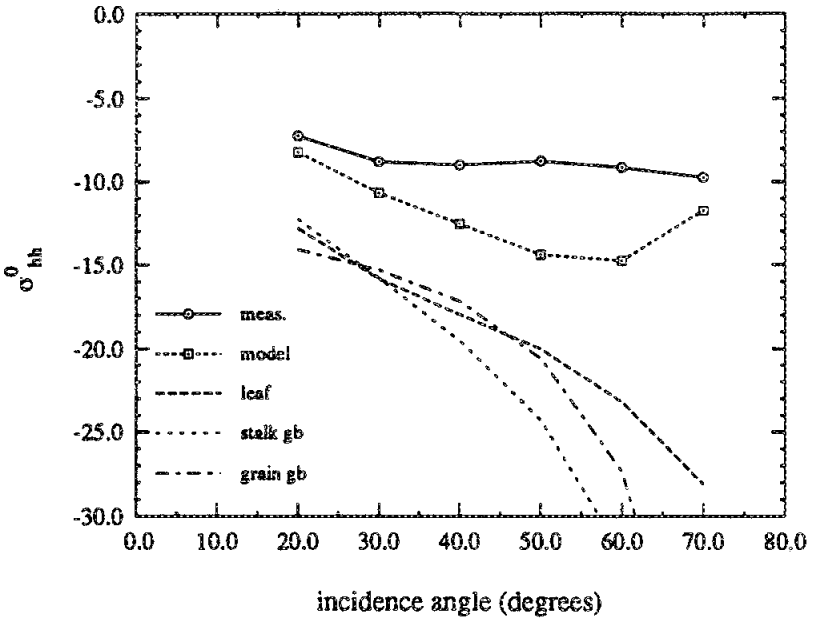

(b)

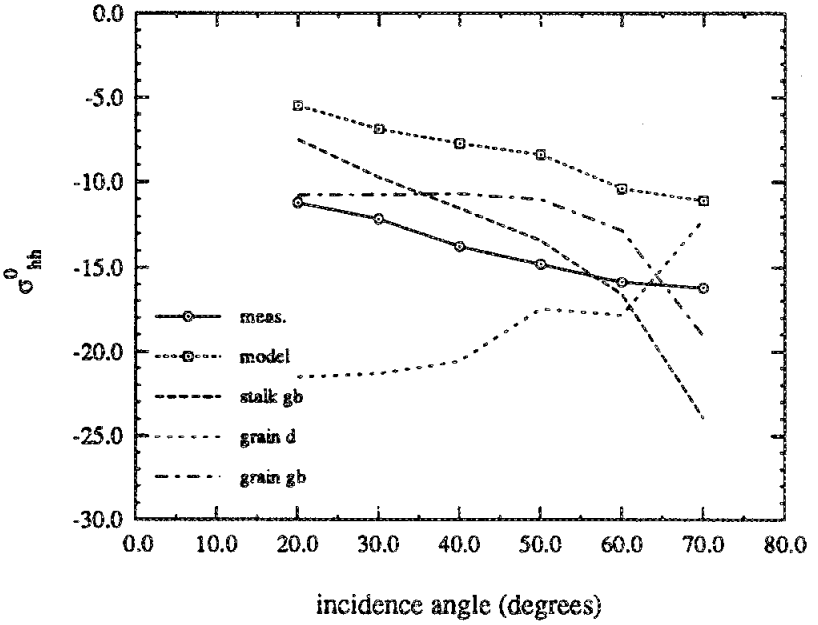

Figure 7.30: The measured and modeled backscattering coefficient σ^0_{hh} at X-band, plotted as a function of incidence angle for (a) June 10 and (b) July 7.

(a)

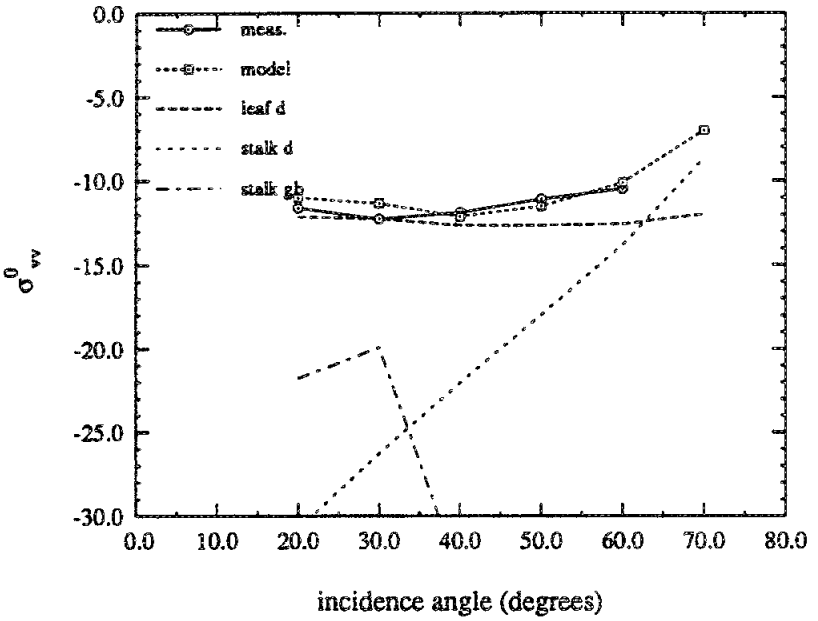

(b)

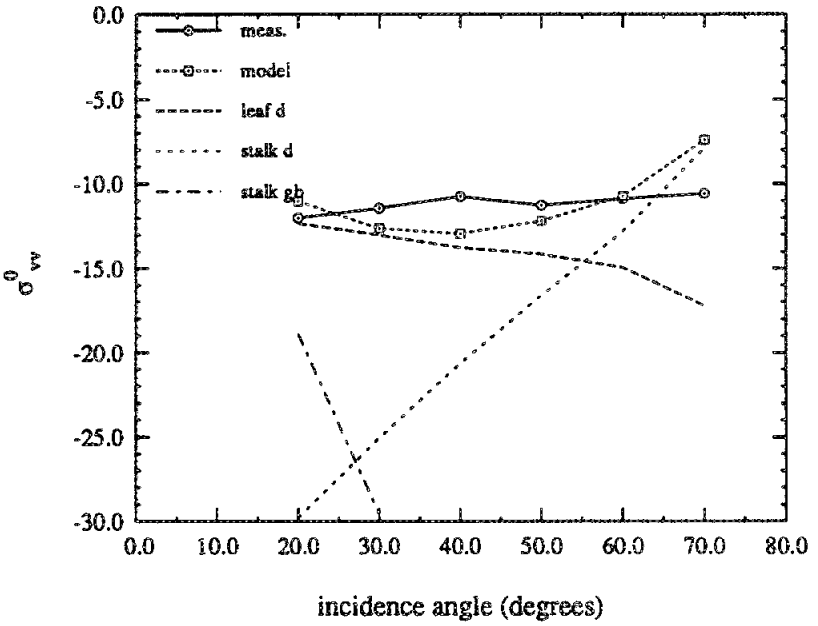

Figure 7.31: The measured and modeled backscattering coefficient σ^0_{vv} at X-band, plotted as a function of incidence angle for (a) May17 and (b) May 25.

is reduced while the *hh* data increases with the decreasing attenuation of the long, ground-bounce propagation path.

7.4.3 HV Polarization

Determining the cross-pol component for X-band with the numeric model turned out to be problematic. At incidence angles greater than 50 degrees, the model takes a prohibitively long time to compute the data. Figure 7.33 shows data to 50 degrees for the two early test days. As with the other frequencies, the model under estimates the cross-pol data, by an error of as much as 5 dB. The main cross-pol contributor for these cases is shown to be the direct leaf scattering, although this clearly is insufficient to explain the measured data. As before, the cause of this erroneous data could be the lack of second-order scattering mechanisms within the model.

7.5 Conclusions

The L-band data demonstrated the importance of the coherent effects on the overall accuracy of the scattering model. Not only was the correlation between dissimilar mechanisms and elements important, but the correlation between the plants of the row structure where shown to dominate when the incidence propagation direction is nearly perpendicular to the rows. The incoherent scattering alone was shown to be inadequate to correctly predict either the magnitude or the behavior of the scattering at L-band, especially for *hh* polarization. Additionally, the Bragg scattering model for periodic row structures was shown to be quite necessary to adequately predict the scattering from the wheat canopy.

For the C and X-band data, the coherent terms were not significant, and thus only

the incoherent scattering was evaluated (with backscattering enhancement). For the *hh* data where the grain head was not present, the model provided an excellent match to the measured data. However, the grain scattering model used for this formulation was apparently insufficient for at least the *hh* polarization, as the model did not fit the measured data particularly well for the days where grain elements were present. The match to *vv* data was mixed, with the errors attributable to the breakdown of the Rayleigh approximation at high frequencies, grain model error, and errors in the extinction formulation which occur for extreme attenuation cases. Additionally, it was found that generally the low attenuation of the *hh* polarization resulted in a sensitivity to the soil moisture, whereas for *vv* the backscattering is independent of soil moisture for all but the smallest incidence angles.

Another important result of this chapter is that the scattering from the rough soil surface was found to be insignificant for all frequencies, polarizations, and incidence angles. However, perhaps the most significant outcome of this chapter is the demonstration of the importance of the shape, in addition to size, of the vegetation elements. Although the structure of elements such as the leaves are often simplified, the model suggests that this can have a tremendous effect on the accuracy of the model.

is not extreme.

However, to determine the polarizability tensor elements required for this formulation, the numerical solution of a set of integral equations is required. The time required for this numerical computation would significantly limit the utility of this formulation, and thus in Chapter III a method for providing the same electromagnetic accuracy at far greater speed was determined. The cross-section shapes encountered in grass canopies are far from arbitrary, generally being either circular or the "vee" shape of a grass blade. Just as a circular cross-section can be defined with a single variable (radius), the general shape of a blade cross-section can be parameterized and defined with a set of variables. In Chapter III, this was accomplished using four variables. By limiting the values of these variables to those observed in nature, a parameter space was therefore defined and bounded. The numerical solution for the polarizability tensor elements was then evaluated a points throughout this bounded space, and the results where used to derive a polynomial approximation relating the blade shape parameters to their polarizability tensor elements. This approximation provides an accurate evaluation of the polarizability tensor for arbitrary blade shapes, but provides also the answer in a fraction of the time required by the numerical solution. In this manner, an element scattering model with great fidelity and accuracy was implemented without harming model utility.

Thus having an accurate scattering model for the elements of a grassland canopy, the next step was to determine the scattering from a collection of these elements above a soil surface. Since a vegetation layer attenuates the incident wave as it propagates through it, the general problem was to determine the scattering of a line dipole element in an extinction layer above a dielectric (soil) half-space. For a number of reasons, radiative transfer is not applicable to grass canopies, so instead a discrete

A clash between accuracy and fidelity again occurred when considering the scattering from the leaf element. The arbitrary curvature of the leaf is considered, but the three random variables used to define this curvature lead to expected value operations with prohibitive computational length. However, it was recognized that these three parameters are correlated, and therefore by performing an eigen analysis on their correlation matrix, the three correlated parameters can be transformed into a new parameter space consisting of independent variables. The variable associated with the largest eigen value will effect the curvature of the leaf the most, thus the other two variables were set to their mean value while the expected value integration is performed over the remaining single variable. In this manner, the fidelity and accuracy of the model is again mostly preserved without adversely affecting model utility.

In addition to the coherent effects which occur between elements, the scattering from the individual plants of a canopy can be significant. This is especially true for row structured canopies, where the periodic vegetation can lead to Bragg effects. Therefore in Chapter V the coherent scattering from this vegetation was likewise determined, in addition to a formulation for the extinction associated with these row structures.

To validate this model, an experiment was conducted in which polarimetric back scattering data was collected for a wheat field over its entire growing season. To provide a wide range of data, measurements were taken at L, C and X band frequencies, as well as incidence angles from 20 to 70 degrees. In addition, an extensive set of ground-truth data was measured for each test day. The measured data showed that at L-band, the scattering varied greatly over a wide range of azimuth angles. Additionally, the scattering peaked at around forty degrees incidence, and then dropped precipitously as incidence angle increased. Another scattering behavior much differ-

at high frequencies) was significantly reduced when the grain elements were present. Therefore, it is recommended that a better formulation be developed and tested. Additionally, the dielectric values for these elements should be determined across frequency, as the starchy material exhibited by grain elements may not fit the El-Rayes dielectric formulation, and thus could also be a source of model error. Another problem which should be addressed is the improvement of the extinction approximation for row structures. Perhaps an approach such as that used by Whitt [36] could be implemented, where a periodic canopy was evaluated by implementing a Fourier series. The opportunities for improving cross-pol are uncertain, generally this is done by adding second-order effects, but a second-order, coherent scattering model would be prohibitively complex. Finally, it is recommended that the data be taken on a simpler vegetation structure than wheat. Specifically, one with no grain element, no row structure, and no thick stalks. This would allow for greater examination of the main theory of this work, and would replicate more closely the non-cultural grass canopies found on the earth's surface.

[11] Kleinman, R.E., and T.B.A. Senior, "Rayleigh scattering", in *Low and High Frequency Asymptotics* (ed. V.K. and V.V. Vardan), North-Holland, Amsterdam, 1986; pp. 1-70.

[12] J.A. Kong, *Electromagnetic Wave Theory*, John Wiley, New York, 1990.

[13] Y. Kuga, M.W. Whitt, K.C. McDonald, and F.T. Ulaby, "Scattering models for distributed targets", in *Radar Polarimetry for Geoscience Applications* (ed. F.T. Ulaby and C. Elachi), Artech House, Norwood, MA, 1990.

[14] K. C. McDonald, M. C. Dobson, F. T. Ulaby, "Using MIMICS to Model L-Band Multiangle and Multitemporal Backscatter From a Walnut Orchard", *IEEE Trans. Geosci. Remote Sens.*, vol. 28, pp. 477-491.

[15] K. C. McDonald, "Modeling microwave backscatter from discontinuous tree canopies", Ph. D. dissertation, The University of Michigan, Ann Arbor, Michigan, June 1991.

[16] Y Oh et al.,"An Empirical Model and an Inversion Technique for Radar Scattering from Bare Soil Surfaces",*IEEE Trans. Geosci. Remote Sens.*, vol. 30, no.2, pp. 370-381, 1992.

[17] A.J. Poggio and E.K. Miller, "Integral Equation Solutions of Three-dimensional Scattering Problems", in *Computer Techniques for Electromagnetics*, (ed. R. Mittra), Hemisphere Publishing, New York, 1987.

[18] W. H. Press, *Numerical Recipes*, Cambridge: Cambridge University Press, 1989.

[19] Ruck, G.T., D.E. Barrick, W.D. Stuart and C.K. Krichbaum, *Radar Cross Section Handbook, Volume 1*, Plenum Press, New York, 1970.

[20] K. Sarabandi, P.F. Polatin and F.T. Ulaby, "Monte Carlo Simulation of Scattering from a Layer of Vertical Cylinder", *IEEE Trans. Antennas Propagat.*, vol. AP-41, pp. 465-475, April 1993.

[21] K. Sarabandi, T.B.A Senior, "Low-frequency scattering from cylindrical structures at oblique incidence," *IEEE Trans. on Geoscience and Remote Sensing*, Vol. 28, No. 5, pp. 879-885,1990.

[22] K. Sarabandi, "Derivation of Phase Statistics from the Mueller Matrix" *Radio Sci.*, vol. 27, No. 5, pp. 553-560, 1992.

[23] K. Sarabandi et al, "Measurement and Calibration of Differential Mueller Matrix of Distributed Targets", *IEEE Trans. Antennas Propagat.*, vol. AP-40, no. 12, pp. 1524-1532, 1992.

[24] K. Sarabandi et al, "A Convenient Technique for Polarimetric Calibration of Single-Antenna Radar Systems", *IEEE Trans. on Geoscience and Remote Sensing*, vol. 28, no. 6, pp. 1022-1033, 1990.